Université de Limoges

ED 653 : SCIENCES ET INGENIERIE

Institut de recherche XLIM

Thèse pour obtenir le grade de **Docteur de l'Université de Limoges**

en Sciences et Ingénierie pour l'Information

FABRICATION AND CHARACTERIZATION OF GREEN LIGHT-EMITTING DIODES BASED ON HALIDE PEROVSKITES

Présentée et soutenue le 19 Décembre 2023

par **QUANG-HUY DO**

Dirigée par Bernard RATIER et Johann BOUCLÉ

JURY

Présidente du jury

Mme. Emmanuelle Deleporte, Professeure, ENS Paris-Saclay

Rapporteurs

M. Georges Zissis, Professeur, Université Toulouse III Paul Sabatier

M. Dmitry Aldakov, CNRS CR1 chercheur, IRIG/SyMMES – CEA Grenoble

Examinateurs

M. Rémi Antony, Maître de conférence, Université de Limoges

M. Bernard Ratier, Professeur, Université de Limoges

M. Johann Bouclé, Professeur Associé, Université de Limoges

" Tình bằng có cái trống cơm

Khen ai khéo vỗ

Ố mấy bông mà nên bông

Ố mấy bông mà nên bông."

- *"Trống cơm"*, a Vietnamese folk song -

ABSTRACT

Over the last decade, many studies have attempted to progress light-emitting diodes based on halide perovskites (PeLEDs) in terms of brightness, efficiency, or stability and exploit their uses in diverse contexts, from display technology to lighting and even biomedical imaging. In this thesis, we studied different strategies for the development of efficient and reliable green PeLEDs towards potential applications in optical wireless communications or high-resolution displays. First, the fabrication process of conventional PeLEDs based on bulk halide perovskites was carefully examined, revealing essential impacts of extraneous variables associated with glovebox environment on perovskite crystallization and device-to-device reproducibility. Consequently, a set of best practices for polycrystalline perovskite deposition in inert environment was proposed to ensure acceptable device repeatability. Then, based on this foundation, we aimed to improve the efficiency of PeLEDs by employing novel emissive materials based on perovskite quantum dots (QDs) synthesized via soft-chemistry route. In particular, an original method to incorporate the perovskite colloids with high-processability inert polymers was introduced to enable the deposition of high-quality emissive thin films. Subsequently, the PeLEDs constructed from these QD/polymer composite materials demonstrated remarkable performance metrics, marking the first successful application of the soft-chemistry-synthesized perovskite QDs in optoelectronic devices. Lastly, an innovative strategy to enhance light-outcoupling efficiency in PeLEDs via nanostructuration of the bulk perovskite emissive layers was exploited. Although desirable morphological, optical, and electroluminescent properties of the perovskite metasurfaces have been observed, consistently producing high-quality perovskite photonic structures remained challenging to us due to the reproducibility issue intrinsic to the employed nanoimprint technologies. Nonetheless, this preliminary research lays the groundwork for further investigation into metasurface-driven PeLEDs.

Key words: LED, halide perovskites, electroluminescence, interface

RÉSUME

Au cours de la dernière décennie, de nombreuses études ont tenté de faire progresser les diodes électroluminescentes à base de pérovskites halogénées (PeLEDs) en termes de luminance, d'efficacité ou de stabilité et d'exploiter leurs utilisations dans divers contextes, de la technologie d'affichage à l'éclairage, voire à l'imagerie biomédicale. Dans cette thèse, nous avons étudié différentes stratégies pour le développement de PeLEDs vertes efficaces et fiables en vue d'applications potentielles dans les communications sans fil optiques ou les écrans haute résolution. Tout d'abord, le processus de fabrication des PeLEDs à base de pérovskites halogénées massives a été examiné en détail, révélant les impacts essentiels des variables extérieures liées à l'environnement sous boîte à gants sur la cristallisation des pérovskites et la reproductibilité d'un dispositif à l'autre. Par conséquent, un ensemble de meilleures pratiques pour le dépôt de pérovskites en boîte à gants afin d'assurer une reproductibilité acceptable des dispositifs a été proposé. Ensuite, sur cette base, nous avons cherché à améliorer l'efficacité des PeLEDs en utilisant des points quantiques de pérovskite (QDs) synthétisés par une nouvelle méthode de chimie douce en tant que couche émissive. Une méthode originale d'incorporation du matériau pérovskite avec des polymères inertes à haute aptitude au traitement a été introduite pour permettre le dépôt de films minces émissifs de haute qualité. Ensuite, les PeLEDs construites à partir de ces matériaux composites QD/polymère ont montré des performances remarquables, marquant la première application réussie des QDs de pérovskite synthétisés par chimie douce dans des dispositifs optoélectroniques. Enfin, une stratégie innovante visant à améliorer l'efficacité de l'émission de lumière dans les PeLEDs grâce à la nanostructuration des couches émissives de pérovskite massive a été exploitée. Bien que des propriétés cristallines, optiques et électroluminescentes souhaitables des méta-surfaces de pérovskite aient été observées, la production cohérente de structures photoniques de pérovskite de haute qualité est restée un défi en raison du problème de reproductibilité inhérent aux technologies de nanoimpression utilisées. Néanmoins, cette recherche préliminaire jette les bases pour de futures investigations sur les PeLEDs pilotées par des méta-surfaces.

Mots clés : LED, pérovskites halogénées, électroluminescents, interfaces

ACKNOWLEDGEMENTS

In Vietnamese, we have a saying "Không thầy đố mày làm nên" that emphasizes the importance of the guidance from teachers to their students. Therefore, I am immensely grateful to my supervisors, Bernard Ratier, Johann Bouclé, and Rémi Antony, for their pivotal role in making this project a reality. Their unwavering support and invaluable advice they provided were instrumental in the success of the thesis. Then, I would like to extend my heartfelt appreciation to all my colleagues at XLIM, especially those within our small and dynamic RF-ELITE group: Marie-Laure, Nico, Sébastien, Sylvain, Pierre, Lionel, Issoufou, etc… And, in particular, Gabin, who helped me a lot during my initial days at XLIM.

I wish to express my sincere gratitude to the French National Research Agency for providing vital funding for this thesis within the framework of the EMIPERO and STRIPE projects. Moreover, I would like to acknowledge the outstanding efforts and expertise of our esteemed partners at LUMIN and INL: Dr. Cedric Mayer and my dear colleague Hugo Levy-Falk from LUMIN for their invaluable contributions in our research concerning perovskite quantum dots; and Dr. Hai-Son Nguyen, Dr. Christian Seassal, Dr. Chevalier Celine, Dr. Emmanuel Drouard, Dr. Raphael Mermet-Lyaudoz, and the diligent PhD student Trong-Tam Nguyen for the active participation in our study with perovskite metasurfaces.

I also want to give a huge shout-out to my awesome labmates: Clara, who cheered me up every morning; Ceren, my fellow perovskite warrior; Eva, my kimchi-sharing buddy; Colman, with whom I celebrated birthdays; Mathieu, our reliable driver, and, not to forget, my Brazilian brother, Daniel. You guys have not only been by my side but also added so much joy and unforgettable memories to my days. To Huân and Châu Anh for making our weekends at Limoges more hilarious and cosy. And the list goes on and on with other individuals like Manal, Shuwen, Flavien, Francesco, and many more.

To Dad, Mom, and Sâu who have always supported me unwaveringly and unconditionally, even though sometimes we might have argued, I love my family from the bottom of my heart. To my grandpa who is no longer with us, I carry his memory and the love he gave me close to my soul.

Most importantly, I wish to extend my deepest thanks to my lifetime partner, Vân Nguyễn. Words cannot fully describe how much I appreciate her presence and continuous support throughout this journey. Her support extends beyond mere emotional encouragement as I also wish to acknowledge Vân's invaluable assistance in transporting our samples between Saclay and Limoges. Without her, this thesis would have been significantly more challenging to complete.

Lastly, I would like to acknowledge the support from artificial intelligent tools such as Grammarly and Chat GPT in helping me enhance the writing quality of this manuscript, noted that their employment is limited exclusively to providing suggestions for grammar and vocabulary choices.

CONTENT

LIST OF ABBREVIATIONS

perovskite light-emitting diodes	PeLED
power conversion efficiency	PCE
methylammonium lead bromide	MAPB
methylammonium lead iodide	MAPI
phenylethylammonium	PEA
hybrid organic-inorganic perovskite	HOIP
all-inorganic perovskite	AIP
Ruddlesden-Popper perovskite	RPP
Dion-Jacobson perovskite	DJP
quantum dot perovskite	QDP
highest occupied molecular orbital	HOMO
unoccupied molecular orbital	LUMO
full-width at half-maximum	FWHM
multiple quantum wells	MQW
perovskite solar cell	PSC
perovskite photodetectors	PePD
hole/electron transfer layers	HTL/ETL
hole/electron blocking layers	HBL/EBL
hole/electron injection layers	HIL/EIL
current density - luminance - voltage	J-L-V
external/internal quantum efficiency	EQE/IQE
luminous efficiency	LE
current efficiency	CE
visible light communication	VLC
polyethylene dioxythiophene-polystyrene sulfonate	PEDOT:PSS
1,3,5-Tris(N-phenylbenzimidazol-2-yl)benzene	TPBi
photoluminescence quantum yield	PLQY
oleic acid	OA
Dimethylformamide	DMF
indium tin oxide	ITO
standard deviation	std
atomic force microscopy	AFM
scanning electron microscopy	SEM
focused ion beam	FIB
transmission electron microscopy	TEM

LIST OF FIGURES

LIST OF TABLES

INTRODUCTION

Halide perovskite materials have recently sparked interest among academics working on renewable energy and optoelectronic applications, such as solar cells, light-emitting diodes, lasers, or photodetectors. Amongst these applications, perovskite light-emitting diodes (PeLEDs) are expected to revolutionize the lighting industry thanks to the outstanding characteristics of these materials, including high carrier mobility, defect tolerance, chemically tunable bandgap/color, and emission purity. Over the last decade, many studies have attempted to progress these devices in terms of luminance, efficiency, or stability and exploit their uses in diverse contexts from display technology to lighting and even biomedical imaging. In this thesis, we will study the development of green PeLEDs towards potential applications in underwater wireless communication and high-resolution display.

Accordingly, the first chapter of the thesis will provide an overview of the research on halide perovskites and PeLEDs. It begins by introducing the fundamentals of halide perovskites, including their crystal structures, compositions, optoelectronic properties, and practical applications. Then, we will shift our focus to PeLEDs, providing insights into their principles and characterization techniques before highlighting the state of the art in this domain. Finally, it outlines the scope of the thesis project, defining its objectives and goals.

The second chapter will be dedicated to comprehensively examining the processes involved in the synthesis and fabrication of reference PeLEDs based on bulk halide perovskites, with a focus on their reliability. In the first half, the synthesis and deposition methods for electroluminescent perovskite thin layers will be explained, including the selection of materials, optimization procedures to improve thin-film morphology and emission properties, and the methodology for designing and fabricating practical PeLEDs. These devices will also systematically characterized and optimized to meet specific criteria in term of device performance as well as to collect data for simulations. Then, the other half of the chapter delves into the underlying reasons and solutions for the low reproducibility of PeLEDs based on low-dimensional perovskites. Various experimental set-ups for spin-coating perovskites under inert conditions will be entailed and examined to understand the effects of factors, such as oxygen/moisture concentrations, temperature, and solvent traces, on the formation of the polycrystalline thin films and the variation in PeLED's performance metrics. The chapter concludes by discussing best practices for perovskite deposition in the glovebox to achieve highly reproducible PeLEDs.

The third chapter focuses on developing efficient PeLEDs using perovskite quantum dots (QDs) synthesized via a soft-chemistry method. In detail, the technological difficulties related to the processability of the perovskite QDs that hinder direct deposition of high-quality thin films from this material will be thoroughly studied and discussed, emphasizing the impracticality of realizing operational PeLEDs based on these pristine QD films. Therefore, an innovative approach to incorporate the perovskite material with high-processability inert polymers will be introduced. Subsequently, an

empirical study on the preparation, deposition, and characterization of composite QD/polymer materials will be presented, concentrating on the effects of QD-to-polymer ratio in the fabrication process. As a result, we will demonstrate bright PeLEDs based on these novel composite materials.

The fourth and final chapter will aims at improving light extraction efficiency in green PeLEDs via employing the concept of photonic crystal in order to create a perovskite metasurface with favorable photonic properties. Accordingly, we will begin the chapter with a brief discussion about the current study on perovskite metasurfaces in optoelectronics before detailing our process to design a periodic nanostructure based on bromide perovskite for emission enhancement. We will also explain and investigate the thermal nanoimprint lithography technique and their impacts on the optical characteristics of the quasi-2D perovskite thin films. Consequently, the last section of the chapter will concentrate on integrating these imprinted perovskite layers into our PeLED structure. Indeed, several limitations of the nanoimprint technique in particular and the fabrication process in general will be pointed out, demonstrating the difficulties in manufacturing true metasurface-driven PeLEDs.

Chapter I. CONTEXTUALIZATION OF THE STUDY

1.1   Fundamentals of hybrid halide perovskites

Halide perovskites and hybrid halide perovskites are a class of materials that have recently sparked interest among academics working on renewable energy. Their illustrious history began in the nineteenth century with the discovery of a naturally occurring mineral in Russia's Ural Mountains. The mineral, named after Russian mineralogist Lev Perovski, is a calcium titanate ($CaTiO_3$) compound with a cubic crystal structure and a perovskite-like lattice (Figure I.1.a) [1]. In the 1960s, it was discovered that this structure could be used as a template to synthesize a wide variety of compounds with similar crystal structures, including halide perovskites.

The first halide perovskites were synthesized in the 1970s and 1980s, primarily for solid-state lasers and photodetectors. However, their use in these applications was limited due to low efficiency and poor stability. It was not until 2009 that the potential of halide perovskites in solar cells was discovered when researchers at the University of Tokyo reported a power conversion efficiency (PCE) of 3.8% using a methylammonium lead iodide (MAPI) perovskite thin film [2]. This was a significant breakthrough, as it represented a major improvement over the previous best PCE of 2.2% for a dye-sensitized solar cell. Since then, the development of halide perovskites for photovoltaics has exploded, with researchers worldwide working to improve their efficiency and stability. In addition to their use in solar cells, halide perovskites have shown promise in a range of other optoelectronic applications, including light-emitting diodes (LEDs), lasers, and photodetectors.
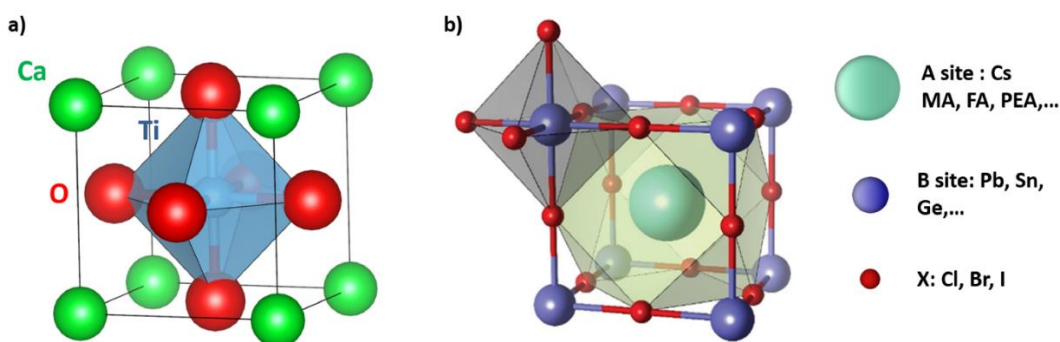
Figure I.1. Similarity in crystal structures of a) CaTiO₃ perovskite [3] and b) cubic halide perovskites [4].

1.1.1 Crystal structure, composition, and dimensionality

Conventionally, halide perovskites exhibit a crystalline structure similar to the natural mineral perovskite and can be described by the general formula ABX_3 (as illustrated in Figure I.1.b). This structure is composed of an inorganic corner-sharing BX_3 octahedral framework and an ammonium cation A occupying the 12-coordinate position of the octahedra. In particular, X represents a halide anion or mix of anions such as chloride (Cl^-), bromide (Br^-), or iodide (I^-). B refers to a divalent metal cation, such as lead (Pb^{2+}), tin (Sn^{2+}), or germanium (Ge^{2+}), where lead is the most common option since lead-based perovskites show strong optical absorption in the visible spectrum as well as high charge carrier mobility

[5], [6]. On the other hand, the *A* cation can either be organic (such as methylammonium (MA$^+$) or formamidinium (FA$^+$)) or inorganic (typically cesium (Cs$^+$)), which distinguishes halide perovskites into hybrid organic-inorganic perovskites (HOIPs) and all-inorganic perovskites (AIPs) [7].

In regards to HOIPs, the size of the organic molecule *A* plays a critical role in determining the dimensionality (i.e., the geometric structure) of the perovskites [8], [9]. For example, when the ionic radius of the organic cation is smaller than 2.6 Å, as is the case with MA$^+$, it can fit into the interstitial spaces between the octahedra to form a compact three-dimensional (3D) network. For organic cations of larger size, the cubic perovskite structure becomes distorted, and the material is composed of thin two-dimensional (2D) layers of metal-halide octahedra stacked on top of one another and separated by organic layers. When the organic spacers are made of bilayers of monovalent ammonium cations, the 2D configuration is called "Ruddlesden-Popper perovskites" (RPPs). Its chemical formula can be expressed as **$(RNH_3)_2(A)_{n-1}B_nX_{3n+1}$**, where *A* and *B* denote cations, *X* stands for a halide, *R* represents an alkyl chain or other functional groups, and *n* determines the stoichiometry or the number of inorganic sheets [10], [11]. Figure I.2.a shows the transitioning of the RPP networks from 3D to 2D with decreasing *n*. Another type of 2D perovskites is "Dion-Jacobson perovskites" (DJPs) with a formula of **$(NH_3RNH_3)(A)_{n-1}B_nX_{3n+1}$**, in which the spacing cations comprise monolayers of divalent organic ammonium [12].
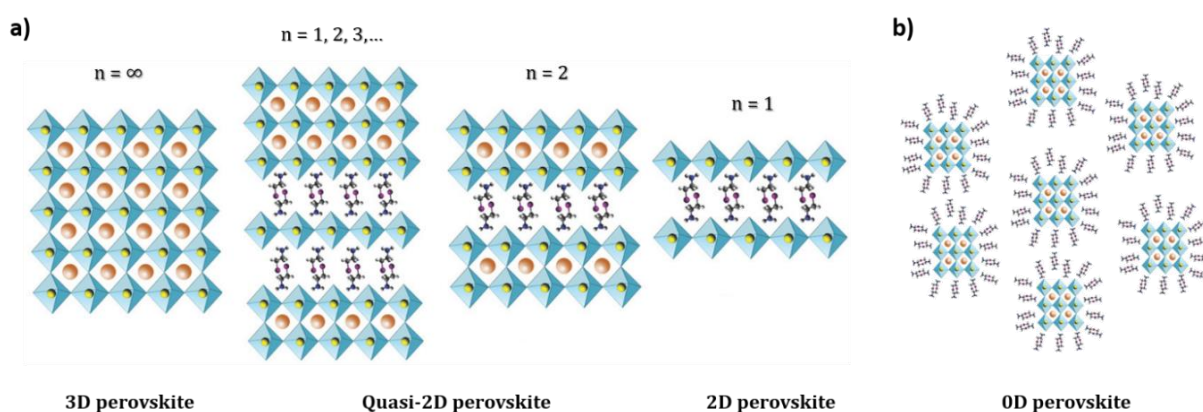
Figure I.2. a) Tailoring perovskite dimensionality via substitution of organic ammonium cations, extracted from [13] and b) Halide perovskite as colloidal nanocrystals.

For $1 < n < \infty$, the layered perovskites can also be classified as low-dimensional or quasi-2D perovskites. Remarkably, it has been observed that quasi-2D perovskite thin films, synthesized using solution methods, consist of a mixture of *n* phases rather than solely of one phase. The composition and distribution of these phases are critical determinants of the perovskite properties [10], [14]–[16].

In addition, the morphology of perovskites can be altered to reduce perovskite crystals into individual octahedra or clusters encircled by surface ligands to obtain colloidal perovskite nanocrystals, or so-called 0D perovskites (but not to be mistaken as a low-dimensional perovskite) or quantum dot perovskites (QDPs) (Figure I.2.b). The most popular perovskite nanocrystal in optoelectronics is currently CsPbBr$_3$; however, there has been a recent shift in focus towards its inorganic-organic counterparts, such as FAPbBr$_3$ [17]–[19].

In summary, the halide perovskite structures provide a high degree of compositional, dimensional, and morphological tunability, which can be leveraged to develop multifunctional compounds with tailored optoelectronic properties.

1.1.2 Optoelectronic properties

a. Optical absorption

The primary characteristic to discuss regarding halide perovskites is their linear optical absorption. Thanks to their direct bandgap (despite ongoing debate on this topic [20], [21]), metal halide perovskites exhibit a relatively high absorption coefficient [22], [23], which allows for high photocurrent output using sub-micron films. For example, the absorption coefficient of MAPI was found to vary between 1.5×10^4 cm^{-1} and 1.3×10^5 cm^{-1} at 550 nm, depending on the estimation methods [22], [24] and to be 0.5×10^4 cm^{-1} at 700 nm [22]. This implies that a thin layer of less than 2 μm thickness of the perovskite material can absorb most of the visible light from the sun. These values, as demonstrated in Figure I.3.a, are comparable to those of other active materials used in solid-state solar cells.
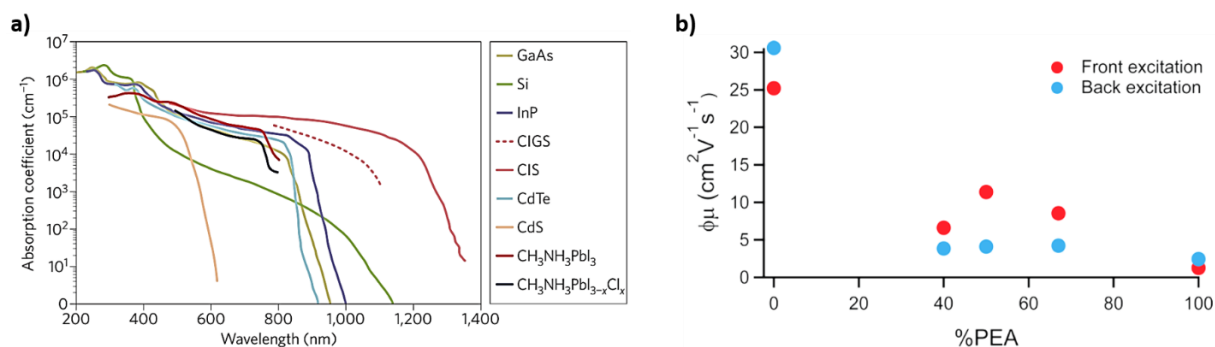
Figure I.3. a) Absorption coefficients of two HOIPs compared to conventional photovoltaic semiconductors [25] and b) Evolution of charge carrier mobility with the dimensionality of mixed MA-PEA iodide perovskites [26].

b. Carrier mobility

Another important feature of halide perovskites is their outstanding carrier mobility considering solution-processed materials [27]–[30], with reported values ranging from a few tens cm^2/Vs (for lead-based perovskites) to several thousand cm^2/Vs (for tin-based perovskites) [31]. The high mobility is attributed to the 3D structure of halide perovskites, which promotes fast charge transport along the inorganic halide layers owing to their high crystallinity and low defect density [30]. When the cubic structure is distorted, such as in low-dimensional perovskites, the effective charge-carrier mobility could decrease by one order of magnitude (Figure I.3.b) [26]. The high carrier mobility of halide perovskites has significant implications for their potential applications in electronic devices. For instance, in solar cells, high carrier mobility can improve the charge collection efficiency and enhance the overall power conversion efficiency. Similarly, in LED devices, fast charge transport is crucial for achieving high light emission efficiency.

c. Bandgap tunability

Apart from their absorption coefficient and charge mobility, the most prominent aspect that distinguishes halide perovskites from other semiconductor materials is their bandgap tunability via

controlling chemical composition or crystal structure [32], [33]. Firstly, tuning the bandgap of halide perovskites can be achieved via homovalent substitution of the B-site cation (e.g., replacing Pb^{2+} by Sr^{2+}, illustrated in Figure I.4.a), which has been shown to widen the bandgap from visible to near-UV regions [34]. Similarly, by varying the composition of the halides X, the bandgap of perovskites can be tuned to cover a wide range of energies (Figure I.4.b) [35]–[37]. Figure I.4.c summarizes the highest occupied molecular orbital (HOMO) and lowest unoccupied molecular orbital (LUMO) values of several 3D perovskite materials commonly found in scientific literature.
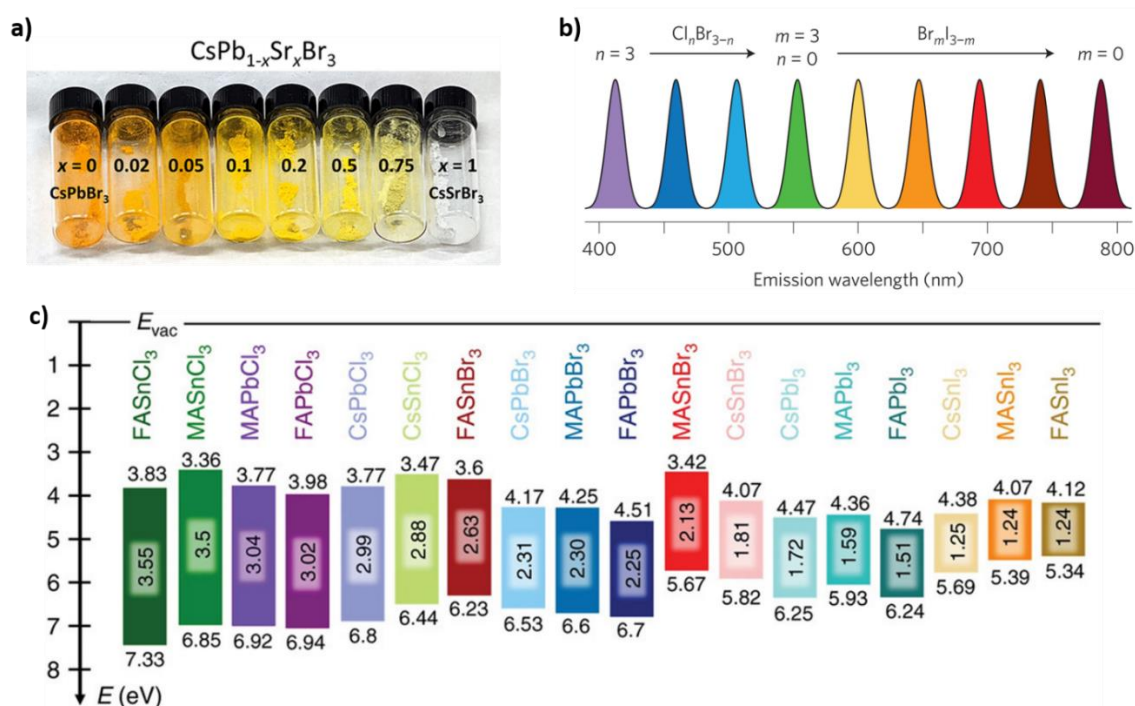
Figure I.4. Optical bandgap tunability in metal halide perovskites via a) substitution of metal cations [34] and b) substitution of halide anions [36], and c) Energy bandgaps of several organometal halide perovskites [38].

Furthermore, the bandgap of halide perovskites can also be tuned by changing their dimensionality (which in turn can be altered via substitution of the A-site cations). The mechanism underlying this effect is intricate, but for quasi-2D lead halide perovskites, it is generally observed that the bandgap increases when the size of the cation is reduced (Figure I.5.a) [39] or the number of inorganic layers is reduced (Figure I.5.b) [40]. On the other hand, morphological engineering, such as in the case of 0D halide perovskites, enables reduce the material's bandgap via increasing the size of the nanocrystals, or vice versa (Figure I.5.c) [41]. Overall, this tunability allows the bandgap of halide perovskites to cover a wide range of energies from visible to near-infrared wavelengths, making them highly versatile for optoelectronic applications. In photovoltaics, by tuning the bandgap of the perovskite absorbers to match the solar spectrum, researchers can optimize the absorption of sunlight and improve the overall efficiency of perovskite solar cells. In lighting applications, bandgap tunability allows tailoring the emitted light's color to match specific requirements.
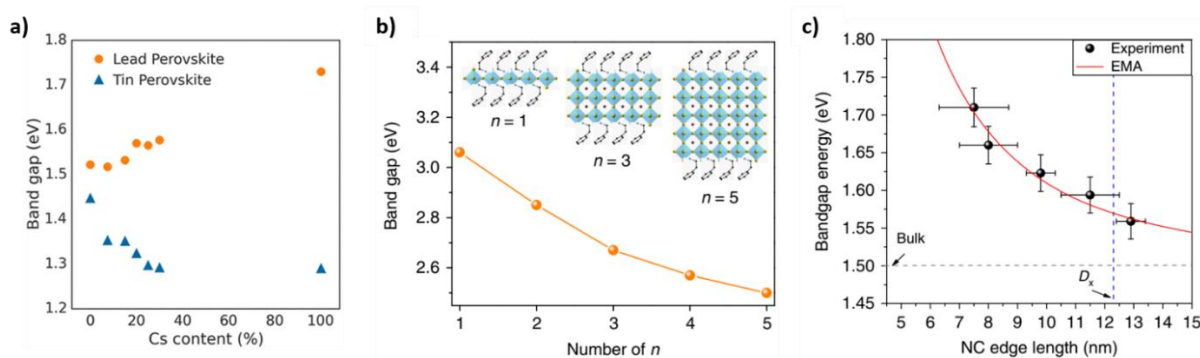
Figure I.5. Optical bandgap tunability via either dimensional engineering in a) all-inorganic perovskites [39], and b) hybrid perovskites [40], or morphological engineering in c) perovskite nanocrystals [41].

d. Defect tolerance and emission purity

Last but not least, halide perovskites are often praised for their superpower of being invulnerable (or, more precisely, less vulnerable) to intrinsic defects or impurities in the crystal structures compared to conventional organic emitters [42]. It is not to say that perovskites' lattices are perfectly defectless; in contrast, the existence of crystallographic imperfections in perovskites, especially when they are synthesized in forms of mono or poly-crystalline films via solution processes, has been widely reported [43]–[45]. Usually, defects in semiconductors induce localized electronic traps inside the bandgaps and severely affect the charge transport properties of the materials. However, in the case of halide perovskites, the defects are more likely to form electronic states close to the band edges (often referred to as "shallow states") such that that these traps are less capable of capturing a charge carrier [46], [47].

Whether halide perovskites are truly defect-tolerant is still a topic of discussion, as several studies have also reported significant impacts of defect states on the performance and stability of perovskite-based devices [48]–[51]. Nevertheless, we can be certain that the combination of shallow defect states, excellent charge transport properties, and inherent bandgap tunability provides an ideal platform for these materials to achieve intense and narrow emission spectra. For example, most perovskite emitters have a full-width at half-maximum (FWHM) of < 20 nm, compared to 30 nm and 50 nm for inorganic QDs and organic semiconductors, respectively [52]. The outstanding color purity will be one of the deciding factors of perovskites' success in display and lighting applications as it enables accurate and vibrant color reproduction with a more comprehensive gamut range [53].

1.1.3 Radiative recombination, exciton, and energy funnel in halide perovskites

Radiative recombination is a key process that governs the efficiency of optoelectronic devices, which involves the emission of a photon when an excited electron in the conduction band combines with a hole in the valence band following an optical or electrical excitation [54]. In metal halide perovskites, the radiative recombination process can be divided into two categories: recombination of free excitons (i.e., bimolecular recombination) and recombination of bound excitons (i.e., monomolecular recombination) [55]. Briefly, excitons are electrically neutral quasiparticles formed when an electron in a semiconductor absorbs energy and moves to a higher energy level, leaving behind a positively charged hole. The electron and hole are held together by Coulomb force, characterized by an exciton binding energy E_b. The strength

of the Coulombic attraction determines whether it is a free exciton ($E_b \ll$ 200 meV) or a bound exciton (E_b of a few hundred meV) [56]. In 3D perovskites, the excitons are loosely bounded and have relatively low binding energies. For example, the E_b of $CH_3NH_3PbI_3$ (MAPI) and $CH_3NH_3PbBr_3$ (MAPB) single crystals have been estimated at 50 meV and 76 meV, respectively [57], while a low-temperature measurement in MAPI polycrystalline thin films revealed an even lower E_b of only 16 meV [58]. This is due to the fact that in 3D perovskites, the excitons are spread out over a large volume of space, which reduces the Coulombic attraction between the electron and hole and weakens the binding. This also means that excitons in 3D perovskites are more easily dissociated into free charges at room temperature, leading to a higher probability of non-radiative losses [59].

To improve the radiative recombination efficiency in halide perovskites, one effective strategy is to modify their electronic structure through reducing the dimensionality to quasi-2D structures [11], [36], [55], [60], [61]. The band structure of RPPs (as shown in Figure I.6) represents self-assembled multiple quantum wells (MQW) formed by the heterostructure of the inorganic sheets and the organic spacers. The inorganic and organic layers can be thought of as alternating wells and barriers, respectively, since the band gap of the inorganic layers is lower than that of the organic layers by at least 3 eV [62]. As a result, charge carriers such as free electrons/holes or excitons can be trapped within the thickness of the inorganic slabs, where they are simultaneously influenced by quantum and dielectric confinement effects [61].

Confinement energies in VB and CB:

$$E_{conf} = \frac{\pi^2 \hbar^2}{2(m_{VB/CB} L_w)^2}$$

(with *m* is the effective mass of the carriers in the VB and the CB correspondingly)

Optical transition energy:

$$E_g = E_g(bulk) + \frac{\pi^2 \hbar^2}{2(m_{VB} L_w)^2} + \frac{\pi^2 \hbar^2}{2(m_{CB} L_w)^2}$$
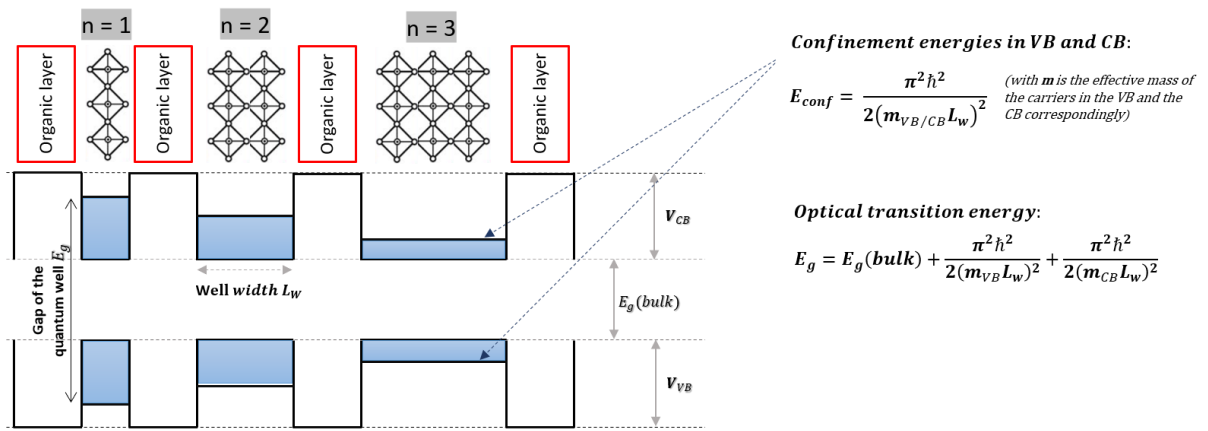
Figure I.6. Energy band variation in MQW perovskites with the increasing number of inorganic layers [63].

While the quantum confinement effect causes a decrease in the material bandgap with the increasing number of the inorganic sheet, the dielectric confinement enhances the interaction between electron-hole pairs and leads to strong excitonic resonances. In fact, experimental data has shown that the optical transition energy of the quantum well decreases as **n** increases, suggesting that the total variation of confinement energies is larger than that of the exciton binding energy [64], [65]. Figure I.7.a illustrates how the photoluminescence of single-phase quasi-2D perovskites changes with the stoichiometry, with increasing **n** resulting in a shift of the emission peak towards the red region.
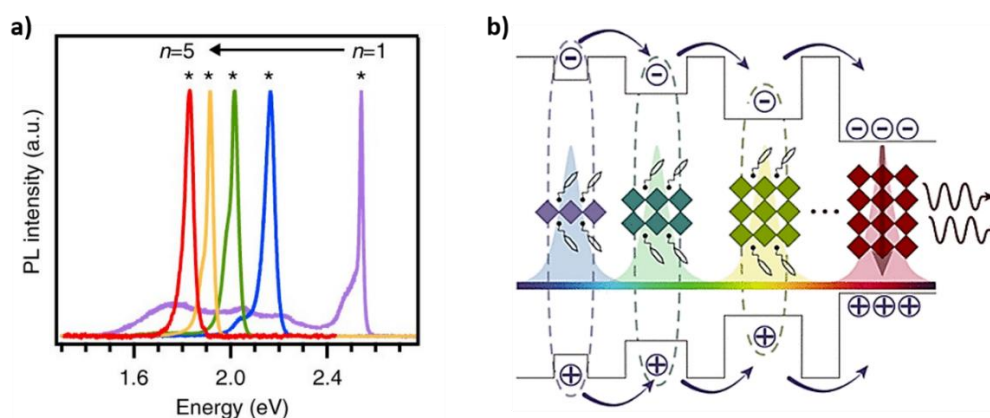
*Figure I.7. a) Photoluminescent spectra of single-phased quasi-2D iodide perovskites with different values of **n** [64] and b) Energy funnel in mixed-phased low-dimensional perovskites [66].*

As mentioned above, quasi-2D perovskite thin films are not typically single-phased but instead composed of nanograins with varying stoichiometry. Energetically speaking, this morphology leads to the formation of a downward energy landscape (as shown in Figure I.7.b), which facilitates the transfer of charge carriers from phases with highest bandgaps (n=1, 2, 3...) to those with lowest bandgaps (n=∞) [66]–[68]. This energy funneling process is highly efficient and occurs on a timescale of 100 femtoseconds to 100 picoseconds, significantly faster than the recombination processes that occur over nanoseconds [67]. As a result, the PL emission peaks of quasi-2D perovskite films, regardless of their phase compositions, are always found similar to or near the peaks of the corresponding 3D perovskites. Additionally, this transfer mechanism allows the charge carriers to be collected and recombined in the lowest-bandgap phases while effectively avoiding defect-related non-radiative recombination, thus enabling high PLQY even under low excitations.

1.1.4 Applications in photovoltaics and optoelectronics

Halide perovskites possess exceptional optoelectronic characteristics, are highly adjustable, and have relatively low production costs, thus giving them the capacity to transform the field of optoelectronics. For the last decade, numerous studies have been conducted to exploit the material for a wide range of applications, including photovoltaics, electroluminescence, photodetection, and lasing. Milestones in the development of perovskite-based optoelectronic devices are consolidated in Figure I.8.

1994:	2009:	2012:	2014:
• First EL device using 2D hybrid perovskite at liquid-nitrogen temperature	• First PSC prototype based on perovskite nanocrystals at room temperature	• Perovskite-based solar cells reach an efficiency of over 10%	• First reports of perovskite LEDs, photodetectors and lasers

2019:	2018:	2016:	2015:
• Solution-processed perovskite tandem cells reach PCE of 23% • PeLEDs achieve 5000-hour lifetime	• PeLEDs reach an EQE > 20% • Electrically pumped perovskite lasers • Perovskite-based X-ray detectors	• Room-temperature perovskite lasers	• PSCs reach EQE > 20%

2020:	2021:	2022:	2023:
• First report of perovskite-based X-ray detectors • Perovskite-based self-powered photodetectors	• White PeLEDs with trapped optical modes • PeLEDs reach EQE of 28% • Large-area PeLEDs maintaining high performance	• Perovskite/silicon tandem solar cells with EQE > 30%	• PSCs achieve a record PCE of 26% • PeLEDs surpass the EQE milestone of 30%

Figure I.8. Key accomplishments in the progress of optoelectronic devices using halide perovskites between 1994 and 2023.

a. Perovskite solar cells

Firstly, perovskite solar cells (PSCs) have received significant attention in the past decade because they are highly efficient and inexpensive to manufacture. The first reported PSCs in 2009 by Kojima et al. utilized MAPB and MAPI nanocrystals, having a power conversion efficiency (PCE) of only 3.8% [2], mainly due to the poor charge transport and low stability of the perovskite material. However, in the following years, the PCE of PSCs rapidly improved due to the introduction of new materials and fabrication methods. In 2012, solid-state PSCs were reported with the use of organic hole-transporting materials and inorganic electron-transporting materials to help improve the charge transport in the devices, leading to a PCE of 9.7% [69]. The development of mixed halide perovskites and low-dimensional perovskites also contributed to the evolution of PCE in PSCs thanks to the improved stability to moisture and favorable energy landscape [70]–[75]. In addition, the introduction of anti-solvent methods [76]–[78], together with the optimization of the perovskite film thickness [79], [80], has led to further improvements in PCE. Furthermore, utilizing tandem structures, which combine multiple layers of perovskites with different bandgaps or alternative cells of perovskite and silicon, has exhibited PCE values approaching 30% [81]–[83]. To date, researchers at KAUST Solar Center achieved a PCE of 33.7% with their tandem perovskite/silicon solar cells, breaking the efficiency barrier [84]. The remarkable improvement of PCE in PSCs over the last 14 years is demonstrated in Figure I.9.
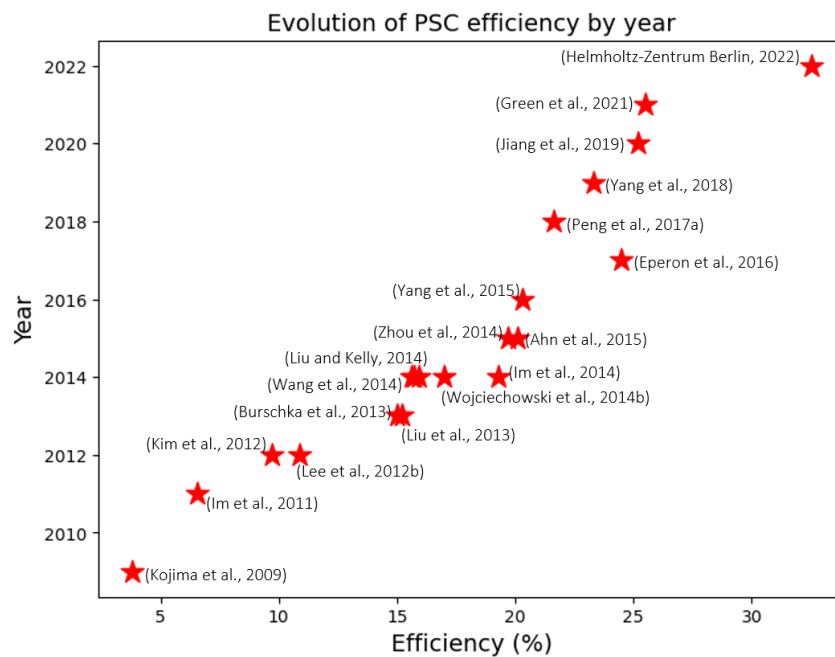
*Figure I.9. Rapid development of perovskite solar cells in the period between 2009 and 2022
(The statistics are extracted from [85]).*

b. Perovskite photodetectors

Secondly, halide perovskites are also a promising material for use in photodetectors. An example of X-Ray detectors based on low-radiative perovskite films is shown in Figure I.10.a. In fact, photodetectors made from halide perovskites can be built with different device architectures, such as photodiodes, phototransistors, or photoconductors, each with their own benefits and drawbacks in terms of device performance [86]. The initial work on halide perovskite photodetectors (PePDs) began in 2014, with the first devices based on MAPI showing high responsivity and quantum efficiency [87]. However, the long-term stability of these devices was a major concern due to the instability of perovskite materials when exposed to moisture and air. Subsequent research has focused on improving the stability and performance of PePDs. One approach has been introducing different cations and anions to the perovskite structure to enhance its stability [88], [89]. For example, all-inorganic PePDs showed higher stability than HOIP-based devices [90]. Another approach has been to modify the device structure in order to reduce the impact of defects and enhance charge transport [91], [92]. In recent years, researchers have made significant progress in developing PePDs with high sensitivity, fast response times, and stability [93]–[96]. To the best of our knowledge, PePDs have demonstrated a record responsivity of up to 132 A/W [97] and a detectivity of up to 10^{14} Jones [98], making them among the most sensitive photodetectors available.
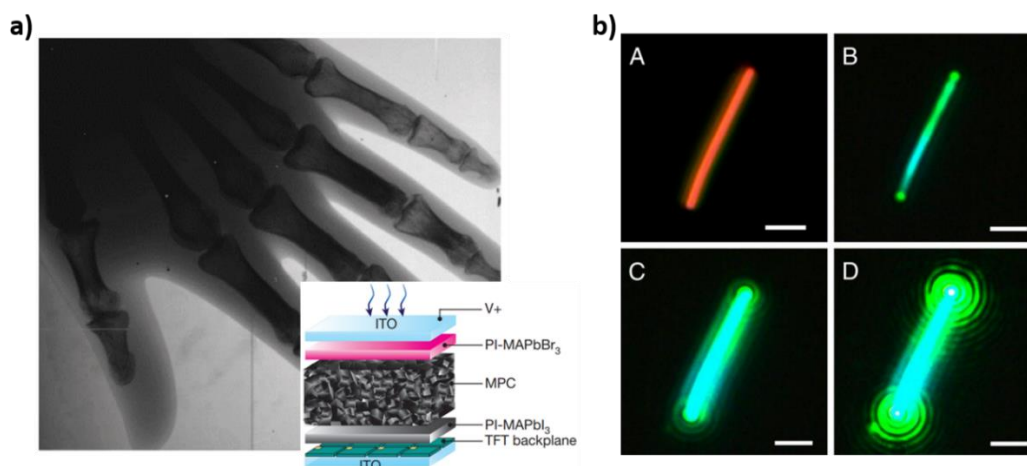
Figure I.10. a) An example of X-Ray detectors based on solution-processed hybrid perovskites developed by Samsung Electronics (the inset showing the device structure), extracted from [99] and b) Lasing effect from a 1D all-inorganic perovskite under increasing optical excitation, extracted from [100].

c.   Perovskite light-emitting diodes

Thirdly, PeLEDs have taken the spotlight in the last decade due to their high luminous efficiency, color purity, and tunable emission. A prototype of PeLEDs at room temperature was published in 2014 by Tan et al., which used organic-inorganic halide perovskite materials as the active layer [101]. Since then, various perovskite materials have been explored, such as all-inorganic $CsPbX_3$ (X = Cl, Br, I), mixed-cation perovskites, and hybrid organic-inorganic perovskites [11], [14], [55], [60], [102], [103]. The choice of perovskite materials depends on their optoelectronic properties and stability under operating conditions. For example, all-inorganic perovskites have excellent stability and high quantum yield, while mixed-cation perovskites can offer tunable emission. The performance of PeLEDs has improved significantly over the years, from initial reports of external quantum efficiency (EQE) below 1% to the latest record of EQE exceeding 30% (as of May 2023) [104]. Such improvement can be attributed to several factors, such as better material quality, optimized device structures, and improved device processing techniques. A precise review and more thorough description of these aspects will be provided in the following section of the chapter.

d.   Perovskite lasers

Last but not least, it is worth mentioning another optoelectronic application of halide perovskites, namely perovskite lasing light sources. In fact, soon after the first reported PePD, researchers from the University of Cambridge reported the first room-temperature perovskite lasers by sandwiching a thin film of mixed halide hybrid perovskites between two reflective mirrors, forming a Fabry-Perot laser cavity [105]. It was able to tune the coherent light emission across a broadband spectrum between 390 nm and 780 nm, with a low threshold of 12 $\mu J/cm^2$. Since this breakthrough, researchers have been investigating various perovskite materials for laser applications. One promising development is the use of hybrid perovskites to create optically-active materials with improved stability and photoluminescence properties [106]–[109]. Additionally, perovskite nanocrystals (mostly cesium lead halide) have been shown to exhibit excellent photoluminescence properties, with high quantum yields and narrow emission

linewidths, rendering them attractive candidates for laser sources (Figure I.10.b) [110]–[113]. More recently, electrically pumped perovskite lasers have emerged as an exciting development, in which a voltage is applied to the perovskite material to induce stimulated emission, eliminating the need for an external light source [114]. This has the potential to enhance the efficiency and compactness of perovskite lasers, enabling new applications in portable and wearable devices.

1.2 Focus on perovskite light-emitting diodes (PeLEDs): overview and challenges

The development of LEDs has revolutionized the lighting industry due to their several advantages over traditional lighting sources such as incandescent and fluorescent bulbs. Unlike incandescent bulbs, which convert only about 10% to 20% of the electrical energy into light and the rest into heat, LEDs can convert up to 93% of the electrical energy into light [115], [116]. Moreover, they have a lifespan of around 50,000 hours, much longer than traditional bulbs [117], making them highly energy-efficient and cost-effective while reducing environmental impacts.

PeLEDs are the latest and fourth generation of the LED family [118]–[120]. First-generation LEDs utilize inorganic materials, such as gallium arsenide (GaAs), and have a basic p-n junction structure. These initial LEDs produce point sources and must be encased in epoxy capsules. Conversely, the second generation of LEDs uses organic materials, such as polymers or small molecules, and has a more intricate multilayer structure. Organic LEDs, also known as OLEDs, produce area sources and can be employed in small, flexible displays, providing advantages such as high efficiency, a wide range of colors, and viewing angle. The third generation of LEDs, called QLEDs, utilizes quantum dots to broaden the color gamut and reduce energy consumption, making them a major player in today's high-end display market. After OLEDs and QLEDs, PeLEDs are anticipated to revolutionize the lighting industry due to the outstanding optoelectronic properties of halide perovskites.

1.2.1 Principles of perovskite light-emitting diodes

A PeLED operates based on the principle of electroluminescence, which is the ability of certain semiconductors to emit light in response to electrical excitation. It consists of a thin-film stack of several layers, including electrodes, hole-transfer layers (HTL), electron-transfer layers (ETL), and an active layer made up of a halide perovskite material, as illustrated in Figure I.11.a. When a forward bias is applied, electrons and holes are injected into the emissive layer via the ETL and HTL respectively, leading to the formation of excitons. These excitons decay radiatively, emitting energy as photons (Figure I.11.b). The color of the emitted photons is determined by the energy bandgap of the perovskite material [60], [121].
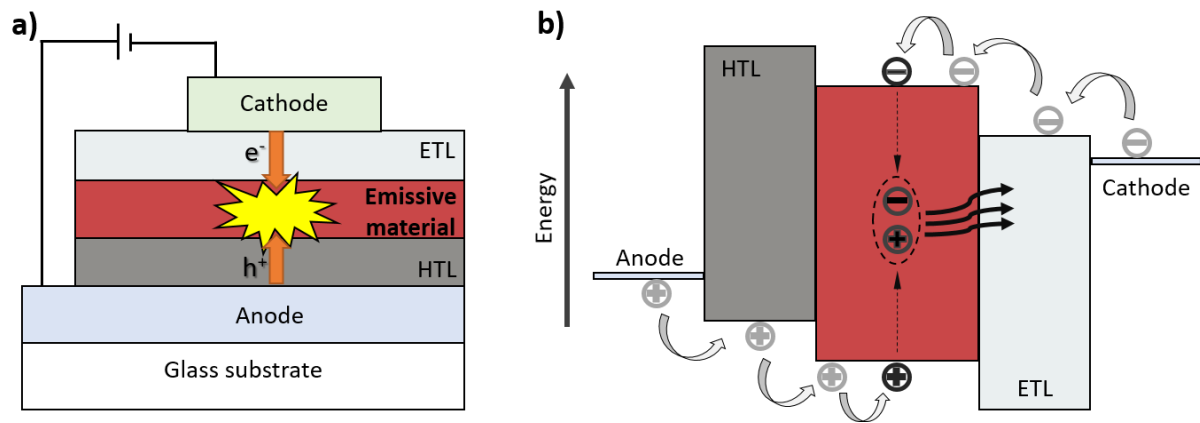
Figure I.11. a) Device structure of a typical PeLED (modified from [122]) and b) Illustration of the electroluminescent process in a PeLED [60].

In addition to the radiative recombination, several optoelectronic processes occur and compete simultaneously in PeLEDs. One such process is non-radiative recombination, in which an electron and a hole combine and release their energy as heat instead of light [123]. Non-radiative recombination can occur through several mechanisms (Figure I.12), such as:

- Defect-induced recombination: Any impurity or defect in the crystal lattice acts as a trap for charge carriers that are present in the material. When a charge carrier is trapped, it can become immobilized or release its energy and recombine with an opposite charge carrier, leading to energy loss and reduced device efficiency.

- Auger recombination: An excited charge carrier can transfer its excess energy to another charge carrier rather than emitting a photon and returning to its ground state. The second charge carrier then gains enough energy to create a third, high-energy carrier through a non-radiative process. The third carrier can then contribute to further recombination or lead to other undesirable effects, such as heating or breakdown of the material. Auger recombination occurs mostly in high-injection regimes when carrier densities are large.

- Interface-induced recombination: When two materials are brought into contact, an energy misalignment occurs at the interface due to the difference in their energy levels. This band discontinuity can trap charge carriers at the interface, which can then decay non-radiatively.
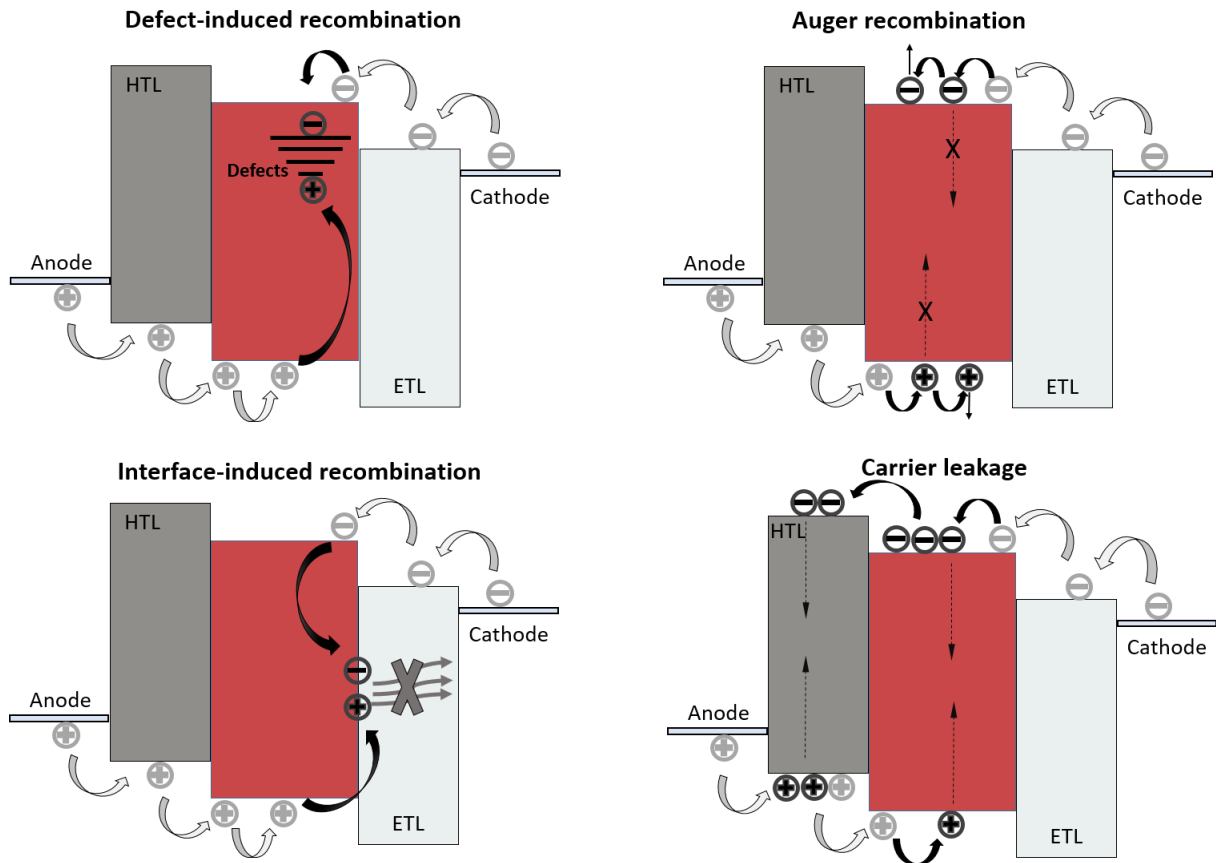
Figure I.12. Non-radiative recombination pathways in PeLEDs.

Another process is carrier leakage, which occurs when electrons or holes escape from the active region of the LED without recombining radiatively, giving rise to a leakage current with no light out of the device. Carrier leakage can therefore reduce the efficiency of a PeLED by reducing the number of electrons and holes that contribute to light emission. To minimize carrier leakage, the active region of the LED is typically sandwiched between layers of materials with higher bandgap energies, which act as barriers to carrier diffusion. It is also crucial to ensure a homogeneous active layer area without pinholes to avoid such processes.

Indeed, the secret sauce behind the design of an efficient LED lies in the balance control of charge injection (i.e., the number of injected electrons equals those of injected holes) and the confinement of excitons within the emissive layer. Therefore, PeLED designs often comprise other functional layers, such as hole/electron injection layers (HIL and EIL), which are used to reduce the energy barriers and facilitate the injection of charge carriers between the electrodes and the charge transport layers, or hole/electron blocking layers (HBL and EBL), which can prevent holes or electrons from diffusing into the opposite charge transport layers and confining the excitons inside the active semiconductor. Furthermore, a material can play several roles simultaneously, such as an ETL with a deep HOMO level can sufficiently prevent hole leakage without using any specific HBL.

1.2.2 Characterization of PeLEDs

a. Electrical characteristics

An LED, first of all, is a diode; therefore, it is important to characterize its electrical behaviors by measuring the evolution of the current passing through the device in response to the bias voltage, such as the current-voltage (I-V) curve. However, in LED studies, the current density-voltage (J-V) curve, which is the normalization of the current by the active area of the device, is more popularly used as it allows researchers to encounter the LED's size or geometry when comparing devices with different designs. Different information can be collected by analyzing the J-V plots, such as:

- The ***forward voltage V_F***: at which the current starts to flow through the diode. In an ideal diode, this value will correspond to (but not necessarily equal) the energy bandgap of the semiconductor material. Yet, in practice, it is not always straightforward where V_F is on the curve since the diode cannot switch from resistive to conductive mode instantaneously but rather exponentially [124].

- ***Leakage current***: In practice, the LEDs might allow a small "leakage" current to flow even at a voltage below V_F. For example, in high-performance OLEDs, a negligible current of $< 10^{-4}$ mA/cm^2 can be typically measured under the forward voltage [125]. On the other hand, this value of PeLEDs can vary significantly between 10^{-5} mA/cm^2 [15] to 10^{-0} mA/cm^2 [126], depending on the device structures and the perovskite materials. By analyzing the amplitude of such leakage, one can have insights into the imperfections in the perovskite layer itself (such as the existence of pinholes or defects) or in the design of the multilayer structure (such as the choice of the charge transfer/injection/blocking layers).

b. Optical characteristics

Figure I.13 shows standard experimental set-ups to measure the emissivity of PeLEDs [127]. The first technique involves using a photodiode with a larger surface area than the LED to collect emitting photons in the forward direction. This approach provides a straightforward way to measure the LED's output, but it does not account for all of the light emitted from the LED, and one needs to precisely evaluate the solid angle of the emission cone towards the photodetector to extract the absolute luminance value. A more comprehensive technique involves using an integrating sphere to capture all emitted photons, thereby providing a more accurate measurement of the LED's output.
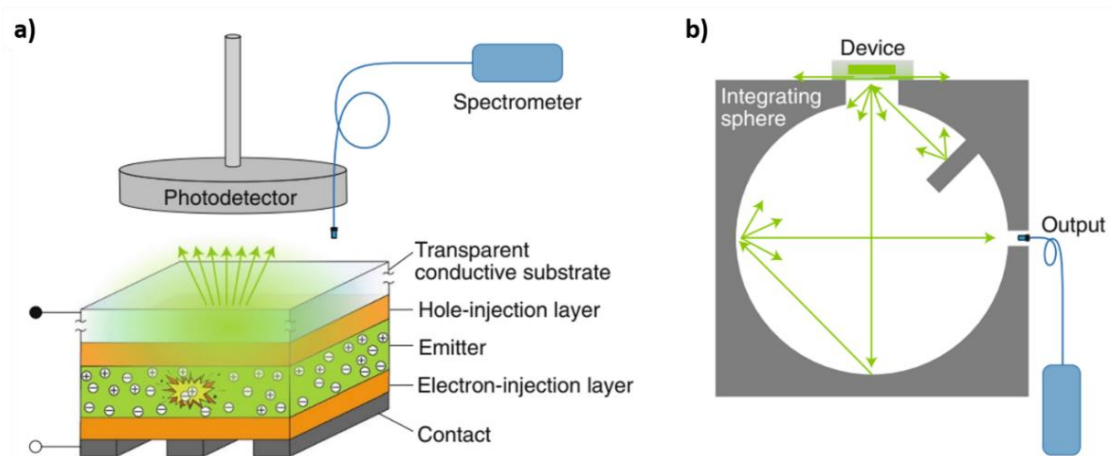
Figure I.13. Two different methods for characterizing PeLEDs are available: a) using a photodiode with a large active area and a spectrometer placed close to the LED, and b) using an integrating sphere [127].

To evaluate the optical behavior of a PeLED, we need to consider various parameters as follows:

1) Emission color:

- ***EL spectrum***: The distribution of colors, or photon wavelengths, emitted from the EL process is a crucial factor in determining the color rendering properties of the LED. Generally, characterizing the emission wavelength involves using a spectrometer or spectrophotometer to measure the intensity of light emitted by the LED in the free space and at a specific solid angle at different wavelengths (as show in Figure I.13.a). The resulting spectrum can be used to deduce the LED's dominant emission wavelength and spectral bandwidth.

- ***Color purity***: Furthermore, it is necessary to characterize the width of this emission to determine if the emitted light is composed of a single or a specific interval of wavelengths, often referred to as color purity. In other words, it is a measure of how "pure" or "intense to the eye" a color appears without involving a large mixture of colors. The color purity of a LED can be associated with the FWHM of the device's spectral bandwidth.

- It should also be noted that color purity is not the only factor that determines the perceived color of an illuminant. Other metrics such as color temperature, color rendering index, and luminous efficiency can also indicate how a color appears to the human eye. For example, the ***color temperature*** of an illuminant (measured in Kelvin) describes its color appearance (warm to cool) by reference to the temperature of an ideal black-body radiator of the same color, while the ***color rendering index*** (characterized on a scale from 0 to 100) measures its ability to reproduce colors as they would appear under natural daylight accurately.

2) Emission intensity:

- ***Radiance (R)***: The brightness of an emitter (either UV, visible, or infrared) can be measured in terms of radiance, which is the power of emitting photons divided by the active area of the LEDs and the effective solid angle, with a unit of W/m^2sr^2.

- ***Luminous intensity***: Particularly for visible LEDs, it is more meaningful to take into account the sensitivity of human eyes in perceiving the emitted wavelengths by measuring the visual luminous

intensity. It quantifies the power of light per unit solid angle in a specific direction. The SI unit for luminous intensity is the candela (cd).

- **_Luminance (L)_**: By normalizing the luminous intensity to the active area of the light source, we will get its luminance, expressed in a unit of candela per square meter (cd/m²).

- **_Luminous flux_**: Another way to quantify the emission intensity of a visible illuminant is using luminous flux, which is the total amount of visible light emitted by the LED per unit of time, expressed in lumens (lm). One lumen equals one candela multiplied by one steradian.

- **_Luminance-voltage (L-V) curve_**: Although researchers typically focus on the maximum luminance to advertise their devices, it is crucial to examine the luminance of an LED as a function of applied voltage. The L-V curve is beneficial for assessing the LED's performance and optimizing its operation for specific applications.

- **_Turn-on voltage (V_{ON})_**: The L-V curve allows us to define the minimum driving voltage required for a device to start emitting, usually determined at a luminance of 1 cd/m². However, in this report, since the precision of our photodetectors is higher than this value (varying around 5 cd/m²), we will use a threshold of 10 cd/m^2 to determine the V_{ON} values of our devices.

c. Device efficiency

From the measurements of the electrical input and optical output, we can easily deduce the efficiency of the energy conversion process in a PeLED, which can be expressed either in terms of external quantum efficiency, luminous efficiency, or current efficiency:

- **_External quantum efficiency (EQE)_**: is the ratio of the number of photons emitted by the LED in the free space to the number of electrons injected into the LED. Another way to describe EQE is a multiplication of all intrinsic efficiencies of correlative processes that occurs inside the device, such as:

EQE = Efficiency of charge injection × Efficiency of radiative recombination × Efficiency of light extraction
(Equation I.1)

In detail, the efficiency of charge injection indicates the proportion between the number of charge carriers injected into the emissive layer and the total number of charge carriers passed through the device. Next, the efficiency of radiative recombination refers to the number of electron-hole pairs that can radiatively recombine compared to the total number of excitons formed inside the emissive layer. Lastly, the efficiency of light extraction, also called outcoupling efficiency, is the fraction of light that can successfully escape the LED and propagate into the free space [103].

- **_Luminous efficiency (LE)_** is the ratio between the output luminous flux and the input electrical power, measured in lm/W.

- **_Current efficiency (CE)_** represents the luminous intensity produced by the device per unit of electrical current flowing through it, expressed in units of cd/A.

It is clear that all three quantities are closely correlated as they are just different tunes of the same song; for example, a higher EQE will contribute to higher LE and CE and vice versa.

d. Device stability

In addition to luminance and efficiency, it is important to consider device stability, which reflects the reliability and consistency of the LED's performance over time and under varying operating conditions. The most basic measure to assess the operational stability of an LED is its ***operational lifetime*** which refers to the duration that an LED can operate before its performance degrades to a specified level or the device fails completely [127], [128]. The device lifetime is typically characterized using T_{50}, T_{70}, or T_{95}, representing the time it takes for the LED's performance metrics (such as luminance or EQE) to degrade to 50%, 70%, or 95% of its initial value, respectively. Typically, the lifetime measurement should be conducted at a meaningful value of initial luminance, such as 100 cd/m^2 or 1,000 cd/m^2 [128]; it is noted that this initial value can impact the outcome of the measurement. Other performance metrics can also be used to define the end of life of an LED, such as color shift or failure of electrical contacts.

In this report, because of the relatively short lifetimes of our devices as well as significant device-to-device variability in their key performance metrics, we cannot set a specific brightness or efficiency value at the beginning of our stability test. Instead, another approach to measure the lifetime has been chosen, in which we will drive the PeLEDs at a bias voltage corresponding to 70% of the peak luminance based on the L-V curve of the best-performance device in the batch and measure the T_{50} of the devices.

The details of measurement set-ups and calculations employed for PeLED characterization in this manuscript are presented in Annex 1.4.

1.2.3 State of the art in PeLED technology

Since Tan et al. demonstrated operational PeLEDs using three-dimensional halide perovskites at room temperature in 2014 [101], many studies have aimed to improve the luminance, efficiency, and stability of these devices. We can classify the literature on this topic according to their focus and approach:

- Material-focused studies: These studies focus on synthesizing and characterizing halide perovskite materials for use in PeLEDs. They investigate the effects of different processing parameters, such as precursor concentration, temperature, and time, on the optical and electronic properties of the perovskite materials, aiming at improving the intrinsice efficiency and stability of the materials.
- Device-focused studies: These studies focus on the design, fabrication, and optimization of PeLED devices. They investigate the effects of different device architectures, such as planar, hybrid, and perovskite-quantum-dot hybrid, on the efficiency, stability, and color purity of PeLEDs. These studies aim to improve the performance of PeLED devices and make them more suitable for commercial applications.
- Fundamental studies: These studies focus on understanding the fundamental physics and chemistry of PeLEDs. They investigate the mechanisms behind the light emission in PeLEDs, such as the role of defects, excitons, and charge carriers. The objective of these studies is to provide insights into the underlying mechanisms of PeLEDs and guide the design and optimization of PeLED devices.

- Application-focused studies: These studies focus on the practical applications of PeLEDs. They investigate the potential uses of PeLEDs in various fields, such as display technology, lighting, or biomedical imaging, and identify the most promising avenues for their commercialization.

Given the extensive research in this field and the limited space available in this document, our review will concentrate exclusively on *green PeLEDs* as they hold great promise for applications in visible light communication (VLC) and high-resolution display. In particular, underwater wireless communication requires using the visible blue-green band (from 450 nm to 550 nm) to minimize power loss, with which the present technologies of radio or acoustic communication cannot provide satisfactory data rate and bandwidth [129], [130]. The principle of data communication using LEDs as a signal generator - at its core - is via on-off switching of the emitters at very high frequency, which is nevertheless limited by the charge carrier mobilities of the emissive semiconductors [119]. As seen above, halide perovskites with high and balance mobilities for holes and electrons become a favorable candidate to be exploited for fast transmission on large emissive areas. In addition, examples of using halide perovskites as color converters and data receivers in VLC systems have been demonstrated with operating bandwidths of up to 491 MHz and 800 kHz, respectively [129], [131]–[135]. On the other hand, green emission is one of the three primary colors (red-green-blue) in trichromatic pixels, which enable the recreation of full-color images in modern high-definition displays. With the advantages of low-cost manufacturing, superior color purity, and wide color gamut, perovskites are believed to replace conventional organic or quantum-dot materials for high-end display panels in the foreseeable future [53], [136]. Recently, a prototype of green micro-PeLED arrays with a high resolution of 1270 pixels per inch (ppi) was successfully demonstrated at Yonsei University [137], opening a new era in the study of perovskite display technology.

Material-wise, green PeLEDs can be categorized based on the emitting material's morphologies, which generally exist in the forms of polycrystalline thin films and perovskite nanocrystals. More specifically, the first group can be further divided into two sub-classes based on the dimensionality of the perovskite components, including 3D and quasi-2D perovskites.

a. PeLEDs based on 3D perovskite polycrystalline thin films

Early efforts in this field focused on 3D perovskites, with the first visible PeLEDs utilizing MAPB thin films to produce green emission, resulting in a luminance of 400 cd/m^2 and an EQE of less than 0.1% [101]. Subsequent research by Cho et al. revealed that the low efficiency of these early PeLEDs was due to excess Pb atoms that caused exciton quenching as well as trap states from inhomogeneous morphology. To address these issues, they adjusted the molar proportion of MABr in the perovskite precursors to suppress exciton quenching and also introduced a certain amount of antisolvents (e.g., chloroform with and without additives) during the spin-coating process to promote the crystallization rate of the perovskite thin-films. These modifications led to significant improvements in the luminance and EQE of green PeLEDs, with the devices achieving a high luminance of around 10,000 cd/m^2 and an EQE of 8.53% [138]. Cho et al.'s findings have since served as a foundation for subsequent research aimed at enhancing the performance of PeLEDs using 3D perovskites. For example, a research group at the Ulsan National

Institute of Science and Technology proposed a method to grow pinhole-free nanograins in MAPB thin films by adding a bulky amine ligand to chlorobenzene antisolvent. This modification allows the growth of perovskite crystals as small as 30 nm, enabling the realization of highly-efficient PeLEDs with luminance and EQE reaching 55,000 cd/m^2 and 12% respectively [139]. The highlights of these studies are summarized in Figure I.14.
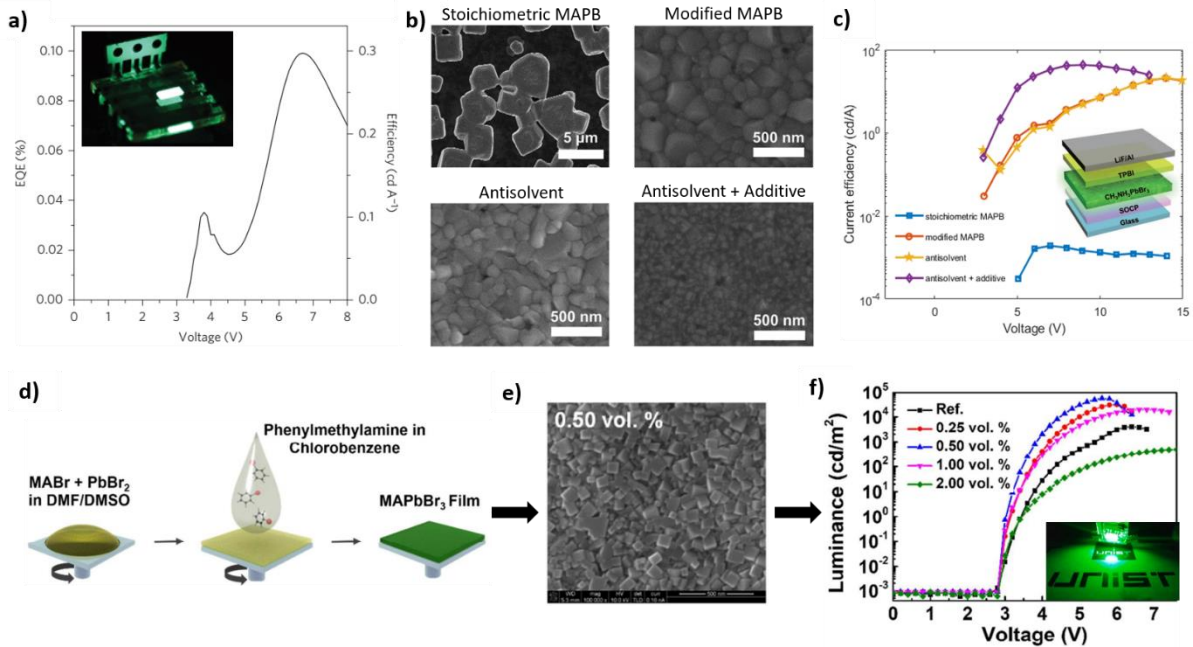
Figure I.14. Morphology engineering in 3D perovskite LEDs: a) The first green PeLED by Tan et al. showing low efficiency [101]; b, c) SEM images of MAPB thin-films deposited via different strategies (top left: MABr:PbBr$_2$ = 1:1, top right: MABr:PbBr$_2$ = 1.05:1, bottom left: antisolvent treatment using pure chloroform, and bottom right: antisolvent of additive-based chloroform) and Current efficiencies of the respective PeLEDs in regard of such strategies, extracted from [138]; d, e, f) Growth and SEM image of a highly crystalline MAPB film using an additive-based antisolvent treatment proposed by Lee et al., and the luminance of PeLEDs fabricated with various concentration of the additive, extracted from [139].

However, the use of antisolvents in perovskite spinning needs to be very precise regarding their volume [140], dropping time, and even dropping distance [141]. Due to these strict requirements, this technique is often characterized by low reproducibility, and automated deposition systems are necessary for consistent results. Another approach to minimize non-radiative recombination in 3D perovskite thin films is surface passivation. In 2017, Lee and colleagues developed green PeLEDs based on bromide perovskites with a maximum luminance of 22,800 cd/m^2 by using amine-based passivating materials to counterbalance the dissipation of Br$^-$ and MA$^-$ ions from the perovskite crystal structure during solvent evaporation (as shown in Figures I.15.a and b) [142]. Another effective strategy for passivating defects in perovskite thin films involves blending transparent polymers, such as poly(ethylene oxide) (PEO) [143]–[146], polyethylene glycol (PEG) [147], or polyimide (PIP) [148], into the perovskite precursors. When spin-coating, the incorporation of these polymers impedes the perovskite precursor from quickly diffusing before crystallization starts and fills the gaps between perovskite grains, leading to the formation of more homogeneous and consistent layers. Additionally, they help enhance the mechanical properties

of the emissive thin films, such as stretchability, making them compatible with applications in flexible displays.
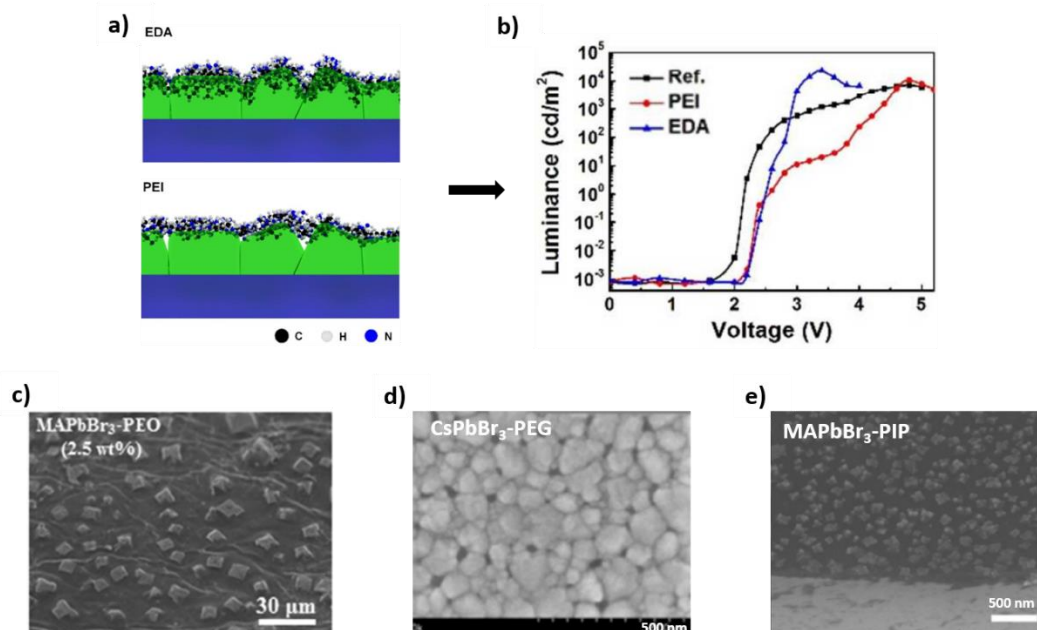
Figure I.15. Surface passivation in 3D perovskite LEDs: a, b) Graphic representation of passivation using different amine-based materials and the luminance of the PeLEDs based on such strategies, extracted from [142] and c, d, e) SEM images of different bromide perovskite-polymer composites, extracted from [145], [147], [148].

b. PeLEDs based on quasi-2D perovskite polycrystalline thin films

Despite the promising results shown by 3D perovskites in PeLEDs, scientists have redirected the focus towards quasi-2D perovskites due to their ability to offer superior optoelectronic properties and solve the issue of emissive surface morphology. The first visible PeLEDs using quasi-2D perovskites were proposed by Byun et al. in 2016, in which they partially replaced the short-chain organic cation (MA$^-$) with a long-chain ammonium cation (PEA$^-$). The results showed that the quasi-2D PeLEDs had higher current efficiency and luminance than pure-3D or pure-2D perovskite devices. Nonetheless, a compromise had to be made between sacrificing electrical conductivity and achieving high-quality films and efficient exciton binding energies. The article also suggested that a suitable 2D perovskite precursor with higher charge carrier mobility than PEA$^-$ could address this issue while maintaining the cascade quantum-well structure [149]. The following years have witnessed a hunt for the most efficient low-dimensional perovskite materials for use in electroluminescent devices.

Xiao et al. incorporated n-butylammonium (BA$^-$) into 3D perovskite precursor solutions, which hindered the growth of the crystalline grains and substantially reduced surface roughness to 1 nm. Subsequently, their green PeLEDs, based on quasi-2D bromide perovskites, achieved 9.3% EQE, a significant improvement compared to the control sample of 3D bromide perovskites, which only reached 0.03%. Furthermore, these devices exhibited significantly greater storage stability, withstanding up to 8 months inside a nitrogen-filled environment [150]. Another aliphatic alkylammonium cation that has been investigated is octylammonium ($C_8H_{17}NH_3^-$, or OA$^-$). Specifically, Yantara et al. successfully designed a

green PeLED architecture incorporating $(OA)_2FA_{n-1}Pb_nBr_{3n+1}$, which demonstrated a current efficiency of 22.9 cd/A. This was partly attributed to the strong electrostatic binding between the OA⁻ cations and the separated 3D perovskite layers, resulting in a homogeneous and defect-free film with small-size grains [68]. Despite these results, in general, the aromatic moieties are still preferable in low-dimensional PeLEDs than the aliphatic spacers due to their better hydrophobicity and electronic properties [14], [55], [151], [152]. Several studies have focused on the integration of PEA ligands to different 3D perovskite systems beyond MAPbBr₃, including FAPbBr₃ [153], [154] and CsPbBr₃ [155], [156], as well as evaluating their impact on the PeLEDs' efficiency. In 2019, a study was published by Shang et al., in which a bidentate ligand (i.e., 1,4-bis(aminomethyl)benzene, or BAB) was utilized as the spacers to enhance the binding energy of the quasi-2D structure. While the EQE of the PeLEDs involving BAB only slightly exceeded 5%, the noteworthy finding was that these devices exhibited a prolonged operational lifetime of up to 100 hours [157]. Most recently, Jiang et al. demonstrated a method to mitigate the adverse effects of Auger recombination in RPP PeLEDs. This was achieved by introducing highly polarized p-FPEA cations to the A-site of the perovskites. Compared to the typical PEA cations, p-FPEA has a fluorine atom at the para-position of the benzene ring which enhances the molecule dipole moment, and thus reduces the binding energy of the perovskite material. The emissive films were then passivated to minimize defect-induced recombination. The resultant devices showed a record-high luminance of 82,000 cd/m² with EQE exceeding 20% [158]. Remarkable results from these studies have been summarized in Figure I.16.
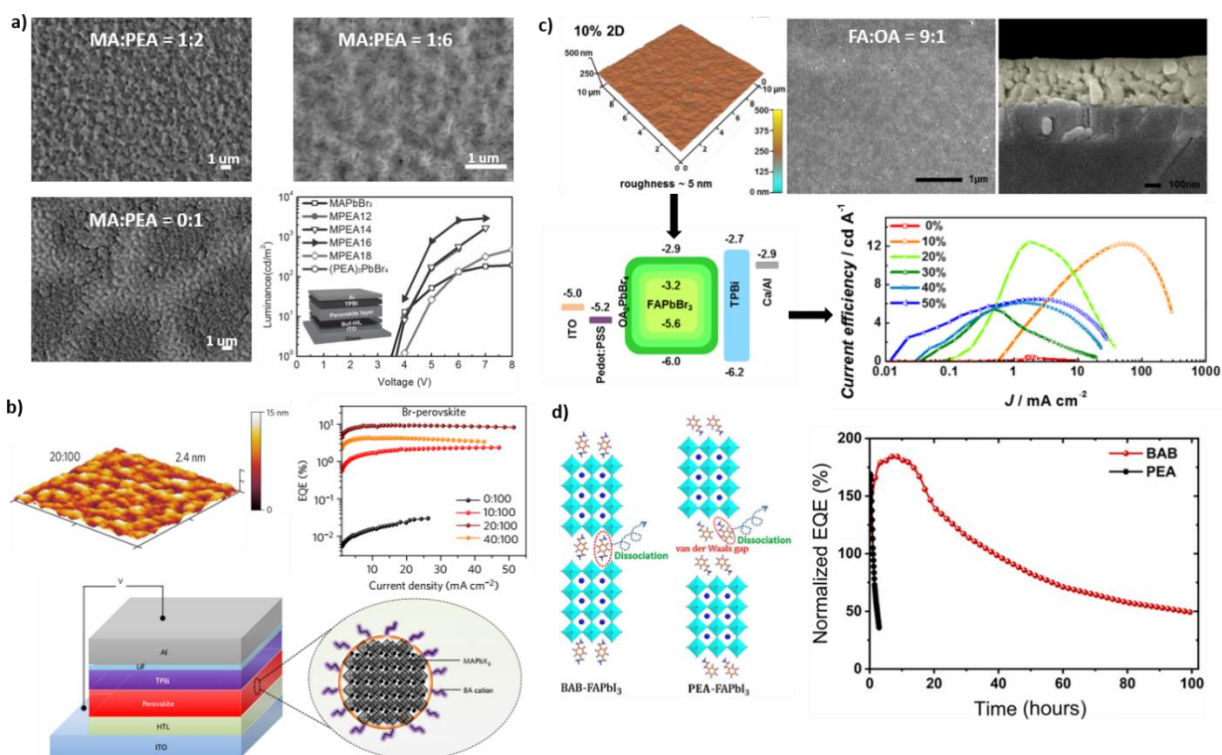
Figure I.16. Engineering of quasi-2D perovskite thin films in PeLEDs: a) SEM images of quasi-2D perovskite thin films with varying ratios of MA⁻ and PEA⁻. The respective PeLED performance proposed by Byun et al. is also presented. Extracted from [149]; b) An AFM image of a perovskite emissive layer passivated with BA⁻ with roughness of 2.4 nm. PeLED performance with different molar ratios of MA⁻:BA⁻ is shown on the right. The device structure is presented at the bottom. Extracted from [150]; c) AFM and SEM images of a perovskite

In addition to efforts to enhance the emissive materials, research on quasi-2D PeLEDs has also explored different device structures to improve the efficiency of charge injection while hindering interfacial quenching. Indeed, typical device structures of PeLEDs (not only for quasi-2D but also including 3D and quantum dot perovskites) can be found in Figure I.16. It is clear that they have adopted the multilayer architecture from their predecessor - OLEDs, as depicted above in Figure I.11.b: The cathode is typically made of indium tin oxide (ITO), a transparent material for light extraction with a high work function of 4.5-5.2 eV. Conversely, reflective materials such as silver (Ag) and aluminum (Al) are preferred for the anode to maximize the emission directionality [159]. Between these two materials, Al has a lower work function and higher electrical conductivity while being less susceptible to oxidation. However, the deposition of Ag is more facile and reproducible. Although both are suitable, Al is more commonly used in literature since most studies aim to achieve the best performance. Concerning HTLs, polyethylene dioxythiophene-polystyrene sulfonate (PEDOT:PSS) has been widely used as a buffer layer between the anode and the emissive layer due to its high conductivity, good film-forming properties, and excellent compatibility with many organic and inorganic materials. As for ETL, 1,3,5-Tris(N-phenylbenzimidazol-2-yl)benzene (TPBi) is a popular choice thanks to its high electron mobility and good energy level alignment with the adjacent layers in the device. In order to enhance the process of injecting electrons, it is common practice to incorporate an ultra-thin layer of lithium fluoride (LiF) typically measuring less than 1 nm in thickness. The purpose of this layer is to reduce the energy barrier between the LUMO of the ETLs and the work function of the anode. Another potential electron injection material that can be used is Calcium (Ca), but it is not as widely used as LiF. An illustration of the device architecture ITO/PEDOT:PSS/Perovskites/TPBi/LiF/Al, which has been used by both Byun et al. [149] and Quan et al. [160], is shown in Figure I.17.a, b, and c.
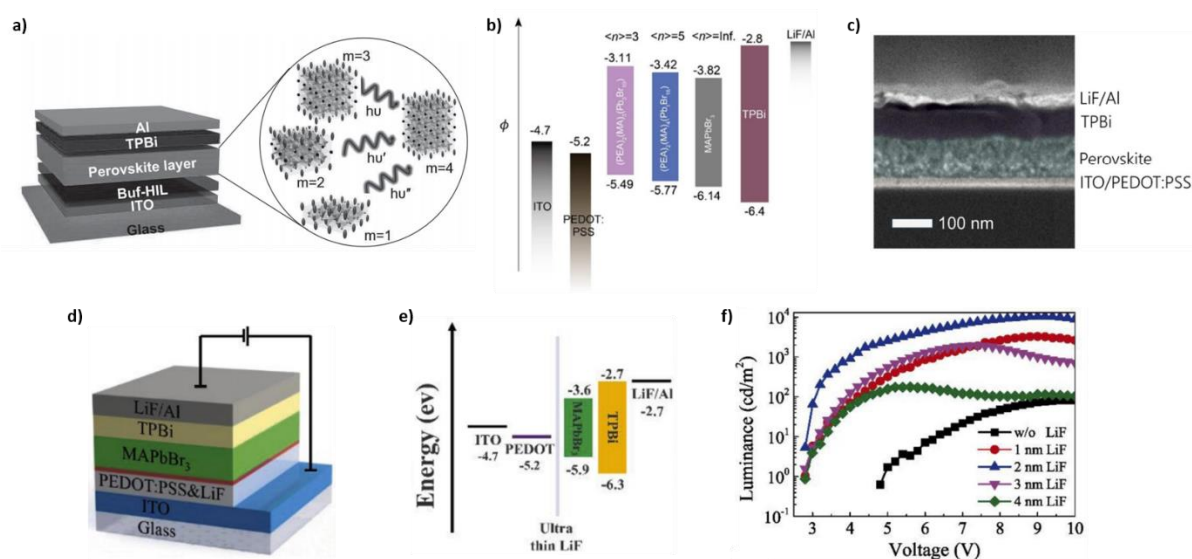
Figure I.17. a, b, c) Schematic illustration, energy band alignment, and cross-section SEM image of a typical PeLED structure: ITO/ PEDOT:PSS/ Perovskite layer/ TPBi/ LiF/ Al, extracted from [149] and [160];

d, e, f) Schematic illustration, energy band alignment, and device performance of PeLEDs with an ultra-thin LiF as a buffer between PEDOT:PSS and perovskite layers, extracted from [161].

However, several studies have revealed the negative impacts of PEDOT:PSS on the performance of PeLEDs. One limitation is the energy gap, approximately 0.5 eV, between the HOMOs of PEDOT:PSS and the perovskite emitters. This disparity creates difficulties in injecting holes into the emissive layers while injecting electrons through TPBi is relatively more efficient. This uneven charge injection results in an imbalance that causes the charges to recombine near the interface of PEDOT:PSS and perovskites. As a consequence, this increases the likelihood of non-radiative recombination induced by the interface [162]. Another drawback pertains to the diffusion of halide anions into the HTL layer during the spin-coating process. It has been observed that the diffusion length of Br^- at PEDOT:PSS/perovskite interface is around 100 nm, which is significantly more than the typical thickness of the conducting polymer of only 50 nm. As a result, this phenomenon changes the electrical profile of PEDOT:PSS and is responsible for current leakage in PeLEDs [163]. To address this obstacle, several attempts have been made to replace PEDOT:PSS with other HTL materials such as nickel oxide (NiO_x) [164], poly[N,N' -bis(4-butylphenyl)-N,N' -bis(phenyl)-benzidine] (poly-TPD) [165], [166], Poly(9-vinylcarbazole) (PVK) [15], [167], or Poly(9,9-dioctylfluorene-alt-N-(4-sec-butylphenyl)-diphenylamine) (TFB) [168], but none of these candidates have demonstrated significant improvements. A more proficient answer to this challenge is integrating a buffer layer between PEDOT:PSS and perovskites. For instance, in the study by Jiang et al. that was previously mentioned, an ultra-thin layer of a conjugated polymer electrolyte with deep HOMO energy level (i.e., Poly(9,9-bis(3'-(N,N-dimethyl)-N-ethylammoinium-propyl-2,7-fluorene)-alt-2,7-(9,9-dioctylfluorene))dibromide (PFN-Br)) is deposited onto the PEDOT:PSS layer. This results in improved contact between the hole transport layer and the active layer, which in turn facilitates hole transport as well as reduces the non-radiative pathway induced by the interface [158]. In 2021. this strategy was employed by Sun et al. to achieve the most luminous PeLED that has been documented, exhibiting a luminance value of 91,000 Cd/m^2 while maintaining an external quantum efficiency of 16% [169]. In addition, another study conducted by Li et al. demonstrated that, instead of the conjugated polymer electrolyte, adding a layer of LiF between the HTL and the perovskite layer could also significantly reduce the pinhole effect on perovskite thin films thanks to an enhancement in the wettability of the PEDOT:PSS layer. Furthermore, since LiF is an insulator, its thickness must be adjusted to balance electron and hole current injection. The study suggested the optimal LiF thickness of 2 nm, resulting in high PeLED performance: device luminance increases from 82 Cd/m^2 (without LiF) to 10,415 Cd/m^2 (with 2-nm LiF) while the EQE increases from 0.007% to 3.5% (as shown in Figure I.17.d, e, f) [161].

c.   PeLEDs based on perovskite nanocrystals

Compared to perovskite polycrystals, the use of perovskite NCs in the development of PeLEDs has been relatively less prevalent. However, in recent years, their popularity has been increasing due to their superior characteristics, including a high surface-to-volume ratio, which facilitates a high photoluminescence quantum yield (PLQY), as well as their capability for large-scale manufacturing. As mentioned above, perovskite NCs are essentially colloidal ABX_3 nanoparticles whose surfaces are coated

with organic ligands; thus, the engineering of the surfactants is important for controlling the properties of the emissive perovskite materials and enhancing the efficiency of optoelectronic devices. Similar to quasi-2D perovskites, there are two types of organic ligands that could be grafted to the surface of the 0D perovskites: long-chain and short-chain.

Firstly, oleylamine (OLA), oleic acid (OA), and n-octylamine (OAm) are some typical long-chain ligands used in the synthesis of perovskite QDs. For example, in the first-ever publication on PeLEDs based on $CsPbBr_3$ QDs, Haibo Zeng's team employed the hot-injection method to synthesize monodisperse QDs. This involved injecting cesium stearate into lead bromide precursors at a high temperature, followed by the addition of OA and OLA to prevent reaggregation. The PeLEDs produced using these perovskite nanocrystals demonstrated a luminance of nearly 1,000 cd/m^2 and an EQE of 0.12% [170]. It was also observed that an overabundance of long-chain ligands could result in poor electrical properties of the perovskite layers, as the excess ligands form an insulating layer. However, insufficient ligands caused significant aggregation, which reduced the PLQY of the QDs. Therefore, they refined the approach through a purification process employing hexane and ethyl acetate mixed solvent to wash out the excessive ligands, enabling the formation of homogeneous and dense films of $CsPbBr_3$ QDs. Subsequently, the devices utilizing the purified QDs exhibited a 15-fold increase in luminance, reaching 15,000 cd/m^2 [171]. Unlike Zeng's group, Huang et al. developed another method to synthesize colloidal MAPB QDs with OA and OAm as surfactants. In particular, they used an emulsion system of polar and non-polar solvents (i.e., DMF and n-hexane) before introducing a demulsifier (such as tert-butanol or acetone) to control the solubility between the two immiscible solvents and drive the perovskite crystallization. This allowed them to tune the size of the $MAPbBr_3$ nanocrystals between 2 and 8 nm and, as a result, fabricate PeLEDs with a luminance of 2,500 cd/m^2 and EQE of 1.1% [172]. Figure I.18 summarizes the main results of these studies. Another group of bulky ligands that has been applied in PeLEDs is quaternary ammonium bromide (QAB), which contains not only one but two symmetric long alkyl chains. In 2016, Pan et al. developed a post-synthesis strategy to substitute OA and OAm in their $CsPbBr_3$ QDs with di-dodecyl dimethyl ammonium bromide (DDAB) without causing destabilization of the spin-coated perovskite layers [173]. Then, Park et al. extended this approach to several QAB molecules with different chain lengths and compared the effect of the ligand's size on the optical and electrical properties of the QDs. Despite limitations in luminance with a maximum of only 2,200 cd/m^2, QAB showed promising efficiency with an EQE of 9.7% [174].
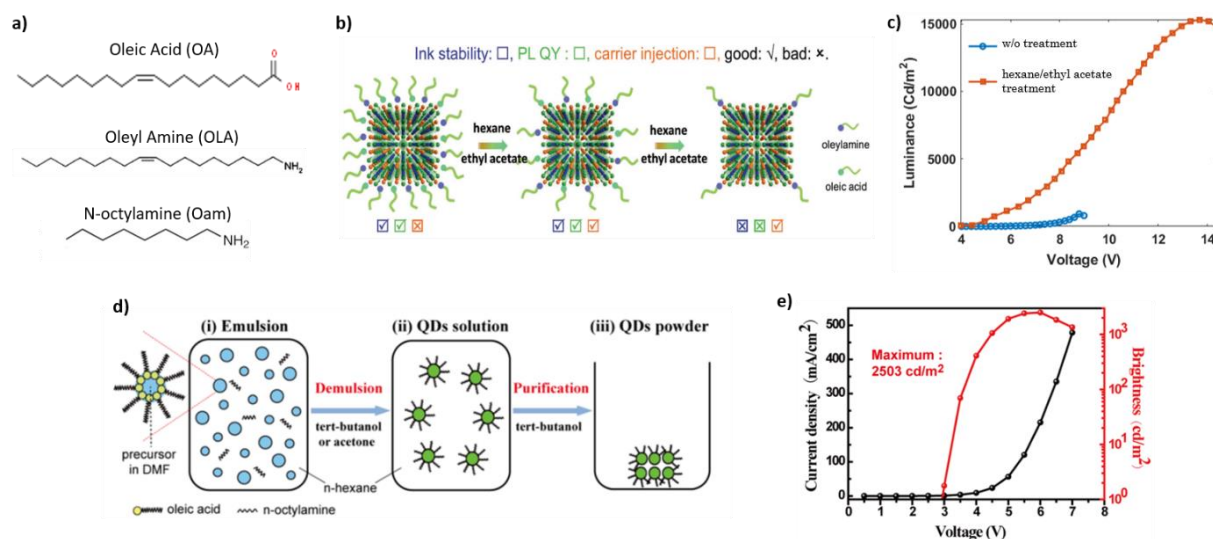
Figure I.18. a) Molecular structure of OA, OLA, and OAm, b) Illustration of mixed-solvent treatment of perovskite QDs prepared via hot-injection method, extracted from [167], and c) Comparison of device luminance with and without the treatment. Data is collected from [170], [171]; d) Illustration of emulsion synthesis of perovskite QDs and e) the corresponding PeLED performances, extracted from [172].

Secondly, to improve the charge transport characteristics of 0D perovskites, several studies have sought to replace the long-chain ligands with short-chain ligands. For example, Song et al. improved upon the strategy of Pan's group by partially replacing the short-chain organic capping ligands with even-shorter inorganic metal bromide ligands, such as $ZnBr_2$, $MnBr_2$, $GaBr_3$, or $InBr_3$. This replacement effectively reduced the insulating barrier while improving the stability of the perovskite QD films. They found that devices passivated with $ZnBr_2$ had the highest EQE of 16.48%, while those passivated with $MnBr_2$ had the highest luminance of 100,000 cd/m^2 [175]. The scheme and device performance of this strategy are shown in Figure I.19.a and b. Furthermore, there have been studies investigating the use of short ammonium halide ligands containing a benzene ring, such as phenylalanine bromide (PPABr) [176] or phenethylammonium bromide (PEABr) [177], for passivation of halide vacancies on the perovskite nanocrystals. Consequently, PPABr-modified PeLEDs achieve an EQE of 15%, while the PEABr-modified devices yield an EQE of nearly 7%. Another short aromatic moiety utilized successfully in perovskite QLEDs is 2-naphthalenesulfonic acid (NSA). Using this ligand, Zhao et al. effectively fabricated devices with a record-breaking EQE of 19.2% and luminance of 67,000 cd/m^2 (Figure I.19.c and d). They attributed the impressive results to the delocalization of conjugated electrons in the benzene ring which improves stability under electrical excitation and enhance the charge-transfer characteristics of the QDs, resulting in better device performance [178].
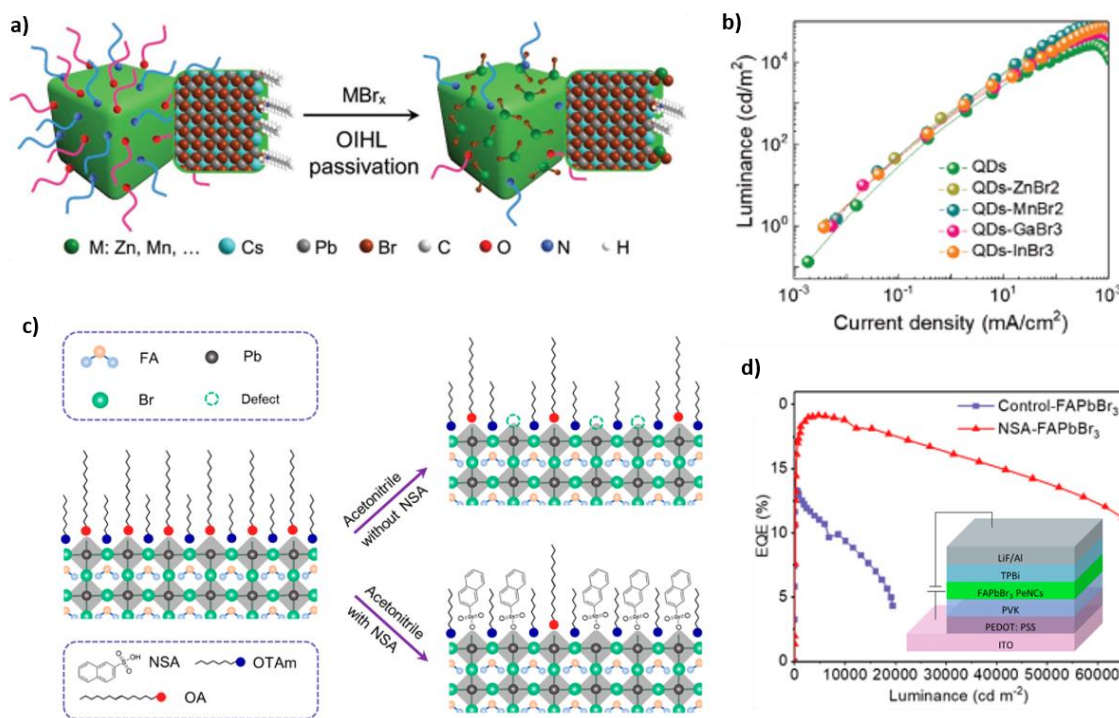
Figure I.19. a, c) Graphic representation of surface passivation in perovskite QD using (a) inorganic metal bromide ligands and (c) 2-naphthalenesulfonic acid (NSA); b, d) Characteristic curves of the PeLEDs based on these strategies. Figures are extracted from [175], [178].

1.2.4 Key challenges and opportunities in the field of perovskite LEDs

Figure I.20 shows the advancements in PeLEDs in terms of their power conversion efficiency and operational durability from 2014 to 2022. The graph indicates a notable and swift advancement in the external quantum efficiency (EQE) of PeLEDs, particularly in green and red emitting devices, within a short period, indicating that they are soon expected to match the industrial standards set by commercial OLEDs (e.g., an EQE of approximately 30%). However, despite these advancements, the practical applications of PeLEDs in real-life situations, such as displays or telecommunication, are still far from being realized due to the presence of bottlenecks in PeLED technology.
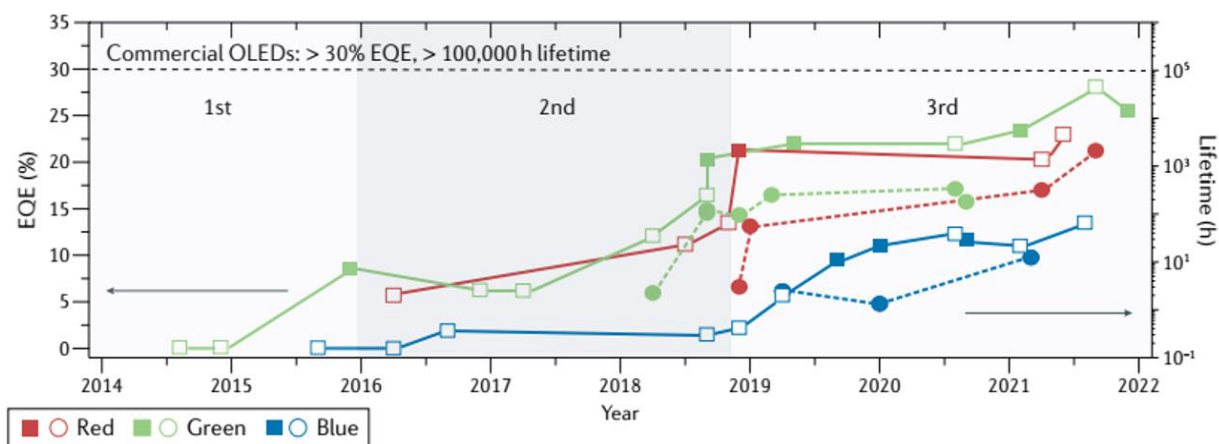
Figure I.20. Progress in EQE (continuous line) and operational lifetime (dotted lines) of PeLEDs for each primary color: red, green, and blue. The black line represents the values of commercial OLEDs for comparison. Extracted from [53]

a. Operational stability

The first obstacle to the commercialization of PeLEDs is their operational lifetime. While OLEDs or QLEDs have boasted T_{50} values of $> 1,000,000$ hours at a luminance of 100 cd/m^2 [128] (or $> 100,000$ hours at 1,000 cd/m^2 [179]), the most durable green PeLED currently available has a much less impressive T_{50} value of only 250 hours at a luminance of 100 cd/m^2 [180] (and it should be noted that this all-inorganic PeLED operated at a relatively low EQE of 10%). On the contrary, green PeLEDs with the highest luminance exhibited an even shorter operational lifetime of just 117 minutes [169]. Similarly, devices with EQE > 20% have not demonstrated a lifetime longer than 2 hours in studies [15], [155], [158], [165], [181], [182].

There are several causes that lead to this stability problem in PeLEDs, including: i) vacancies within the perovskite crystal lattice, ii) charge accumulation at the interface of the perovskite and charge transfer layers, and iii) heating effect under high current injection [128], [179], [183]. When electrically excited, these factors work in concert to induce ion migration, which involves the movement of anions and cations within the crystal lattice to fill pre-existing defects, thereby creating additional structural defects that promote non-radiative recombination. Subsequently, ion migration leads to the decomposition of perovskite materials and unintentional doping of charge-transporting layers, creating interface-induced non-radiative traps and altering the charge injection balance. The accumulation of these effects is proportional to the operational time or applied bias voltage of the PeLED and increases with both parameters. This continual build-up of effects ultimately leads to the rapid diminution of the device over a short time. Despite various efforts that have been undertaken to minimize the impacts of such factors, including those discussed in section 1.2.3, it remains a significant challenge to resolve the intrinsic instability of halide perovskite materials fully. Therefore, further breakthrough ideas and approaches are needed to achieve the necessary level of operational lifetime for these devices.

b. Toxicity

Secondly, the issue of toxicity is a significant concern in the efforts to commercialize PeLEDs. In particular, many electroluminescent perovskites are synthesized using lead (Pb(II)), which is known to pose potential risks to human health and the environment. As a result, the use of lead in commercial electronic devices is subject to strict regulations, and various governments have proposed policies aimed at mitigating the negative impacts of optoelectronic devices, such as solar cells or LEDs, that rely on lead halide perovskites [184]. There are two main approaches to addressing this challenge:

The first one involves developing effective strategies for recycling the toxic metal, which would not only help minimize environmental impacts but also reduce fabrication costs. Fortunately, existing techniques have been proposed to extract lead (as well as other valuable components, such as metal electrodes) from electronic waste, which were initially developed for perovskite PVs. Given the similarities in device structures between PeLEDs and PSCs, these recycling techniques can be applied interchangeably between the two [185], [186].

The other approach is to explore alternative materials to substitute lead with divalent or even mono-/tri-valent cations such as Sn, Ge, In, Cu, Ag, Bi, or Sb, as depicted in Figure I.21. Fundamentally speaking, these environmental-friendly choices have demonstrated better structural stability than lead-based perovskites, but depending on the valence of the substituent, all are not leading to phase-pure perovskite structures. Among them, Sn appears to be the most promising candidate due to its similarity to Pb. However, these alternatives often exhibit low PLQY, which leads to poor device performance. So far, no green-emitting devices based on low-toxicity materials have shown luminance greater than 1,000 cd/m^2 or EQE greater than 3% [187], [188].
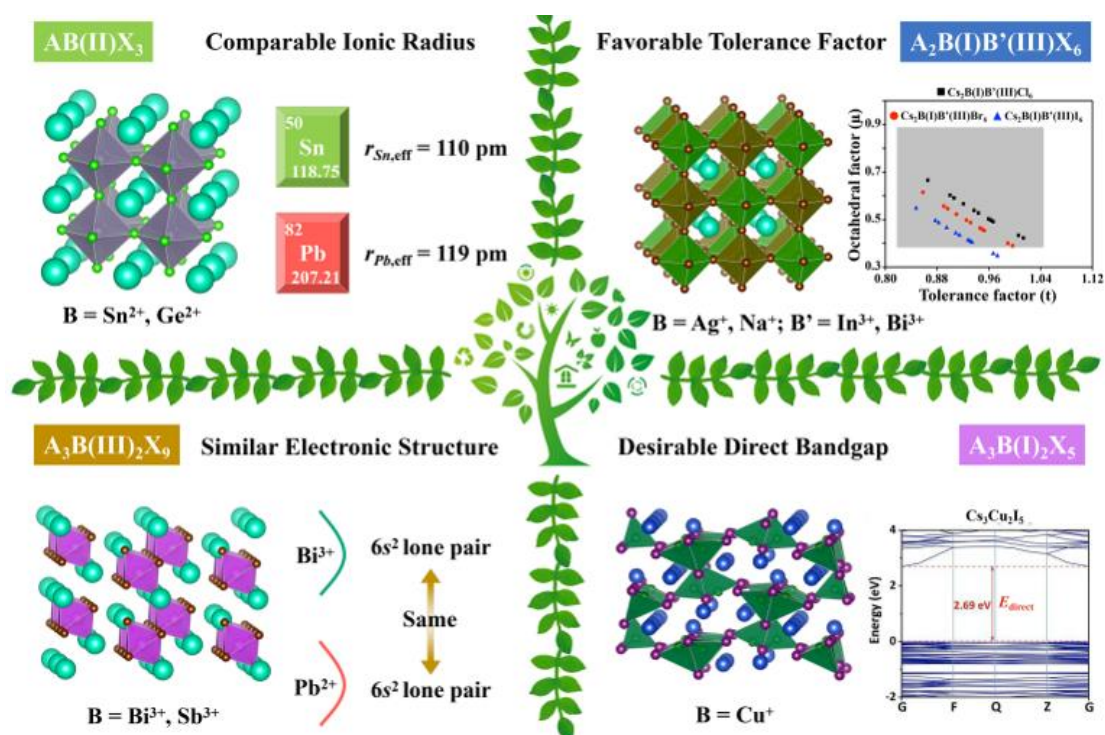
Figure I.21. Different strategies for finding alternative, low-toxicity replacements for lead (Pb) in perovskite materials based on similarities in crystal structures (such as ionic radius or tolerance factor) or electronic structures (such as electronic configuration or direct bandgap). Extracted from [187].

However, despite their potential for reducing the environmental impact, these alternatives have received less attention from the research community due to the current focus on improving device performance rather than addressing environmental concerns. Nonetheless, they deserve more attention for their potential to mitigate toxicity issues.

c. Reproducibility

Reproducibility issue refers to the difficulty of reproducing published results or experiments between different research groups or even within the same group, which is a major concern in scientific research. This statement is even more critical in the field of halide perovskites, as a minor fluctuation in any experimental conditions can have a drastic impact on crystal and grain formation [189]–[195], and especially in the case of layered perovskites, on the composition of the phase domains [196]–[198]. The variation in crystal structure and phase composition of perovskite materials, even with slight variations in growth conditions, is a significant contributor to poor reproducibility. As shown above, controllable

variables, such as the choice of organic ligands, precursor preparation methods, and growth methods, can also significantly impact the crystallization of halide perovskites and, thus, device performance. The use of antisolvents and additives is another controllable variable that can affect the reproducibility of PeLEDs.

Moreover, extraneous variables such as environmental factors, like temperature and humidity, can also contribute to the reproducibility issue associated with perovskite research. In particular, changes in room temperature during the day or climate between seasons can cause noticeable deviations in perovskite crystallization and device performance [199], [200]. To mitigate these issues, most manipulation of 3D or quasi-2D perovskites, including PeLEDs, are typically prepared under glovebox conditions with controlled oxygen and water levels. However, even in glovebox conditions, unintentional temperature fluctuations can occur due to the functioning of annealing hotplates required for post-treatment of perovskite thin films. Furthermore, chemical species and solvents stored in the glovebox can also contaminate the samples, particularly when the glovebox is shared among several users. If the reproducibility issue cannot be addressed, it could result in a lack of confidence in the technology by potential investors and consumers, hindering the widespread adoption of perovskite devices. Additionally, the low reproducibility of perovskite devices may lead to inconsistency in their performance, making it difficult to guarantee their reliability and durability. Therefore, addressing the reproducibility issue is critical for the successful commercialization of perovskite devices.

d. Light outcoupling management

Light management is a crucial aspect of PeLEDs that has not received enough attention in the research community. In order to maximize light emission and improve the overall device efficiency, it is essential to carefully design the optical structures of PeLEDs. One key challenge in PeLEDs is to efficiently extract light from the perovskite emitter layer (i.e., to increase the outcoupling efficiency of the device), which has a relatively high refractive index compared to the surrounding materials. This can lead to a significant amount of light trapped within the perovskite layer, resulting in poor device efficiency [201]. Even if photons can escape the perovskite emitter layer, they may not be efficiently outcoupled into the free continuum, leading to a lower external quantum efficiency. This can be due to the dipole orientation (i.e., isotropic, vertical, or horizontal) of the emitting species, the device structure (planar or patterned), and the viewing angle [202]. Another source of light loss in PeLEDs is the absorption of the multiple layers composing the device, reducing the number of photons available for emission.
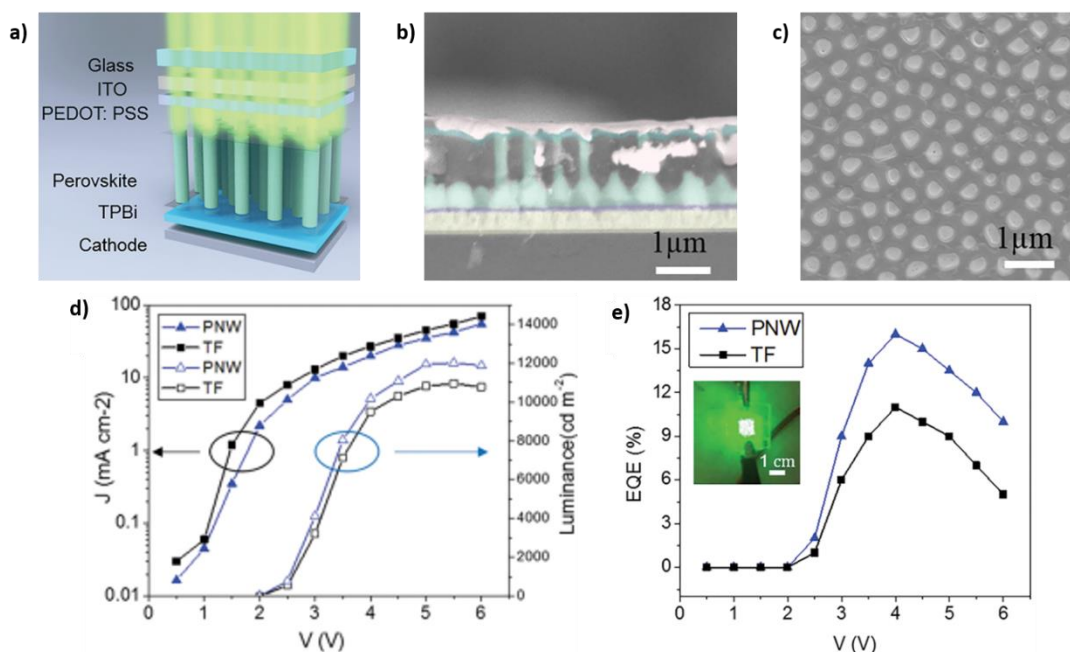
Figure I.22. A PeLED based on 1D perovskite photonic crystals: a) Device design; b) Cross-view SEM image of the device; c) Top-view SEM images of the nanowire perovskites grown on PEDOT:PSS layer; d and e) Characteristic curves and EQE curve of the device, compared to a planar PeLED. Extracted from [203]

A few studies have been conducted to enhance the efficiency of light extraction in PeLEDs, most of which focus on the use of photonic structures to manipulate the propagation of emitted light. For instance, Zhang and colleagues presented a novel PeLED design utilizing nanophotonic substrates with 300 nm silica nanoparticles coated with aluminum. The purpose of this design was to decrease the total internal reflection at the interface between the perovskite layer and the substrates, which would improve the directional emission of light. The researchers found that the devices with nanopatterned substrates had twice the EQE of planar devices [204]. More interestingly, there have been some preliminary results suggesting that perovskite photonic crystals may be utilized to achieve specific patterns of light extraction as evidenced by the increased EQE of nanostructured green PeLEDs based on $CsPbBr_3$ nanowires (Figure I.22) [203], [205]. The photonic crystal can also be engineered to reflect particular wavelengths of light into the perovskite layer of the LED while transmitting other wavelengths of light out into the surrounding environment. This reabsorption (or photon recycling) effect allows for maximizing the amount of light that is extracted from the device and reduces the amount of light that is lost within the device [206]. In conclusion, enhancing light management in PeLEDs is crucial for unlocking the full potential of this promising technology. There is still ample room for further research in this area, and continued efforts to improve light extraction will be essential for advancing the development of PeLEDs.

e. Large-scale production

Besides the challenges already mentioned, a dependable approach for fabricating perovskite emissive layers on a large scale has not yet been fully proven. While it is accurate to state that the majority of perovskite materials can be produced utilizing solution-based methodologies like spin-coating (in polycrystalline thin films) or hot injection (in perovskite nanocrystals), these methods are straightforward and economically viable but more appropriate for producing small quantities at a laboratory scale rather

than for industrial-scale mass production. The techniques of interest here must fulfill specific requirements, such as high throughput, scalability, reproducibility, and cost-effectiveness. They should produce uniform and flawless films over large areas and ensure high stability and long-term reliability of the devices. Furthermore, the techniques must be compatible with existing manufacturing processes and equipment to facilitate integration into the LED manufacturing industry.

In this topic, PeLEDs can learn lessons from their predecessors, such as OLEDs. On the one hand, manufacturing scalability can be achieved using thermal evaporation under high vacuum, which not only enables larger substrate sizes or higher production volumes but also allows for precise control of films' thickness and quality. However, the Achilles heel of this technique is material wastage as it usually requires 3 grams to 5 grams of raw materials for each 1 gram of deposited layer [207], increasing the cost of the fabrication process. For halide perovskites, it is even more challenging since vacuum-evaporated perovskite thin films exhibit high impurities and low emissivity [208], [209]. On the other hand, solution-processing techniques (such as inkjet printing [210], [211], blade coating [212], and spray coating [213]) proved to be capable of producing bright and efficient PeLEDs. However, the number of research on these approaches is still limited due to the cost of equipment installation and difficulties in finding the optimal processing conditions for perovskite crystallization [214]. However, considering the similarities between these techniques and the well-studied spin-coating deposition, it is believable that with further optimization and innovation, they will soon overcome the current limitations and emerge as viable alternatives for scalable PeLED fabrication.

1.3 Scope of the thesis project

This thesis is part of two granted projects dedicated to halogenated perovskites currently conducted by the Printed Electronics for Telecom and Energy group (or ELITE) at XLIM research institute. One project, called "Electrically pumped hybrid perovskites based light-emitting devices" (EMIPERO), involves the teams from the "Lumière, Matière et Interface" (LUMIN) laboratory (CNRS, ENS Paris-Saclay) and the Institute of Nanoscience of Lyon (INL, École Centrale de Lyon) and is funded by France's National Agency of Research (ANR). The other project, called "STRatégies aux Interfaces pour l'optimisation des dispositifs Pérovskite Electroluminescents" (STRIPE), involves the teams from the Institute of Molecular Sciences (ISM) and the Laboratory for Material Integration into Systems (IMS) at the University of Bordeaux and is funded by the Nouvelle Aquitaine Region.

Concerning EMIPERO, it focuses on developing cutting-edge technology for light emission using halide perovskite materials. Specifically, the project aims at demonstrating relevant technology for VLC applications, which can be used in indoor and underwater communication systems. VLC is a promising technology that offers high data rates and secure data transmission, particularly in specific indoor conditions where traditional radio frequency-based communication methods can be challenging. The project will leverage the unique properties of the visible green band (500-550 nm), where water is relatively transparent to light, making it particularly relevant for underwater communication systems. The green emission presents another interest for generating white light using red-green-blue LEDs. Therefore,

in the first part of this thesis, we will focus on developing reference PeLED devices to explore various VLC scenarios, as well as proposing novel PeLED structures based on photonic nanostructures for enhanced emission properties.

STRIPE is a research project which aims at optimizing the performance and stability of perovskite-based light-emitting devices, specifically LEDs and lasers, by improving the properties of their interface layers. The project builds upon the unique properties of hybrid organic-inorganic perovskites, which have demonstrated high electroluminescence efficiency, narrow emission spectra, and tunable band gaps. The key challenge to be addressed in STRIPE is the creation of high-quality interface layers between the perovskite active layers and the electrode contacts, which are crucial for device performance and stability. Through the project, the research team will investigate two approaches to improving the interface layers. The first involves doping the perovskite layers within the bulk or on the surface, similar to traditional strategies used in inorganic semiconductors. The second approach uses self-assembled monolayers to transfer charge between the perovskite and the electrode contacts. By improving the interface layers, STRIPE aims to develop perovskite-based LEDs and lasers that are more efficient, stable, and cost-effective, with the potential for use in a wide range of applications.

Within these projects, XLIM was responsible for developing PeLED devices based on various halide perovskite materials, with or without photonic structures proposed by our partners, and demonstrating their feasibility towards VLC applications. Subsequently, the objectives of this thesis are to:

i. Fabricate a reference PeLED based on previously studied materials, such as 3D or quasi-2D bromide perovskites. A performance target of the reference device is at least 1,000 cd/m^2;

ii. Develop characterization set-ups through standard techniques to evaluate the performance of the PeLEDs in both steady-state and transient conditions. Another aspect of the devices that will need to be assessed carefully is their reproducibility since it is essential for any further real-life applications in VLC;

iii. Develop novel PeLED architectures using newly synthesized perovskite materials by LUMIN or perovskite photonic crystals proposed by INL. This will also involve investigating the effects of the proposed materials or photonic structures on the performance of the PeLEDs, particularly on their efficiency and stability.

iv. Provide recommendations for future developments of PeLED devices for VLC applications, particularly in improving their efficiency, stability, and reproducibility, as well as reducing manufacturing costs.

Chapter II. FABRICATION OF REPRODUCIBLE PELEDS BASED ON POLYCRYSTALLINE HOIPS

The objective of this chapter is to provide a comprehensive account of the various processes involved in synthesizing and fabricating reproducible and efficient green PeLEDs, which can serve as a benchmark for further investigations in this thesis project.

In the first half of the chapter, we will primarily explain the synthesis and deposition methods employed for the formation of electroluminescent perovskite thin layers using HOIPs. We will examine the selection of appropriate materials and the optimization procedures employed to enhance the thin-film morphology and the emission properties of the polycrystalline HOIP thin films, while ensuring their suitability for integration into light-emitting diodes. Furthermore, we will outline the methodology behind designing and fabricating the corresponding multilayered light-emitting devices. Specifically, these reference PeLEDs must perform a decent brightness level (i.e., a luminance of 1,000 cd/m^2 or higher). They must also exhibit a sufficient lifetime in the electroluminescence to ensure their suitability for accurate and reliable calibration. Unfortunately, there is not any widely-accepted definition or norm of "sufficient lifetime" for PeLEDs; therefore, in this report, we will use the lowest lifetime value published in the literature (i.e. $T_{50} = 30$ seconds [103]) as our standard. Additionally, it will also allow a systematic characterization of the device's emission pattern which is important to gather high-quality input for device simulations.

The second half of the chapter focuses on the impacts of extraneous glovebox-related variables in the fabrication of PeLEDs based on low-dimensional HOIPs on their device-to-device reproducibility. In particular, a series of experimental set-ups for spin-coating of the perovskites under an inert atmosphere will be examined to study the influences of concentrations of oxygen/moisture, temperature, and solvent traces on the crystallization of the polycrystalline thin films. Accordingly, our results show a significant degradation in the homogeneity and the optical properties of the perovskite thin films caused by minor but noticeable fluctuations in those inert atmosphere properties. As a result, such variations in the formation of the emissive layers lead to remarkable deviations in the device's performance. Lastly, we will discuss our best practices for perovskite deposition in the glovebox to achieve highly reproducible PeLEDs with reduced standard deviations in key performance parameters.

2.1 Optimization of polycrystalline perovskite thin films for light-emitting diodes

2.1.1 Criteria towards efficient emissive perovskite materials

Since the targeted emission wavelength of our PeLEDs lies in the green region between 500 nm and 550 nm, the materials of interest in this project are limited to bromide perovskites, as depicted in Figure I.4.b. Amongst the HOIPs investigated for green emission, 3D *methylammonium lead bromide (MAPB)* and its quasi-2D counterpart *phenethylammonium methylammonium lead bromide (PEA$_2$MA$_{n-1}$Pb$_n$Br$_{3n+1}$)* has emerged as the most widely studied compounds. PeLEDs based on these materials have demonstrated superior luminance and stability [53], [103], [215], [216], establishing them as leading candidates within their respective categories. Therefore, these materials will be chosen as the active materials in our reference PeLEDs. In order to achieve devices with high efficiency and long-term stability, the perovskite thin films need to meet the following requirements:

- Thickness and homogeneity: The thin film should be uniform throughout its thickness, which ranges between 50 nm and 200 nm. This ensures an increased probability of electron-hole recombination while minimizing the self-absorption effect. It is also desirable to have small crystal sizes, typically in the order of hundreds of nanometers, as they facilitate the transfer of charge carriers across the active layer and reduce the diffusion length of excitons, thus boosting the efficiency of radiative recombination (so-called exciton confinement effect) [138].

- Surface coverage: As mentioned in Chapter 1, voids and defects in the thin film surface are sources of non-radiative recombination that can hinder the device's performance. Therefore, it is a must for polycrystalline perovskite films to be defect-free with high surface coverage.

- Optical properties: The thin film should exhibit a high photoluminescence quantum yield (PLQY). This characteristic serves as an indicator of efficient radiative recombination, reflecting the film's ability to emit light effectively.

The synthesis and characterization of the HOIP thin films will be discussed as follows.

2.1.2 Synthesis and optical characterization of emissive thin films based on HOIPs

a. 3D bromide perovskite

Our approach for the precursor preparation and the deposition of 3D perovskites is based on the methodology developed by Dr. Sudip K. Saha during his postdoctoral fellowship at XLIM in 2015-2016 [217], which demonstrated the relevance of non-stoichiometric mixing of perovskite precursors to achieve homogeneous surface morphology with small grain domains. In this report, the 3D perovskite thin films are deposited using the spin-coating technique. Firstly, a 0.5 M MAPB precursor solution is prepared by dissolving excess MABr and PbBr$_2$ in Dimethylformamide (DMF) solvent. The precursor solution is mixed at 50 °C for 24 hours and filtered using 0.2-μm hydrophobic PTFE 10 minutes before the deposition. To deposit a perovskite thin film, 60 μL of the solution is dropped on glass substrates, which are either pre-treated using UV-O$_3$ or coated with hole transfer material (PEDOT:PSS), and then

spin-coated at 3000 rpm for 40 seconds. The deposition is followed by thermal annealing at 90 °C for 120 minutes.

We note that all experimental manipulation is done in an enclosed nitrogen-filled environment (i.e., an MBRAUN UNIlab glovebox workstation). The content of residual oxygen and moisture inside the workstation is probed using integrated analyzers and maintained at < 10 ppm. The gas purifier of the glovebox is regenerated once every six months in normal operating conditions or whereupon a significant increase in the H_2O/O_2 concentration (> 100 ppm) occurs. The experimental set-up used to grow perovskite thin films is illustrated in Figure II.1 and denoted as Set-up A in this report. It consists of a spin-coater positioned between two hot plates, H1 and H2, that are 20 cm away from each other, to facilitate the manipulation during the deposition process. H1 functions continuously at a constant temperature of 50 °C for precursor preparation, independent of whether or not a deposition process is currently taking place. Conversely, H2 is only turned on at 90 °C at the beginning of the deposition campaign, for post-deposition annealing purposes. All chemical species required for the precursor preparation and deposition are stored on the shelf above the spin-coater.
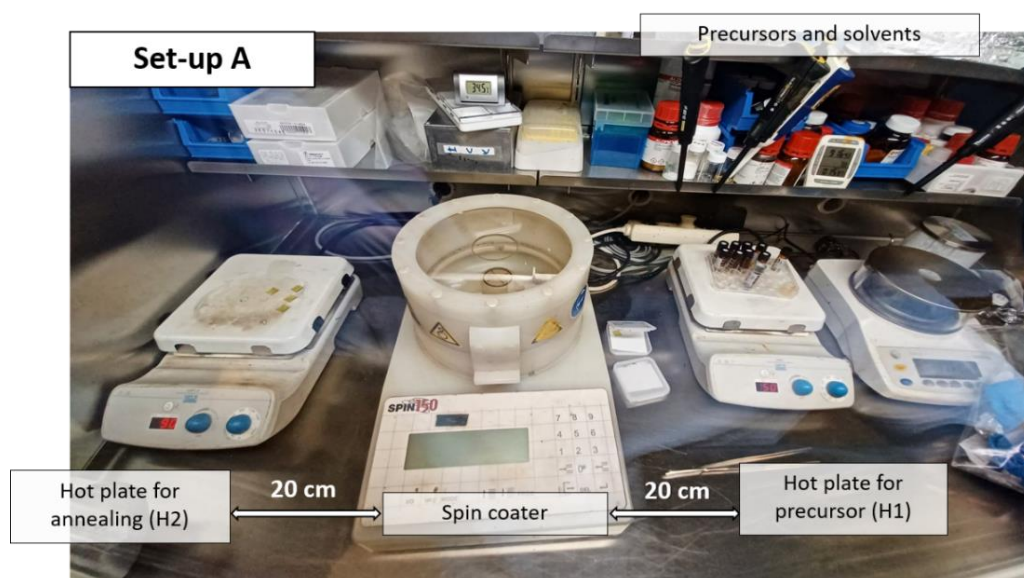
Figure II.1. Set-up of perovskite precursor preparation and spin-coating in an enclosed inert-gas workstation.

The first variable we sought to optimize is the molecular ratio between the perovskite precursors on the crystallization of the emissive thin films. The optical properties of the MAPB layers synthesized on PEDOT:PSS-coated glass substrates in two different cases, MABr:PbBr2 = 2:1 (as studied by S. Saha) and 3:1, are shown in Figure II.2.a. It is evident that the intensity and shape of the absorption curves in both cases are identical with a peak around 520 nm, despite a minor redshift of 3 nm in the absorbance spectra when increasing the amount of MABr in the precursor solution. When we examined the PL spectra of the perovskite films (excited at 380 nm), the two samples emitted intensively in the region from 500 nm to 540 nm, with a peak around 515 nm, demonstrating an overlapping with the absorption curve we observed. Moreover, the 3:1 sample exhibits an emission intensity of 3-order-of-magnitude higher than the 2:1 sample, even though they were excited under the same optical excitation.
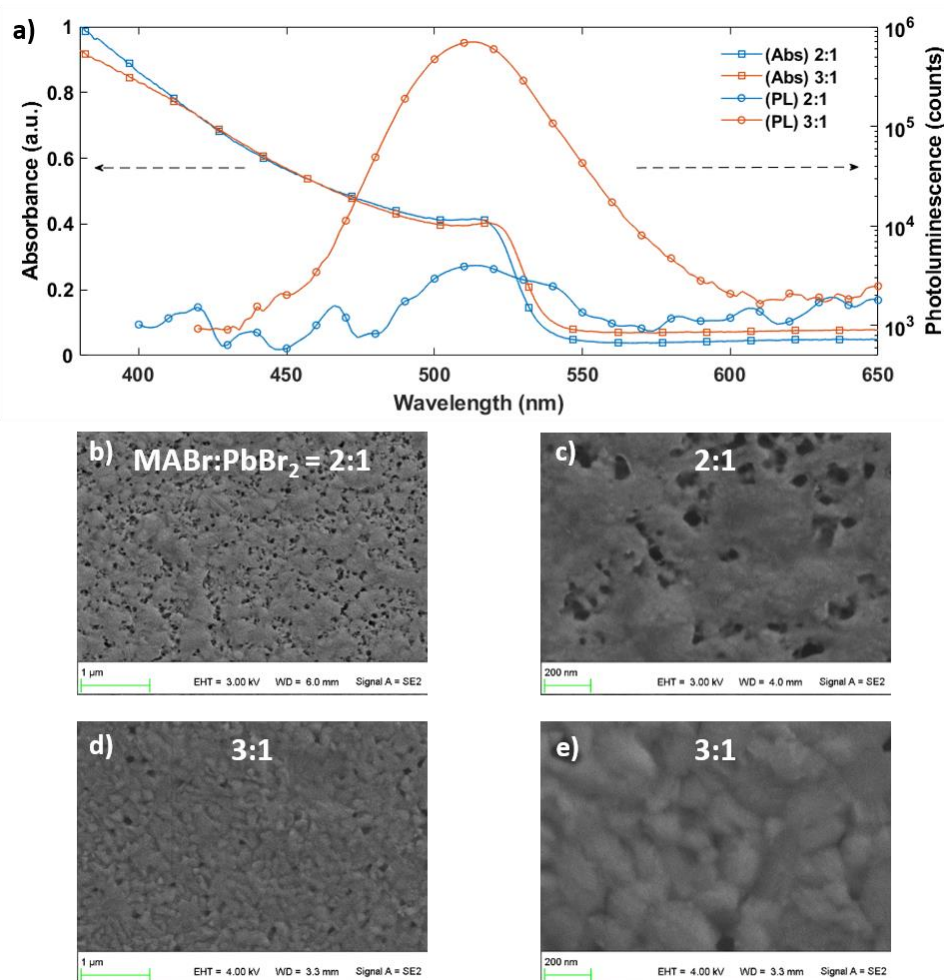
Figure II.2. a) UV-Vis absorption and PL spectra and b-e) SEM images of thin films based on MAPB perovskite, deposited on PEDOT:PSS-coated glass substrates with various precursor ratios: (b, c) MABr:PbBr₂ = 2:1 and (d, e) MABr:PbBr₂ = 3:1

To understand the reasons behind this phenomenon, we need to study the morphology of these thin films. Accordingly, Figures II.2.b-e show the SEM images of the MAPB layers synthesized with the two precursor ratios. It can be observed that, the 2:1 perovskite film exhibits low homogeneity with a large number of defects and unclear crystal grains. Furthermore, the size of the pinholes is relatively large, varying between 50 to 150 nm in dimension. As a result, non-radiative recombination pathways are promoted, causing a reduction in the PL signal. On the other hand, the polycrystalline film synthesized using the molar ratio of 3:1 contains clearer crystal grains and fewer defects with a surface coverage of > 90%, thus facilitating the radiative recombination and leading to a more intensive emission, as we observed above. Here, it should be noted that the grain size varies largely from 100 nm up to 400 nm, which is a typical feature of polycrystalline 3D perovskites synthesized without surface passivation. Additional information on the crystalline quality of the films will be discussed in the following sections.

b. Quasi-2D bromide perovskites

As we will better understand in the section devoted to device performance, we rapidly sought to improve the emissive layers' morphological and optical properties by reducing the dimensionality of the perovskite materials. As discussed at the beginning of this section, our material of interest will be

PEA₂MAₙ₋₁PbₙBr₃ₙ₊₁. In detail, low-dimensional perovskite precursors are prepared by dissolving PEABr, MABr, and PbBr$_2$ in DMF solvent at a molar concentration of 0.5 M. The stoichiometric solution is then mixed for at least 24 hours at 50 °C and filtered before deposition. To control the thickness of the emissive thin films within 150 nm – 160 nm (similar to MAPB thin films studied in the previous section), we spin-coat the precursor solutions at a high speed of 7,000 rpm for 40 seconds, followed by thermal annealing at 90 °C for 15 minutes. The entire experimental process is manipulated using Set-up A as we described above. Here, we will examine the effect of the long-chain ligands on the morphology and photophysics of the perovskite thin films.

Initially, the optical microscopic images of polycrystalline thin films synthesized with two ratios of PEA$^+$ to MA$^+$ (i.e., 1:4 and 1:2) are presented in Figures II.3.a and b. In both cases, the substrate surfaces show high coverage at a macroscopic scale; however, it can be observed that the thin film with a lower concentration of PEA$^+$ exhibits a gritty texture and a small number of pinholes, while the one with a higher concentration appears to be highly homogeneous and defectless. Additional insights into the surface morphology and crystal grain at the sub-micrometer scale are obtained using SEM analysis (Figures II.3.c and d). Evidently, there is a dramatic difference in the shape, dimension, and organization of the crystal grains between the two cases. Concerning PEA:MA=1:4, the perovskite crystals have a thin, rectangular shape with dimensions varying from 50 nm to 250 nm. They are stacked and overlap disorderly, resulting in tilted grain boundaries and small pinholes between the large grains. On the other hand, in the case of PEA:MA=1:2, the polycrystalline films consist of larger grains (varying between 150 nm to 400 nm) arranged next to each other in a well-coordinated manner to form a highly compact and homogeneous surface. The reason behind this observation is the hydrophobicity of the aromatic ligand (PEA$^+$), which increases the contact angle of the precursor solution on a wetting surface such as PEDOT:PSS and, subsequently, reduces the nucleation density at the beginning of the crystallization without spoiling the compactness of the polycrystals [218]–[220]. Overall, these results reaffirm that for 2D/3D lead bromide perovskites, there is a correlation between the concentration of the long-chain cations and the grain size. Furthermore, the ligand substitution from MA$^+$ to PEA$^+$ plays a vital role in improving the crystallinity and smoothness of the perovskite thin films.
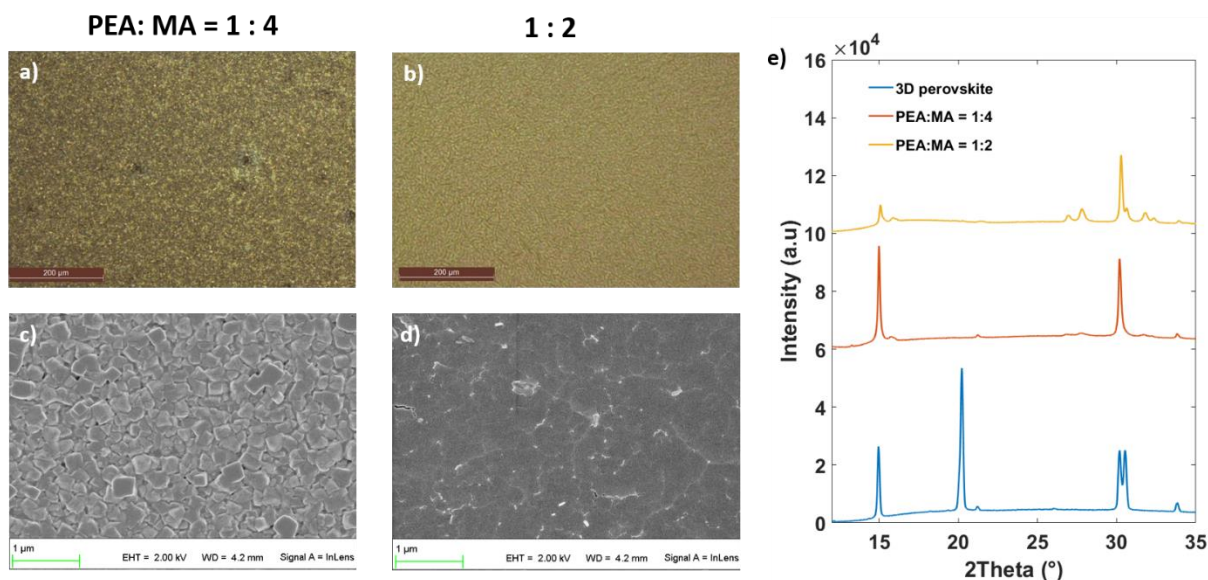
Figure II.3. a, b) Optical images and c, d) SEM images of thin films based on quasi-2D bromide perovskites concerning different PEA:MA ratios; e) XRD analysis of 3D and quasi-2D bromide perovskites.

Then, Figure II.3.e demonstrates changes in crystal orientation when substituting MA^+ with PEA^+ in the quasi-2D perovskites. Firstly, the blue curve represents the X-ray diffraction (XRD) pattern of the 3D MAPB polycrystalline film. It consists of a single peak at a 2θ value of 14.8° and a double peak around 30.2°, corresponding to the (100) and (200) planes, respectively, showing a high crystallinity along the (100) direction [149], [221]–[223]. Another apex at 20.2° can also be observed, reflecting the excess MABr used in the synthesis, which will dissipate in the cases of quasi-2D perovskites. Secondly, by increasing the PEA^+/MA^+ ratio, the relative proportion between the diffraction intensities at 14.8° and 30.2° will decrease, exhibiting a shift in crystal orientation towards the (200) direction. In addition, one can observe an increment in several low-intensity peaks around 27.1° and 32.5°, which correlate with the (111) and (211) planes, indicating a distortion in the perovskite's octahedral inorganic structure [149].

The effects of ligand substitution on the optical properties of the polycrystalline perovskite thin films are demonstrated in Figure II.4. Concerning the UV-Vis absorption, a fundamental difference between 3D and quasi-2D perovskites can be easily spotted, in which the quasi-2D perovskites' spectra show several peaks between 400 nm and 520 nm (compared to the single 525-nm peak as for MAPB). Each of these peaks corresponds to a specific *n* phase formed in the quasi-2D structures, such as 402 nm for *n = 1* (or 2D phase), 435 nm for *n = 2*, 455 nm for *n = 3*, …., 520 nm for *n → ∞* (3D phase). It is noted that, in mixed-dimension perovskites, the energy bandgaps of the high-*n* phases (*n ≫ 5*) are nearly equivalent such that their absorption peaks usually accumulate in the measurement, leading to a shift of 5 nm to 10 nm in the absorption curves as observed in the UV-Vis absorption curves. Accordingly, in the literature, these high-*n* phases are approximately referred to as one 3D phase.
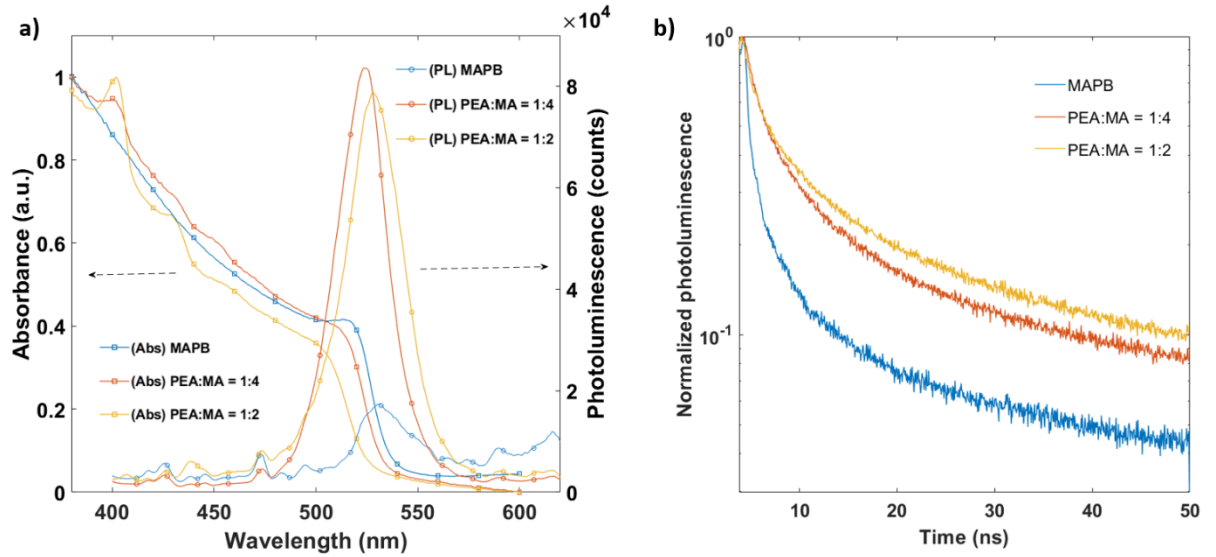
Figure II.4. a) UV-Vis absorption and PL spectra and b) PL decay curves of 2D/3D bromide perovskite films for different ligand ratios.

Moreover, by increasing the proportion of PEABr in the perovskite precursors, the intensities of the absorption peaks corresponding to the low-*n* phases will increase, and those of high-*n* phases will decrease, indicating the favorable formation of low-dimensional domains in the polycrystalline thin films. With respect to the steady-state PL, we can observe a peak around 525 nm in all three cases; however, those of the quasi-2D perovskite samples are one order of magnitude higher than that of the 3D perovskite sample. This result is an evidence of the energy cascade in mixed-dimensional perovskites, as discussed in the previous chapter.

Lastly, the kinetics of charge carrier recombination processes in the bromide perovskite thin films are investigated using Time-Resolved Photoluminescence (TRPL). Accordingly, the PL decays of the perovskite samples are shown in Figure II.4.b and can be fitted using a tri-exponential decay model, in which $\tau_{1, 2, 3}$ represent the lifetime values and $p_{1, 2, 3}$ represent the contribution (or the relative amplitude) of the component processes. The average PL lifetime τ_{ave} for each sample is calculated as:

$$\tau_{ave} = \tau_1 p_1 + \tau_2 p_2 + \tau_3 p_3 \qquad \textit{(Equation II.1)}$$

These values are summarized in Table II.1. The first comment we wish to note herein is that the PL lifetime of MAPB is usually described by a bi-exponential decay model in the literature, which comprises a fast-decay component τ_2 corresponding to the trap-mediated recombination and a slow-decay component τ_3 corresponding to the radiative recombination [149], [224]. However, in our measurement, we saw that the decay of the MAPB thin films could not be sufficiently fitted only using these two components (see Annex 2). Instead, it entails a supplementary sub-nanosecond decay component τ_1 with a contribution factor of ~ 11%, indicating the minor effect of an ultra-fast trapping phase that occurs during the early stage of the excitation [224]. In contrast to the 3D counterpart, the quasi-2D samples have higher τ_1 values, which arise mainly from the recombination in the PEAPbBr$_3$ domains. Similarly, the increase in τ_2 values (from 2.92 ns to 4.19 ns to 4.82 ns) as the dimensionality decreases can also be

attributed to the decay of the low-*n* phases. Interestingly, our experimental data show that increasing the concentration of the long-chain ligands in the precursor solution can help reduce the unfavorable contribution of these fast relaxation processes. This enhancement originates from the homogeneous and compact morphology of the emissive thin films with PEA:MA=1:2, which provides an ideal energy landscape for charge carriers to migrate toward low-bandgap domains and bypass trap-mediated recombination pathways. As a result, this quasi-2D perovskite sample yields the longest average PL lifetime of 18.20 ns, comparable to that has been published by Byun et al. [149].

Table II.1. Estimated values for PL lifetime of the 2D/3D perovskite thin films using tri-exponential decay fitting

PEA:MA	τ_1 (ns)	p_1 (%)	τ_2 (ns)	p_2 (%)	τ_3 (ns)	p_3 (%)	τ_{ave} (ns)
0:1 (MAPB)	0.40	11.58	2.58	26.43	16.35	62.00	10.86
1:4	1.03	5.25	4.19	26.78	18.53	67.97	13.77
1:2	1.16	2.52	4.82	20.51	22.32	76.97	18.20

Overall, the emissive thin films based on reduced-dimensional perovskites, especially for the ligand ratio of 1:2, exhibit the most desirable morphological and optical properties among all of the HOIP samples we have investigated.

2.1.3 Design and characterization of PeLEDs based on polycrystalline perovskite thin films

a. Device design and architecture

To characterize the electroluminescent properties of the HOIP thin films, we utilize a conventional PeLED architecture: ITO (180 nm)/ PEDOT:PSS (40 nm – 45 nm)/ Bromide perovskites/ TPBi (30 nm)/ Ca (20 nm- 40 nm)/ Metal electrode. A schematic illustration of the green PeLED with a simplified energy level diagram is depicted in Figures II.5. a and b.

In detail, our EL devices are fabricated on glass substrates as they possess high transparency and robustness (as opposed to flexible plastic substrates). ITO, PEDOT:PSS and TPBi are respectively chosen for the anode, hole transport layer, and electron transport layer materials owning to their appropriate work functions with regard to the HOMO and LUMO levels of the green-emitting perovskites as well as their demonstrated ability to yield efficient devices as reviewed in Chapter I. Concerning the electron injection layer, calcium is the material of choice because its work function of 2.9 eV matches well those of the ETL and cathode materials. Additionally, using Ca in the EIL has the advantage of reducing the fabrication cost since it is one of the most abundant metals on Earth [225]. Lastly, aluminum and silver are employed alternatively in this report for the cathode material. This decision was made because of the technical challenges we met when attempting to deposit the aluminum contacts either by vacuum thermal evaporation or electron-beam deposition techniques, such as difficulty in accurately controlling the

deposition rate and facile breakdown of tungsten crucibles. The PeLED fabrication process is portrayed in Figure II.5.c and described thoroughly in Annex 1.
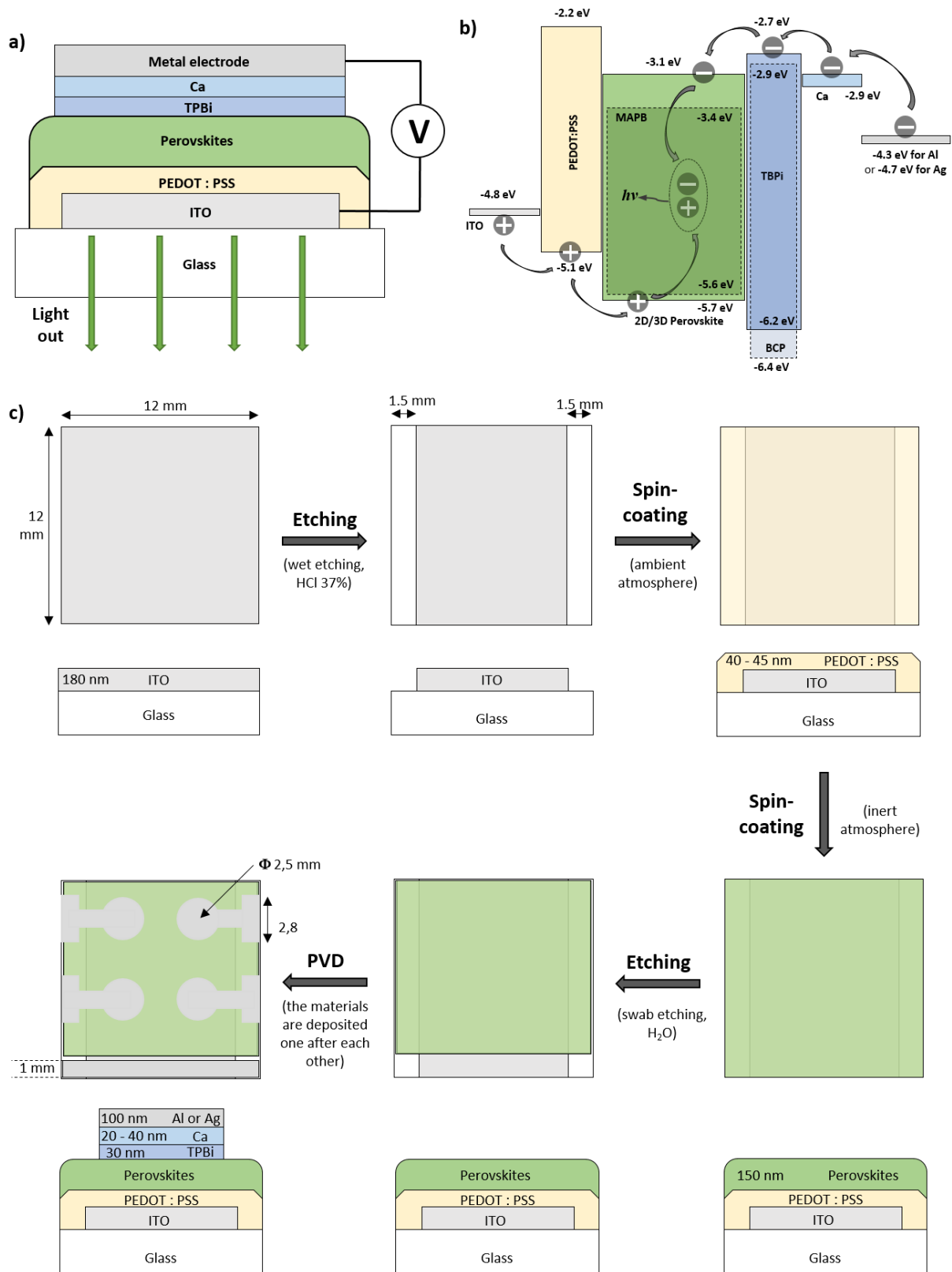
Figure II.5. a) Device structure and b) Energy alignment diagram of PeLEDs studied in this report; c) Step-by-step summary of the device fabrication.

b. PeLEDs using 3D HOIPs

Figure II.6 illustrates the EL performance of our PeLEDs based on 3D bromide perovskites based on the device structure: ITO (180 nm)/ PEDOT:PSS (45 nm)/ MAPB thin film (150 nm)/ TPBi (25 nm)/ Ca (20 nm)/ Al (100 nm). With regard to the emission spectra (Figure II.6.a), the EL intensities peak at 530 nm and 535 nm, respectively, for MABr:PbBr$_2$ = 2:1 and 3:1, indicating a redshift of approximately 20 nm compared to their PL maxima. More importantly, both cases show a spectral bandwidth (i.e., FWHM) as narrow as 30 nm, which is equivalent to results reported by Tan et al. [101] and Cho et al. [138] but slightly larger than Liang's PeLEDs [221].
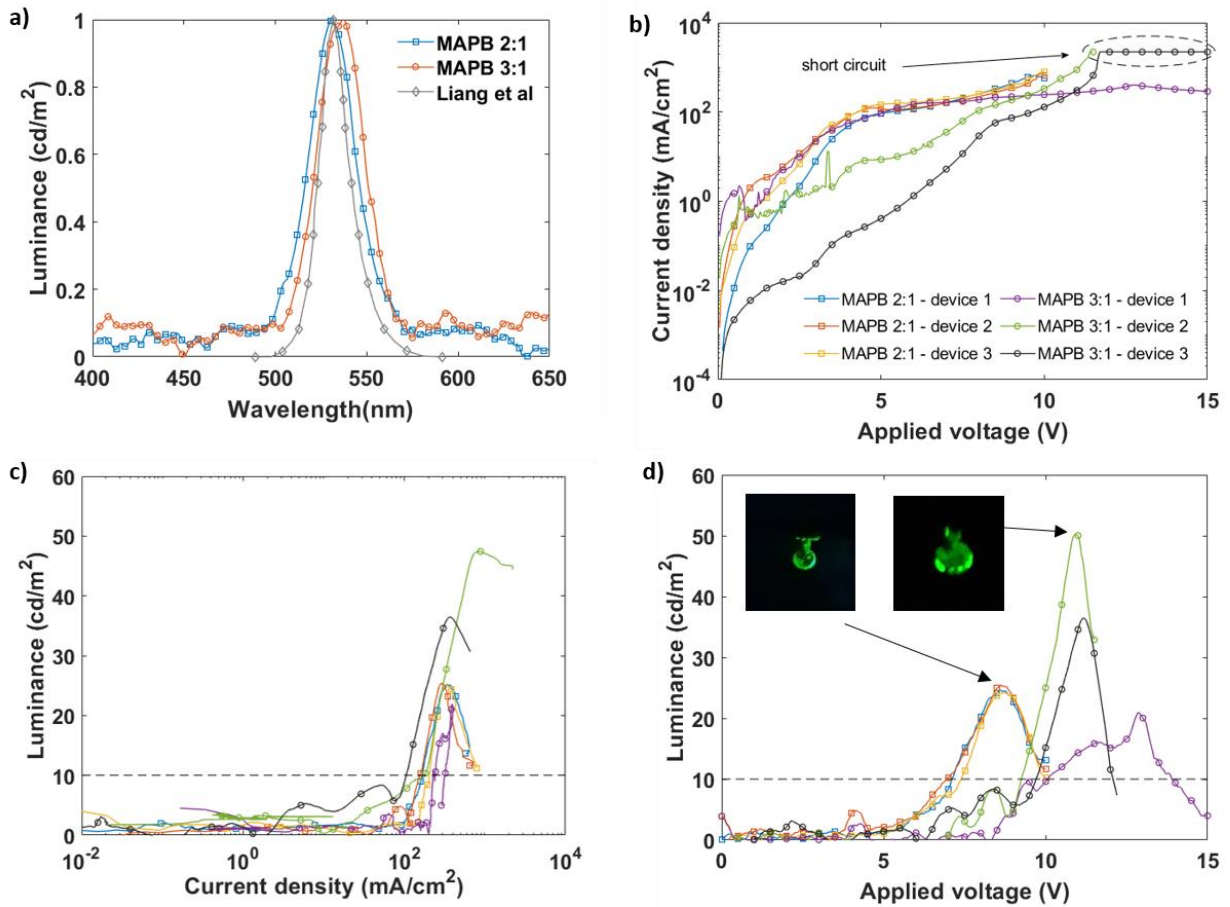
Figure II.6. a) EL spectra of PeLEDs fabricated using our MAPB recipes in comparison to devices reported by Liang et al. in Ref. [221]; Characteristic plots of six PeLEDs devices with MABr:PbBr$_2$ = 2:1 and 3:1: (b) J-V curves, c) L-J curves, and d) L-V curves. The dotted lines represent the luminance threshold of 10 cd/m^2, at which a PeLED can be considered to start emitting. Inset: Photographs of operational devices at their highest luminance.

The J-V, L-J, and L-V characteristics of three EL devices corresponding to each MABr: PbBr$_2$ ratio are shown in Figures II.6.b, c, and d. Generally, a relatively low emissivity with a high current density level and unremarkable luminance of < 50 cd/m^2 could be evident for all samples. For instance, in the case of 2:1, the J-V curves resemble a poor diode characteristic with an exponential leakage current even at low driving voltages < 1 V. Also, from the L-V curves, high driving voltages (V$_{ON}$ of 7 V) and, accordingly, high current density (J > 10^2 mA/cm^2) needed to turn on the devices can be remarked. This data suggests a prevailing prevalence of non-radiative recombination losses over the radiative pathway

to the extent that the EL can only be initiated in the presence of a substantial population of injected charge carriers. Compared to the 2:1 PeLEDs, the 3:1 devices perform a slightly better brightness yet show higher V_{ON} values and considerable device-to-device variability. It can as well be observed that the samples composed of MAPB 3:1 layers have a lower level of leakage current than those of MAPB 2:1, which can be attributed to the improved surface coverage and better homogeneity of the MAPB 3:1 thin films, as seen in section 2.1.2.

Additionally, for both cases, the photos of the PeLEDs at their maximum brightness demonstrate inhomogeneous emission, and in practice, we can even observe blinking effects from several tiny areas on the emitting surface. Both are indications of charge trapping and ion migration under electrical bias, either inside the bulk perovskite structure or at the interfaces between the perovskite layer and the adjacent charge transport layers [139], [226]. Lastly, we would like to remark on a decay of the PeLED's brightness when the applied voltage increases beyond a certain threshold, such as 8.6 V for MAPB 2:1 or from 10.9 V to 12.9 V for MAPB 3:1.

Then, the dependence of the devices' EQE on the current density in the regime where the devices effectively emit photons (e.g., 100 mA/cm^2 < J < 100 mA/cm^2) is depicted in Figure II.7. As we can expect when examining the devices' J-L-V characteristics above, the PeLEDs based on 3D MAPB exhibit low energy conversion efficiency, characterized by EQE values of < 0.004% (or, equivalently, LE values of < 0.01 lm/W). Furthermore, the EQE-versus-J curves illustrate a roll-off in the efficiency when the devices operate at high current density. This phenomenon directly associates with the diminution of the brightness mentioned above and has been frequently observed and reported in EL devices using organic or halide perovskite materials. The causes of roll-off in perovskite optoelectronic devices can be attributed to exciton quenching, imbalance of charge carriers [227], [228], and Joule-heating effect [229], [230] under intensive electrical excitation. Of these, the luminescence quenching (such as Auger recombination) stems from the intrinsic properties of the emissive material, the charge injection disparity is rooted in the device architecture (such as choices of transporting and injection materials), and the heating effect is rather a consequence of the high current density.
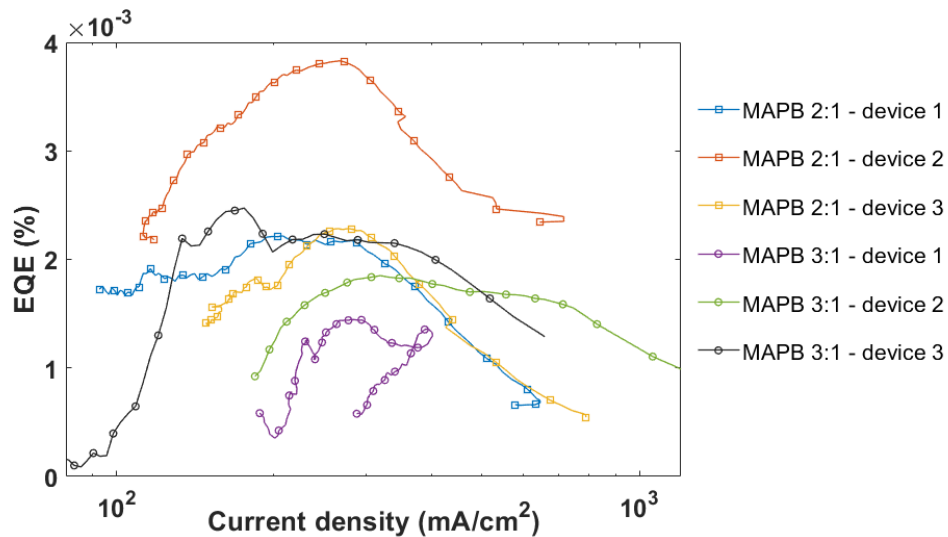
Figure II.7. Characterization of 3D PeLEDs' EQE in relation to current density.

After carefully examining the characteristic curves shown above, there is still another missing puzzle we must report in order to complete the picture about our MAPB PeLEDs: their operational stability. Unfortunately, all of our device prototypes exhibit a critically short lifetime (i.e., in a few seconds when observed by eyes). Such short operational stability, along with the low emissivity, makes it very difficult to choose an appropriate operating point to conduct the measurement. For example, the luminance at 70% of L_{max} is often too brief and transient for the photodiode to capture and measure accurately. This observation emphasizes the negative impacts of structural defects in organometal halide perovskites on the device lifetime, as well as reaffirms our previous comments on the importance of charge carrier kinetics and self-heating effects in PeLED degradation [128], [229], [231].

In conclusion, with the solid evidence of sustaining non-radiative recombination losses (i.e., leakage current, high turn-on voltage, and particularly efficiency roll-off), we understood that it was utmostly necessary to resolve the existing morphological issues of the MAPB thin films (such as pinholes, grain boundary, homogeneity) by reducing the perovskite dimensionality, as we have seen in section 2.1.2, in order to optimize the PeLEDs for achieving our performance target.

c. PeLEDs using quasi-2D perovskites

Figure II.8 illustrates the EL characteristics of the quasi-2D PeLEDs based on a device structure ITO/ PEDOT:PSS/ Quasi-2D perovskites (150 nm)/ TPBi/ Ca/ Ag (100 nm).
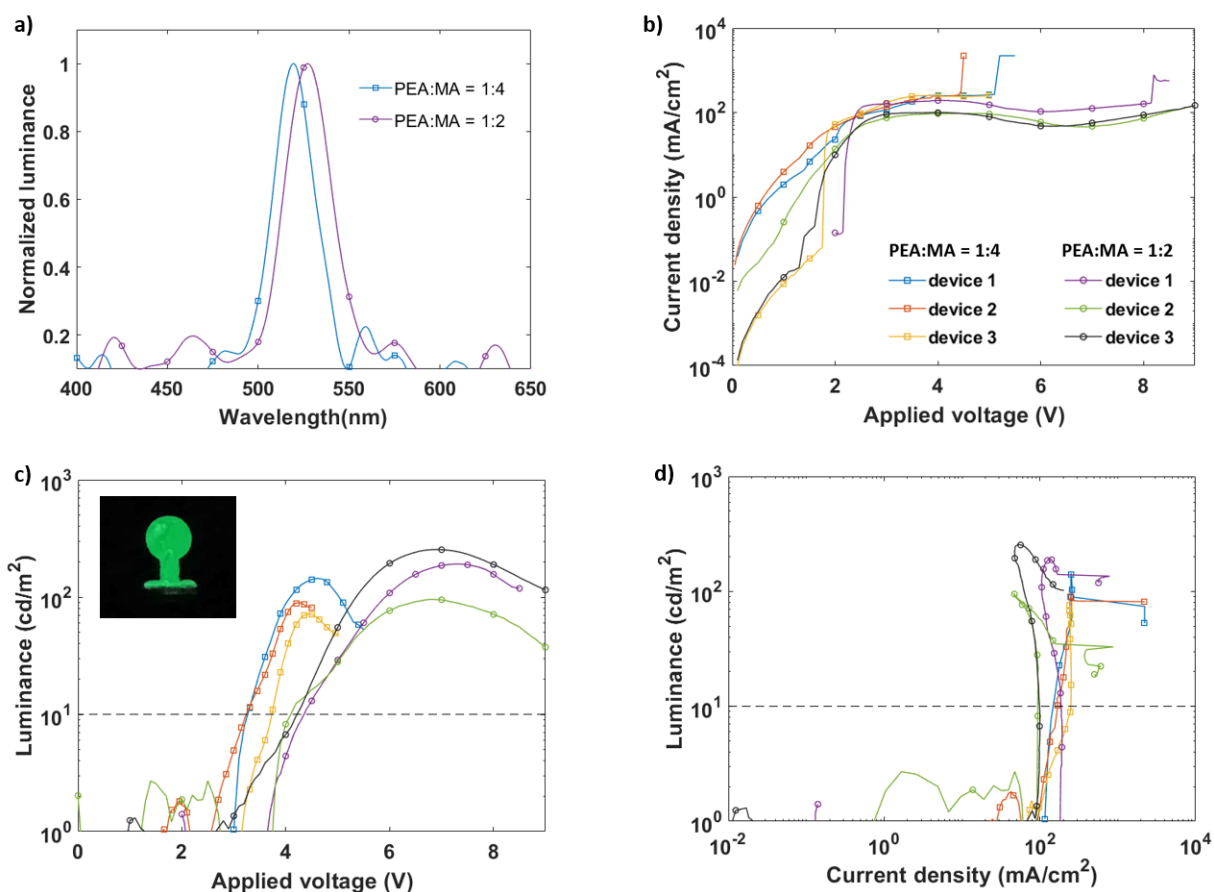
Figure II.8. Characteristic curves of PeLEDs based on quasi-2D bromide perovskites with regards to different PEA+:MA+ ratios: a) EL spectra, b) J-V, c) L-V (Inset: photograph of a functioning PeLED with PEA:MA=1:2), and d) L-J. The dotted lines represent the turn-on threshold of 10 cd/m².

As shown in Figure II.8.a, the emission spectra reach their climaxes at 520 nm and 528 nm, respectively, for the precursor ratios of 1:4 and 1:2. These EL peaks correspond to the maximal wavelengths in the steady-state PL measurement. It is noted that the 8-nm redshift of the EL peaks emphasizes the improved energy funnels towards the lowest-bandgap domains due to the increasing incorporation of the long-chain ligands into the perovskite lattice. The FWHM varies from 29 nm to 33 nm when the proportion of PEA+ ligands increases and is slightly larger than those reported for green PeLEDs in earlier publications [15], [53], [103]. These broader spectral bandwidths suggest a higher level of energetic disorder in the high-n domains, implying that the energy-cascading landscape in our quasi-2D thin films is not as homogeneous as in the reference studies.

Concerning the J-L-V characteristics, the PeLEDs based on quasi-2D perovskites share some electrical properties with those based on 3D perovskites, including a high leakage current (> 10^{-4} mA/cm²) at low driving voltages and a high current density (~ 10^2 mA/cm²) at V = V_{ON}. In contrast, reducing the dimensionality of the perovskites evidently improves the emissivity of the PeLEDs. For example, the highest luminances are captured at 144 cd/m² for PEA:MA=1:4 and 253 cd/m² for PEA:MA=1:2. Furthermore, V_{ON} is reduced significantly to 3 V and 4 V, respectively, implying enhanced competitiveness of radiative recombination compared to other recombination pathways. The photograph of a working PeLED at its maximum brightness also manifests a homogeneous emitting surface without

the "blinking" issue. Lastly, in the L-V scans, it can be observed that the luminances of the 1:4-ratio samples start to roll off much earlier than the other devices (i.e., 4.5 V versus 7 V), suggesting an improvement in the device's operational stability under high electric fields thanks to the reduction of the emissive material's dimensionality.

The relationship between the PeLEDs' efficiency and the input current is depicted in Figure II.9. Overall, the devices with a higher proportion of PEA$^+$ demonstrate better EQE values than their counterparts. For instance, the average value of maximum EQE (EQE$_{max}$) of the 2:1 samples is six-time higher than that of the 4:1 (i.e., 0.04% compared to 0.007 %). Besides, the plots of devices' luminous efficiency versus different performance metrics are provided in Annex 3.1. Furthermore, an unconventional trend in the efficiency roll-off can be evident in both cases. Taking the third PEA:MA=1:2 device (shown in the inset) as an example, we observe a high current of 100 mA/cm^2 at the beginning of the emission, associated with a low EQE (about 0.002%). Then, as the luminance increases, the flow of charge gradually declines, but the EQE rises quickly and peaks at 0.07%. When J = 50 mA/cm^2, the EQE starts decaying rapidly, signaling a degradation of the device. Such depletion in current density with augmenting brightness fundamentally differs from what has been observed in MAPB PeLEDs, where the current density and the EQE would proportionally correlate (before roll-off). Since no scientific reports have documented a similar observation, we lack a definitive explanation for this finding. Nevertheless, the data strongly suggest a modification of charge injection during high electrical excitation, leading us to consider ion migration in halide perovskites as a potential cause. For example, under electrical bias, the halide anions and, especially, the ammonium cations at the grain boundary of the perovskite's polycrystals become highly mobilized. They segregate and redistribute towards the interfaces between the perovskite and the charge transfer layers, forming a "built-in electrical field" and subsequently altering the kinetics of charge injection [128], [232]–[234].
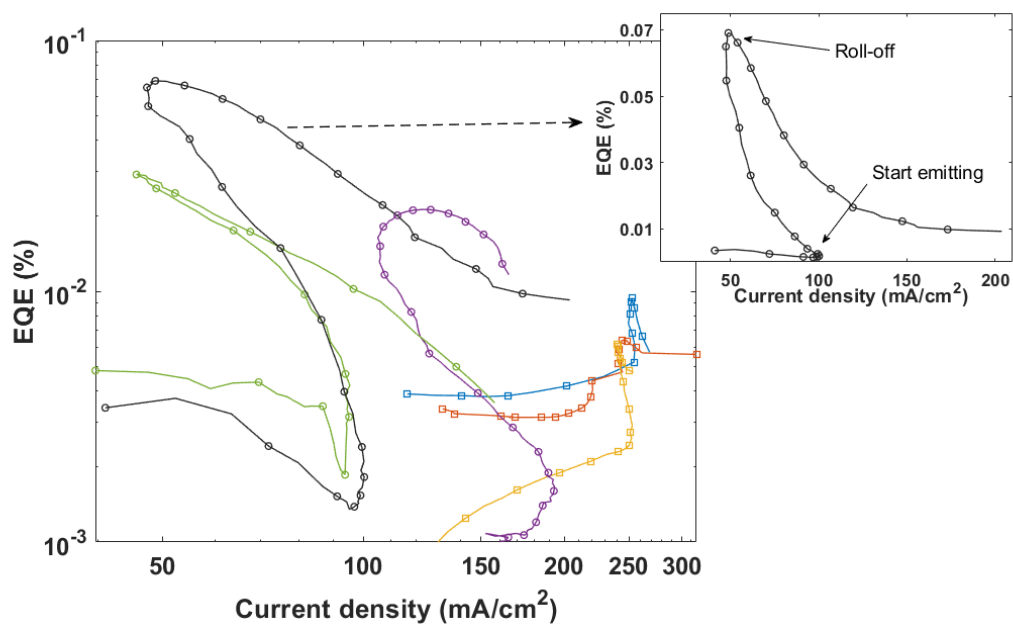
Figure II.9. Characterization of quasi-2D PeLEDs' EQE in relation to current density (Inset: EQE-J plot of the best-performance device in linear scales).

In summary, by reducing the dimensionality of the perovskite materials, we are able to mitigate the adverse effects of non-radiative recombination pathways on the performance of the PeLEDs, evidenced by the enhanced luminance and efficiency as well as the reduced turn-on voltage, particularly for the ligand ratio of 1:2. This enhancement can be attributed to the homogeneity, compactness, and superior optoelectronic properties (such as exciton confinement, energy funneling, etc.) of the quasi-2D perovskite thin films. Nonetheless, the performance exhibited by this device architecture still falls short of our requirements and is considerably below what has been reported in the literature for PeLEDs using similar emissive materials. Consequently, in the next section, we will focus on optimizing the device's charge injection and transport properties via surface passivation to improve the electroluminescence efficiency of the low-dimensional perovskites.

d. Optimization of charge-injection balance in quasi-2D PeLEDs

Our focus is on the interface between the HTL and the perovskite layer, driven by the publication from our colleagues at the University of Bordeaux [163], which demonstrated the severe influences of the perovskite deposition on the electrical properties of thin PEDOT:PSS HTLs in perovskite LEDs and solar cells. This entails the need to introduce a buffer layer between the PEDOT:PSS and the perovskite layer in our PeLED architecture in order to 1) effectively prevent the involuntary doping of the HTL during perovskite deposition (i.e., the diffusion of ionic species into the PEDOT:PSS thin layer, as reviewed in the previous chapter), 2) neutralize the mobility and carrier injection balance, and 3) eliminate electron overflow under electrical bias. Of all the alternatives we mentioned in our review in Section 1.2.3.b, using an ultra-thin insulating film of LiF appears to be the most appropriate approach.

An energetic illustration of PeLED design with LiF as a buffer layer is demonstrated in Figure II.10.a. In our experiment, the LiF layer (with a thickness of ~ 1 nm) is directly deposited on top of the PEDOT:PSS-covered ITO substrates using high-vacuum thermal evaporation. It is worth noting that the deposition rate is carefully controlled to be as slow as 3 Å/s to ensure the ultra-thin layer's high quality and coverage. Concerning the perovskite layer, owing to the promising results shown previously, we will fix the composition of PEA:MA=1:2 for the perovskite precursors.
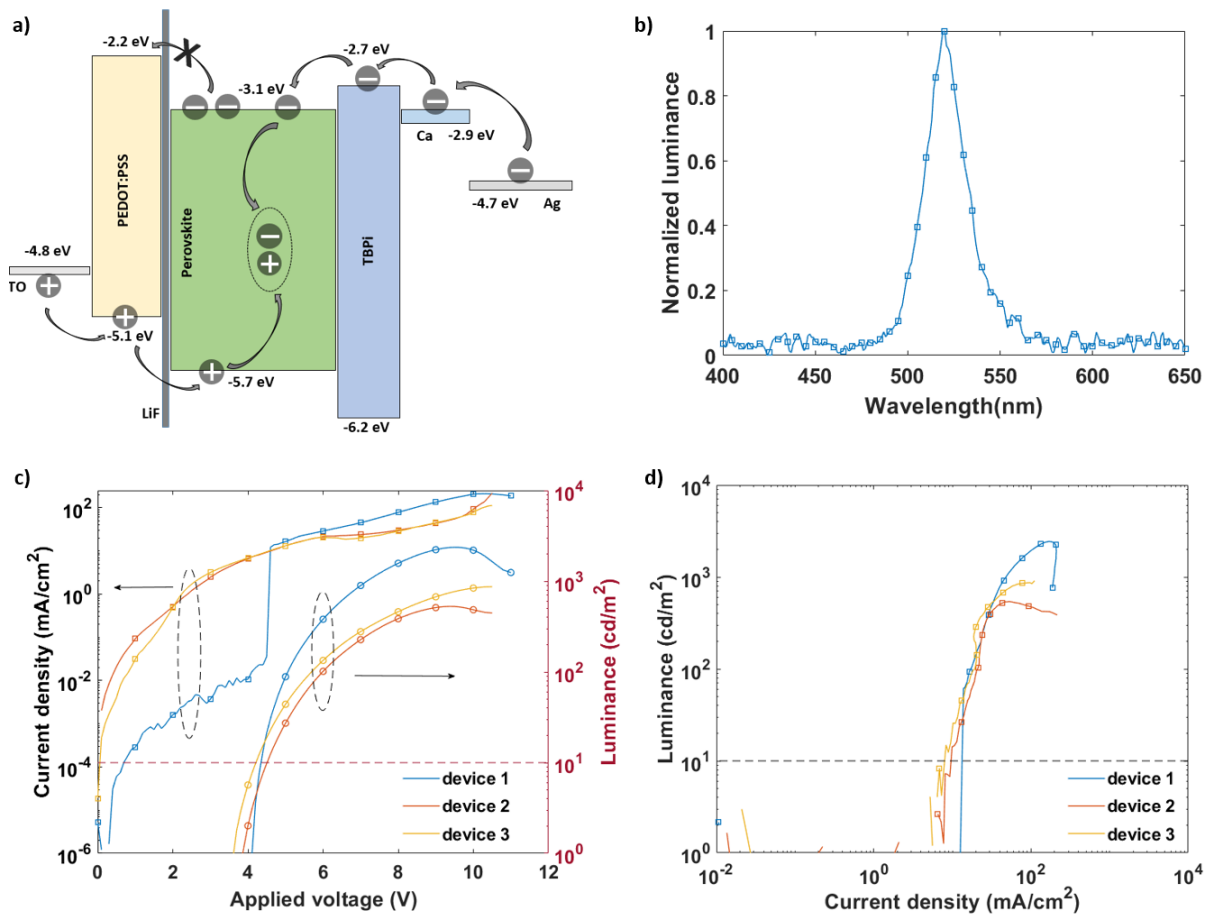
Figure II.10. a) Energy alignment diagram and b) EL spectrum of a quasi-2D PeLED with LiF as a surface passivator; Characteristic curves of three devices from our first batch of LiF-based quasi-2D PeLEDs: c) J-L-V and d) L-J. The dotted lines represent the luminance threshold of 10 cd/m².

The EL characteristics of LiF-integrated PeLEDs are shown in Figures II.10.b-d. First of all, the emission spectrum exhibits a peak at 519 nm with an FWHM of 28 nm, indicating a trivial blueshift compared to the pristine devices we examined above. Secondly, regarding the J-L-V plots, the devices demonstrate a relatively low current density over the entire window of the voltage scan, yet better brightness. For example, the best sample has a L_{max} of nearly 2,500 cd/m², while the average value of this quantity for all three devices also reaches 1,250 cd/m² – an order-of-magnitude improvement compared to the devices without LiF. In addition, the turn-on voltage remains unchanged, varying around 4 V, although the voltage at L_{max} increases considerably from 7 V to 9 V. Furthermore, the current needed to turn the PeLEDs on is significantly reduced to 10 mA/cm². These results originate from the insulation nature of LiF, which will partly restrain the flow of charge carriers inside the device, resulting in a low current density level, as we have seen. On the other hand, thanks to the passivation effect and its high energy barrier, the buffer layer allows the excitons to be closely confined within the active material instead of accumulating and migrating into the adjacent layers. As a result, the probability of non-radiative recombination is dramatically reduced, and therefore, more photons are emitted.

The dependences of the luminous efficiency and EQE on different optoelectronic metrics are presented in Annex 3.2 and Figure II.11.a. Compared to devices without the EBL, the LiF-integrated PeLEDs demonstrated an LE and EQE as high as 1,000 mLm/W and 0.6%, corresponding to an order-of-

magnitude enhancement. Also, similar to other cases previously investigated, the issue of efficiency roll-off can be remarked on here. For instance, the efficiency starts decaying at a bias voltage of approximately 7 V (when considering LE) or at a current density of around 40 mA/cm^2 (when considering EQE).
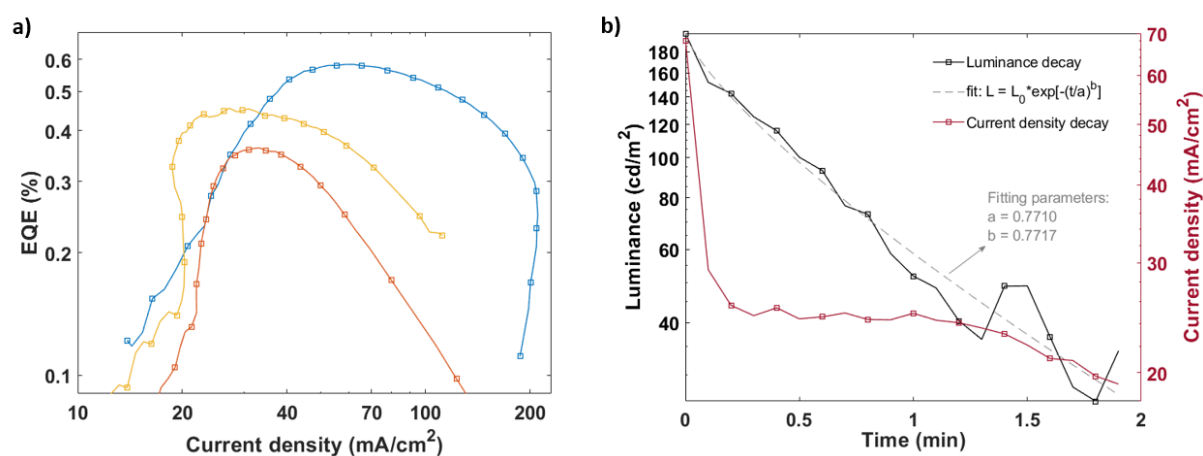
Figure II.11. Characterization of passivated PeLEDs: a) Correlation between EQE and current density and b) Evolution of luminance and current density by time, at constant bias of 8 V. The dotted line represents the stretched exponential fitting of the device lifetime.

Furthermore, we demonstrate the operational stability of a PeLED at an initial luminance $L_0 = 200$ cd/m^2 (bias voltage = 8 V) in Figure II.11.d, from which the T_{50} can be measured at 30 seconds. This lifetime value is exceedingly short when compared to state-of-the-art green PeLEDs [53], [103], [128]. By reflecting the luminance decay to the evolution of the current over the same window of time (noted that the graphs are plotted in logarithmic scale), we saw that the current density drops sharply by 65% of its initial value in the first 10 seconds before slowly decreasing over time. Conversely, the EL decay is less rapid and can be sufficiently described using a stretched exponential decay model [235]–[237]. Accordingly, we attribute the sharp drop in the current at the beginning of the electrical bias to the migration of halide ions inside the perovskite layer, which occurs immediately within a sub-second timeframe after an excitation [234], [238]. In quasi-2D PeLEDs, the migration of bromide anions leads to a combination of effects, such as modification of the perovskite's carrier mobility, distortion of crystal structure, and defect fill-in. While the first two effects depreciate charge injection efficiency, the latter can temporarily favor radiative recombination; therefore, the luminance decreases much slower than the current density. On a longer time scale, several other mechanisms are involved in the rapid degradation of our PeLEDs, including cation migration at the grain boundary, electrochemical reaction, electrode corrosion, interfacial reaction, and Joule heating [128], [239], [240]. To effectively suppress these issues would require careful engineering at the levels of the emissive materials and the device structure. For instance, introducing electron-donating functional groups, such as hydroxyl or carboxyl derivatives, can help passivate bulk ion migration at the Pb^{2+} sites. Additionally, some research groups proposed the use of different interlayers such as zinc oxide or nickel oxide as alternatives to conventional electron/hole transfer materials [128]. However, given that our primary performance objective has already been achieved, we made a decision that exploring such approaches would entail a significant temporal investment and, subsequently, should not be examined in this report.

In summary, the PeLED prototypes we design, which involve using low-dimensional perovskites with an optimal precursor ratio and inserting an insulating buffer layer, achieve to emit bright light $> 1,000$ cd/m^2 with an acceptable device lifetime. As we aim to make them a benchmark for our further studies in PeLEDs with different emissive materials or structures, in the following section, we will study the reproducibility of such devices to confirm the validity of the findings and ensure a consistent fabrication.

2.2 Reproducibility of quasi-2D PeLEDs

2.2.1 Reproducibility challenge in the fabrication of bright quasi-2D PeLEDs

Figures II.12.a and b show the J-L-V characteristics variation of 17 inter-batch PeLEDs (i.e., devices fabricated from different batches) based on the design we presented in section 2.1.3.d. Among these devices, three have luminances < 10 cd/m^2, considered incapable of emitting light. Of the other 14 devices, the electrical and optical behaviors fluctuate significantly over wide ranges of values. For example, the turn-on voltages vary from 3.2 V to 6.7 V, and the voltages at maximum brightness diverge between 4.7 V and 8.4 V. The luminances of the best and worst-performance devices are recorded at 6,400 cd/m^2 and 11 cd/m^2, respectively. The average luminance of the entire data set is 814 cd/m^2 with a standard deviation (std) of 235 %, which exceedingly surpass the margin of error of our measurement set-up (estimated at 17.4%, see Annex 1.4).
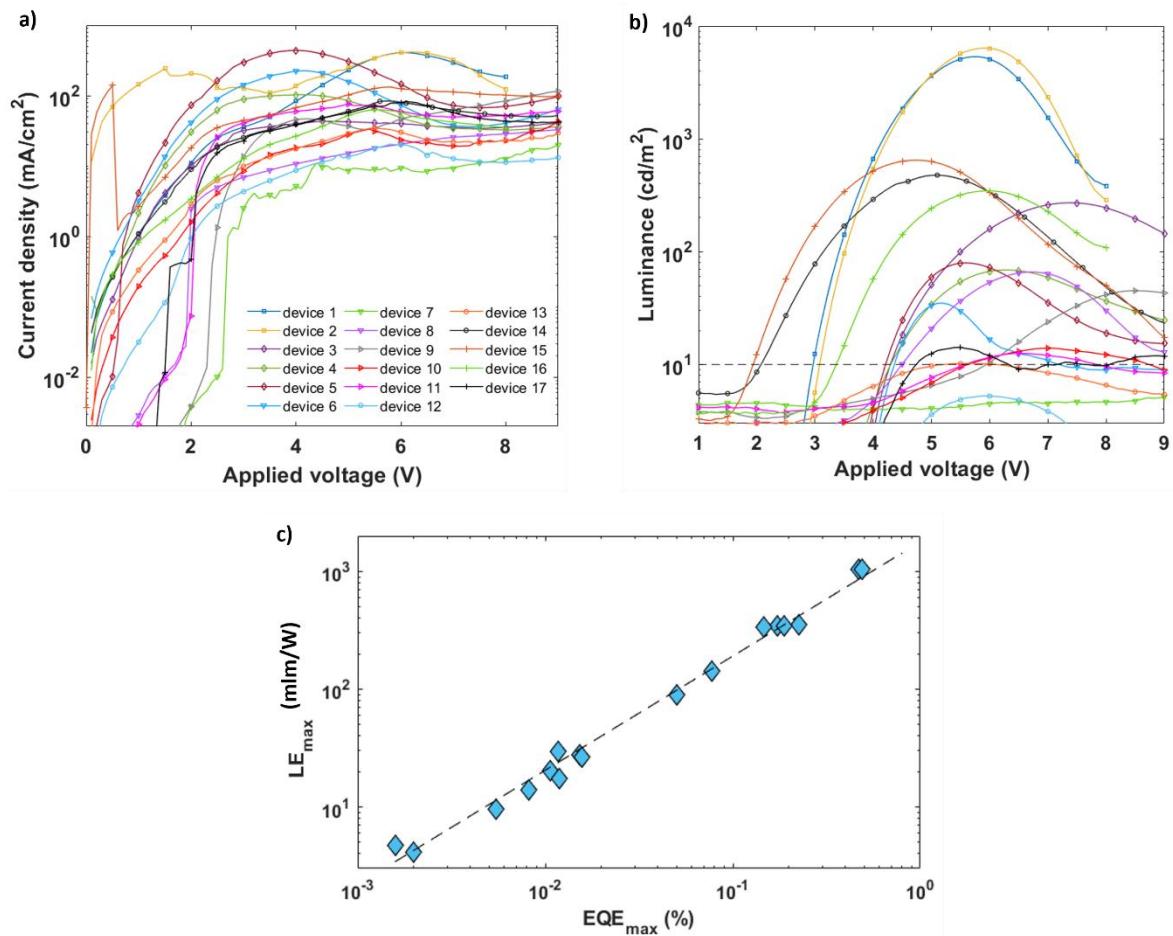
Figure II.12. Low reproducibility in a set of 17 quasi-2D PeLEDs: a) J-V curves, b) L-V curves. The dotted line indicates the threshold luminance of 10 cd/m^2, and c) statistics of maximum EQE and LE values. The straight line represents the linear relation between the two quantities.

Correspondingly, the statistics of maximum LE and EQE values (Figure II.12.c) also exhibit differences of up to 3 orders-of-magnitude between inter-batch devices. As further examining the low reproducibility observed in our PeLED fabrication, we can neglect the impacts from the spin-coating of the PEDOT:PSS layers as well as the vacuum evaporation of other interlayers and electrodes since they are widely recognized for their high repeatability (i.e., < 5% std in thickness, surface roughness, and optical properties) when deposited using similar experimental conditions. In contrast, the sensitivity of the perovskite crystallization to several deposition variables is clearly a main factor that we investigate in the first place.

Figure II.13 illustrates the variation in the optical and morphological properties of five quasi-2D perovskite thin films processed in our batch. The preparation of the samples is done one after another, with 2 minutes taken for each sample (which is the time needed to place the substrates on the holder, drop the solution onto the substrates, operate the spin-coater, and transfer the coated samples to the annealing plates). Clearly, there is a difference in the distribution of the crystallized phases among the 5 samples, even though they were processed in the same batch from the same mother perovskite precursor solution, employing very similar experimental conditions (i.e., Set-up A). On the other hand, the PL signals show a similar emission peak around 520 nm with insignificant shifts between the samples. In addition, the morphologies of the first and the last thin films processed in this series are captured using atomic force microscopy (AFM), revealing a decline in the surface roughness and coverage between the start and end of the process, even though the deposition set-up was unchanged. These results indicate hidden influences of extraneous variables of the set-up, which can deviate quickly between the successive spin-coating manipulations, on the crystallization kinetics of quasi-2D perovskite thin films, and as a consequence, on the low device reproducibility.
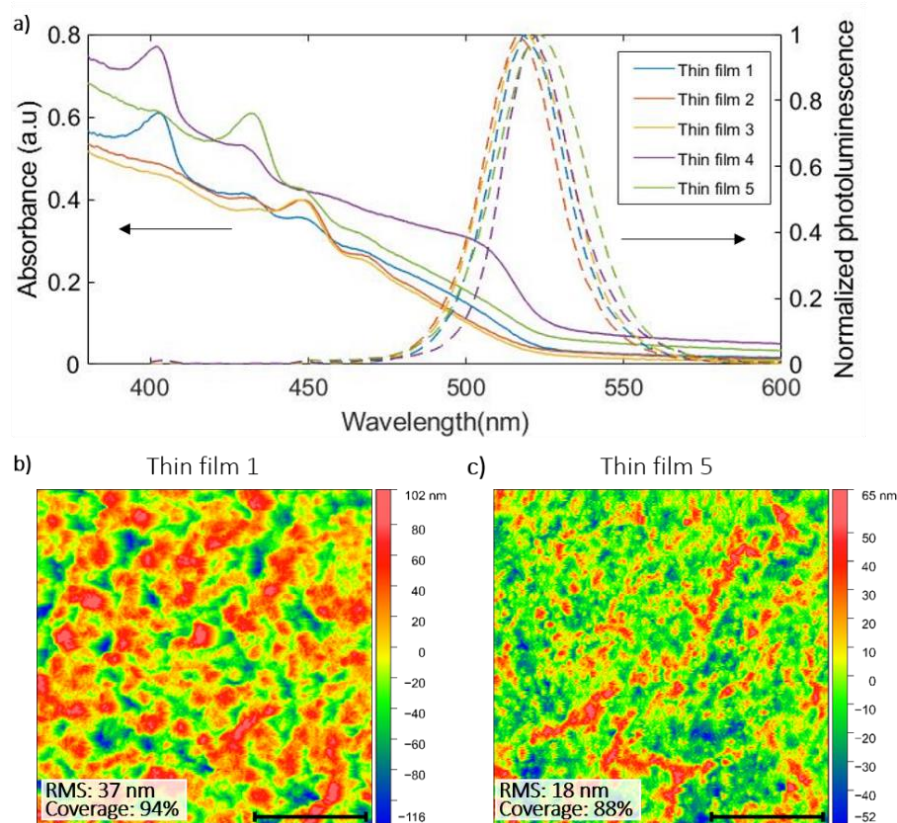
Figure II.13. (a) Absorption and steady-state PL spectra of intrabatch perovskite samples deposited successively using Set-up A; (b), (c) AFM images of the batch's first and last samples. The scale bar is 10 µm.

Subsequently, we have identified three principal factors that may govern the significant deviation in PeLED's performance, including:

i)   Thermal volatility of the deposition environment:

Changes in glovebox temperature can occur either due to fluctuation in the room temperature outside the workstation or from the heat sources inside it (such as the functioning of the hot plates H1 and H2 located near the spin-coating chambers). In particular, previous research by Han et al. has shown that changes in room temperature between 21 °C and 31 °C can result in a standard deviation of 70% in the performance of PeLEDs [199]. However, in our experiments, the temperature of the experimental room is maintained between 29 °C and 31 °C using an air conditioning system, as well as the 10-minute window of an intra-batch manipulation is relatively short for any significant changes in ambient temperature to occur. Nevertheless, the reproducibility of our PeLEDs remained significantly lower than reported by previous studies. Therefore, we can rule out the influence of ambient temperature as a significant contributing factor to the low reproducibility rate of our devices.

The other factor is thermal radiation generated by the operation of the annealing plates, which potentially causes temporary increases in localized temperature in the spin-coating chamber. In the following section, we will study whether this variable exhibit sufficient influence to alter the nucleation process and contribute to the observed variations in morphologies and optical properties.

ii) <u>The presence of residual oxygen and moisture in the deposition environment:</u>

We set up our glovebox to maintain the concentration of residual O_2 and H_2O below 10 ppm, which is generally accepted to avoid a significant impact on perovskite thin-film formation. However, in practice, we can still observe a quick surge in these parameters to exceed the concentration limit owing to sudden changes in the box's air pressure (as we move our hands during the manipulation). Furthermore, the surge can also occur when we open a solution vial, such as the perovskite precursor vial, due to solvent vaporization. Once the limits of O_2 and H_2O are exceeded, the box will be purged automatically with nitrogen gas; however, this re-stabilization process can take several minutes and unintentionally induce more fluctuations in the deposition conditions.

iii) <u>Chemical contamination from evaporated solvents in the glovebox atmosphere:</u>

Contamination can occur when multiple researchers share the deposition glovebox and its set-up. In our experiments, the glovebox is dedicated explicitly to perovskite-related processes but employed for various syntheses of different perovskite families (e.g., mixed halide, mixed cations, etc.) with the use and storage of various solvents or antisolvents (such as DMF, DMSO, chlorobenzene, toluene, or diethyl acetate). These solvents and antisolvents can substantially interfere with the crystallization of multi-dimensional perovskites and may dramatically impact their properties.

2.2.2 Effects of extraneous variables in the deposition set-up on the formation of quasi-2D perovskite thin films

First of all, to study the potential impacts of the operating hot plates and the residual O_2/H_2O on the spin-coating deposition, we designed a new experimental scenario, so-called Set-up B1 in this report, in which the distances from the hot plates H1 and H2 to the spin-coater are increased to the maximum feasible extent without introducing excessive difficulties in the manipulation process (i.e., 40 cm and 55 cm, respectively, as shown in Figure II.14). Furthermore, we lowered the limit values of O_2 and H_2O to 0.1 ppm and purge nitrogen gas into the workstation for one hour the afternoon before the deposition.
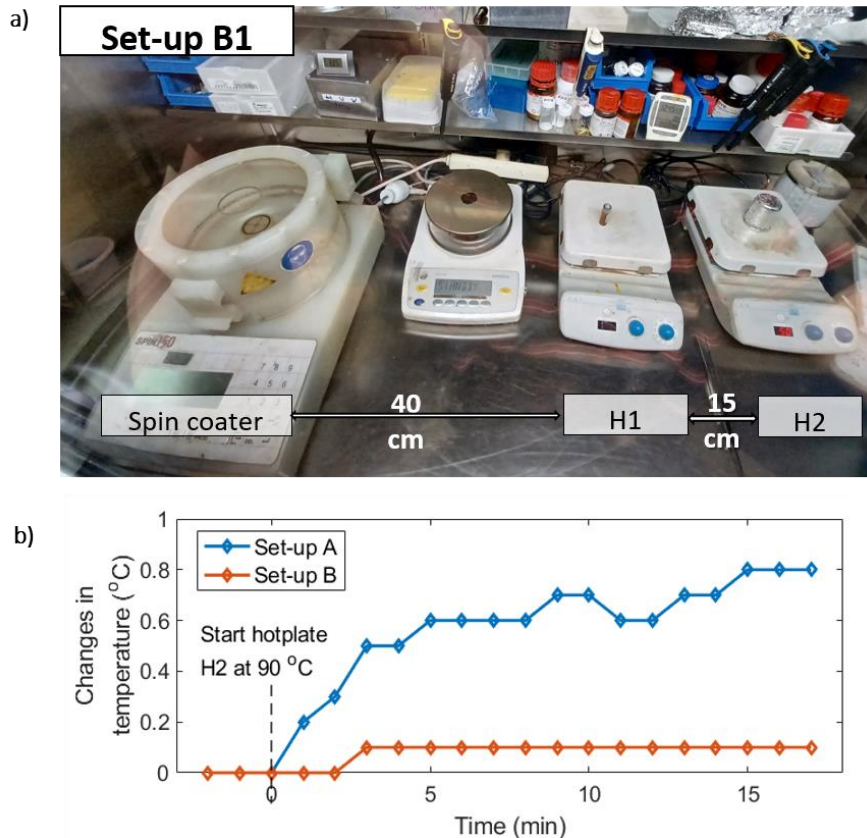
Figure II.14. a) Rearrangement of equipment in the perovskite deposition set-up and b) Temperature variation at the spin-coating holder during the perovskite deposition and annealing processes.

We then monitor and compare the changes in the spin-coating temperature during the deposition of several perovskite samples between the two set-up scenarios, A and B1, as depicted in Figure II.14.b. Using Set-up A, a slight increase of 0.8 °C in the temperature in close proximity of the spin-coating holder can be evident in the first 10 minutes of the experiment (which is the time window needed to deposit one batch of 4 or 5 devices). On the contrary, in Set-up B1, the thermal radiation from the hotplates has almost no influence on the temperature of the spin-coating chamber. Based on this observation, we can conclude that there is a difference in the deposition temperature between Set-up A and B1; however, considering the subsidiary variation of temperature in both cases and the accuracy of our temperature probe, we will not discuss the potential impact of such slight thermal fluctuation on the emissive layers' properties.

Figures II.15.a and b display the optical properties of 4 intrabatch perovskite thin films synthesized using Set-up B1. It is evident that the similarity in the phase compositions of the 4 samples is remarkably improved compared to Set-up A. Likewise, even the minor variations in the PL peaks that have been pointed out in the case of Set-up A are reduced. Concerning the time-resolved PL measurement, a variation in the average PL decay between 13 ns and 16 ns can be remarked. The morphologies of the first and last samples in the batch are compared using AFM characterization, as illustrated in Figures II.15.c and d. In both samples, the film surfaces appear compact and homogeneous, with a roughness of 29-30 nm and coverage of approximately 95%. Subsequently, we can conclude that there is a reduction in the variation of the perovskite's properties when utilizing the deposition set-up B1 instead of Set-up A. This improved repeatability can be attributed to the better control of oxygen and moisture inside the

inert atmosphere. We note that some influence of the hotplates remains a viable hypothesis, but again, the very small local temperature change monitored between Set-up A and B1 is difficult to rationalize.
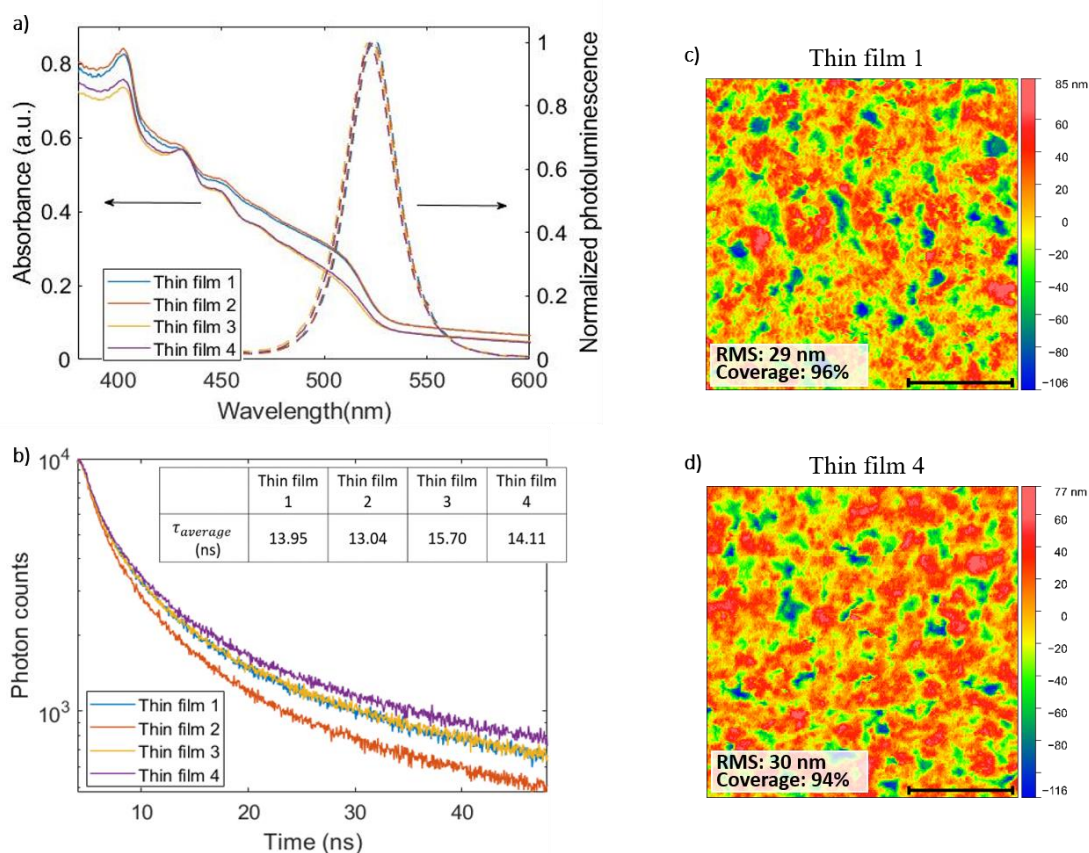
Figure II.15.a) UV-Vis absorption and steady-state PL spectra and b) PL decays of 4 intrabatch perovskite samples deposited successively using Set-up B1; c) and d) AFM images of the first and the last samples in the batch. The scale bar is 10 μm.

Next, to assess the effects of chemical contamination on the low reproducibility of the emissive material, we further modified the deposition set-up, in which we used a second glovebox (MBRAUN MB200B, oxygen limit of 1 ppm, humidity of 5% - 10%) to store the chemical species (including all of our solvents and antisolvents, as well as perovskite precursors, except for MABr) and to prepare the precursor solutions. Subsequently, the MBRAUN UNIlab workstation is now only used the deposition to avoid any possible contamination from the vaporization of the solvents. On the day of the experiment, we start the manipulations early in the morning to ensure the workspace remains uncontaminated by any other procedures. This experimental scenario is denoted as Set-up B2.

The optical properties of intrabatch perovskite thin films synthesized under scenario B2 are demonstrated in Figure II.16.a. In the UV-Vis absorption, an identical pattern in the distribution of quasi-2D perovskite domains can be pointed out, with a relatively strong peak at 445 nm (corresponding to n=3 phase) while the excitonic peaks of n=1 and n=2 become less visible. Interestingly, the multi-dimensional composition with a dominant n=3 phase has been shown to promote radiative processes in quasi-2D perovskites [35]. Besides, the PL spectra with the peaks at 520 nm confirm once again the emission from the lowest bandgap phase. Secondly, Figure II.16.b demonstrates the solid consistency in

the radiative decay kinetics of all 4 perovskite thin films. For all samples, the average PL lifetime varies around 15.5 ns, comparable to that of Set-up B1 but yields a minor deviation. Lastly, the roughness and coverage of the first and fourth samples are shown in Figures II.16.c and d. Compared to the case of Set-up B1, the root-mean-square values are increased considerably, varying between 42 nm to 55 nm, while the surface coverages are in the same order. Moreover, the average grain size, as revealed by AFM mapping, is significantly larger in Set-up B2 compared to Set-up B1. This larger grain size, observable for the two intra-batch samples, is responsible for the increased surface roughness in this case.
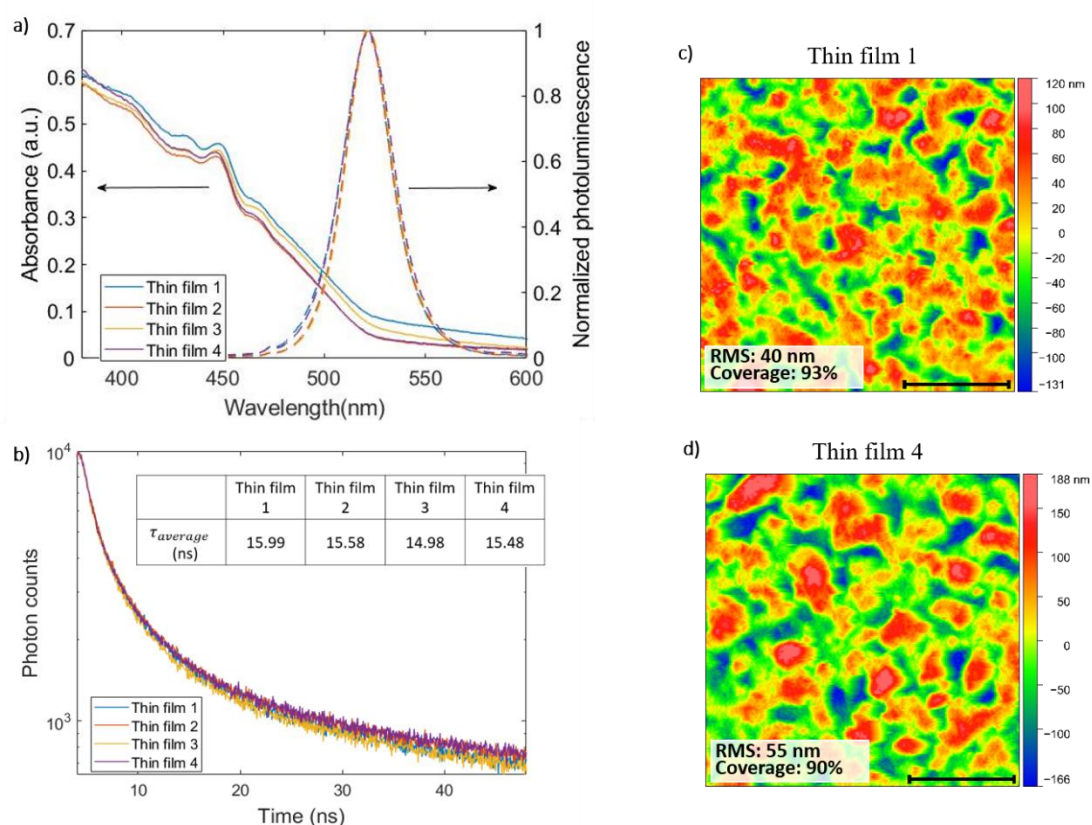
Figure II.16. a) UV-Vis absorption and steady-state PL spectra and b) PL decays of 4 intrabatch perovskite samples deposited successively using Set-up B2; c) and d) AFM images of the first and the last samples in the batch. The scale bar is 10 μm.

Altogether, these results suggest that, with coherent equipment set-up, careful disposal of chemicals in the glovebox, and regular purification of the deposition environment, a more reproducible growth of layered perovskites can be promoted, allowing for excellent uniformity in their morphology and optical properties. Such aspects are likely to be crucial to achieving reproducible optoelectronic devices, as we intend to demonstrate in the last section of this chapter.

2.2.3 Effects of extraneous variables in the deposition set-up on the reproducibility of quasi-2D PeLEDs

The L-V characteristics of inter-batch devices fabricated using Set-up B1 and B2 are illustrated respectively in Figures II.17.a and b. Compared to the L-V plots of Set-up A seen previously, it is clear that using Set-up B2 yields the lowest variance in key EL parameters, and following in second place is Set-up B1. For example, in the best scenario, the set of 14 devices exhibits an average turn-on voltage of 3.3 V, which varies within a narrow range between 3 V and 3.8 V. Also, the bias voltage at maximum

luminance can be averaged at approximately 6 V. The improvement in the device-to-device reproducibility as we change the experimental set-ups can be confirmed thanks to the statistical illustrations in Figures II.17.c and d. Impressively, while the mean values remain comparable (approximately 1,000 cd/m^2), the std of the L$_{max}$ values is noticeably reduced from 235% in Set-up A and 76% in Set-up B1 to only 38% in Set-up B2. Similarly, the std of the EQE maxima in the case of Set-up B2 is found to be as low as 42%, representing an improvement of over 3 folds compared to the utilization of the original set-up.
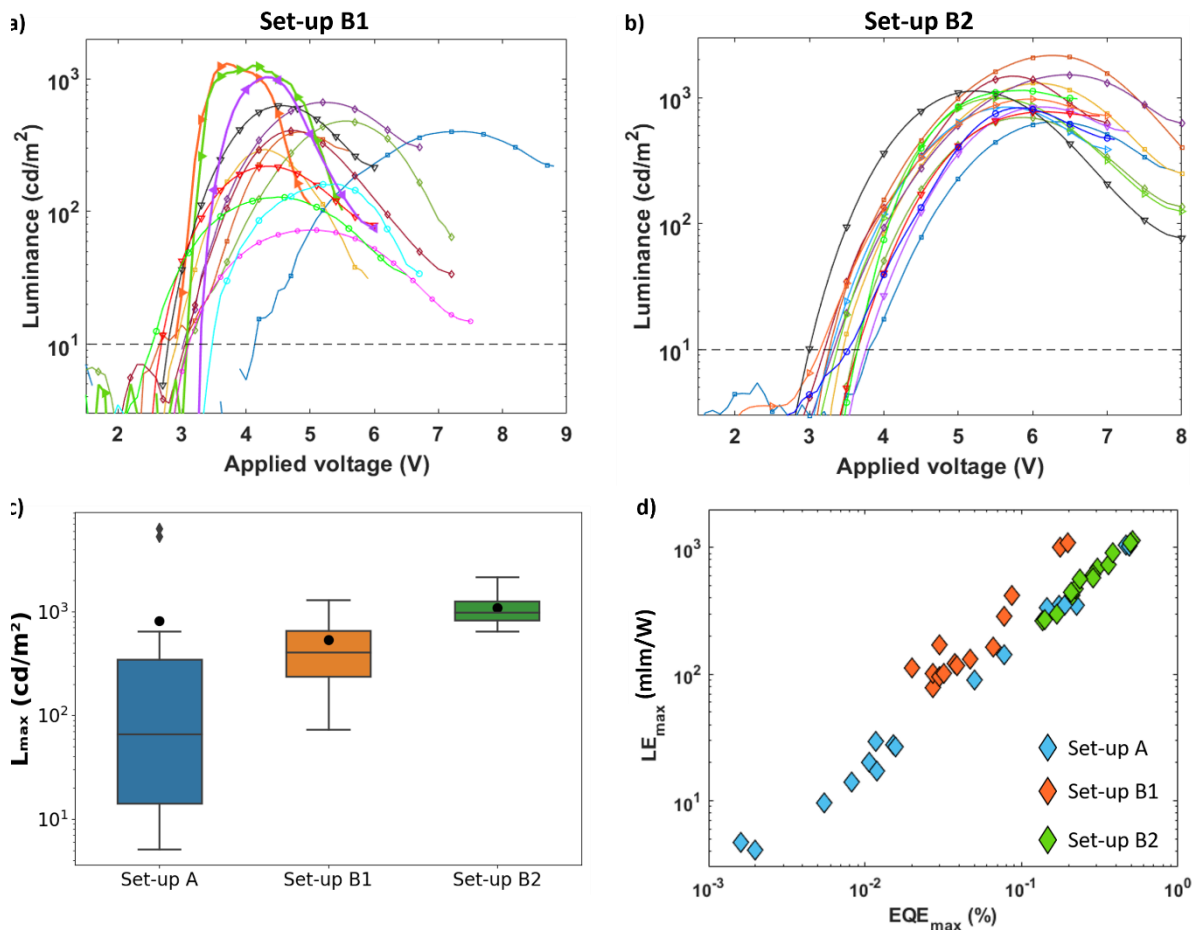
Figure II.17. L-V curves of two sets of 14 PeLEDs corresponding to a) Set-up B1 and b) Set-up B2; c) Statistical distributions of the maximum luminance of these devices, compared to those in Set-up A. The whiskers represent the upper and lower quartiles, the diamond markers represent the outliers, the middle lines represent the median value, and the black dots represent the mean value of each dataset.; and d) maximum EQE versus maximum LE of all devices fabricated using Set-ups A, B1, and B2.

Before concluding this section, it is worth acknowledging the reasons behinds the enhanced yet still unneglectable variability (of about 40%) in the PeLED's performance even with the implementation of our optimized fabrication protocols. In particular, this variation stems from inevitable manufacturing defects, especially in the processing steps requiring manual execution (such as the etching of ITO or perovskites). Another limiting factor is the potential dissolution of the LiF interlayers when exposed to the ambient air - during the transfer of samples between the thermal evaporator and the perovskite gloveboxes – because of their hygroscopic nature [241]. Despite our efforts to expedite the sample transfers (in a matter of only 10 to 20 seconds), the extent of impacts from such issue remain unpredictable

and difficult to completely prevent as it varies largely with the air's humidity levels on the days of experimentation.

In summary, these results clearly demonstrate the negative impacts of fluctuating residual O_2 and H_2O concentrations, together with untraceable chemical pollution, in the glovebox atmosphere on the reproducibility of quasi-2D perovskite research, particularly in the contexts of thin film deposition and fabrication of EL devices. It is worth noting that the slight variations in these extraneous parameters of the experimental set-up are usually considered insignificant and often neglected in the literature; however, we emphasize the importance of controlling such factors in the deposition of quasi-2D perovskites. As a result, we have minimized the deviations in the device's luminance and efficiency to approximately 40%. This improvement could be attributed to the consistency in the phase domain distribution and the morphology of the perovskite layers discussed above.

2.3 Summary

This chapter delved into the synthesis, optimization, and characterization processes of fabricating reproducible green PeLEDs based on HOIPs.

Initially, we studied the deposition of strong photo-emissive perovskite thin films, focusing on the use of methylammonium lead bromide and its reduced-dimensional counterparts. In each case, the effects of the precursor ratios on the crystallization and optical properties of the perovskite layers were carefully investigated. Accordingly, for the 3D perovskite thin films, we found that the optimal ratio between the ammonium cations and lead bromide anions to achieve acceptable surface morphology and PL properties is 3 to 1. Concerning the quasi-2D perovskites, the polycrystalline thin films, synthesized using our precursor recipes with different ratios between the short-chain and long-chain ligands, demonstrated even more favorable features, such as low density of defect, small grain size, homogeneous surface, or efficient energy cascade. In particular, the samples of $PEA^+:MA^+=1:2$ exhibited the most outstanding homogeneity and PL emission.

Next, we utilized the perovskite thin films as an emissive layer in our PeLED architecture (i.e., ITO/ PEDOT:PSS/ Perovskites/ TPBi/ Ca/ Ag). Compared to 3D perovskites, it has been shown that the devices based on quasi-2D perovskites yield better electroluminescent performance. However, by analyzing the characteristic behaviors of the device prototypes, we could also point out the interfacial degradation between the PEDOT:PSS and perovskite layers, which causes charge injection disparity and, thus, diminishes the device's luminance and efficiency. To resolve this technological challenge, we integrated an ultra-thin LiF buffer layer between the HTL and the active layer, serving simultaneously as a surface passivator and an EBL. Subsequently, the modified PeLEDs have achieved our target performance, with a luminance $> 1,000$ cd/m^2 and an operational lifetime T_{50} of about 30 seconds.

Lastly, we studied the effects of extraneous variables in the glovebox environment on the reproducibility of the quasi-2D perovskite formation and the performance of the PeLEDs based on this material. While the impact of temperature fluctuations due to the functioning of the hot plates remains

unclear to us, our research has effectively showcased the remarkable influence of even minor variations in residual oxygen and moisture concentrations, as well as undetectable chemical contaminants, on the crystallization process of perovskite materials. Consequently, the variation in the morphology and optical properties of the emissive materials would result in exceptionally high divergence in key PeLED performance parameters. We then introduced our best practices, which involve regular inertisation of the glovebox atmosphere, careful storage of chemical species, and appropriate arrangement of equipment, in improving the inter-batch device reproducibility. Accordingly, the standard deviations of maximum luminance and EQE values were reduced impressively from 230% and 140% in the original scenario to 38% and 42%, respectively, in the best scenario. Not only this finding can be applied to the study of PeLEDs but it may also be considered for other types of optoelectronic devices based on layered perovskites, such as solar cells and photodetectors. Furthermore, considering the large diversity of configurations between laboratories or between industrial actors, we emphasize that all experimental details, even those which seem trivial or irrelevant to the process, are crucial to ensure reproducible performance which can be compared by different researchers and groups in the broad and dynamic halide perovskite community.

Before moving on to the next chapter, it is essential to note the significance of systematically characterizing all electroluminescent (EL) devices presented in this chapter, even those that did not emit light. The data obtained from these characterizations holds valuable insights and will serve as valuable input for training our simulation models in a forthcoming project.

Chapter III. FABRICATION OF PELEDS BASED ON PEROVSKITE QUANTUM DOTS

Perovskite quantum dots (QDs), often referred to as perovskite nanocrystals (NCs) or 0D perovskites, have emerged as promising candidates in the field of optoelectronics due to their ability to tune the emission wavelength, high quantum yield in photoluminescence, and exceptional color purity (as reviewed in Chapter 1). In a recent breakthrough, Dr. Cédric Mayer and his colleagues from the "Laboratoire Lumière, Matière, et Interfaces" (LUMIN, Saclay, France) introduced a novel soft-chemistry approach to synthesize $CsPbBr_3$ quantum dots with remarkable uniformity and in large quantities under ambient conditions while preserving their optical properties [242]. Building upon this development, this chapter aims to shed light on the electroluminescent applications and performance characteristics of these innovative materials when employed as emissive layers in PeLEDs.

The initial section of the chapter is dedicated to establishing a concise review of Mayer's innovative method for synthesizing perovskite QDs and, more importantly, draw attention to the distinctive attributes that set it apart from conventional techniques. By highlighting these differences, we lay the foundation for our readers to better understand the scientific uncertainties and their implications in the context of fabricating PeLEDs based on the novel perovskite QDs. The participation of the collaborating laboratories and particularly the contribution of the author in realizing this study will also be detailed in this section.

The second section will concentrate on the challenges encountered during our efforts to fabricate PeLEDs with emissive layers directly derived from the soft-chemistry-synthesized $CsPbBr_3$ QDs. In particular, we will describe our observations concerning the processability of the perovskite QDs and subsequent treatment strategies aimed at enhancing the macroscopic morphology of the corresponding emissive layers. Furthermore, this section will detail and analyze our unsuccessful attempts to realize practical devices based on these pristine nanocrystal films, revealing the low surface coverage issue at microscopic scales inherent to the poor film formation of the perovskite QDs.

To overcome such issues, a pioneering approach to employ polymer materials as a versatile platform to disperse the QD emitters and improve film-forming capability will be introduced in the third section of the chapter. Accordingly, our empirical study on the preparation, deposition, and characterization of such composite QD/polymer materials will be presented, focusing on the impacts of varying the mass ratio between the perovskite QD and polymer components in the fabrication process. Subsequently, for the first time, bright PeLEDs based on the novel perovskite QDs synthesized via the soft-chemical route will be demonstrated.

3.1 Synthesis of luminescent perovskite quantum dots using soft chemistry

In the literature, perovskite QDs for light-emitting applications are usually synthesized using conventional techniques, such as hot injection (HI) [170], [171], [173], [243] or ligand-assisted reprecipitation (LARP) [176], [244], [245]. Each of these synthetic routes has benefits and drawbacks [19], [102], [246], [247]. For example, the HI technique enables synthesizing QDs with high crystallinity and uniformity yet requires complex experimental set-ups and an inert environment for precise control of reaction parameters (e.g., reaction temperature, precursor injection rate, etc.); therefore, it is more suitable for laboratory-scale synthesis than industrial production. Conversely, LARP is a relatively simple technique to assemble a large quantity of QDs quickly (within only a few seconds [248]) at ambient conditions; however, the synthesis outcomes often yield large distribution in the QDs' size and shape, which limits the ability to tailor properties for specific applications. In 2022, Mayer and colleagues at LUMIN successfully developed a scalable method for synthesizing perovskite NCs at room temperature using soft chemistry, which allows for rapid preparation of highly uniform nanoparticles in large quantities without requiring inert-gas workstations. Figure III.1, extracted from [242], illustrates the synthetic route and optical properties of inorganic $CsPbBr_3$ QDs prepared via this soft-chemical strategy. Briefly, it involves: (Step 1) synthesizing polydisperse $CsPbBr_3$ NCs (of about 40 nm) from cesium oleate (Cs_2CO_3) and lead bromide ($PbBr_2$) precursors dissolved in a stabilized toluene solvent and (Step 2) cutting the polydisperse NCs into highly-calibrated colloids of 10 nm using π-organic amine "scissors", such as phenylethylamine (PEA).
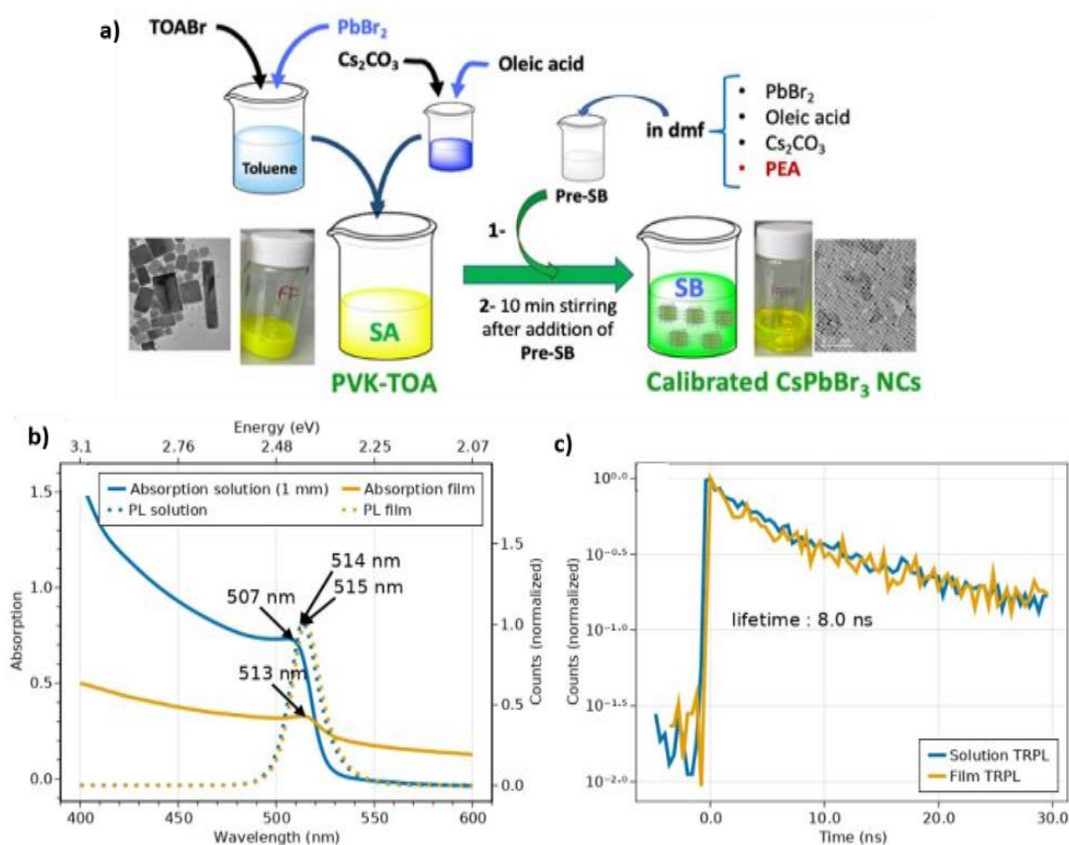
Figure III.1. a) Soft-chemical processing of calibrated inorganic perovskite quantum dots; b) UV-Vis absorption and PL spectra and c) PL decays of the quantum dots in solution and thin film. Extracted from [242].

As a comprehensive explanation (including the step-by-step procedure) of this method has been clearly provided in [242], we will provide herein our comments concerning important experimental details intrinsic to this methodology, which set it apart from conventional approaches and can potentially impact the deposition processes of the corresponding emissive thin films.

First, the choice of the organic amines as a transformation reagent can affect the optoelectronic properties of the perovskite QD films. Specifically, in their paper, Mayer et al. utilized a mixture of reagents containing PEA, oleic acid (OA), $PbBr_2$, and Cs_2CO_3, in which the authors emphasized the essential role of the PEA molecules in "cutting" large sheets of polydisperse NCs into uniform colloids of small sizes. Subsequently, the $CsPbBr_3$ QDs were reported to achieve a high photoluminescence quantum yield (PLQY) of approximately 60% and a luminescent stability of about 2 to 3 weeks in the ambient environment, both in colloidal solutions and in drop-casted films [242]. Recently, the research group went one step further to improve the emission properties of the perovskite QDs by replacing PEA with its longer-chain sibling phenylpropylamine (PPA). As shown in Figure III.2, the PPA-based nanocrystals exhibit reduced particle size (~ approximately 8.1 nm in average) with improved steady-state emission intensity (PLQY of 80%) and longer PL decay (14.5 ns), implying the positive effects of the aromatic capping ligands on the radiative recombination within the QDs. It is noteworthy that the dimension of the nanocrystals is quite larger than the exciton Bohr radius, meaning that the optical properties of the materials are not crucially influenced by the quantum size effect. Indeed, as reviewed in section 1.2.3, the phenylalkylamine ligands have been demonstrated to effectively promote the electroluminescence of the corresponding 0D perovskite thin films in LED applications. This is attributed to: 1) the small nanocrystal's dimensions (compared to commonly-used long-chain stabilizing agents such as oleic acid or oleylamine), which allows for improved packing and closer intermolecular interactions between the perovskite QDs, and 2) the extended conjugation of electrons along the aromatic structures, contributing to more facile charge transport through the material [175], [176], [249], [250]. Smaller QDs are also favorable for efficient exciton confinement, which is a requirement for high radiative efficiencies.
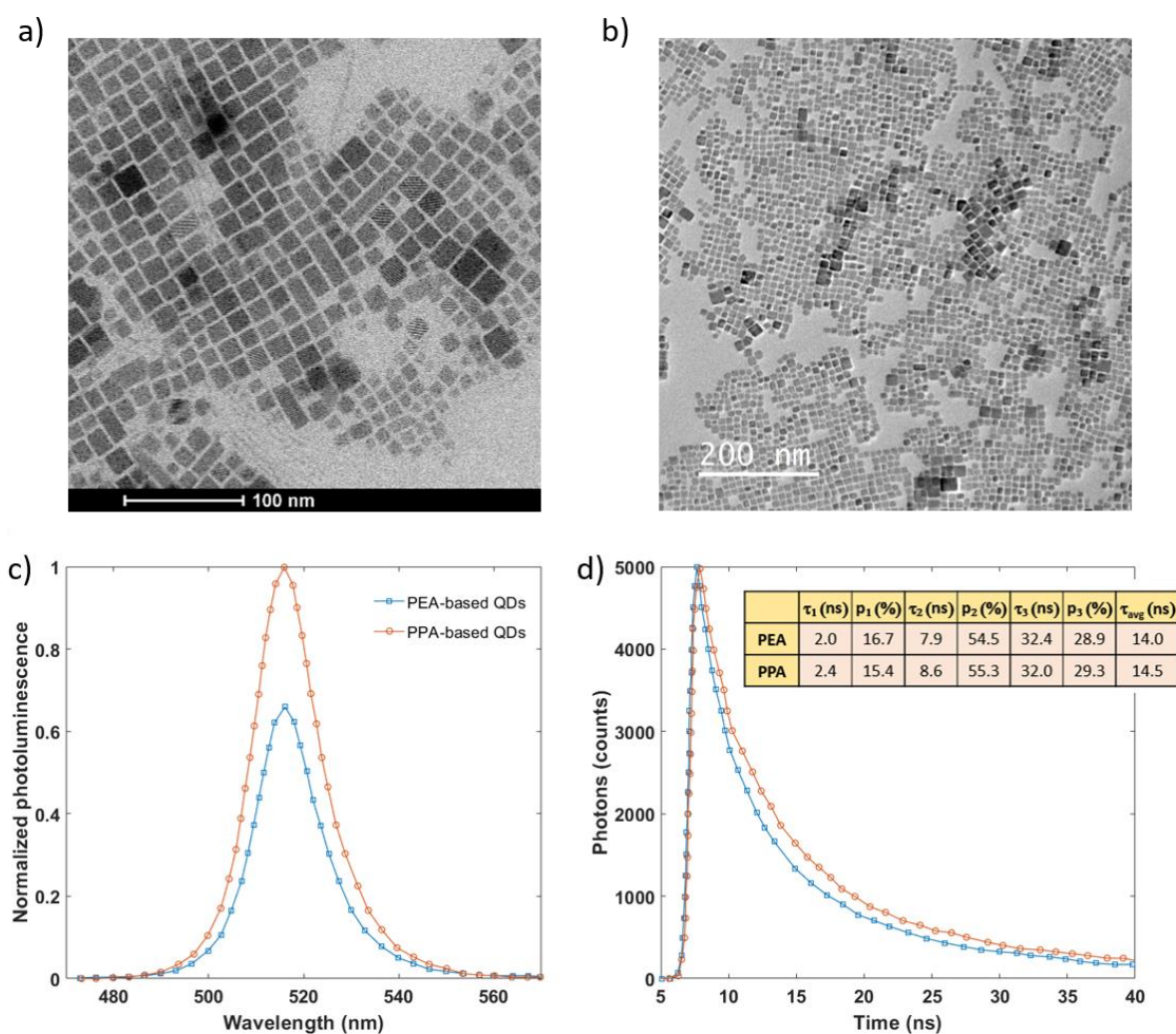
Figure III.2. TEM images of CsPbBr₃ QDs synthesized with PPA at scale bars of a) 100 nm and b) 200 nm, respectively; and Comparison of optical properties of CsPbBr₃ QDs synthesized with PEA and PPA: c) steady-state PL emission and d) PL lifetime (The inset shows the fitting parameters and estimated average lifetime). The data is provided by C. Mayer.

Second, the choice of the dispersing solvent to prepare the final monodisperse QD products should also be remarked. While most of the work on PeLEDs based on perovskite QDs utilize alkane solvents, such as n-octane [170], [173], [175], n-hexane [172], [251]–[254], or mixture of n-octane and dodecane [249], as the final dispersing solvents, Mayer et al. chose to disperse the calibrated CsPbBr₃ QDs in toluene. Although classified in the same group of non-polar organic solvents, n-octane, n-hexane, and toluene have varying chemical and physical characteristics (such as polarity, boiling point/vapor pressure, viscosity, absorption wavelength), as shown in Table III.1. Such parameters play an important role in determining the formation kinetics and, subsequently, the quality of the QD layers deposited via solution-processed techniques such as spin-coating. For example, a study by Chen et al. demonstrated a direct correlation between dispersing solvents and distribution of hot-injection-synthesized CsPbBr₃ QDs deposited on glass substrates [255]. Accordingly, the solvents with higher boiling points (or, equivalently, lower vapor pressures) are more inclined to form thin films, yet the films contain more aggregations and exhibit poorer emission properties. Additionally, even though the polarity of toluene is relatively low when compared to typical polar solvents (such as tetrahydrofuran (4.0), ethyl acetate (4.4), N,N-

dimethylformamide (6.4), or dimethyl sulfoxide (7.2)), it is still found about 20 times higher than that of n-octane or n-hexane, suggesting that it can react at a certain degree with the surface ligands and eventually affect the stability of the perovskite QDs [256], [257].

Table III.1. Chemical and physical properties of non-polar organic solvent for perovskite QD dispersion [255], [258]

Solvent	Polarity	Boiling temperature (°C)	Vapor pressure (mmHg)	Viscosity (Pa·s)	Absorption wavelength (nm)
n-octane	0.06 - 0.2	125	10	0.53	200
n-hexane	0.06 - 0.1	69	124	0.33	210
Toluene	2.40	111	21	0.59	285

In conclusion, there is no doubt to us that the 0D bromide perovskites prepared using the new soft-chemical route hold great promise for scalable applications in electroluminescent devices. In the following sections, we are set to explain our systematic approach for incorporating this material into our PeLED structure, starting with the deposition of thin yet compact emissive layers based on CsPbBr$_3$ QDs. Due to the project's time constraint, we will focus on the QDs synthesized with the PPA reagent, as they exhibit better optical properties than those synthesized with PEA.

Before moving on to the next section, we note that, in this study, the initial preparation and characterization of the colloidal perovskite QD solutions were primarily undertaken by Cédric Mayer's group at LUMIN. Nevertheless, the author of the thesis actively engaged in several mobilities to LUMIN (under the framework of the EMIPERO project) to acquire essential knowledge as well as provide assistance in these processes. The QD solutions were then transferred to XLIM for device fabrication. In particular, the transfer between Saclay and Limoges could take 2 to 3 days, during which the perovskite NC solution was contained in a glass vial enveloped by several layers of parafilm and placed inside a plastic box. Beyond that, there were no other protocols governing the transferring procedure. Consequently, it is anticipated that the solution may be subjected to fluctuations in the ambient environment (e.g., temperature, humidity, etc.) during transport. However, data from Mayer et al.'s article confirmed that the perovskite QDs can preserve their properties in solution for about three weeks without special packing conditions. The realization of prototype devices (including the preparation of composite precursors, the deposition and characterization of emissive thin films, the fabrication of multilayered structures) and associated device measurement were carried out at XLIM. The analysis of experimental results was a collaborative effort involving both XLIM and LUMIN.

3.2 Challenges in fabricating PeLEDs based on perovskite QDs synthesized via soft chemistry

3.2.1 Deposition of CsPbBr₃ QDs on flat substrates

a. Drop-casting

To study the formation of perovskite QD films on flat surfaces, we initially attempted to deposit the monodispersed CsPbBr$_3$ QD solution on glass substrates via drop-casting. The purpose of starting the study using this technique is to assess the film-forming capability of the QD solution, such as the wetting behavior, the spreading dynamics, and the quality of the initial films formed, even though drop-casting is known for its limitation in controlling film's thickness and uniformity. Besides, it has been employed by Mayer et al. to prepare solid films on quartz substrates with optical properties similar to the NCs dispersed in solution [242].

In particular, after being transferred to Limoges, the CsPbBr$_3$ QD solutions would be almost ready for use. The only requirement is a brief manual agitation of the solution vial for a few seconds immediately before the deposition to ensure the uniform dispersion of the QDs. Then, 25 µl of the QD solution is dropped onto pre-treated glass substrates. The samples are left to dry naturally (e.g., no thermal annealing is needed) for 15 minutes. Before characterization, we carefully clean the opposite side of the substrates using cotton tips soaked in toluene to avoid residual QDs perturbing our measurement data. All manipulation is conducted under a fume hood at room temperature (i.e., 25 °C).

Regarding the glass surface pre-treatment, the substrates are cleaned consecutively with ethanol and isopropanol in an ultrasonic bath for 15 minutes each and then dried under a nitrogen flow. After cleaning, the substrates can be directly used for deposition or processed with UV-Ozone for another 15 minutes to improve wettability. Another method we studied to improve the wettability of the glass substrates, in place of the UV-Ozone exposure, is to use the dispersing solvent itself. For instance, we spin-coated the substrates with 100 µl of Toluene solvent at 3000 rpm for 1 minute and allowed them to dry naturally for roughly 5 minutes before the deposition.

Figure III.3 demonstrates the effects of the pre-treatment protocols on macroscopic morphologies of the drop-casted QD layers. It can be observed that, without any further treatments than cleaning, the 0D perovskite does not form a film and tends to distribute near the center of the substrate (i.e., the green-emitting region under UV light in Figure III.3.a). Looking closer at this area using optical microscopy, as shown in Figure III.3.d, reveals intricate and heterogeneous spatial patterns with clustered aggregates, characterized by the presence of variously-sized black circles on the image. This observation can be attributed to the hydrophobic nature of the toluene solvent, together with the use of the long-chain reagents in the QD synthesis, which results in a low wettability of the perovskite NC solution on pristine glass [259], [260]. Subsequently, more solution is drawn towards the substrate's center and solvent evaporation becomes uneven, thus deducing the original droplet into numerous smaller droplets of various sizes and causing irregular aggregates. Even when the surface chemistry of the glass substrates is

modified using UV-Ozone treatment, the outcomes are still unfavorable, as seen in Figures III.3.b and e. Conversely, the perovskite QDs deposited on the glass substrates treated with toluene solvent appear more homogeneously distributed across the entire substrate surface (Figures III.3. c and f), with a thickness estimated around a few micrometers. Nevertheless, we must remark that these drop-casted QDs do not form a complete thin film but rather assemble into discrete macroscopic agglomerates, which are inapplicable to light-emitting devices.
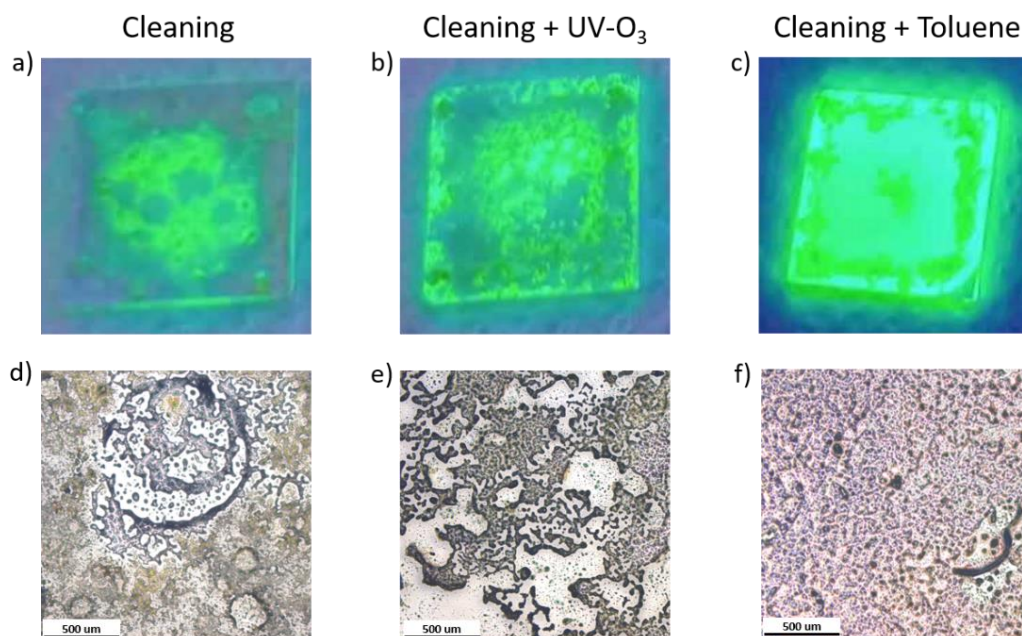
Figure III.3. Optical images under 350-nm UV excitation (first row) and Microscope images (second row) of drop-casted perovskite QD films on glass substrates subjected to different pre-treatment procedures: a, d) Cleaning; b, e) Cleaning + UV-Ozone; and c, f) Cleaning + Toluene wash.

b. Spin-coating

After finding the drop-casting technique deficient in forming a high-coverage and homogenous thin film of perovskite QDs, we hypothesized utilizing the spin-coating method to spread the solution more uniformly as well as accelerate the solvent evaporation, which helps minimize concentration gradients for preventing accumulation. In detail, 60 µl of the NC solution is dropped on toluene-treated glass substrates and spin-coated at 3000 rpm for 40 seconds. The samples are also left to dry naturally for 15 minutes and cleaned before further characterization. Figures III.4.a and b demonstrate an optical image under UV light and a 5x- magnification microscope image of a spin-coated $CsPbBr_3$ QD layer. It is clearly seen that the materials are distributed evenly across the entire surface area without forming macroscopic aggregates. However, black dots of micrometer size appear apparent in the microscope image, indicative of potential nanocrystal accumulations. Besides, the thickness of this emissive layer is estimated less than 200 nm.
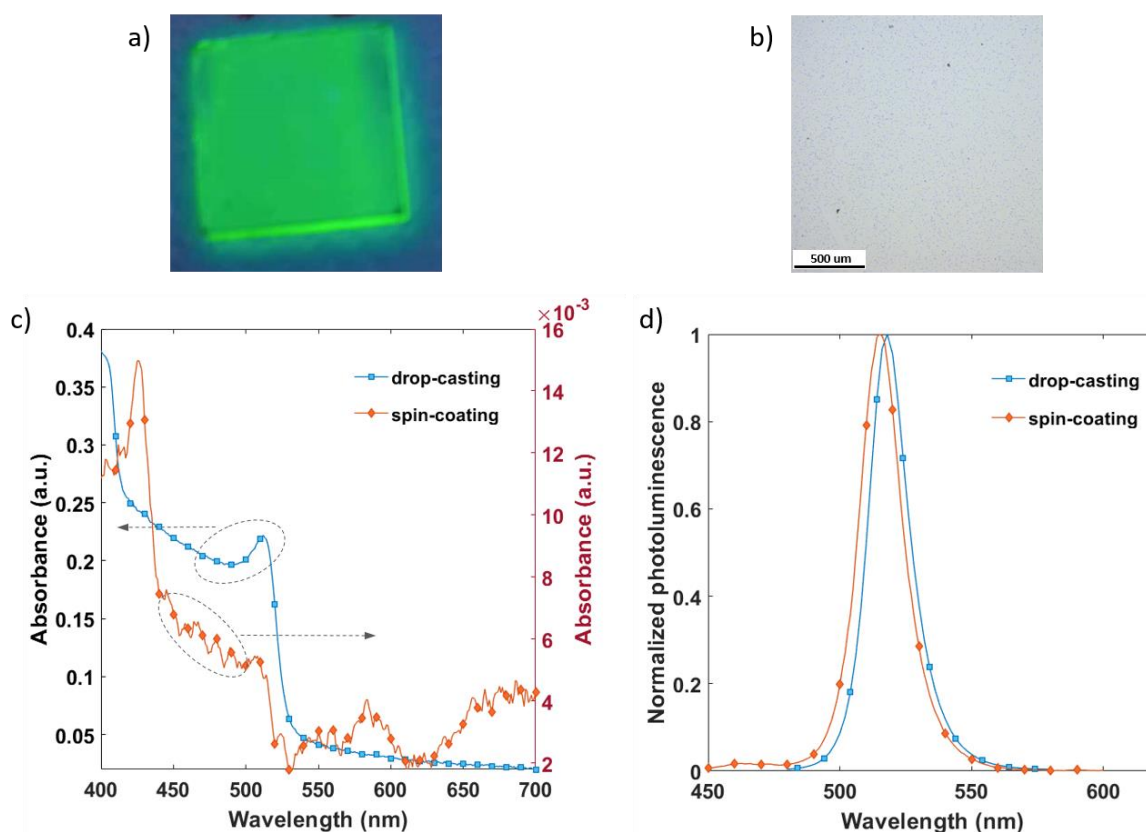
Figure III.4. Perovskite QDs spin-coated on glass substrates: a) Optical image under 350-nm UV excitation, b) Microscope image, c)UV-Vis absorption and d) steady-state PL spectra, compared to those of perovskite QD films deposited using drop-casting.

In addition, we compare the optical properties of perovskite QD layers deposited using drop-casting and spin-coating to examine the impacts of the deposition techniques on the QD thin film formation, as depicted in Figures III.4.c and d. Firstly, it is observed that the absolute value of the UV-Vis absorption in the case of spin-coated sample is noticeably lower than that in the drop-casting sample, attributed to the very thin layer of perovskite obtained using spin-coating deposition. This is also the reason why several noisy peaks appear in the long-wavelength region (> 550 nm) of the spin-coated sample's absorption spectrum. Besides, the characteristic peak of the $CsPbBr_3$ perovskite at 512 nm can be easily spotted in both cases, along with those of low-dimensional perovskite phases. For example, the drop-casting film has a 405-nm peak regarding the monolayer $(PPA)_2PbBr_4$ perovskite while the spin-coating possesses a maxima at 425 nm regarding the bilayered $(PPA)_2CsPb_2Br_7$. This result suggests a phenomenon of ligand substitution between the PPA's amino group and the inorganic cation Cs^+ of the QDs when transforming from the colloidal solution into the solid phase. Additionally, concerning the steady-state PL emission, the spectra of both samples exhibit their maxima around 515 nm, with a trivial shift from each other (~ 4 nm), indicating a governing emission from the $CsPbBr_3$ domains.

The next step is to evaluate the formation of the $CsPbBr_3$ QD emissive films on charge transfer layers (PEDOT:PSS) using the aforementioned deposition parameters. Figure III.5.a demonstrates an optical image of a QD layer spin-coated on PEDOT:PSS-coated glass substrate under UV light, showing a uniform luminescence from the entire substrate surface. This observation is supported by the low-

magnification microscopy image (Figure III.5.b), which distinctively depicts a quite homogeneous distribution of the black dots across the examining area. Furthermore, the steady-state optical properties of the perovskite QDs deposited on PEDOT:PSS-coated glass substrates are illustrated in Figure III.5.c. Evidently, the characteristic PL peak of $CsPbBr_3$ at 515 nm can be pointed out in the emission spectrum, similar to the data we observed in the previous cases. However, in comparison to the samples deposited on toluene-treated glasses, the peaks associated with the low-dimensional domains are absent from the material's absorption. It implies that the hydrophilic nature of the HTL enables effectively eliminating the unintended ligand exchange when spin-coating the colloidal perovskite QDs into thin emissive layers.
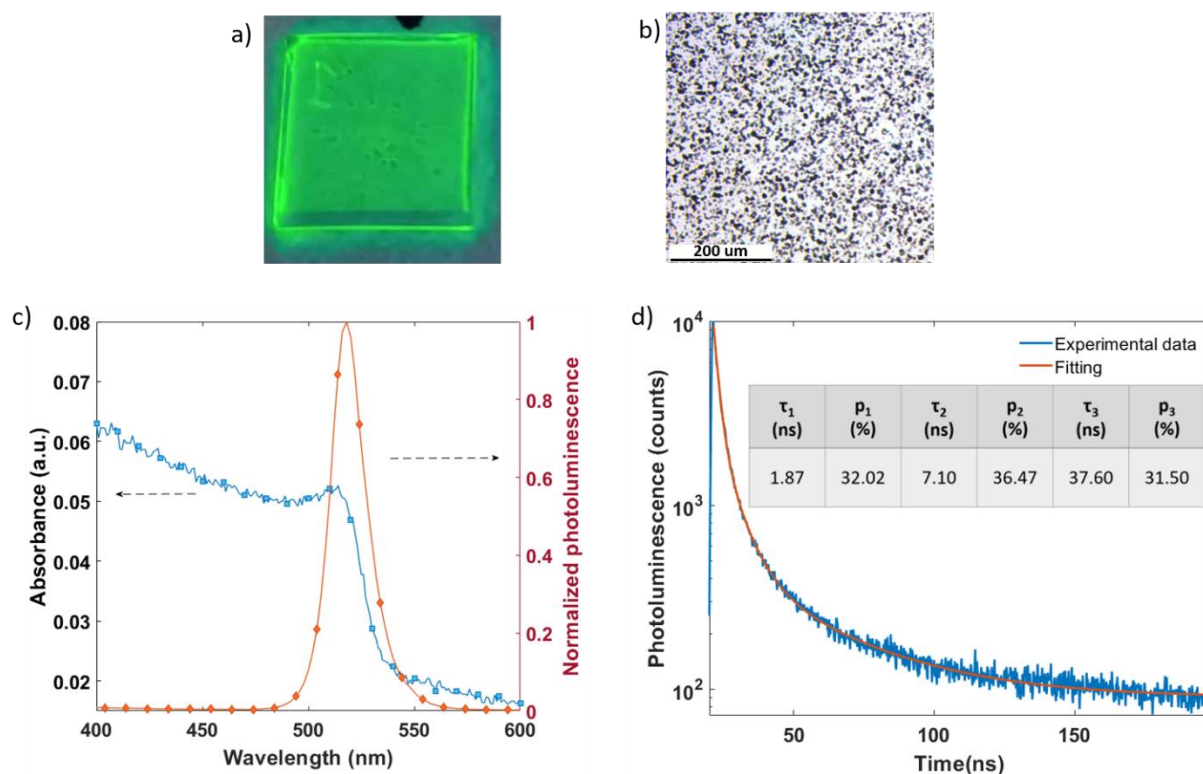
Figure III.5. Perovskite QDs spin-coated on PEDOT:PSS-coated glass substrates: a) Optical image under 350-nm UV excitation, b) Microscope image, c) UV-Vis absorption and PL spectra, and d) Time-resolved PL measurement (Inset: Fitting parameters of the PL decay).

Additionally, we measured the PL decay of the perovskite QD solids, which can be fitted using a tri-exponential decay function, as depicted in Figure III.5.d. In particular, neat perovskite films are often fitted using bi-exponential decays: The slow decay (τ_3) is generally the radiative free-exciton lifetime while the fast decay (τ_2) is a consequence of fast trap-mediated non-radiative recombination. In the presence of a hole transfer layer (HTL) such as PEDOT:PSS, the positive charge carriers can be extracted from the perovskite to the HTL. This hole extraction process brings an additional non-radiative recombination pathway, characterized by the ultra-fast decay τ_1 [261]. On average, it will take 12.9 ns for the QD emitters to return to their ground states after being optically excited. This is slightly faster than the PL lifetime of the colloidal QDs dispersed in toluene solvent, which can be attributed to the clustering of the QDs after being spin-coated. As discussed in earlier chapters, the longer it takes for the

perovskite material to decay radiatively, the more favorable it is for optoelectronic devices, as it allows radiative recombination to occur without facing competition from non-radiative processes.

3.2.2 Incorporating CsPbBr₃ QD thin films into PeLED structures and the associated device failures

Following the deposition of emissive thin films from monodisperse QD solutions, we decided to conduct a preliminary test on integrating the spin-coated perovskite layers into fabricating PeLEDs based on the design outlined in Chapter II. A schematic representation of the hypothetical device structure is shown in Figure III.6.a. The targeting thickness and deposition parameters of the top layers are similar to those in the bulk perovskite LEDs (i.e., TPBi – 30 nm, Ca – 40 nm, and Ag – 100 nm). We note that the LiF buffer layer is not employed here as it is unstable in ambient conditions, under which the perovskite QD layer is prepared.
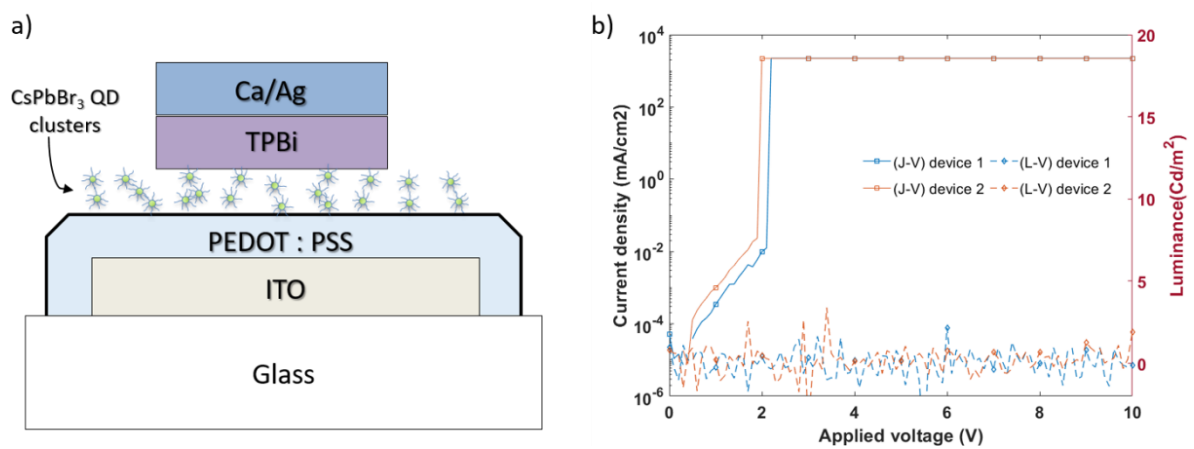
Figure III.6. a) Graphical illustration and b) J-L-V curves of PeLEDs based on pristine perovskite QDs.

Figure III.6.b shows the EL characteristics of two PeLED prototypes using the novel CsPbBr₃ QDs. Inevitably, the devices do not emit light, as witnessed by the zero L-V curves. By analyzing the J-V curves, we can observe a rapid rise of current at 2 V, which corresponds to the injection barrier of the devices, due to the nature of the interfacial layer chosen and the architecture. This issue can be attributed to direct electrical paths between the charge transport layers which allows the current to bypass the semiconductor layer. In fact, in LED technologies, there are several sources that may lead to this short-circuit issue, such as misalignment of the layers, defects or contamination in the thin films, improper layer thickness, or material degradation during the operation of the device. Therefore, to understand the root causes contributing to the catastrophic current leakage observed in our QD PeLEDs, a cross-sectional image of the device was taken, as presented in Figure III.7.a. Accordingly, instead of forming a uniform and intact layer with clear boundaries with the ETL (TPBi) and HTL (PEDOT:PSS), the perovskite nanocrystals rather appear to assemble into discrete QD clusters. Furthermore, due to the large gap between these nanoscale aggregates, the evaporated ETL material can be deposited into these spacings, mixed with perovskite QDs and having direct interface with the HTL. As a consequence, the morphology of the top layers (i.e., Ca and Ag) is also varied significantly.
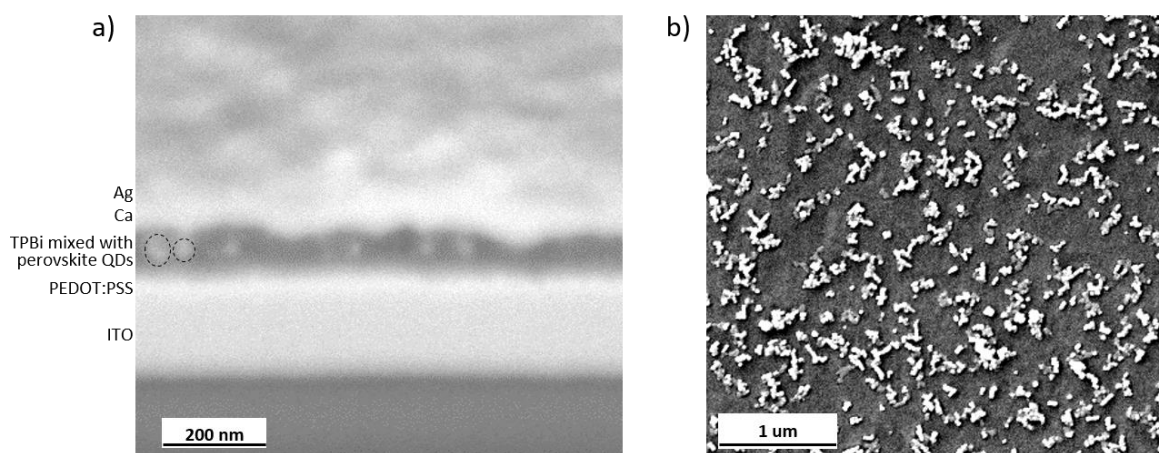
Figure III.7. a) FIB-SEM image of PeLEDs based on spin-coated perovskite QDs (with nanocrystal clusters highlighted by the dotted circles) and b) SEM images perovskite QDs spin-coated on PEDOT:PSS HTL.

To reinforce this argument, we utilized the SEM technique to visualize the surface morphology and structure of the perovskite QD layer deposited on PEDOT:PSS HTL. As depicted in Figure III.7.b, the QDs group into numerous nanoparticle islands of 100 nm – 200 nm in dimension, separated from each other and leaving large voids of space between them. However, we must note that the resolution limitations of the SEM equipment employed in our study do not allow us to definitively exclude the presence of individual QDs on the spin-coated perovskite layer. This insight leads us to conclude that, even though the macroscopic visuals of the perovskite films give an impression of homogeneity, they practically form a discontinuous layer of QD ensembles with a low surface coverage. The incoherence of the emissive layer then causes the LED to short-circuit as we have demonstrated above.

After this issue was identified, a comprehensive review of the literature and multiple tests were undertaken to uncover the secret sauce behind the deposition of highly dense perovskite QD layers, which has been recurrently demonstrated in other work using similar device structure and deposition technique. Nonetheless, it was observed that none of the published methodologies (such as spin-coating the QD solution several times to enhance the coverage or tuning the QD concentration) showed their effectiveness with our novel perovskite QD materials, primarily due to the fundamental differences in the nature of the dispersing solvents employed (i.e., toluene in our case versus octane or hexane in most of other research, as discussed in Section 3.1). During our discussions with Mayer's group, several potential approaches were considered to address this challenge. The first strategy involves re-dispersing the QDs in a commonly-used alkane solvent. However, implementing this approach would require revising the synthesis parameters to ensure that the inherent properties of the QDs remain unchanged; therefore, it falls under the responsibility of the Mayer's group and is out of scope for this thesis. The second strategy we proposed is to integrate the QDs into another material with higher processability, of which polymer materials are promising candidates. The realization of this approach will be detailed in the next section.

In summary, we have observed that depositing perovskite QDs prepared via soft chemistry onto flat substrates using the spin-coating technique is achievable without altering their inherent optical properties. However, a significant challenge arises from the non-uniform formation of thin films using these

materials. Specifically, the QDs tend to aggregate into distinct clusters that remain isolated from one another. Our forthcoming objective is to address this issue by effectively enhancing the surface coverage via perovskite QD/polymer collaboration, aiming to inhibit the occurrence of short circuits when PeLEDs are in operation.

3.3 Integration of perovskite QDs in polymer matrices

Collaborating inorganic QDs with polymer matrices for light-emitting applications has been a well-known and promising approach to exploit the exceptional optoelectronic properties of the QDs while harnessing the mechanical durability and environmental stability of polymeric materials [262], [263]. Remarkably, there are several practical approaches for encapsulating QDs in polymers, such as:

1) The polymer is employed as a surfactant ligand to coat and protect the QD surface [264];
2) The polymer matrix acts as a host material in a host-guest system, in which the host will form a covalent bond with the QD guests via reactive functional groups [265]–[267];
3) The polymer materials work simply as a medium to disperse the QDs without forming direct bonding [268], [269].

Nevertheless, when it comes to PeLEDs, the number of studies on a hybrid system between perovskite QDs and polymers remains relatively limited. For example, in 2019, Yu et al. succeeded in modifying the surface of MAPB QDs (synthesized via the LARP method) by doping a small content of the ionic conducting polymer poly(ethylene oxide) (PEO) into the QD solution immediately after the nucleation stage [270]. Accordingly, the incorporation of PEO helps reduce the size of the perovskite nanoparticles and improve their emission properties (e.g., PLQY or ambient stability), allowing for the realization of bright PeLEDs based on MAPB QD-polymer nanocomposite. Another research on MAPB-PEO blends as an active material for PeLEDs was published by Kim et al. [145], in which the polymer is mixed with the perovskite precursor in order to improve the stretchability of the emissive thin films. We note that the perovskite material, in this case, is not in the form of quantum dots but rather exists as three-dimensional crystals. However, the work has suggested the compatibility of ionic polymers in general and PEO in particular with the PeLED technology. Besides, perovskite QDs can also be integrated into non-conducting polymers, such as poly(methyl methacrylate) (PMMA) [271], polyvinylidene fluoride (PVDF) [272], or polystyrene [273], for light convertors in white inorganic LEDs.

Herein, we will focus on leveraging commercially available polymer materials as a versatile thin-film platform to accommodate and disperse the colloidal $CsPbBr_3$ QDs. In these QD-polymer composites, the favorable wettability between the polymer materials and the depositing surfaces (such as the PEDOT:PSS HTL) will facilitate the deposition of the QD-contained composites, targeting more homogeneous depositions compared to pure QD dispersions. Also, the polymers can fill and passivate the voids between the QDs in order to reduce the roughness of the emissive layer and eliminate shunt currents. In other words, the polymeric scaffold performs the function of a surface passivator between the charge transfer layers and the perovskite emitters. For this reason, the selection of polymer materials needs to satisfy

different criteria: 1) high transparency to maximize the light outcoupling efficiency of the emitting layer; 2) electrical insulation to prevent charge carriers bypassing the QDs and to avoid direct short-circuits through the active layer; and 3) facile processability at room temperature, given that high temperature can increase the probability of QD aggregation. Subsequently, two polymer materials will be examined for the deposition of composite thin films in this study: PMMA and PEO.

3.3.1 Perovskite QD-PMMA composites

a. Thin film deposition and optical characterization

To prepare the composite solutions, we first dissolved PMMA powder ($M_W \sim 15,000$) in Toluene at a weight concentration of 10 mg/mL at room temperature (which has been experimentally optimized to produce neat PMMA thin films of 20 nm to 30 nm). The polymer precursor is then mixed with the $CsPbBr_3$ QD solution at different $CsPbBr_3$/PMMA mass ratios, such as 1:1, 10:1, and 20:1. It is clear that the larger amount of the polymer solution is added, the lower concentration of the perovskite QDs will be in the final solutions. Before deposition, the composite solutions are shaken manually to ensure the uniform distribution of the monodisperse QDs within the solutions. Next, the composite solutions will be deposited on PEDOT:PSS-coated glass substrates using spin-coating at 3000 rpm for 40 seconds. In particular, the targeting thickness should be less than 100 nm and, in our estimation, the ideal range is hypothetically around 50 nm in order to: 1) reduce the driving voltage, 2) enhance exciton confinement, 3) minimize the electrical resistance of the non-conductive PMMA, and 4) ensure the compactness of the thin films. After this deposition, the samples dry naturally for 15 minutes. All processes are conducted at standard room conditions.

Initially, the morphological properties of the composite thin films with respect to various QD-to-PMMA ratios are studied. As shown in Figures III.8.a-c, we can observe a characteristic green luminescence upon exposing the spin-coated films to UV light. The bright and uniform emission indicates good surface coverage from the macroscopic perspective, regardless of the blend composition. The microscopy images (Figures III.8.d-f) also suggest a uniform distribution of the QD/PMMA composite materials over the entire substrate surface. Additionally, we attempted to measure the thickness of these samples using profilometry, but the softness of the composite surface prevents us from accurately probing the surface profile. Later on, FIB-SEM analysis gave an estimation of the samples' thickness varying between 84.5 nm (for the 1:1 sample) and 72 nm (for the 10:1 sample). Our efforts to further reduce the thickness, such as significantly decreasing the concentration of the polymer precursor or tuning the spin-coating parameters, would lead to noticeable deterioration in the thin film quality.
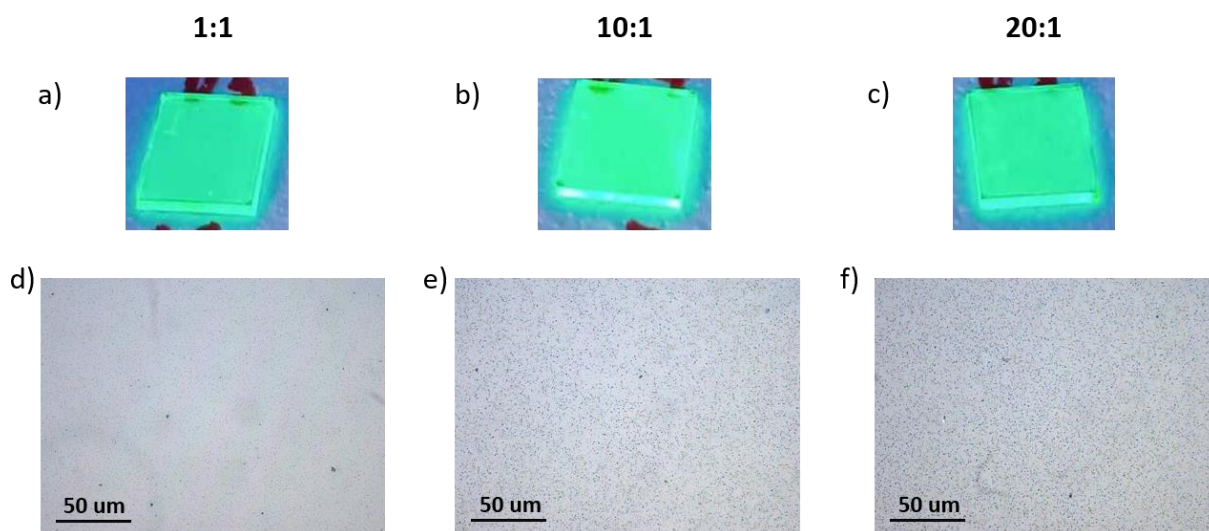
Figure III.8. a-c) Optical images under 350-nm UV excitation and d-f) Microscope images of perovskite QD-PMMA thin films with respect to different precursor ratios: a) 1:1, b) 10:1, and c) 20:1.

As the QD content increases, we observe more dark spots on the microscopy image, which could indicate some aggregations at the micrometer scale. Furthermore, the morphology of the emissive layers at nanometric resolution is captured using the AFM technique, revealing a contrast in the surface texture between the polymer-rich (i.e., QD/polymer ratio = 1:1) and QD-rich (i.e., 10:1 and 20:1) composite thin films. Accordingly, the AFM image of the 1:1 composite film (Figure III.9.a) depicts a formation of deep teardrop-shaped valleys varying between 1 µm - 2 µm in size and 40 nm - 55 nm in depth. These textural flaws originate from air bubbles formed inside the polymer-rich composite solution during the preparation. As the proportion of the PMMA precursor decreases, the film surface becomes more homogeneous. For example, the 10:1 sample (Figure III.9.b) demonstrates several grainy features with a height profile of 20 nm - 30 nm and a root-mean-square (RMS) roughness of about 6 nm, while that of 20:1 (Figure III.9.c) exhibits exceptionally low surface roughness of < 2 nm.
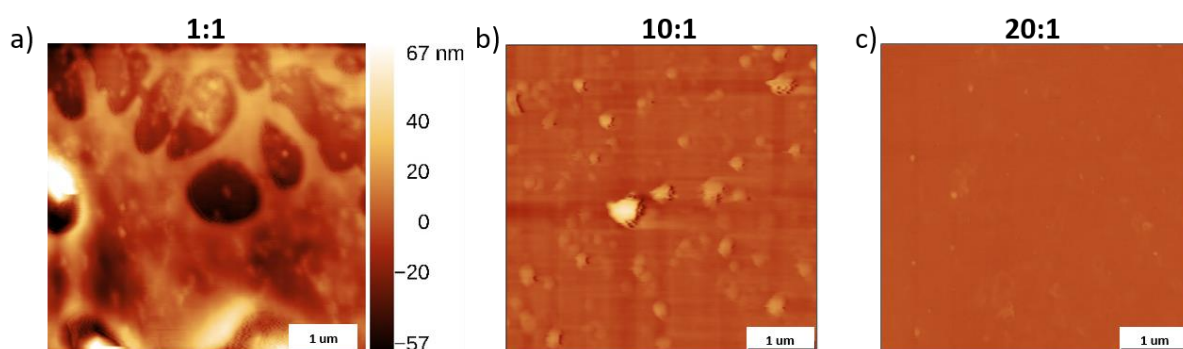
Figure III.9. AFM images of perovskite QD-PMMA thin films with respect to different precursor ratios: a) 1:1, b) 10:1, and c) 20:1.

We then utilized the SEM technique to examine the arrangement and distribution of the perovskite QDs in the composite thin films in the cases of high (1:1) and low (10:1) polymer loading, as illustrated in Figures III.10.a and b. In both cases, the perovskite NCs, characterized by the white features on the images, assemble into several small clusters spread uniformly across the surface, similar to our

observation in the pristine spin-coated QD films investigated previously. Furthermore, to investigate the possibility that the observed QD clusters may represent higher-dimensional crystal phases, such as 3D crystallines, we conducted a high-resolution TEM analysis of a 10:1 composite film deposited on observation grids using the drop-casting method. Subsequently, the TEM image (Figure III.10.c) affirms a uniform dispersion of the QDs inside the PMMA matrix. Therefore, we can conclude that the incorporation of the PMMA polymer into the QD solution does not disrupt the dispersion pattern of the QDs but mainly impacts the texture of the composite films containing these QD materials. It must be noted here that the infusion of the PMMA into the gaps between the nanocrystals is not readily visible neither in the optical images nor in the SEM photos due to the optical transparency of the polymer as well as the low contrast between the polymer and the underlying layer. We will comment on this point later in this section when examining the cross-sectional image and the performance of the corresponding devices.
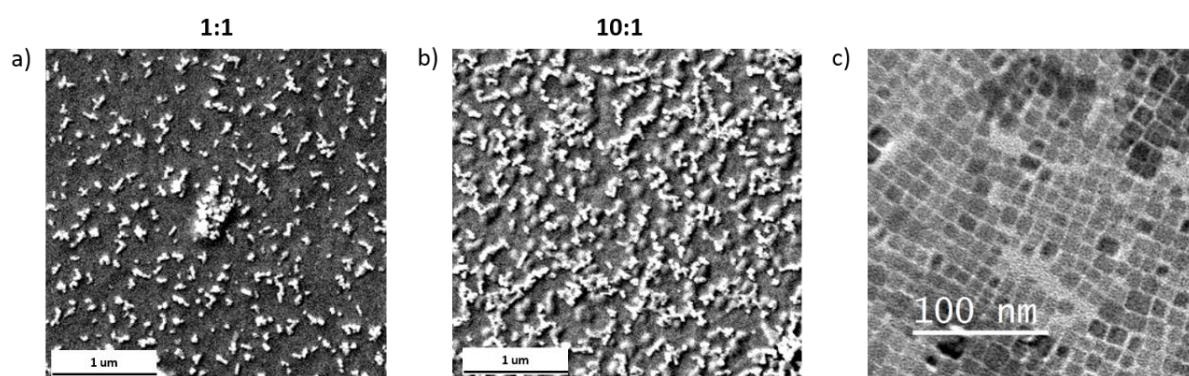
Figure III.10. SEM images of perovskite NC-PMMA composite thin films with the precursor ratios of a) 1:1 and b) 10:1; and c) TEM image of a 10:1 composite film deposited via drop-casting technique.

The effects of polymer encapsulation on the optical properties of the perovskite QDs are demonstrated in Figure III.11. Firstly when comparing the absorption spectra of the three samples, one can notice an absence of the absorption peak at 425 nm regarding the 1:1 thin film. It is because, with a lower QD concentration, there is less chance of the PPA reagents to react with the $CsPbBr_3$ QDs to create quasi-2D $(PPA)_2CsPb_2Br_7$ domains. Another uncommon feature we can notice here is the lower absorption of the 20:1 sample compared to the 10:1 in spite of the higher concentration of perovskite nanocrystals in the composite solution. A definitive explanation to this observation remains unclear to us, but it is tentatively attributed to the difficulty to obtain a "true" thin film with well-defined thickness when the proportion of the polymer becomes notably minor compared to that of the emitters. Secondly, concerning the emission spectra, all three PMMA-encapsulated QD films exhibit similar spectral shape and position. Their PL lifetimes are also equivalent, resembling that of the pristine perovskite QD film, as shown in Figure III.11.b. Putting all the pieces together, we conclude that in our $CsPbBr_3$ QDs/PMMA blends, the polymer does not have any significant influence on the size, composition, and optical properties of the QD emitters.
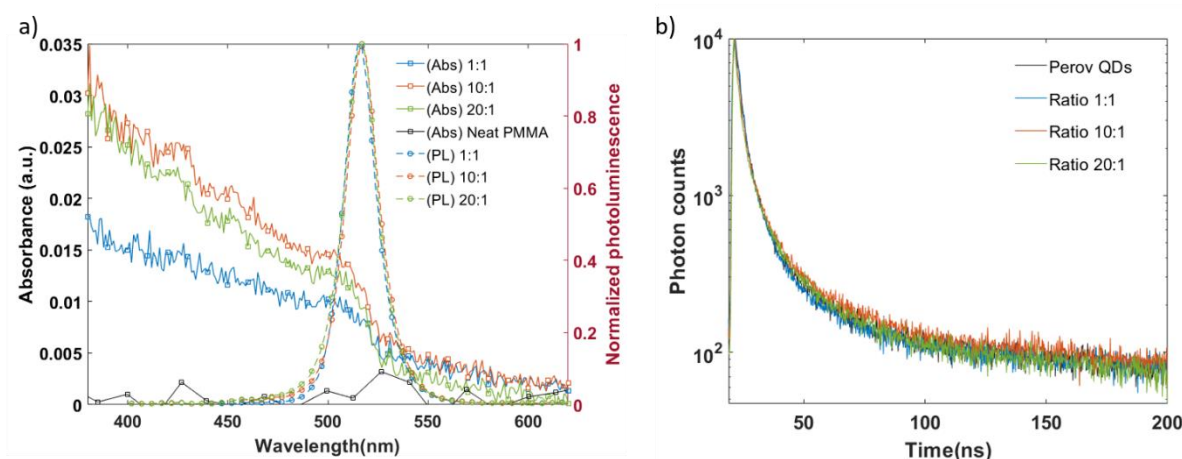
Figure III.11. Optical properties of perovskite QD-PMMA composite thin films with respect to different precursor ratios: a) UV-Vis absorption and steady-state PL spectra and b) Time-resolved PL decay.

In the following section, we will proceed to investigate the electroluminescent (EL) characteristics of the composite films within the context of PeLEDs.

b.   Performance of PeLEDs based on $CsPbBr_3$ QD/PMMA composite

A graphical representation and its corresponding energy alignment diagram of the PeLED design using perovskite QD/PMMA composites as an emissive layer are demonstrated in Figures III.12.a and b. Since PMMA is a non-conductive material, it evokes a concern regarding the transporting property of the emissive layer, such as whether the charge carriers can traverse the PMMA matrix to reach the QD emitters. We hypothesize that the transporting pathway is viable thanks to the clustering of the QDs, which fosters localized energy levels to mitigate the barriers encountered when transitioning between non-conductive and conductive materials. Such hypothesis is also relevant considering that thin active layer are targeted, preventing any strong accumulation of polymer beneath or above the QD assemblies in the blend. On the other hand, the extensive energy bandgap of the PMMA compared to those of the perovskite layer and charge injection materials (PEDOT:PSS at the bottom, TPBi at the top) is capable of effectively passivating carrier leakage or interface-induced recombination pathways.
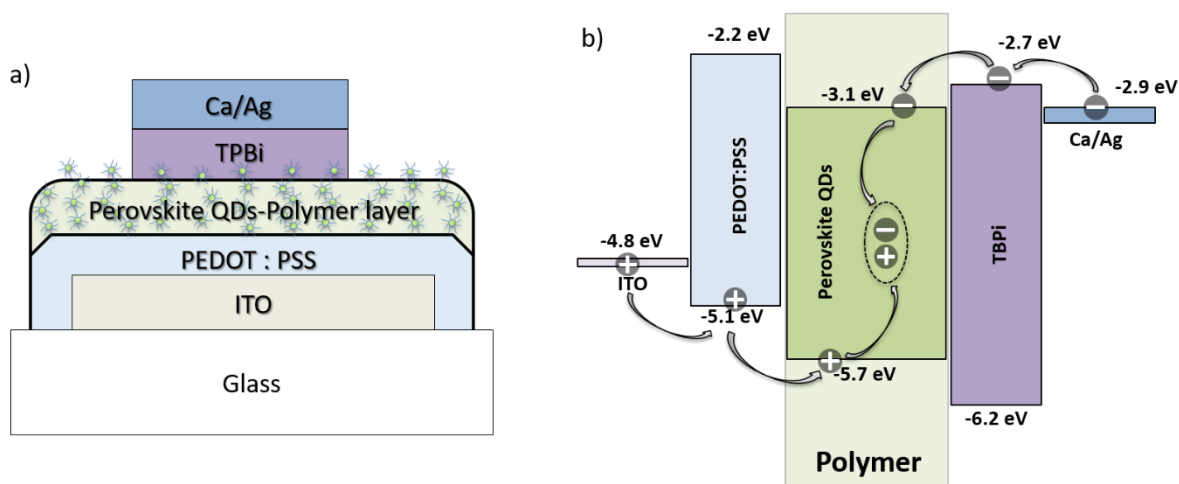
Figure III.12. a) Schematic illustration and b) HOMO/LUMO energy arrangement of PeLEDs based on perovskite QD/PMMA composites.

The integration of polymer-rich and QD-rich composite films in PeLEDs is investigated using the FIB-SEM technique, as demonstrated in Figures III.13.a and b respectively. Compared to the pristine QD PeLEDs, the composite devices appear to be immune from interlayer mixing, with sharp and contrast boundaries between the adjacent layers. As a result, the morphology of the thermal-evaporated top layers (TPBi, Ca, and Ag) is also noticeably enhanced. Furthermore, in the case of high QD concentration (10:1), it is suggested that the spacial organization of the perovskite clusters helps create channels for the charge carriers to be injected and recombine within the QD semiconductors. As the QD/PMMA ratio decreases to 1:1, the density of the perovskite emitters is reduced noticeably, and the QD clusters become less visible in the cross-sectional image.
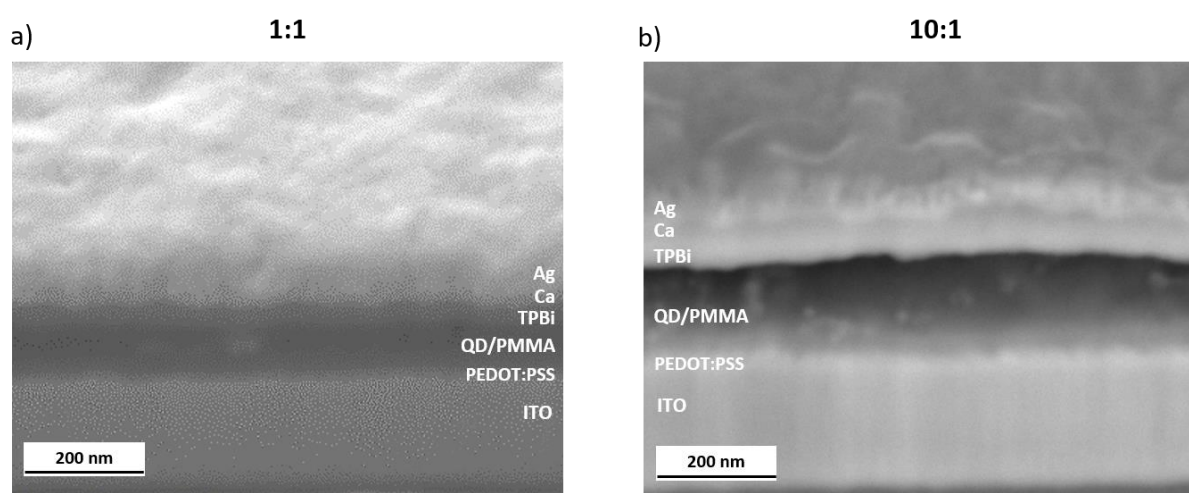
Figure III.13. FIB-SEM images of PeLEDs based on perovskite QD/PMMA composites: a) 1:1 and b) 10:1.

Next, the EL behavior of the QD/PMMA-composite PeLEDs is analyzed. Firstly, in Figure III.14.a, we showed the emission spectrum of the 10:1 composite PeLED which peaks at a wavelength of 519 nm. This EL peak corresponds to that of the emissive layer's PL spectrum. Also, the emission spectrum has a relatively narrow FWHM of 20 nm, comparable to published data concerning $CsPbBr_3$ QD PeLEDs [103]. Secondly, the dependence of the device' current on the applied voltage with respect to various QD-to-PMMA ratios is investigated, as depicted in Figure III.14.b. It can be seen that the 1:1 device exhibits relatively high current density at low voltage, implying a leakage current stemming from the uneven and highly-textured thin film morphology. The 10:1 device, in contrast, has a relatively low leakage current and threshold voltage thanks to the good smoothness and coverage of the composite film. Our experimental data also points out that an insufficient loading of polymer (20:1) will intensify the leakage.
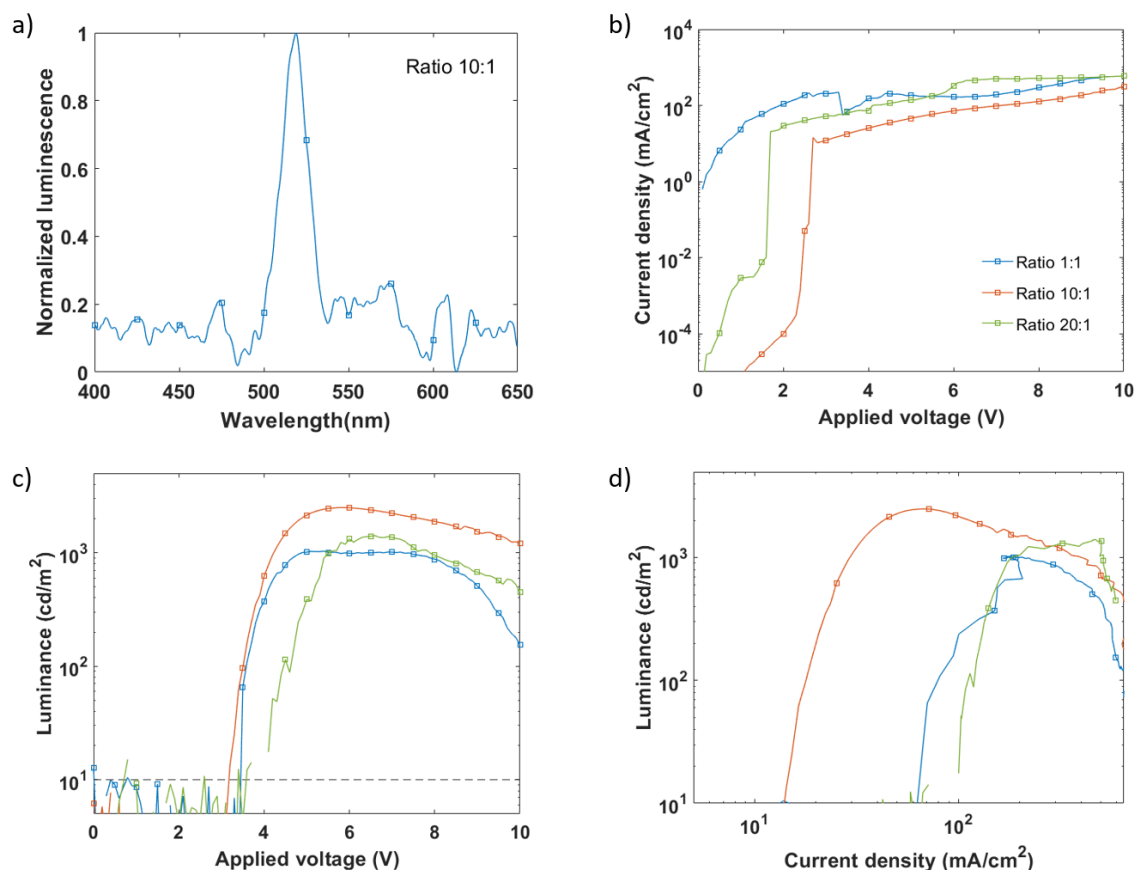
Figure III.14. Electroluminescence performance of PeLEDs based on perovskite QD/PMMA composites: a) EL spectrum, and b) J-V, c) L-V, d) L-J curves. The EL intensity is measured at 520 nm.

Regarding the PeLED' L-V curves (Figure III.14.c), all three devices demonstrate low turn-on voltage (~ 3.5 V, similar to that of the reference quasi-2D PeLEDs) and quite intense luminance (> 1000 cd/m^2). In particular, the maximum luminance is captured at 2500 cd/m^2, corresponding to a forward voltage of 5.8 V for the 10:1 device. The similarity in these L-V patterns reinforces our prior observation that changes in the PMMA concentration assert minimal impact on the intrinsic radiative recombination of the perovskite QDs. Nevertheless, it is not to say that the PeLEDs' performance is independent of the QD/polymer ratio. Contrarily, the luminance-current density correlation, as shown in Figure III.14.d, reveals that polymer loading can determine the electrical loss of the devices. For example, the PeLEDs demonstrate high current injection either in the case of excessive (1:1) or insufficient (20:1) polymer encapsulation when compared to the optimal ratio of 10:1. Such electrical loss can originate from multiple sources, including leakage pathways via defects on the emissive layer's surface and imbalances in charge injection resulting from the incorporation of the electrically-insulating PMMA polymer.

The effect of optimizing the QD-to-polymer ratio on the device efficiencies is explicated further in Figure III.15 by plotting their current-dependent EQEs. It is clear that the 10:1 PeLED gives the best energy conversion efficacy with the maximum EQE value of 1.4 %, which is one order of magnitude higher than the EQE of the 1:1 or 20:1 devices. Besides, this EQE value is achieved at relatively low current density (approximately 40 mA/cm^2), suggesting that the device consumes less electrical power to produce light. The low current density is also favorable since it produces less heat during operation, which

is critical in extending the device lifespan. Additional information about the devices' luminous efficiency in response to different input and output parameters, such as bias voltage and luminance, is provided in Annex 3.3. The data reveals that the peak luminance and peak efficiency are closely aligned, meaning the devices are capable of maintaining their performance without significant losses at high brightness level. From the device engineering's point of view, these results are promising since there is no need for compromising between brightness and efficiency.
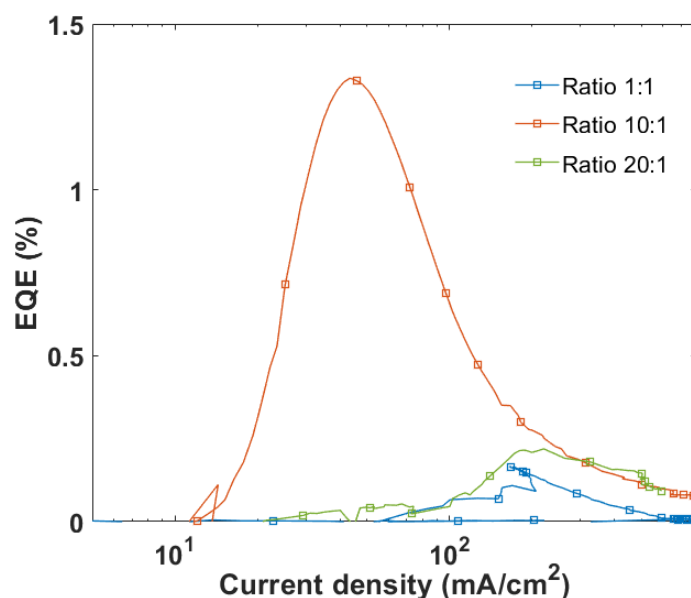
Figure III.15. Correlation of EQE and current density in PeLEDs based on perovskite QD/PMMA composites.

Subsequently, we examined the operational stability of the PeLEDs based on perovskite QD/PMMA composites, focusing on the optimal 10:1 case. In particular, the devices were placed inside an enclosed holder filled with nitrogen gas to prevent any potential impacts from the ambient atmosphere. Figure III.16 represents the evolution of a PeLED's luminance and current density with respect to the operating time, with an initial luminance value at 70% of the highest achievable luminance (corresponding to an applied voltage of 4.6 V). Evidently, the EL intensity drops significantly to less than 20% of its initial value after only 6 seconds of the measurement, indicating a short T_{50} of only a few seconds. Furthermore, this EL decay cannot be sufficiently fitted using the stretched exponential aging model (which has been proved to effectively describe the aging behavior of quasi-2D PeLEDs, as shown in Chapter II). The reason is that the accuracy of the fitting strongly depends on the variance of the input current over the operational timeframe [274]. In fact, one can observe a transient effect in the current density, such as a remarkable increase from 700 mA/cm² to 1,000 mA/cm² in the first 12 seconds before gradually declining over time.
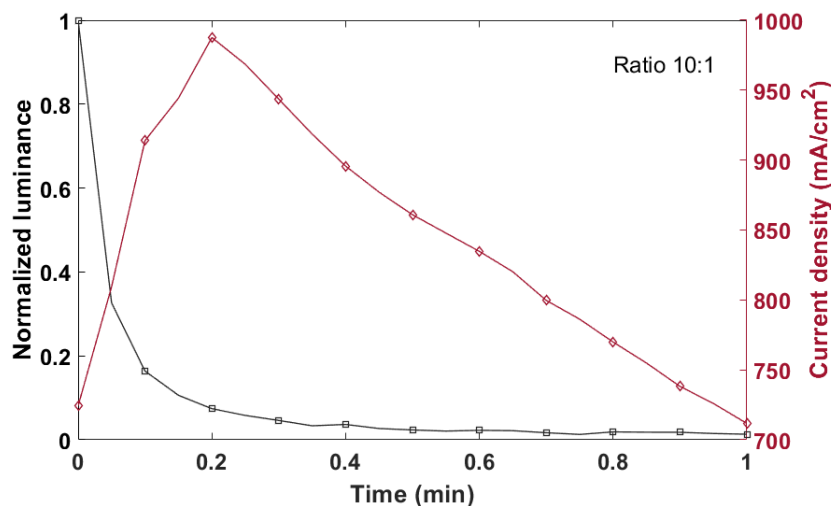
Figure III.16. Device durability of a PeLED based on perovskite QD/PMMA composite.

Accordingly, both the rapid degradation in the device's luminance and the fluctuation in the current density can be attributed to the facile decomposition in the 0D perovskite's crystal lattice during operation [102], [275]–[277]. In detail, the weak bonding between the QDs and the ligand surfactants can be easily broken due to the intense electrical field. On one hand, it leads to ion migration that temporarily increases the number of charge carriers passing across the device (and therefore increase the current density as we saw). On the other hand, it results in irreversible adverse effects on the QD's structure, forming more and more structural defects and trap states that favor non-radiative recombination. This degradation process is even accelerated due to the high surface-area-to-volume ratio of the QDs. Apart from the intrinsic stability of the 0D perovskite materials under high drive conditions, other contributing factors can include the Joule heating effect, the electrochemical reactions between the charge transfer layers and the electrodes, and the imbalance of charge injections.

The damage of the intense electrical field on the integrity of the QD/PMMA PeLEDs can also be witnessed by capturing the surface of the device at several moments during a forward-bias scan (see Figure III.17). We can see that at low biased voltages ($\leq 5.5V$), the EL appears highly uniform with photons coming out from the entire surface. As the forward voltage further increases, the EL starts decreasing (which is aligned with the J-L-V characterization) with a large emitting surface area becoming "deactivated" and incapable of emitting effectively. The growth of this dark area on the illuminating surface is an evidence of the perovskite decomposition caused by electrical stress [240].
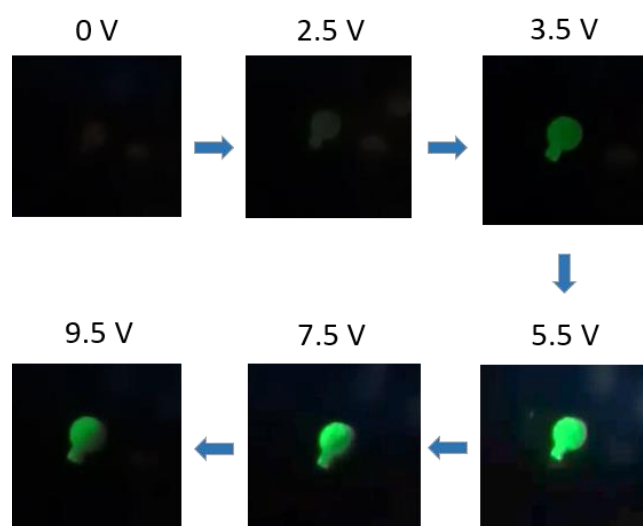
Figure III.17. Optical images of a working perovskite QD/PMMA composite PeLED during a forward bias scan.

Besides, it is important to acknowledge that the issue of limited lifetime in the PMMA-based composite PeLEDs may have introduced certain inaccuracies into the J-L-V characterization data. To be more clear, in our set-up, we utilized a measurement protocol based on staircase voltage scanning, with a step size of 0.1 V and scanning rate of 100 ms per step. Thus, during a forward voltage scan, the device will be constantly exposed to the electrical stress with a total scanning duration exceeding the device's lifetime, implying that the device is potentially degraded during the measurement. Nevertheless, these limitations are unlikely to significantly impact the core findings of this research, but they would require more precise characterization protocols to be implemented in the future.

In summary, we successfully fabricated green PeLEDs based on pioneering $CsPbBr_3$ QD/PMMA composites. Despite PMMA's inherent insulating nature, we optimized the ratio between the emissive QDs and the polymer to enable the deposition of uniform and homogeneous thin films without altering the optoelectronic properties of the perovskite emitters. In these composites, the PMMA matrix allows for evenly distributing the emissive materials across the substrate's active areas and effectively passivating short-circuit channels on the active layers. The resulting composite thin films were then introduced into our PeLEDs design, capable of illuminating brightly and efficiently. Amongst the perovskite QD/PMMA ratio that we examined, the ratio of 10:1 exhibited the best electroluminescence performance, with the highest luminance and EQE values recorded at 2,500 cd/m^2 and 1.4 %, respectively, approaching the results published by Yu et al. for PeLEDs of the same category [271]. Nevertheless, our QD PeLEDs based on the PMMA matrix presented a drawback in terms of operational durability inherited from the intrinsic instability of the perovskite QDs when subjected to electrical stress. Thereby, these performing devices is a proof-of-concept for the potential applications of the soft-chemistry synthesized perovskite QDs as an active layer in light emitting diodes. Furthermore, to the best of our knowledge, this is also the first demonstration of incorporating PMMA into perovskite materials to produce thin films with encouraging electroluminescent behaviors.

3.3.2 Perovskite QD-PEO composites

While the emissive composite material utilizing PMMA polymer exhibits relatively favorable electroluminescent characteristics, we hypothesize that the non-conductive nature of PMMA imposes a notable limiting factor on the electrical properties of the composite layer, which may have hindered the output of the corresponding devices. Therefore, we are motivated to enhance the performance of our originally-designed QD PeLEDs by replacing the inert polymer with a less resistive, more PeLED-compatible polymer, such as PEO.

a. Thin film deposition and optical characterization

Slightly different from the preparation of the PMMA precursor solution, we prepare a PEO solution by dissolving PEO powder ($M_W \sim 600,000$) in Toluene at a concentration of 5 mg/mL. The dissolution is performed at a temperature of 70 °C. After complete dissolution, the polymer precursor is allowed to return to ambient temperature (for about 20 minutes) before being incorporated with the $CsPbBr_3$ QD solution. It is noted that higher concentrations of PEO were also tested, but they led to rapid gelification of the precursor solutions at room temperature, which is not preferred for thin-film deposition. Next, three $CsPbBr_3$/PEO mass ratios are investigated, including 1:1, 5:1, and 10:1. The final composite solutions are shaken to ensure the uniform dispersion of the QDs before being spin-coated on PEDOT:PSS substrates (at 3000 rpm for 40 seconds). No thermal annealing is required apart from a natural drying process over 15 minutes.

The morphology of the blend films at different scales is demonstrated in Figure III.18. At the macroscopic level (Figures III.18.a-c), the 1:1 sample only emits weakly under the UV lamp, contrasting with the intense luminescence from the 5:1 or 10:1 samples. The reason behind this observation has been revealed when we examined the samples using optical microscopy. In particular, in the case of high polymer concentration (1:1), the perovskite QDs tend to form substantial aggregates which coalesce into sizable islands (up to ~ 250 μm in dimension), encircled by scribble polymer matrices (see Figure III.18.d). Subsequently, the perovskite emitters occupy only a small portion of the overall surface, making the substrate appear relatively transparent under UV light. With an increase in the QD-to-PEO ratio, not only the dimension of these perovskite islands is noticeably reduced but also the composite films are incorporated with more emissive materials (Figures III.18.e and f). Therefore, the surface coverage and luminescence are improved remarkably. As seen in Figures III.18.g-i, the AFM analysis of the QD/PEO composite films also implies a formation of thin films with higher homogeneity and fewer defects by favoring the loading of QDs over PEO in the composite solution, i.e., QD-to-PEO ratios = 5:1 or 10:1. Between these two cases, the quality of the 5:1 surface appears slightly better, characterized by its quite low RMS roughness (1.2 nm, compared to 7.9 nm in the 10:1 sample).
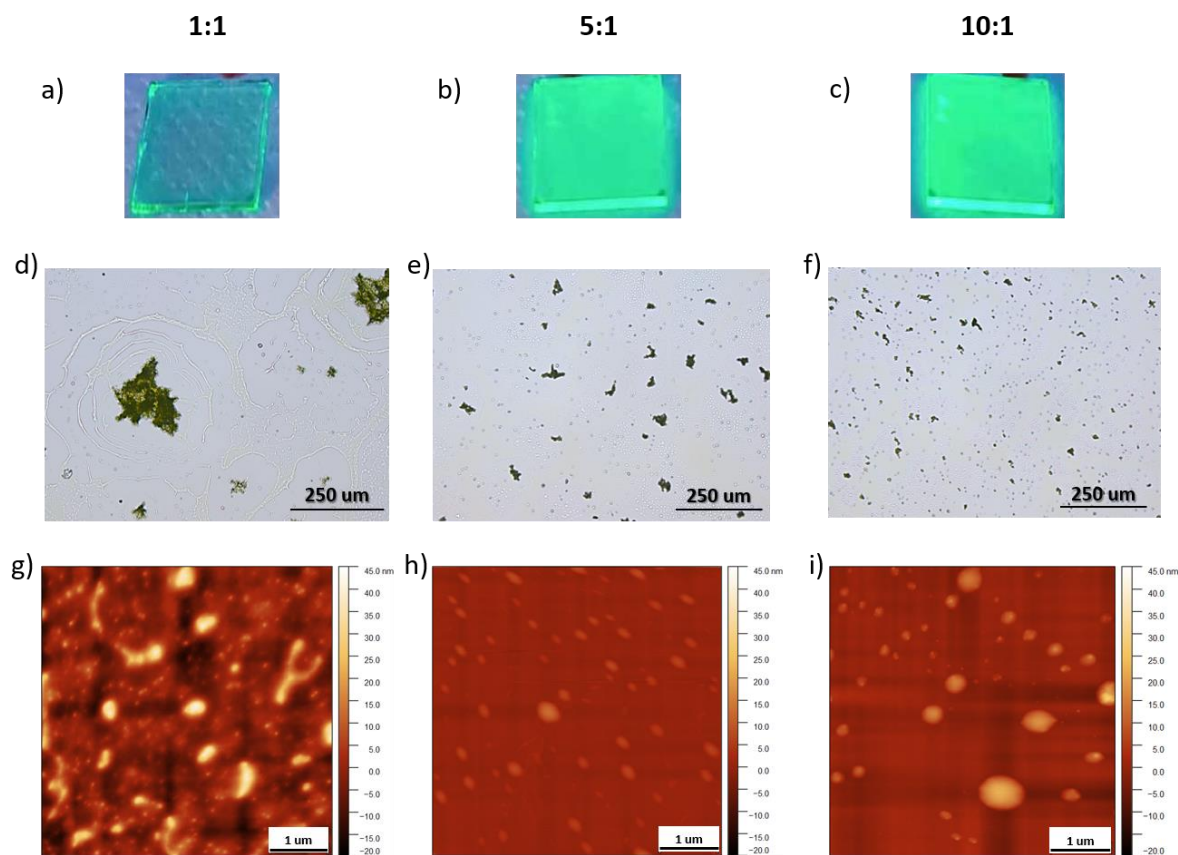
Figure III.18. Perovskite NC-PEO composite thin films: a-c) Optical images under 350-nm UV excitation, d-f) Microscopy images, g-i) AFM images with respect to different precursor ratios.

Next, SEM analysis was utilized to study the distribution of the perovskite emitters inside the PEO matrix when the composite is rich in the polymer precursor (1:1) or in the QDs (5:1), as depicted in Figure III.19. Accordingly, a contrast in the QD dispersion can be clearly emphasized. In the former case, the QDs aggregate in a heterogeneous manner, forming densely-packed and chain-like clusters of different sizes and shapes. These densely populated aggregates are scattered unevenly, rather than being uniformly distributed, and spanning several micrometers in size across the substrate surface. Conversely, in the latter case, the QDs are grouped into small (approximately 100 nm), relatively uniform, and homogeneously dispersed clusters, similar to the surface landscapes of the pristine QD films or the QD/PMMA composite films we observed above.
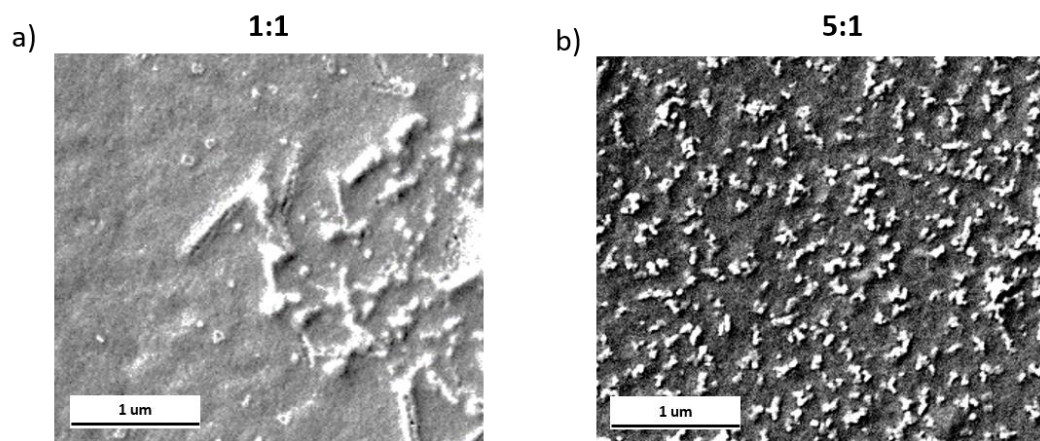
Figure III.19. SEM images of perovskite QD-PEO composite thin films with respect to perovskite QD/PEO ratios of a) 1:1 and b) 5:1.

Figure III.20.a illustrates the UV-Vis absorption and steady-state PL spectra of the composite films, showing typical characteristic patterns of the perovskite QDs in thin film (e.g., absorption peaks at 512 nm, PL peaks at 515 nm, formation of quasi-2D phases in the case of high perovskite concentration, etc…). More interestingly, the PL decay measurement, as shown in Figure III.20.b, reveals the significant influence of incorporating PEO on the optical properties of the perovskite emitters. In detail, the PL lifetimes of the composite films are reversely proportional to the PEO concentration. These findings are opposed to the time-resolved PL measurement of $CsPbBr_3$ QDs/PEO hybrid synthesized via the LARP method proposed by Yu et al. [270], in which the authors reported a prolonged average PL lifetime as they increased the polymer loading.
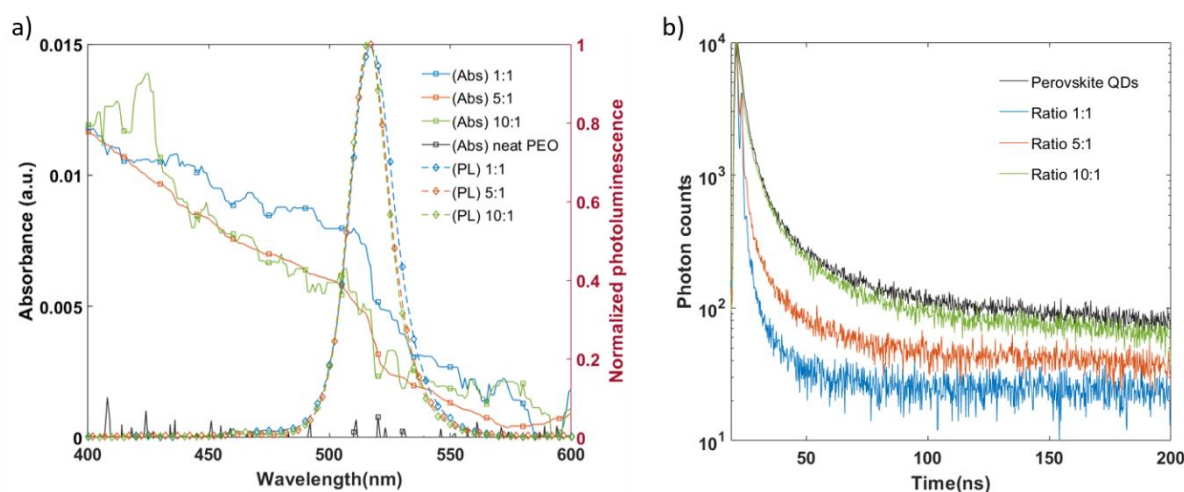
Figure III.20. a) UV-Vis absorption and steady-state PL spectra and b) time-resolved PL measurement of the perovskite QD-PEO composite films.

We must look closer at Yu's perovskite QD/PEO composite system to understand the contrast between the two data sets. Notably, in their method, the PEO molecules form a direct bonding with the halogen ions on the surface of the perovskite, functioning as a long-chain capping ligand for stabilizing the QD's surface and protecting the QDs from structural deformation due to external factors, such as humidity, oxygen, or intense optical/electrical excitation. This explains the improved optical properties of their

composite thin films with increasing PEO content, as the authors observed. Meanwhile, in our system, the QDs have been well passivated by the phenylalkylamine ligands, and the PEO's role is solely to facilitate the formation of thin films. Moreover, the accelerated PL decay of the composite thin films deposited by our method suggests an increase in the non-radiative recombination centers caused by the PEO incorporation. Nevertheless, the precise underlying mechanisms governing such quenching phenomenon remain unclear to us. To the best of our knowledge, we hypothesize that the potential non-radiative recombination channels may include (but are not limited to) the following:

- Occurrence of energy transfer from the QDs to the surrounding medium due to the ionic conductive behavior inherent to the PEO polymer.

- Delocalization of excitons between neighboring QDs in densely packed aggregations, which have been observed to increase with a reducing QD/PEO ratio.

- Surface traps and defects, arising from aggregated states or partial substitution of PPA ligands with PEO molecules. However, this hypothesis appears less likely, as we observed no differences in the shape and position of the steady-state PL peaks between the three composite ratios, as well as when comparing them with the emission of the pristine QDs.

It requires conducting a more comprehensive study to uncover the impacts of PEO incorporation on the characteristics of the perovskite QD emitters; however, for this report, we will refrain from delving further into this matter and instead proceed to integrate the emissive composite films based on PEO polymer into our PeLED structure.

b. Performance of PeLEDs based on $CsPbBr_3$ QD/PEO composite

The design of the PeLEDs using PEO-based composites is similar to that of the devices incorporating perovskite QDs and PMMA polymer (see Figure III.12). Figure III.21 presents cross-sectional images of the devices using the 1:1 and 5:1 QD-to PEO ratios, showing the changes in the active layers' thickness and morphology with decreasing polymer loading. First, it is evident that a higher polymer concentration will lead to a thicker emissive film (e.g., 103 nm in the case of 1:1 compared to 74 nm in the case of 5:1) since more polymer molecules are available to form a continuous matrix. Second, interlayer mixing is effectively prevented in both cases, as we can observe sharp interface boundaries and distinct layer contrast between the composite and neighboring hole/electron transfer layers. However, the FIB-SEM image of the 1:1 sample does not fully reflect the aggregation patterns we noted in the top-view SEM image, possibly because it was captured in an area with poor QD dispersion. Alternatively, the 5:1 image clearly depicts the formation of the QD clusters inside the polymer layer. The lateral dimension of these clusters is comparable to the overall thickness of the composite film, suggesting a charge transfer pathway from the adjacent layers into the perovskite emitters to overcome the energy barriers posed by the polymer coating (as illustrated in Figure III.12.b).
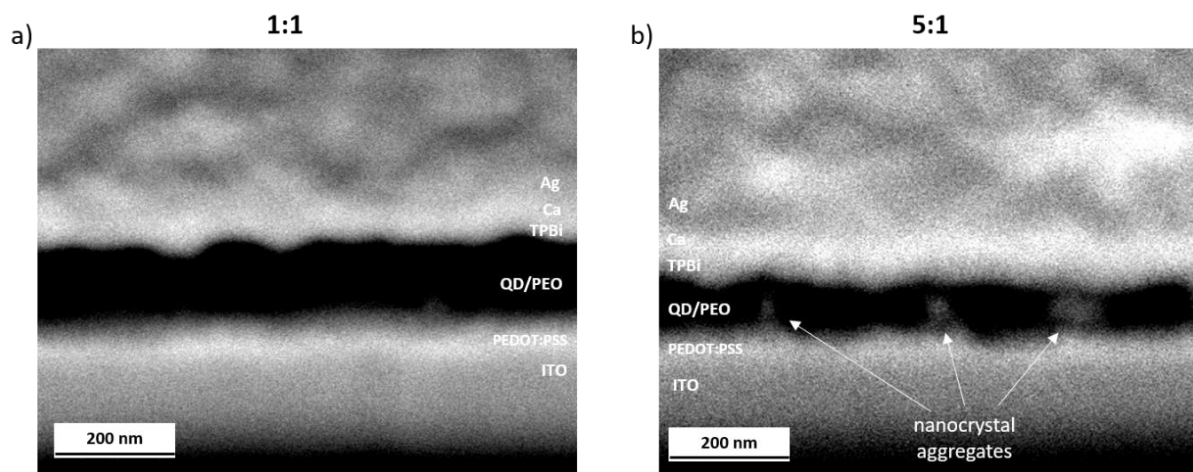
Figure III.21. FIB-SEM images of PeLEDs based on perovskite QD/PEO composites: a) 1:1 and b) 5:1.

The J-L-V characteristics of the PEO-incorporated PeLEDs are shown in Figure III.22. Overall, the 5:1 device exhibits the lowest current density and highest brightness amongst the three samples. Indeed, the J-V curve of the 5:1 PeLED resembles one of an ideal diode with a clear contrast between the insulative and conductive regimes and a threshold voltage of about 2.4 V. Conversely, the 1:1 and 10:1 PeLEDs demonstrate unfavorable electrical response. For example, the high-polymer-loading sample has a remarkably high current passing through the device at low biased voltages (e.g., 1 mA/cm^2 at 0.1 V), implying a critical leakage channel due to the development of the extensive QD aggregations on the composite surface. The issue is even more vital in the high-QD-loading PeLED, in which the high current density is not only observed at low biased voltage but instead throughout the entire scanning window. We attribute this observation to the leakage channels due to the insufficiency of polymer passivation. In addition, the 1:1 PeLED performs only a weak electroluminescence, with a maximum luminescence L_{max} of 100 cd/m^2, followed by the 10:1 device with L_{max} of < 800 cd/m^2. Exceptionally, the 5:1 PeLED demonstrates a high luminance peak of nearly 5,000 cd/m^2. Compared this value to the highest luminance recorded by the PMMA-based composite PeLEDs, it exhibits a two-fold increase.
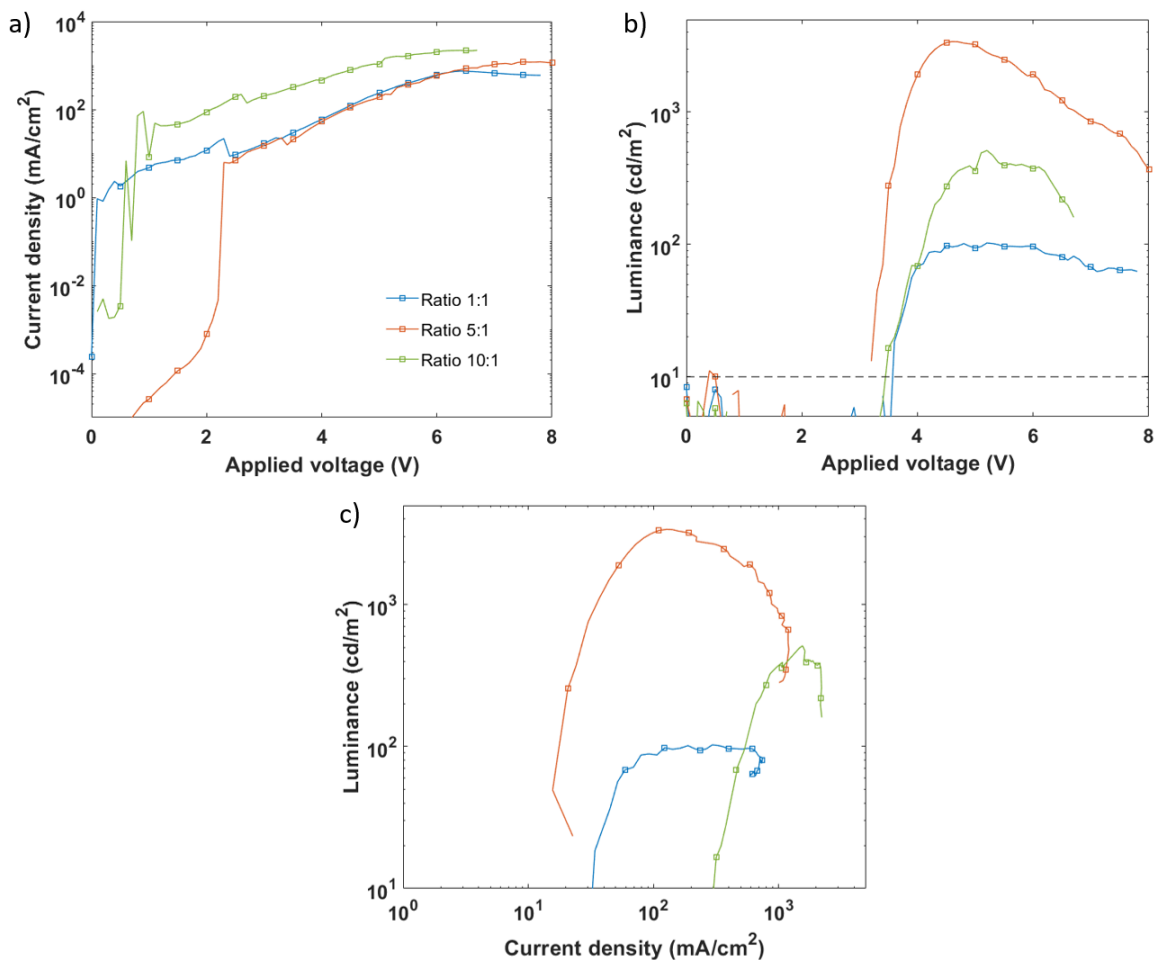
Figure III.22. Electroluminescence performance of PeLEDs based on perovskite QD/PEO composites: a) J-V, b) L-V, c) L-J curves.

Besides, it is worth emphasizing low turn-on voltage of the QD/PEO PeLEDs – approximately 3.4 V for all three cases. The similarity in the V_{ON} values between the PEO and PMMA-based devices, regardless of the composition ratio, is an evidence that the polymer molecules do not directly react with the QD surface or alter the quality of perovskite emitters. Also, it suggest that the presence of the polymers in the composite is sufficiently limited to avoid causing additional resistive pathways or energetic barrier for charge injection. We believe such feature is associated with the restricted thickness (< 100 nm) and directly results from the favorable morphology of the active layers, as presented for both PEO and PMMA-based composite thin films. Another shared characteristic between the two types of composite PeLEDs is how the polymer loading can influence the minimum current required to initiate light emission (so-called the threshold current). As shown in Figure III.22.c, it requires to blend the perovskite QDs and PEO precursors with an optimal ratio (i.e., 5:1) to achieve a low threshold current, which is important for saving energy consumption and reducing self-heating effect on the device's components. Either over-loading (1:1) or under-loading (10:1) of the PEO polymer would result in an increase in the threshold current.

Consequently, the 5:1 sample demonstrates a notable power conversion efficiency - approximately reaching 1% in term of EQE, as illustrated in Figure.III.23.a, or 3 lm/W in term of luminous efficiency

(see Annex 3.4). In particular, this maximal EQE value can be achieved at a relatively low current injection of 60 mA/cm², corresponding to a driving voltage of 4 V. Another behavior we should highlight here is the dramatic efficiency roll-off, which has also been observed in the PMMA-based devices. In quantum dot PeLEDs, the causes to this phenomenon are generally ascribed to Joule-heating effect, charge injection imbalance, generation of QD's surface trap states under intense electrical field, and Auger recombination [278], [279].
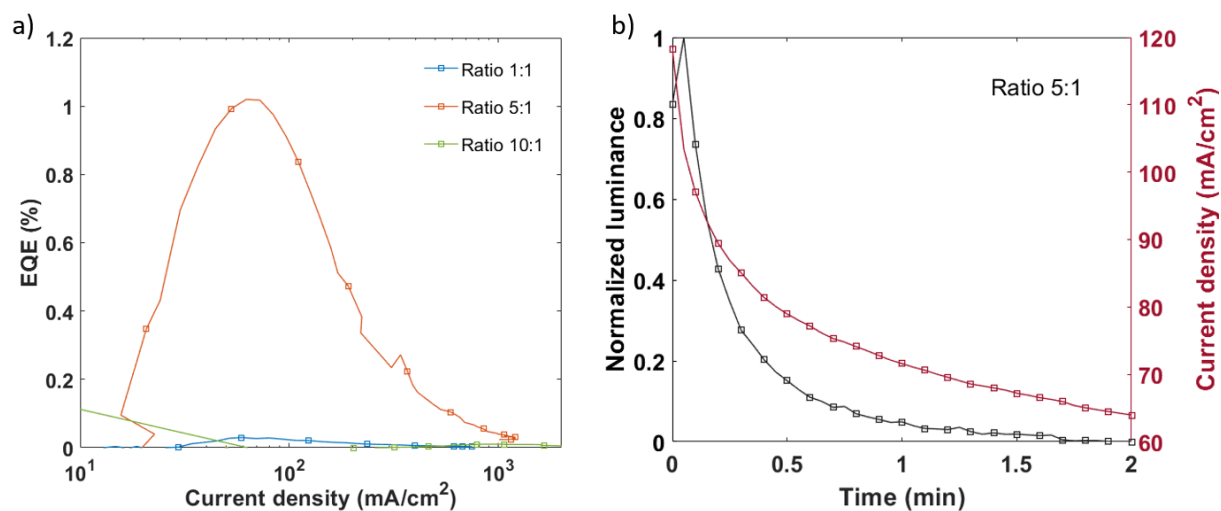
Figure III.23. a) Correlation of EQE and current density and b) Device durability in PeLEDs based on perovskite QD/PEO composites.

On the subject of device's durability, the PEO-based device exhibits a slightly better operational stability than the PeLED based on PMMA, even though the device's lifetime remains notably limited (Figure III.23.b). Interestingly, the temporal evolution of the luminance in this particular case shows a transient behavior (i.e., rapid changes in the device's luminance over a short time interval when an electrical current is applied to the device). We deduce that this device degradation arises from the same physical origins as the transient effect observed in the perovskite QD/PMMA PeLEDs, such as the decomposition of the QDs under intense electrical field, the migration of ionic species towards the interfaces, and the Ohmic heating. The difference here potentially lies in the timeframes for these phenomena to occur. For example, the ionic conducting nature of the PEO molecules may facilitate the redistribution of the electric field inside the emissive thin film, thus allowing the transient state in the current response to occur in a much faster timespan than the scanning rate of the measurement (i.e., ≪ 3 seconds). On the other hand, the transient response in the EL intensity is more easily observed thanks to the prolonged trap-filling and emptying effects due to ion migration.

To recapitulate, our study has demonstrated that PEO represents a favorable alternative to PMMA for the preparation of hybrid perovskite QD/polymer materials towards applications in PeLEDs. Unlike PMMA, the morphological and optical properties of the composite materials based on PEO significantly depends on the proportion between the QD and PEO precursors. Accordingly, our findings have suggested an optimal QD-to-PEO ratio of 5:1, which maximizes the emissive layer's morphology without compromising its optical behaviors. As a result, we achieved operational devices with reasonably good

performance metrics (L_{max} = 5000 cd/m^2 and EQE_{max} = 1%). However, the drawback of our composite PeLED prototypes is their working lifetime, which is primarily limited by the electrically-induced decomposition of the emissive materials.

3.4 Summary and outlook

a. Summary

In this chapter, we presented our systematic study on fabricating green PeLEDs utilizing CsPbBr$_3$ QDs synthesized via soft chemistry. This is the first time that bright and efficient devices based on these novel perovskite QDs have been successfully demonstrated, unleashing the potential of this material for optoelectronic applications, particularly in LED technology.

Despite the favorable optical properties this material possesses, it has been shown that achieving a simple technique to effectively deposit an emissive layer from the colloidal solution or pure QD for electroluminescence (EL) applications is impractical. When drop-casted or spin-coated on flat substrates, instead of forming a continuous film, the QDs have a tendency to aggregate into small islands separately distributed across the substrate surface. This morphology results in unwanted interlayer mixing between the perovskite and the electron transfer layers. This, in turn, causes catastrophic leakage current within the PeLED, impeding its capacity to host radiative recombination.

Therefore, to facilitate the formation of thin films, we attempted to embed the perovskite QDs into polymer matrices. Two polymer alternatives have been investigated, including polymethyl methacrylate (PMMA) and poly(ethylene oxide) (PEO). For both cases, by tuning the QD-to-polymer ratio (i.e. 10:1 for PMMA and 5:1 for PEO), we succeeded depositing composite thin films with good surface coverage and homogeneous QD dispersion. In such composite systems, the polymer materials play an important role in enhancing the processability of the QD solution as well as passivating the voids between the QD islands. Subsequently, the PeLEDs based on these composite films exhibits notable EL performances. For example, the QD/PMMA device records a maximum luminance of 2,500 cd/m^2 and a maximum EQE of 1.4%. These values in the case of QD/PEO PeLEDs are 5,000 cd/m^2 and 1%, respectively. To compare, our devices yield equivalent output data to those utilizing PEO-doped CsPbBr$_3$ nanocrystals proposed by Yu et. al., who have L_{max} of 5,500 cd/m^2 and EQE of 2.4 % [270]. In spite of the noticeable performance, these composite PeLEDs demonstrate a shortcoming in the operational stability. Particularly, we observed an extremely brief EL lifetime of only a few seconds in both cases, which can be attributed to the intrinsic instability of the perovskite QDs when exposed to electrical field, together with the charge injection imbalance and the self-heating induced degradation of the device structure

b. Outlook

Although having promising results on the EL behaviors of the perovskite QD-embedded composite layers, we are still uncertain about the underlying mechanisms that govern the photo-physics processes in such QD-polymer systems. Our experimental findings demonstrated a contrast in how the PMMA or PEO matrix would interact with the QD emitters and subsequently alter the kinetics of the radiative and

non-radiative recombination. For instance, while the use of PMMA exerts trivial effects on the time-resolved PL of the perovskite QDs, blending the QDs with PEO molecules can noticeably reduce the PL lifetime of the perovskite materials. Similarly, we observed different transient response patterns in the EL decays of PMMA and PEO-based devices. A rigorous investigation on this subject will be required in the upcoming period to shed light on the interaction between the perovskite QDs, specifically those prepared via soft-chemical routes, and the polymer materials.

Due to the time constraints we faced when conducting this project, we were only able to study the applications of the two specific polymers, PMMA and PEO, in developing optoelectrically active QD/polymer composite thin films. Notable, our method deviated from the conventional approaches as we chose to employ non- or low-conductive polymers as a versatile platform for incorporating the QD emitters. Our success in exploiting the polymers' film-forming capabilities to fabricate efficient and performant PeLEDs paves the way for further advancement in optimization of perovskite QD-based optoelectronic devices. Beyond these two materials, there is an extensive array of polymer alternatives with diverge properties and functionalities, such as mechanical flexibility, chemical resistance, or color-adapting ability. By strategically selecting and tailoring these polymers, it holds great potential to develop a new generation of brighter, more efficient, more stable, and more versatile QD/polymer hybrid devices.

Chapter IV.   FABRICATION OF PELEDS DRIVEN BY NANOIMPRINTED PEROVSKITE METASURFACES

This chapter is dedicated to the development of an original approach aimed at improving light extraction efficiency in green PeLEDs via the nanostructuration of the emissive layer. Accordingly, we will begin the chapter with a brief discussion about the concept of perovskite metasurfaces and their applications in optoelectronics, with particular attention to optically-pumped emitting devices. Based on that ground, our novel concept of incorporating a photonic structure based on hybrid halide perovskites into PeLEDs is designed to serve the dual purpose of effectively emitting light and guiding the light to a free space continuum. Subsequently, the section will analyze the technological challenges associated with developing such metasurface-driven PeLEDs. Furthermore, we will highlight the partnership between XLIM and the "Institut de Nanotechnologies de Lyon" (INL) and demonstrate the collaborative nature of this project.

Then, in the second part of the chapter, we will thoroughly explain the logic behind the design process of the perovskite metasurface, tailored to meet specific requirements for electroluminescent applications. Additionally, a comprehensive account of the thermal nanoimprint lithography processes employed to fabricate these metasurfaces will be detailed therein. Furthermore, the impacts of the imprint process and the nanostructuration on the morphological and optical properties of the quasi-2D perovskite thin films will be investigated, shedding light on how these alterations can potentially improve light extraction in PeLEDs.

The last section focuses on the integration of these imprinted perovskite films into our blueprint PeLEDs. Indeed, our approach is distinctive in prioritizing the analysis of both successful and unsuccessful device fabrication efforts. Rather than only showcasing well-working devices, we inspect closely the obstacles we encountered while nanoimprinting the active layer of PeLEDs. Through this extensive investigation, we aim to gain a deeper understanding of the limitations inherent to our fabrication processes and pinpoint areas for future improvement. Despite these challenges, reasonably functioning prototypes based on nanoimprinted perovskite thin films will be demonstrated, marking the primary milestone of our pioneering study toward realizing true metasurface-driven PeLEDs.

4.1 Conceptualization of perovskite metasurface-driven PeLEDs

4.1.1 Overview of metasurfaces and perovskite metasurfaces

Generally, optical metasurfaces are composed of photonic structures at a sub-wavelength scale that are realized on planar thin films and, therefore, they inherit the ability to tailor and manipulate light-matter interaction in ways that conventional bulk optics cannot [280], [281]. Since their properties largely depend on the size, shape, arrangement, and material composition of the building unit cells, it opens up a virtually infinite number of scenarios to harness the power of metasurfaces with various artificially designed functionalities. In practice, the concept of metasurfaces has been intensively introduced in many research fields, such as quantum computing [282], [283], optical imaging (e.g., super-lens, hyper-lens) [284], [285], coherent light sources [286], nonlinear photonics [287], perfect absorbers/emitters [288], [289], and wavefront shaping [290]. Concerning LED technologies, these artificial nanostructures have also been widely applied to enhance the light extraction efficiency and control the color contrast in organic and quantum-dot LEDs [291]–[296], as well as to enable the miniaturization of these devices for ultra-high-resolution micro-displays (micro-LEDs) [297], [298]. However, it must be noted that the metasurface structures are usually integrated as an optical component rather than capable of emitting light themselves.

In addition to metals and conventional semiconductors, halide perovskites have recently gained attention as the materials of interest for metasurface construction thanks to their superior properties (bandgap tunability, high refractive index, defect tolerance, high PLQY, solution processability, etc…). The hybridization of photonic crystal (PC) designs with such exceptionally versatile materials enables novel superstructural tunability [299], which researchers have exploited to advance the progress of perovskite-based light-emitting devices. For example, Soci's group succeeded in fabricating resonant metasurfaces with a quite basic nanograting and nanoslit geometries to control the photoluminescence (PL) intensity [300] (see Figures IV.1.a and b) and wavelength [301] in bulk perovskite thin films. Furthermore, engineering geometric anisotropy of the photonic structures enables manipulation of the emitting light's polarization [302]–[304]. Owing to these findings, coherent light sources based on perovskite metasurfaces have been recently introduced with different levels of governing the polarization patterns [305]–[308].
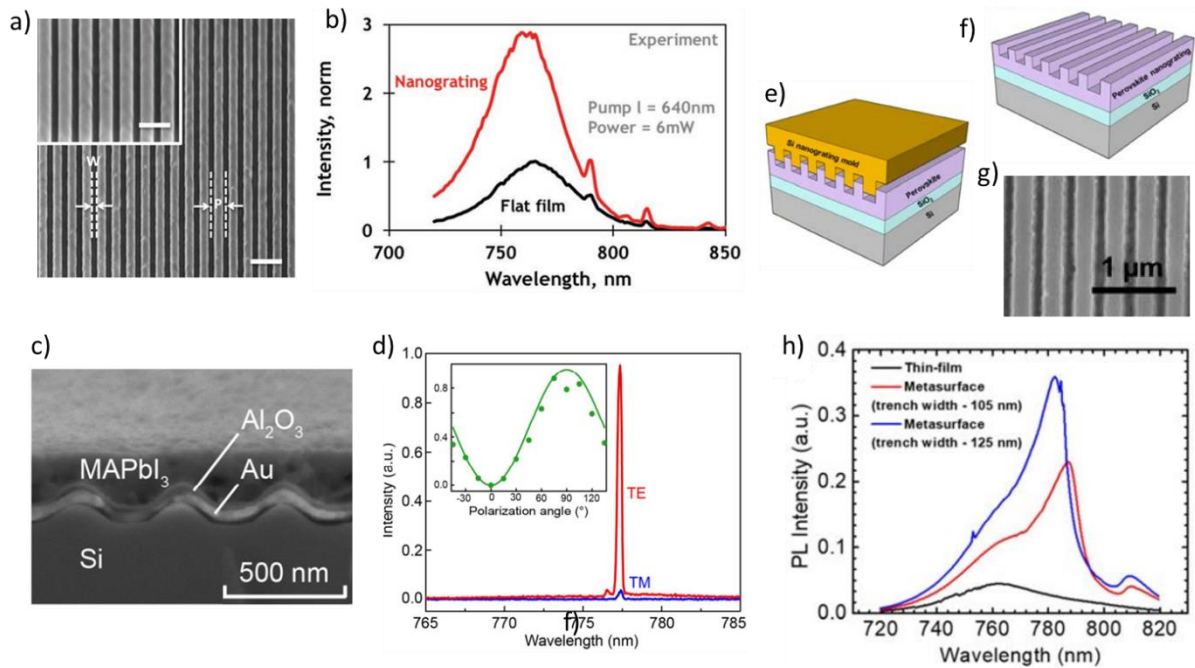
Figure IV.1.Examples of literature on perovskite metasurfaces: a) SEM images and b) Photoluminescence enhancement in perovskite nanograting realized using focused ion beam technique, extracted from [300]; c) Cross-sectional SEM image and d) Lasing effects of a periodic structure based on halide perovskite, extracted from [309]; and e, f) Schematics, g) SEM image and h) Emission property of perovskite metasurfaces realized using nanoimprint technique, extracted from [310].

Several methods have been demonstrated to realize nanostructures on perovskite thin films, which can be classified into two groups. One strategy is to deposit perovskite materials onto pre-patterned substrates. For example, Jia et al. spin-coated methylammonium lead iodide ($MAPbI_3$) on top of gold-coated Si gratings to create a perovskite nanosheet with similar periodicity [309] (as illustrated in Figures IV.1.c and d). Alternatively, with a slight modification, Gu et al. deposited a well-defined array of perovskite nanowires via chemical vapor deposition by employing a porous alumina membrane template with predefined hexagonal nanochannels [311]. Other solution-based techniques, such as laser direct writing [312], solvent-assisted printing [313], or inkjet printing [314], are only efficient in forming structures at a micrometer scale but cannot achieve smaller dimensions. Another strategy is to directly pattern the perovskite thin films with uniform orientation either via using focused ion beam etching [300], [315] or employing nanoimprint lithography (NIL) [307], [310]. Of these two techniques, the former has the critical disadvantages of inducing surface damages caused by implanted ions and requiring relatively complex fabrication systems (e.g., ultra-low vacuum environment, specialized instrument for ion beam control). On the other hand, NIL is a more straightforward, scalable method for crafting nano-scale structures over a large surface area. Briefly, the principle of nanoimprint is to transfer the desired patterns from a master mold (or stamp) to a soft, thin film made from the material of interest by mechanically pressing the mold onto the film. This process is assisted by thermal annealing or ultra-violet light exposure to consolidate the patterned structure. In a larger context, nanoimprint has been repeatedly used for metasurface fabrication on various materials, such as gold, silver, poly-silicon, porous silicon dioxide, polystyrene, polyethylene terephthalate, etc… [316]. An example of perovskite phonic structures patterned via NIL, together with their emission properties, is depicted in Figures IV.1.e-h.

4.1.2 Study of perovskite metasurfaces for optically-pumped emitting devices at Institut de Nanotechnologies de Lyon

As introduced in the first chapter of the thesis, the Nanophotonics group at Institut des Nanotechnologies de Lyon (INL) is one of our collaborating partners under the framework of the EMIPERO project (together with LUMIN). Their research of perovskite metasurfaces revolves around light management strategies to improve the efficiency of perovskite-based optoelectronic devices and demonstrate strong coupling effects between the perovskites and the photonic structures. In this direction, INL's Nanophotonics group has observed several promising results concerning the optical and optoelectronic properties of perovskite photonic crystals fabricated using the thermal-assisted nanoimprint technique. For example, Dr. Mermet-Lyaudoz showed in his doctoral thesis an observation of remarkable PL enhancement in nanopatterned perovskite films compared to reference flat lattices (Figure IV.2), which was ascribed to the improved light extraction via the coupling of the emitting light's guided modes with the periodic structure. Similar effects were also recorded when they integrated the perovskite metasurface into a multilayered stack made of common charge transfer layers, such as TiO_2 and 2,2',7,7'-Tetrakis[N,N-di(4-methoxyphenyl)amino]-9,9'-spirobifluorene(Spiro-OMeTAD)) [205]. Besides, the nanostructuration of perovskite thin films has been proved to effectively give rise to lasing effects with tunable emitting direction [307]. In addition, the group has conceived and experimentally demonstrated the concept of a polaritonic metasurface based on two-dimensional hybrid perovskites to engineer exciton-polaritons at ambient conditions [317], [318].
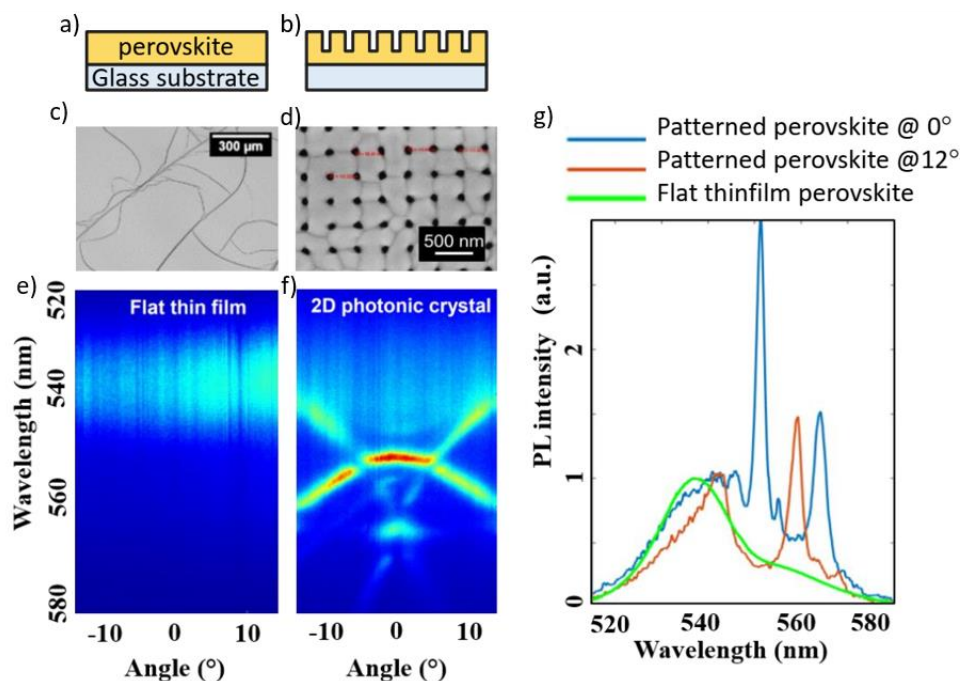
Figure IV.2. Comparison of morphological and optical properties of methylammonium lead bromide (MAPB) perovskite in flat thin film and 2D photonic crystal: a, b) Schematic representations; c, d) SEM images; e, f) Angle-resolved PL measurement; and g) Steady-stead PL spectra. Extracted from [205].

4.1.3 Opportunities and challenges in the development of metasurface-driven PeLEDs

On the grounds of the successful employment of perovskite photonic crystals in optically-pumped micro-lasers at INL, we are motivated to exploit these nanostructures for integration into XLIM's PeLED design as an active layer. In our hypothesis, the utilization of perovskite metasurface can bring several benefits to the device performance, including:

i)   *Improve light extraction efficiency:* As mentioned in the first chapter, monitoring light extraction is an important strategy to enhance the overall efficiency of a PeLED. Indeed, the outcoupling of light is primarily governed by the total internal reflection phenomenon at the interface between the perovskite and adjacent charge transfer or contact layers, for which a large portion of optical energy will be detained inside the emissive layer. From the photonic point of view, a perovskite thin film can be considered as a two-dimensional waveguide, and the trapped light propagates along this waveguide following specific guided modes. In a flat PeLED (where the boundaries between the layers are relatively homogenous compared to the sub-wavelength dimensions), these guided modes cannot be coupled to the free space and result in optical losses (Figure IV.3.a). Conversely, introducing an in-plane periodic structure can induce diffraction to redirect the confined light and couple it to free-space modes so that more light can be extracted to the outside environment (Figure IV.3.b).
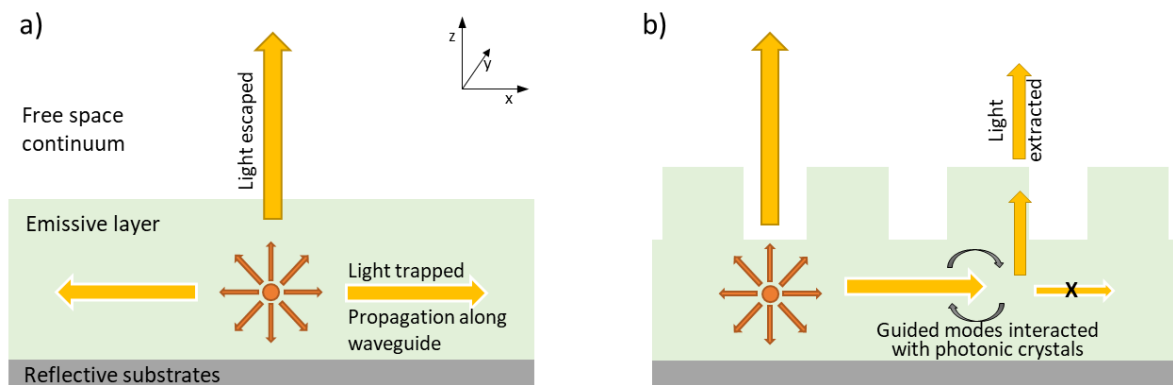
Figure IV.3. Concepts of light confinement and extraction in a multilayered light-emitting stack with: a) Flat surface and b) Metasurface.

ii) *Control emission pattern:* The wavefront, such as the angular distribution or the polarization, of the emitted light can be manipulated on-demand by changing the perovskite metasurface's patterning parameters. This feature is useful for applications in visible light communication, which often requires wide-angle radiation of the LED light, or in optically-pumped polariton systems, which – in contrast - entails directional emission [319].

However, in practice, demonstrating electroluminescence (EL) from nanoimprinted thin films presents a formidable challenge because their not-flat surface may induce heterogeneous carrier injection, which can lead to localized charge accumulation, augmented heating effect, and subsequent non-radiative recombination. Such limitations are even more critical when it comes to perovskite active materials

considering their high softness and sensitivity to extrinsic factors. The transposition of interfacial layers from the micro-laser technology to PeLED, and vice versa, is also vastly problematic due to the fundamental differences in the operational regimes of the two devices. In particular, LED is often designed to emit broadband light and operate at relatively low current injection. Conversely, micro-lasers require very high carrier density and produce coherent, narrowband output with strict requirements on spectral purity and temporal stability. To the best of our knowledge, there has yet been any published literature reporting the realization of metasurface-based light-emitting diodes (not only limited to perovskites but also including inorganic, organic, polymer, and quantum dot materials) *where the metasurface is employed as the emissive layer*.

Considering perovskite light-emitting transistors (PeLET) - a variant of PeLEDs, Soci's group has recently demonstrated successful integration of dielectric nanograting metasurfaces into the active layer made of MAPbI$_3$. As a result, their metasurface-driven PeLET exhibited a remarkable increase in the EL intensity, which was attributed to the improved light outcoupling efficiency and the Purcell effect induced by the resonant modes of the perovskite photonic crystals [320]. Nonetheless, the dissimilarities between PeLED and PeLET structures (for instance, the emissive layer in PeLETs is an open surface rather than being sandwiched between organic transfer layers) make it impractical to directly apply Soci's technique into fabricating our targeting device.

For these reasons, we determined that the preliminary goal of this project was to realize a prototype of operational PeLEDs with a metasurface directly patterned onto the perovskite thin films and subsequently characterize these devices' performance under electrical injection.

4.1.4 Collaboration between XLIM and INL for development of metasurface-driven PeLEDs

To fulfill this outlined objective, we described various subtasks and divided the workload distribution between XLIM and INL as follows:

1) **Design of perovskite nanostructures**: In this study, we employed the photonic crystal designs previously proposed in Dr. Mermet-Lyaudoz's thesis as a basis. INL would be responsible for assessing and optimizing these structures in terms of their geometry and corresponding photonic behaviors toward the integration into green PeLEDs.

2) **Design of PeLEDs integrated with perovskite metasurface:** A detailed design of the multilayered structure (including the material, thickness, and coverage area of each layer, as well as the number, dimension, and position of the pixels on a substrate) was proposed based on the blueprint of our quasi-2D PeLEDs studied in Chapter 2. Accordingly, XLIM – particularly the author of this thesis – was in charge of this task, and the design would later be revised and approved by INL.

3) **Deposition of perovskite thin films on charge transfer layers:** In this project, we employed the _quasi-2D phenylethylammonium methylammonium lead bromide (PEA$_2$MA$_{n-1}$Pb$_n$Br$_{3n+1}$)_, whose recipe has been developed at XLIM for the fabrication of the reference PeLEDs. At the beginning

of the project, pristine quasi-2D perovskite layers deposited on glass substrates or hole transfer layers would be prepared at XLIM and then transferred to INL for nanoimprinting and associated characterization. Later on, the know-how of this deposition process was transferred to INL; then, the deposition of the low-dimensional perovskites could be conducted at INL to minimize the potential degradation of samples due to the transportation.

4) **Nanoimprint of metasurface patterns on perovskite thin films:** Although the technique to fabricate photonic crystals in MAPB has been thoroughly established in previous studies at INL, it required optimization of imprint parameters (imprint pressure and time, annealing temperature, etc…) explicitly targeting the quasi-2D perovskites due to the differences in the crystallization nature of the two types of bulk perovskites. In addition, optical characterization of the quasi-2D perovskite metasurfaces would be necessary to understand the photo-physics in such structures. This task was primarily undertaken at INL.

5) **Fabrication of metasurface-driven PeLEDs:** The deposition of the electrodes and charge transfer/injection layers (including the etching of ITO, spin-coating deposition of PEDOT:PSS, and vacuum thermal evaporation of LiF, TPBi, Ca, and Ag) was primarily realized at XLIM. It should be noted that, as the metasurface required to be imprinted at INL, the samples would subsequently need to be transported back and forth between Limoges and Lyon to complete the entire fabrication process.

6) **Electrical characterization of metasurface-driven PeLEDs:** Similarly to the non-imprinted PeLEDs studied throughout this thesis, the PeLEDs integrated with nanophotonic structures would also be characterized at XLIM by means of standard techniques such as EL spectrum, J-L-V measurement, energy-conversion-efficiency analysis, or device lifetime. If appropriate, measurements of the modulation speed might also be required at the later stages of the project to evaluate the potential applications of these devices in visible light communication.

Before moving into the details of the experiments, despite the allocation of responsibilities mentioned above, we wish to acknowledge and emphasize the joint operation and collaborative exchange between XLIM and INL. In particular, the graduate students from the two laboratories – Trong-Tam Nguyen from INL and the author of the thesis from XLIM – maintained a rigorous level of coordination throughout the project, evidenced by the fact that both of us actively engaged in the conceptualization and execution of experiments. Furthermore, we orchestrated numerous inter-laboratory mobilities between XLIM and INL to foster the exchange and transfer of our technological knowledge regarding the nanoimprint process as well as the full device's fabrication and characterization techniques. Consequently, the results we will demonstrate in this chapter should be equally contributed to both of us.

4.2 Design and fabrication of perovskite metasurface

4.2.1 Design of perovskite metasurface

The first step toward realizing a metasurface-driven PeLEDs is to design the metasurface itself. The most basic geometry of a two-dimensional photonic crystal is based on the concept of perfect symmetry

(Figure IV.4.a), in which the crystal structure remains unchanged when mirrored either along the horizontal or vertical axes. However, the research at INL has shown that breaking the vertical symmetry via a partial corrugation (Figure IV.4.b) could enable hybridized resonant modes favorable for extracting light [321]. For applications in PeLEDs, the use of a metasurface with broken vertical symmetry has another benefit of ensuring good surface coverage between the emissive perovskite and underlying charge transfer layers; otherwise, the air holes on the slab could serve as large defects on the perovskite surface and cause serious electrical leakage.
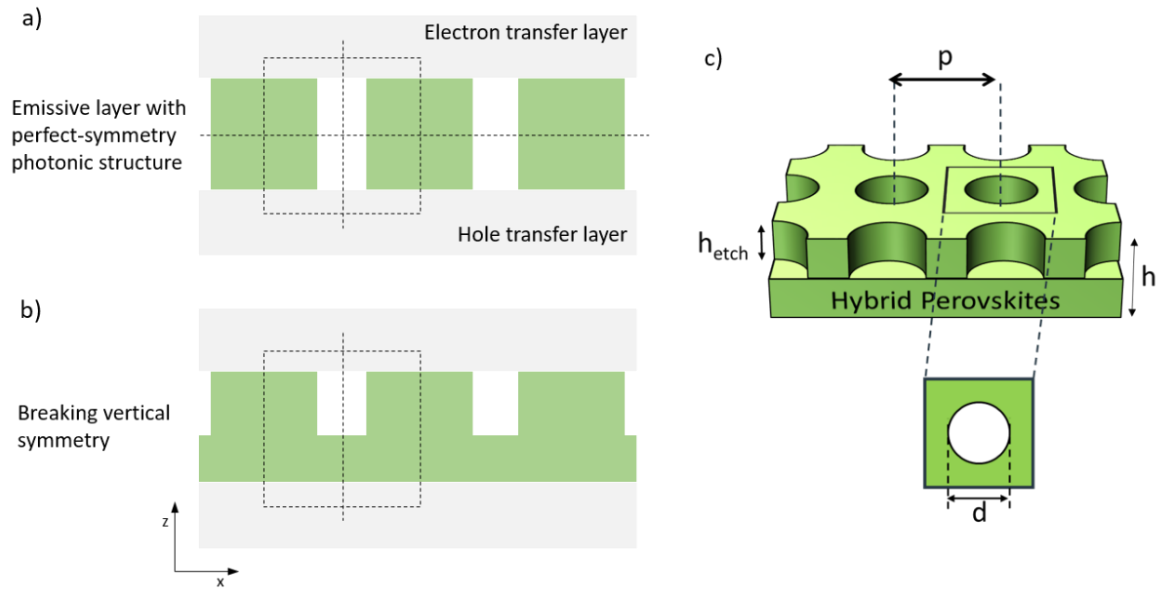
Figure IV.4. 2D photonic crystal structure in hybrid perovskite thin films: a, b) Comparison of slab geometries with perfect and broken vertical symmetry, and c) Geometrical parameters in square-lattice perovskite PCs.

Figure IV.4.c depicts the design of the periodic slab structure with in-plane anisotropy based on hybrid perovskite thin films. In this scheme, h is the total thickness of the perovskite layer, h_{etch} is the thickness of the slabs, p is the period of the photonic lattice (also called lattice constant), and d is the diameter of the air hole. Indeed, for the guided modes of the confined light inside the perovskite waveguide to interact with the periodic structure (so we can extract it), the PC's periodicity needs to satisfy a phase-matching condition [322].

In the case of two-dimensional structures, and by assuming that light only escapes outside from the normal direction of the surface (so that the in-plane wavevector is negligible), this condition can be expressed as:

$$\overrightarrow{\beta_m} = m_x \frac{2\pi}{p}.\overrightarrow{u_x} + m_y \frac{2\pi}{p}.\overrightarrow{u_y} \qquad \text{(Equation IV.1)}$$

in which $\overrightarrow{\beta_m}$ is the in-plane wavenumber vector of the $\mathbf{m^{th}}$ propagating guided mode, $\overrightarrow{u_x}$ and $\overrightarrow{u_y}$ are the in-plane unit vectors, $\mathbf{m_x}$ and $\mathbf{m_y}$ are the diffraction orders. On the other hand, the value of the in-plane wavenumber also depends on the effective index $\mathbf{n_{eff}}$ of the multilayered stack and the emission wavelength λ, such as:

$$\beta = \frac{2\pi}{\lambda} \cdot n_{eff} \qquad \text{(Equation IV.2)}$$

So, for the first-order (and also most efficient) coupling mode ($m_x = \pm 1$ and $m_y = 0$, or vice versa), the lattice period can be estimated as:

$$p = \lambda / n_{eff} \qquad \text{(Equation IV.3)}$$

With respect to green PeLEDs based on quasi-2D perovskite thin films, the emission wavelength varies from 520 nm to 530 nm. Also, the effective index of the device stack can be estimated between 2.0 and 2.2, considering the high refractive index of the bromide perovskites (~ 2.4 to 2.6 [323], [324]) and the low refractive indices of the organic transporting layers (1.5 for PEDOT:PSS [325] and 1.7 for TPBi [326]), the required period must be approximately 250 nm. However, fabricating a nanostructure with such compact spatial periodicity could be demanding since it requires high manufacturing precision. Therefore, we would focus on another case of perovskite metasurface with second-order diffraction modes ($|m_x| + |m_y| = 2$). Correspondingly, the lattice periods can be given as:

- In the case of $m_x = \pm 1$ and $m_y = \pm 1$:

$$p = \sqrt{2} \cdot \frac{\lambda}{n_{eff}} \cong 350 \ nm \qquad \text{(Equation IV.4)}$$

- In the case of $m_x = \pm 2$ and $m_y = 0$, or vice versa:

$$p = 2 \cdot \frac{\lambda}{n_{eff}} \cong 500 \ nm \qquad \text{(Equation IV.5)}$$

For the similar reason as above, we decided to examine the case with more extended lattice constant, i.e., *p = 500 nm corresponding to m = 2*. Other parameters of the photonic crystals are chosen as follows: d = 20 nm, h_{etch} = 50 nm, while h is the actual thickness of the compressed perovskite films after nanoimprint, estimated between 80 nm - 100 nm.

4.2.2 Thermal nanoimprint lithography of perovskite metasurface

In order to effectively investigate the effects of nanostructuring on the performance of PeLEDs, we prepare two configurations of perovskite surfaces: one featuring photonic crystals and the other completely flat. The purpose of employing a flat imprinted surface as opposed to a pristine, non-imprinted perovskite film as a reference sample is to standardize and offset the influences of changes in deposition parameters (such as number of deposition steps, pressure, annealing time, temperature, breaks between deposition, environmental variables) on the perovskite crystal formation. Crafting the nanostructure design onto a perovskite thin film involves three steps: 1) fabricating a mold, 2) preparing flat perovskite layers, and 3) transposing the nanopatterns from the mold onto the thin films.

a. Fabrication and treatment of master molds

Figure IV.5.a depicts the process to manufacture nanoimprint stamps from planar silicon wafers using electron-beam lithography. Briefly, a 100-nm layer of negative resin (hydrogen silsesquioxane) is initially deposited on a silicon dioxide (SiO_2)-coated silicon wafer. Next, the photoresist layer is scanned using electron beam lithography before being chemically developed to define the desired nanopatterns. The

patterns are then transferred to the silicon substrate by plasma etching. The last step is to remove the remaining resin and SiO$_2$ via wet etching in a buffered oxide etch solution, leaving behind the silicon master mold with the desired 2D nanostructure. The details of this process can be found in [205], [321]. In parallel, the flat molds are prepared by simply etching the SiO$_2$ layer from the silicon wafer.
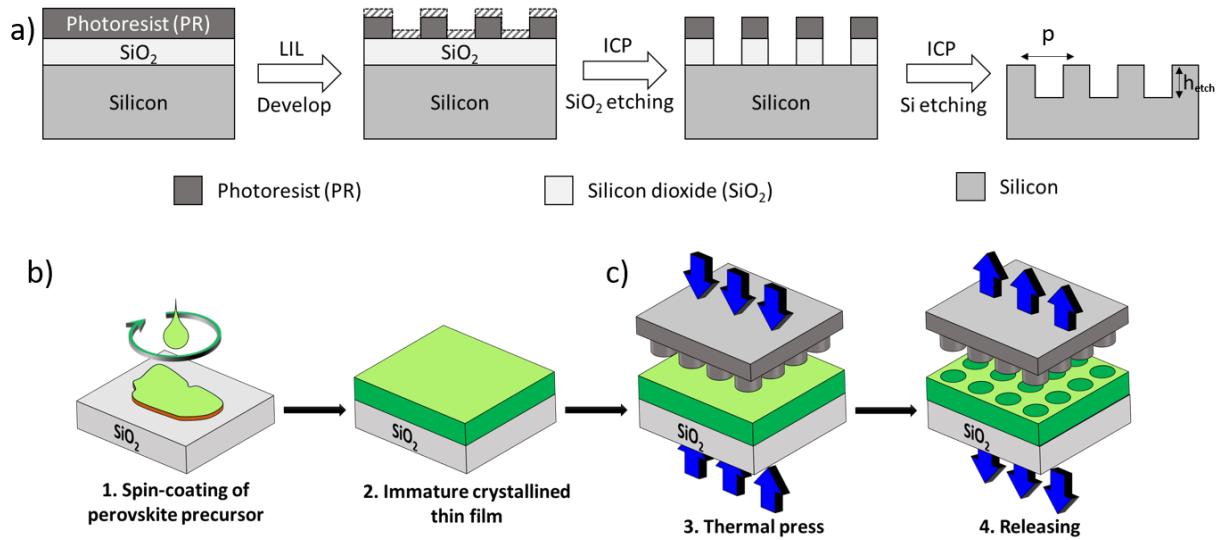
Figure IV.5. Schematic representation of the nanoimprint process: a) Fabrication of a master mold, b) Deposition of flat perovskite layer, and c) Imprinting the nanostructure from the mold onto the perovskite layer.

Before each imprint, the mold needs to be bathed in a silanization solution of henicosyl-1,1,2,2-tetrahydrododecyltrichlorosilane (FDDTS) diluted in n-Heptane, followed by 10 minutes of 100 °C-annealing, in order to increase the hydrophobicity of the stamp's surface. This silanization prevents the perovskite materials from adhering to the mold during the thermal press.

b. Deposition of perovskite layers

The deposition process of the quasi-2D perovskite is mainly similar to the procedure we have shown in Chapter 2 (e.g., PEA/MA ratio of 1:2, spin-coating at 7000 rpm for 40 seconds, thermal treatment at 90 °C). The only difference here lies in the annealing duration, which has been shortened to 5 minutes (instead of 15 minutes when preparing flat PeLEDs), so the output of this step is an immature crystalline thin film. This modification is because the sample will undergo additional heating during the nanoimprinting process, by which the perovskite can be fully crystallized.

c. Thermal imprint on perovskite layers

Once the mold and the perovskite layer have been carefully prepared, they are placed into the pressing chamber of the thermal press machine, with the mold oriented downward onto the perovskite. A total pressure of 3 kN is applied from both the upper and lower plates of the chamber to firmly compress them into each other. Simultaneously, the temperature of the plates is quickly increased to 90 °C. The imprint process lasts 15 minutes, after which the pressure is released, and the mold is separated from the substrate (i.e., demolding). A summary of the thermal imprinting process is demonstrated in Figures IV.5.b and c.

In particular, two systems of nanoimprint lithography have been employed in this project. The first is a manual system (Rondon Thermal Press, as shown in Figures IV.6.a and b), with which the pattern alignment and mechanical press must be carried out manually. In practice, we used this system in the early stage of the project (from October 2022 to May 2023) for studying the optical properties of the imprinted perovskite thin films and developing the first version of metasurface-driven PeLEDs. Nonetheless, it posed several limitations concerning the reliability of the patterning process, including mold-substrate misalignment and inhomogeneous application of mechanical forces over the imprint area. Of these two issues, the latter can further lead to deformation or even breakage of the molds and the substrates, which we encountered very frequently in our experiments. Another drawback of this equipment is that its integrated pressure sensor can only offer a measurement precision of approximately 1 kN, hindering our ability to precisely monitor the imprint pressure and ensure consistent metasurface reproduction. Therefore, at the later stage of the project (starting from June 2023), we decided to utilize an automated nanoimprint system (NPS300 – Smart Equipment Technology Corporation, France), which can afford a high degree of precision in controlling the imprint process (see Figures IV.6.c and d).
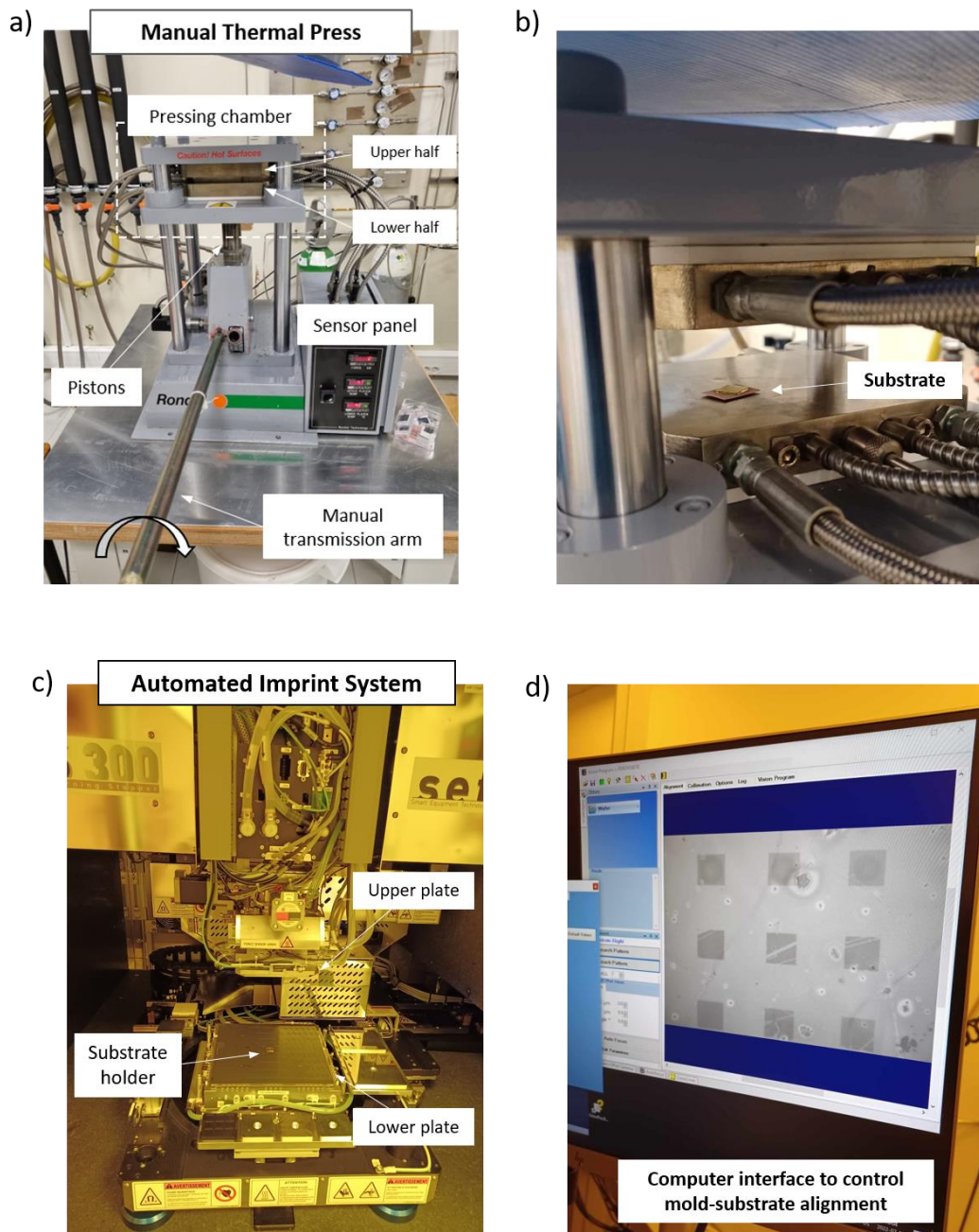
Figure IV.6. Thermal nanoimprinting systems at INL: a) Overview and b) Pressing chamber of Rondon Thermal Press versus c) Automated imprint chamber and d) Computer interface of NPS300 Nanoimprint Lithography.

An additional notable difference when utilizing these two systems is the time gap between the thin film deposition and the subsequent imprinting steps. In the case of the Rondon press, its proximity to the deposition glovebox facilitates the swift transfer of samples from the deposition setup to the press chamber within minutes. In contrast, the NPS300 system is situated on a different campus than the deposition glovebox, thus requiring several hours for the transportation of samples between the two locations. In the discussion, we will specify the equipment employed to fabricate each batch of metasurface-driven PeLEDs.

4.2.3 Characterization of perovskite metasurface

a. Effect of thermal press on the characteristics of perovskite thin films

First, we investigated the impacts of the imprint process on the morphological and optical properties of the emissive perovskite layers, noting that the lithography process was conducted utilizing the manual press machine. Figure IV.7 demonstrates the morphology of a perovskite sample imprinted using a flat stamp, both at a macroscopic and microscopic scale. It is evident that at both levels of observation, the perovskite surface appears remarkably homogeneous and complete. Specifically, the SEM image clearly depicts the formation of a compact polycrystalline thin film composed of highly organized nanograins, similar to pristine quasi-2D perovskite films observed in Chapter 2. In addition, the thickness of the mechanically pressed samples was measured at approximately 80 nm, significantly thinner than the non-imprinted layers (whose thickness is approximately 150 nm).
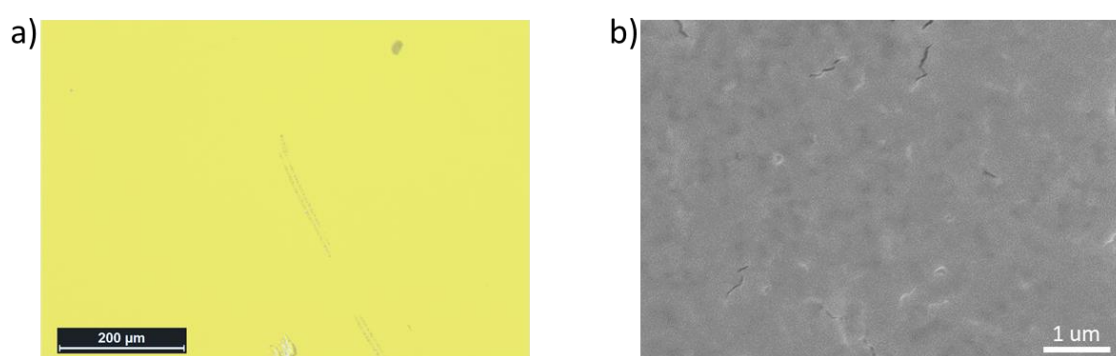
Figure IV.7. a) Microscopy and b) SEM images of a perovskite thin film pressed using flat mold.

While the morphology of the pristine and flat perovskite thin films closely resembles each other, their optical properties exhibit moderately distinct features, as can be seen in Figure IV.8. For instance, from the UV-Vis absorption, one can observe that the absorption coefficient of the flat thin film surpasses that of the pristine counterpart, indicating a higher density of perovskite inside the pressed layer. This increase in material density simply arises from the fact that both films comprise the same amount of perovskite materials as we used identical spin-coating parameters, but the flat sample has undergone compression (i.e., thinner layer with high density versus thicker layer with low density). However, it should be noted that the absorption patterns of the two samples still share some identical features, such as a band edge at 515 nm and low-dimensional peaks at 402 nm and 430 nm, indicating the formation of a similar quasi-2D phase composition.
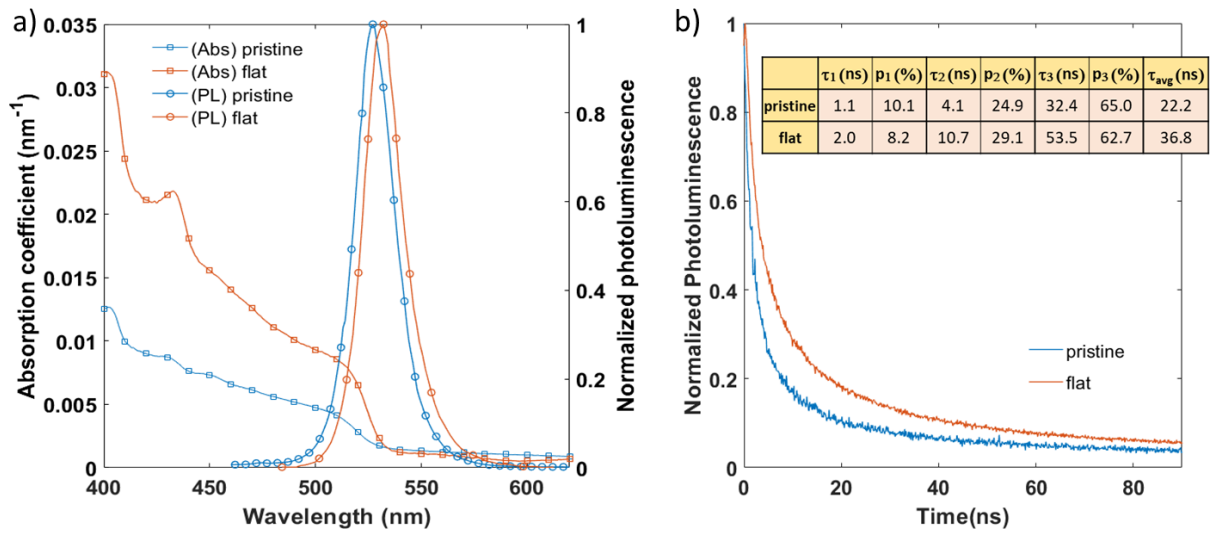
Figure IV.8. Comparison of optical properties between non-imprinted and flat-imprinted perovskite films on PEDOT:PSS-coated glass substrates: a) UV-Vis absorption coefficients and PL spectra and b) Time-resolved PL decay. The inset shows the fitting parameters of the samples' PL lifetime using the tri-exponential model.

	τ_1 (ns)	p_1 (%)	τ_2 (ns)	p_2 (%)	τ_3 (ns)	p_3 (%)	τ_{avg} (ns)
pristine	1.1	10.1	4.1	24.9	32.4	65.0	22.2
flat	2.0	8.2	10.7	29.1	53.5	62.7	36.8

Concerning the steady-state PL spectra (Figure IV.8.a), we can observe a redshift of around 5 nm when mechanically pressing the perovskite surface. This finding can be attributed to the increase in the vertical compactness of the emissive films (as evidenced by the reduced thickness), which facilitates the funneling of optically excited charge carriers from the low-*n* to the high-*n* domains. Furthermore, such compression helps improve the confinement of excitons within the emissive layer, characterized by the increase in the overall PL lifetime and particularly the radiative-recombination-associating τ_3 component of the imprinted perovskite compared to the neat sample, as seen in Figure IV.8.b.

b. Effect of nanopatterning on the characteristics of perovskite thin films

Figure IV.9 illustrates the morphology of a silicon stamp with a lattice constant of 500 nm and the corresponding metasurface based on quasi-2D perovskite. Accordingly, the SEM images show the transposition of the stamp's rod slab into the metasurface's hole slabs. It should be emphasized that even though the metasurface exhibits relatively good morphological quality, as evidenced by the clear patterns present on the slabs, we can still observe some regions where perovskite material has been inadvertently removed due to the suboptimal silanization of the mold. In addition, the inset of Figure IV.9.b demonstrates the diffraction of light reflected from the perovskite metasurface at the macroscopic scale.
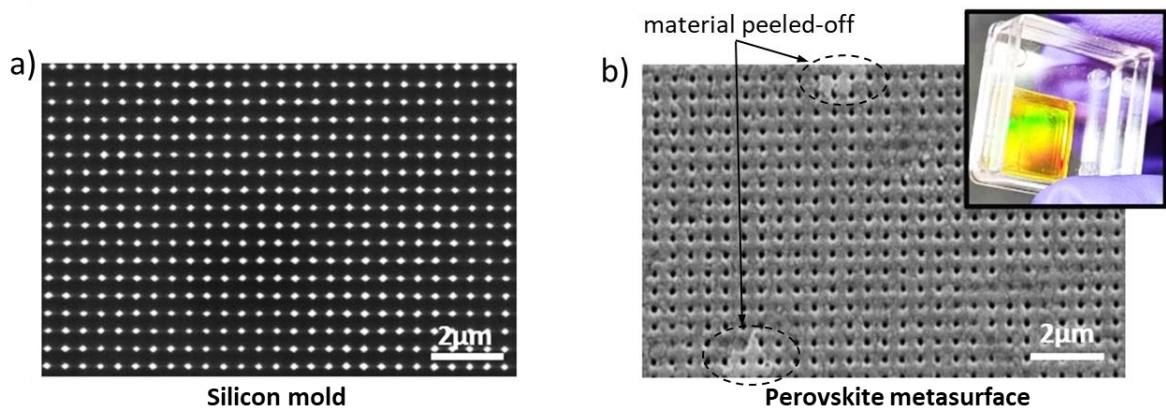
Figure IV.9. SEM images of a) a 500 nm-lattice silicon mold and b) the corresponding perovskite surface after nanoimprint (Inset: Optical image of the perovskite sample).

Next, we examined the angle-resolved emission properties of the perovskite metasurface in comparison to an unpatterned sample (i.e., a perovskite thin film imprinted using a flat mold), employing micro-photoluminescence measurement (see Annex 1.3.b). As can be seen from Figures IV.10. a and b, in both cases, the data shows a robust omnidirectional emission in the green region, which is expected for the low-dimensional bromide perovskite. However, a two-fold increase in the maximum PL intensity when changing from the flat surface to the metasurface is evidence of the enhanced light extraction due to the employment of periodic corrugation. Furthermore, in the case of the perovskite metasurface, one can notice a remarkable broadening of the emission spectrum, together with a blueshift of about 5 nm in the peak emission wavelength and resonant modes beyond the PL emission wavelengths, which can be attributed to strong cavity resonances inside the photonic crystals. These results align with the observations regarding the optical behaviors of MAPB-based metasurface reported in Dr. Mermet-Lyaudoz's thesis [205].
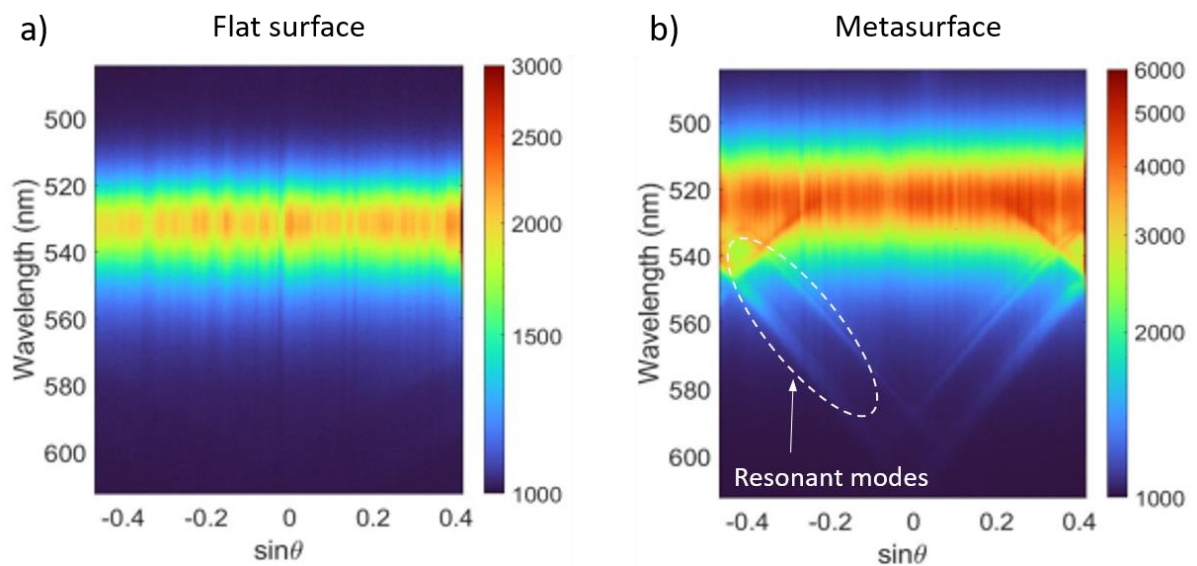
Figure IV.10. Angle-resolved PL measurement of a) unpatterned and b) patterned perovskite thin films.

It is worth emphasizing that the extent of the material detachment issue mentioned above remains insignificant and does not lead to severe effects on the optical properties of the metasurface. Nevertheless,

as we will demonstrate in the subsequent sections, the silanization problem is poised to pose considerable challenges in the fabrication of the perovskite metadevices.

4.3 Fabrication and characterization of metasurface-driven PeLEDs

In general, the device configuration, energy alignment, and fabrication process for metasurface-driven PeLEDs are similar to those of unpatterned devices introduced in Chapter 2. A sketch of the metadevice prototype can be found in Figure IV.11.a. The only difference in the fabrication of the metadevices is an additional step of imprinting the photonic patterns on the perovskite surfaces before depositing the top layers, which fundamentally follows the patterning procedure detailed in Section 4.2.2. Specifically, in order to adapt the technique to be of the right size for XLIM's substrate layout, an 8.6 mm x 8.6 mm mold was cut from the master mold and carefully aligned to cover the active regions of all four PeLED pixels on the substrate (see Figure IV.11.b). An example of nanopatterned PeLEDs, with the imprint area observable via the diffracted light on the substrate surface, is presented in Figure IV.11.c.
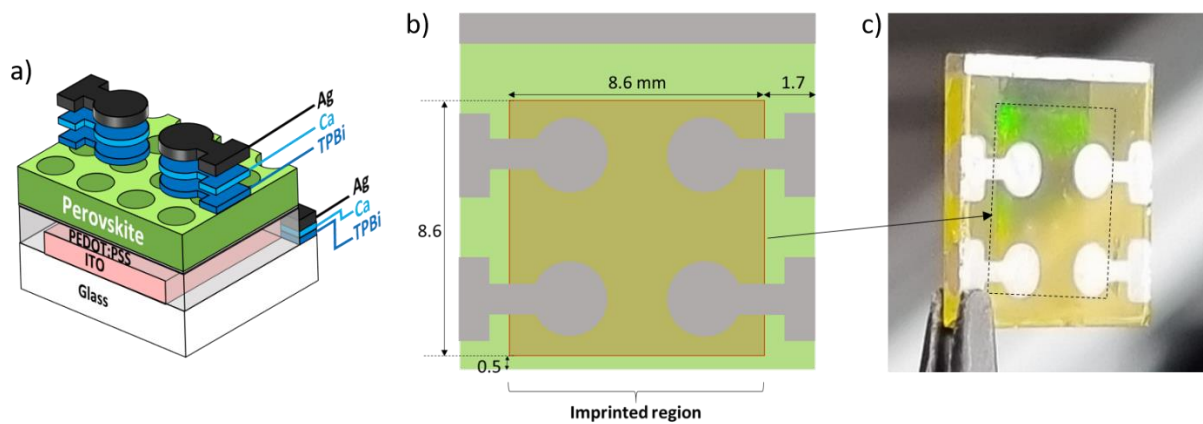
Figure IV.11. Metasurface-driven PeLED: a) Schematic illustration, b) Substrate layout, c) A practical device.

4.3.1 Difficulties in fabricating metasurface-driven PeLEDs

Before examining the electroluminescence performance of these metasurface-driven PeLEDs, we find it appropriate to discuss the challenges we had to confront while developing these innovative devices.

The first difficulty is obtaining a technique to effectively control the imprint parameters for consistently reproducing high-quality perovskite metasurfaces. Accordingly, about half of the substrates subjected to the manual imprinting and a third of those imprinted using the automated system were broken. In nanoimprint lithography, the substrate damages originate from several factors, including:

- Excessive imprint pressure: The manual thermal press did not provide a mechanism for precise control of the applied mechanical pressure and often led to situations where operators inadvertently applied excessive pressure. This issue could only be resolved when we changed to the automated nanoimprint system.

- Misalignment between substrate and mold: As in the prior case, this problem mainly occurred when using the manual imprint, as placing the mold onto the substrate needs to be conducted manually. In the least severe scenario, the misalignment results in incomplete patterning, as

illustrated in Figure IV.12.a; however, in certain specific cases, it has the potential to cause substrate or mold damage due to non-uniform compression.

- Inadequate mold or sample's surface quality: Given that the imprinting process took place within an ambient environment, the presence of dust particles, surface irregularities, or sharp edges on either the substrate or the mold could be observed. These elements can lead to a concentration of stress in specific localized areas and subsequently increase the risk of breaking the substrates. Furthermore, the quality of the imprint stamp could degrade gradually after each use, leading to imperfections in the patterns being transferred onto the material. For example, Figure IV.12.b shows a mold employed for the fabrication of patterned PeLEDs in this study, with the surface having been critically damaged due to repeated contact with the material and operators' improper handling.
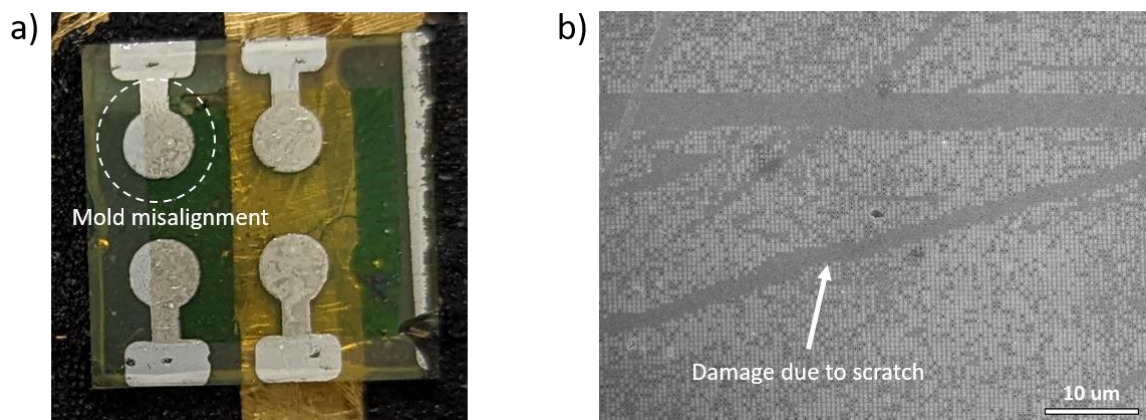
Figure IV.12. a) Incomplete patterning due to mold-substrate misalignment and b) SEM images of a patterning stamp after multiple imprint cycles.

Then, of the samples that survived these imprint processes, we recorded a notably high incidence of devices exhibiting short-circuit current. For example, when examining devices nanoimprinted using the manual thermal press, there were 6 out of 12 devices imprinted with the 500 nm-lattice mold encountering electrical short. This number for the flat mold was 2 over 4. The situation significantly improved when we transitioned to using the automated nanoimprint lithography system, as evidenced by the remarkable reduction in the number of patterned devices with severe current leakage (only 3 out of 14 devices). On one hand, this observation emphasizes the advantages of using the automated system to improve the reliability of the nanostructure fabrication. On the other hand, it indicates the susceptibility of the nanoimprint lithography method to manufacturing defects.

Besides the mold-substrate misalignment or the surface irregularities mentioned above, another issue we repeatedly observed was the detachment of perovskite materials from the imprint surface, with subsequent adhesion onto the silicon stamp upon mold-substrate separation. To clarify the obstacles concerning this demolding process, Figure IV.13 shows a notable case of substantial perovskite patches sticking onto the mold surface, resulting in an incomplete transfer of patterns as well as a formation of non-uniform, deficient emissive layers. The underlying cause of this issue could be traced to the poor

hydrophobic silane coating of the silicon stamps, and although we have attempted several strategies to improve the anti-sticking property of the molds (such as carefully cleaning the molds after each imprint, increasing the silanization treatment time, or utilizing different anti-adhesion solutions), it remains challenging for us to resolve completely. More importantly, this sustaining problem can affect the integrity of the patterning at different levels. On the nanometer scale, the peeling-off phenomenon precipitates distortions in the photonic geometry, which might only introduce minor impacts on the device's performance. On the scale from hundreds of nanometers to a few micrometers, the surface areas where the material is detached will act as surface defects, thereby potentially initiating leakage channels. When these areas extend to hundreds of micrometers or larger, the leakage will become catastrophic, causing the devices to short-circuit. Markedly, while this limitation may not significantly impede the optical characterization of the perovskite metasurfaces, it becomes considerably more vital when the objective is to fabricate PeLEDs. This is because, unlike the micro-PL measurement which is adjustable to target specific and small areas with complete patterning, PeLED demonstration is much less flexible since the position of the pixels on the substrates is predetermined.
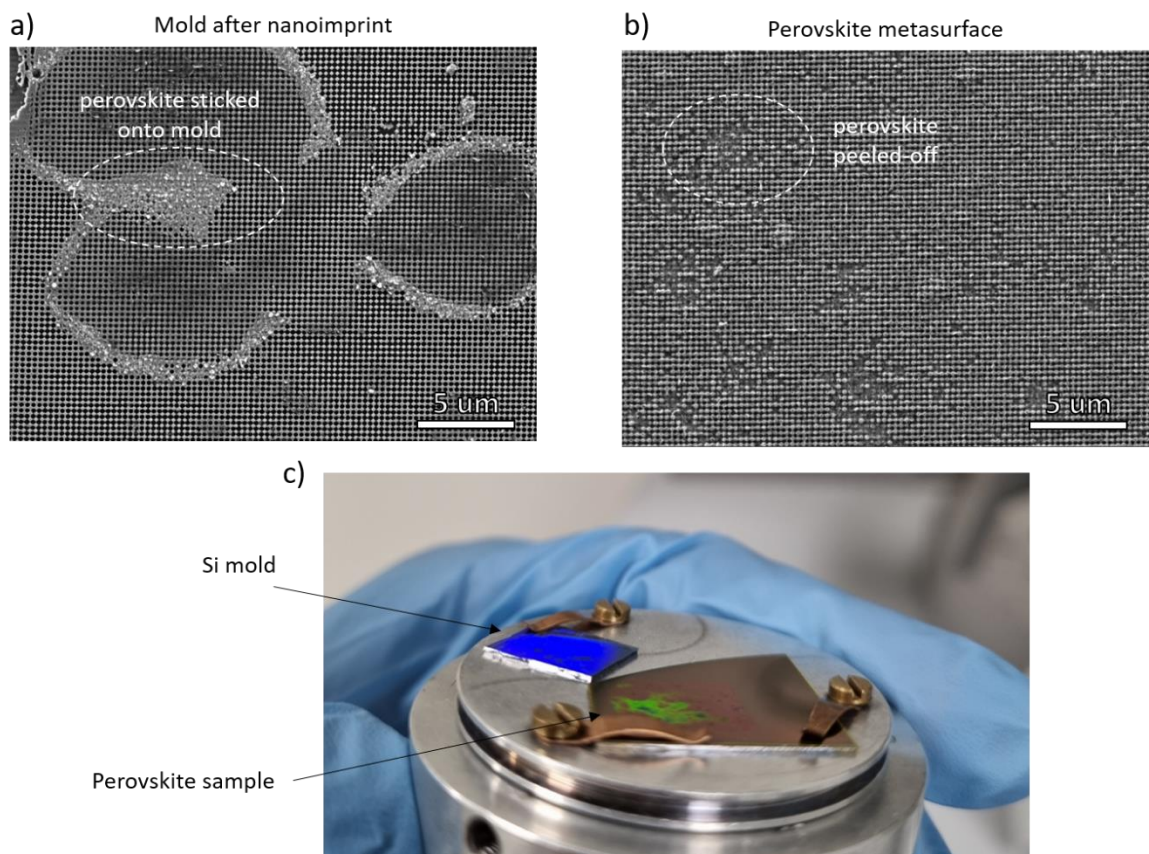
Figure IV.13. Silanization issue in fabricating nanostructures on perovskite thin films: SEM images of a) silicon mold after nanoimprint and b) nanoimprinted perovskite film; and c) Optical images of silicon mold (blue) and perovskite sample (green) after nanoimprint.

Another challenge that needs to be mentioned is the degradation of the emissive and transporting layers during the interfacility transportation of the samples between XLIM and INL. As mentioned earlier, it was necessary to realize the deposition of the bottom layers (i.e., ITO etching, deposition of PEDOT:PSS and LiF) at XLIM prior to the shipment of samples to INL, where the perovskite deposition

and nanoimprint procedure was conducted. After the nanostructuration of perovskite layers at INL, the patterned samples will be returned to XLIM to deposit the top layers (i.e., TPBi, Ca, and Ag). The entire process could span a minimum period of two weeks, raising concern about the degradation of the perovskite and LiF layers as they are known for being susceptible to ambient atmosphere, even when the samples were packed under soft vacuum conditions.

Furthermore, it is essential to remark that the imprint process was carried out in an ambient atmosphere. As consistently demonstrated in this thesis, the quality of layered perovskite thin films and the PeLEDs derived from them are notably influenced by external factors during the crystallization process. These factors include temperature, oxygen and humidity levels, and residual solvent vapors, which are challenging (if not impossible) to regulate when operating in standard room conditions.

To summarize, the issues of mold and substrate quality, pressure and alignment control, along with transportation risk and operator skill, proved to be substantial obstacles significantly slowing down the progression of our research as we had to spend more time troubleshooting and attempting to replicate previous results.

4.3.2 Characterization of metasurface-driven PeLEDs

a. Performance of nanostructured PeLEDs fabricated with manual thermal press

The first data set that needs to be examined is from the devices imprinted using the Rondon Thermal Press. Figure IV.14 depicts the changes in PeLEDs' performance with and without the photonic structure. Considering the L-V curve, we can observe that the nanostructuration does not have an apparent effect on the EL intensity of the PeLEDs as it should have been expected for light extraction enhancement. In contrast, employing the metasurface tends to increase the turn-on voltage of the devices. For instance, the unpatterned devices start light emission at approximately 3 V, corresponding to the turn-on voltage of standard quasi-2D PeLEDs, while the nanopatterned PeLEDs operate at higher voltage bias, such as V_{ON} = 4.5 V. This observation can be attributed to the increased energy barrier for radiative recombination due to the heterogeneous injection of charge carriers at the interface between the perovskite metasurface and the charge transfer layers, as depicted in Figure IV.14.b. In addition, other possible contributors such as charge trapping at the photonic slabs or imperfections in the nanopatterning should not be excluded; however, it is difficult to quantify the extent of their impacts.
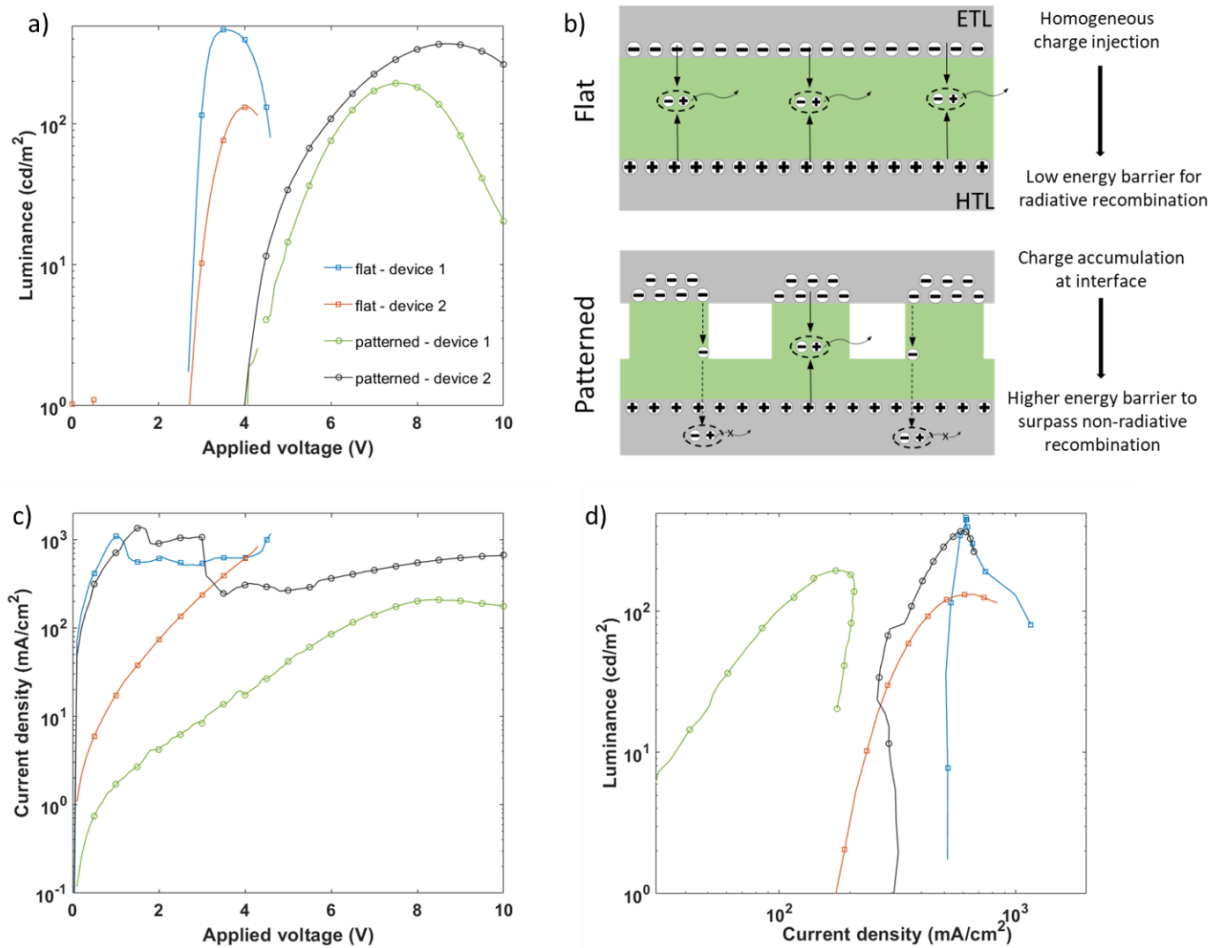
Figure IV.14. Comparison of device performance between flat versus patterned PeLEDs: a) L-V curves, b) Schematics of charge injection at the interfaces, c) J-V curves, and d) L-J curves. The plots show the data of the two best devices in each case.

From the diode perspective (J-V curves), there is no clear trend between the nanostructuration and the dynamic range of the PeLEDs. However, a significant current at low applied voltage can be noticed in all devices, indicating a critical leakage issue due to the demolding issue in the thermal imprint process. As a result, the imprinted (either flat or patterned) PeLEDs need a remarkably high charge injection in order to effectively emit light ($J > 100$ mA/cm^2), as evidenced in the L-J plots. To remind, the current density at 10 cd/m^2 for standard non-imprinted devices varies only around 10 mA/cm^2. In addition, between the flat and metasurface cases, those with planar interfaces appear to be more severely affected by this issue, characterized by the high current density of ~1,000 mA/cm^2 at the turn-on voltage. This finding implies the more critical anti-sticking problem in the flat stamps.

Then, Figure IV.15.a demonstrates the correlation between the EQE and the current injection in the imprinted PeLEDs. In particular, the highest recorded EQE values stood at 0.02% and 0.035%, respectively, for flat and metasurface-driven devices, which is one order of magnitude lower than those observed in the reference devices using pristine perovskite thin films (showed in Chapter 2). This decrease in efficiency is a consequence of the low EL intensity and high current leakage. Besides, we measured the operational stability of a patterned PeLED, as depicted in Figure IV.15.b, which demonstrates a lifetime of roughly 35 seconds. Intriguingly, this data is comparable to the lifetime of the pristine PeLEDs,

suggesting that the imprinted perovskite follows similar degradation mechanisms as their unaltered counterparts.
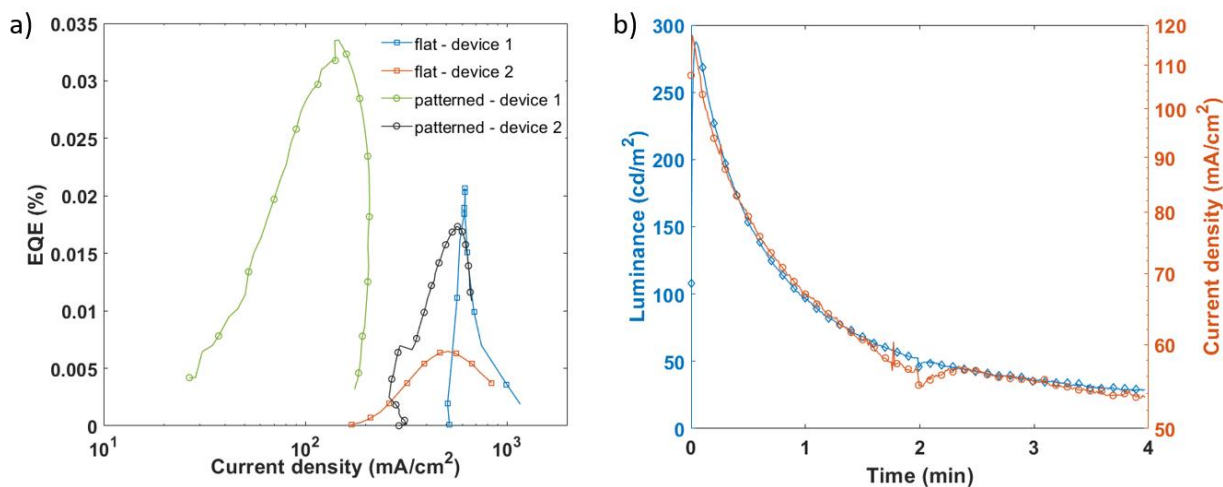
Figure IV.15. a) Comparison of EQE in flat and patterned PeLEDs and b) Evolution of luminance and current density by time in patterned PeLEDs.

b. Performance of nanostructured PeLEDs fabricated with automated nanoimprint lithography

Concerning the fabrication of metasurface-driven PeLEDs using the advanced NPS300 system, we realized two device batches. As mentioned previously, one of the primary difficulties when processing the metasurface with this automated system was transporting the samples between two distant locations. Consequently, in our overall approach, we attempted to minimize the temporal gap between the initial thin film deposition and the subsequent imprint steps as much as possible. For instance, in the case of the first batch, the interval was extended for approximately 24 hours (e.g., the imprint lithography was conducted the day after the film deposition). For the subsequent batch, this interval was reduced to 1.5 hours.

Batch 1: Time gap of 24 hours

For this first batch, we attempted to fabricate 4 reference devices using the flat mold and 8 devices using the patterned mold. However, none of the reference devices functioned as intended due to substrate damage incurred during thermal imprinting. Similarly, among the nanostructured PeLEDs, 3 devices sustained breakage. Consequently, we were left with 5 metasurface-driven devices for further characterization. Accordingly, the J-L-V curves of these surviving devices are presented in Figure IV.16. It is clear that the imprinted PeLEDs in this batch exhibited an inefficacy in emitting light, evidenced by the minimal values of emission intensity. In addition, the electrical currents passing through these devices remained relatively low, even at high bias voltages, suggesting that current leakage is not a major contributor to insufficient electroluminescence. Therefore, we can deduce that the primary cause for the underperformance of these prototypes lies in the degradation of the emissive layer, which is exacerbated by the significant time gap between the deposition and the imprint processes.
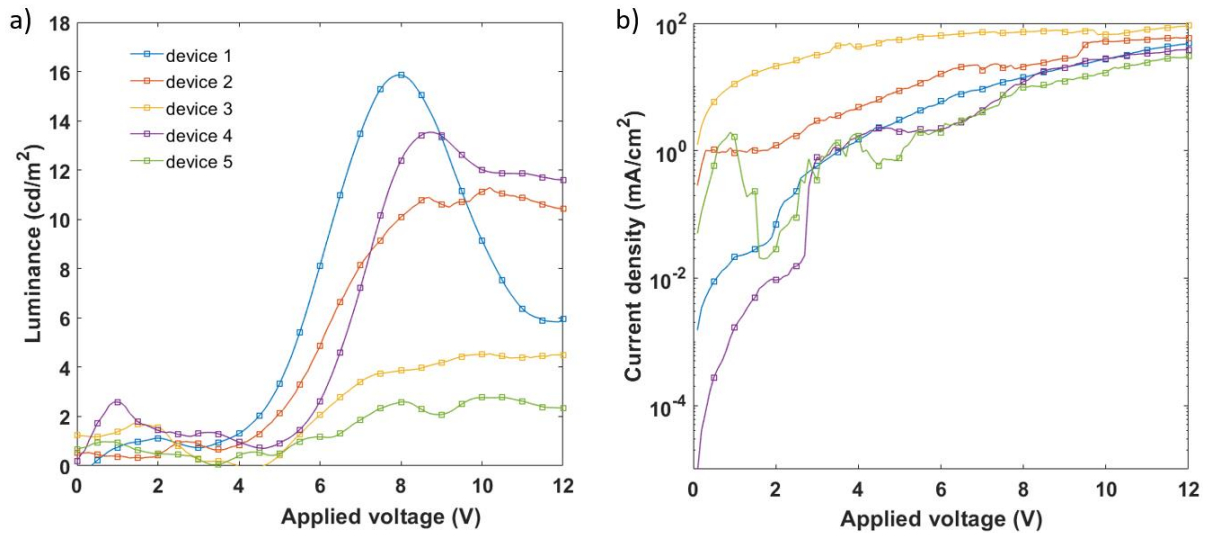
Figure IV.16. Device performance of the metasurface-driven PeLEDs fabricated in the first batch:
a) L-V and b) J-V curves.

<u>*Batch 2: Time gap of 1.5 hours*</u>

Figure IV.17 demonstrates the characteristic curves of the best PeLEDs among a batch of 12 flat samples (of which 4 were broken) and 16 patterned samples (6 broken). Foremost, it is essential to mention the poor performance of the flat devices within this batch, such as the exceptionally low brightness of < 40 cd/m^2. These results were unexpected given that, according to previous data, they should have exhibited performance levels comparable to standard PeLEDs (i.e., luminance of $\sim$ 1,000 cd/m^2). For example, the luminance of the flat devices imprinted with the manual thermal press reached 500 cd/m^2, as observed in Section 4.3.2.a. Subsequently, it became evident to us that the failure in the production of the flat PeLEDs in this batch stemmed from the poor execution of the nanostructuring process and a further investigation into the root causes of this problem would be required in the upcoming period.
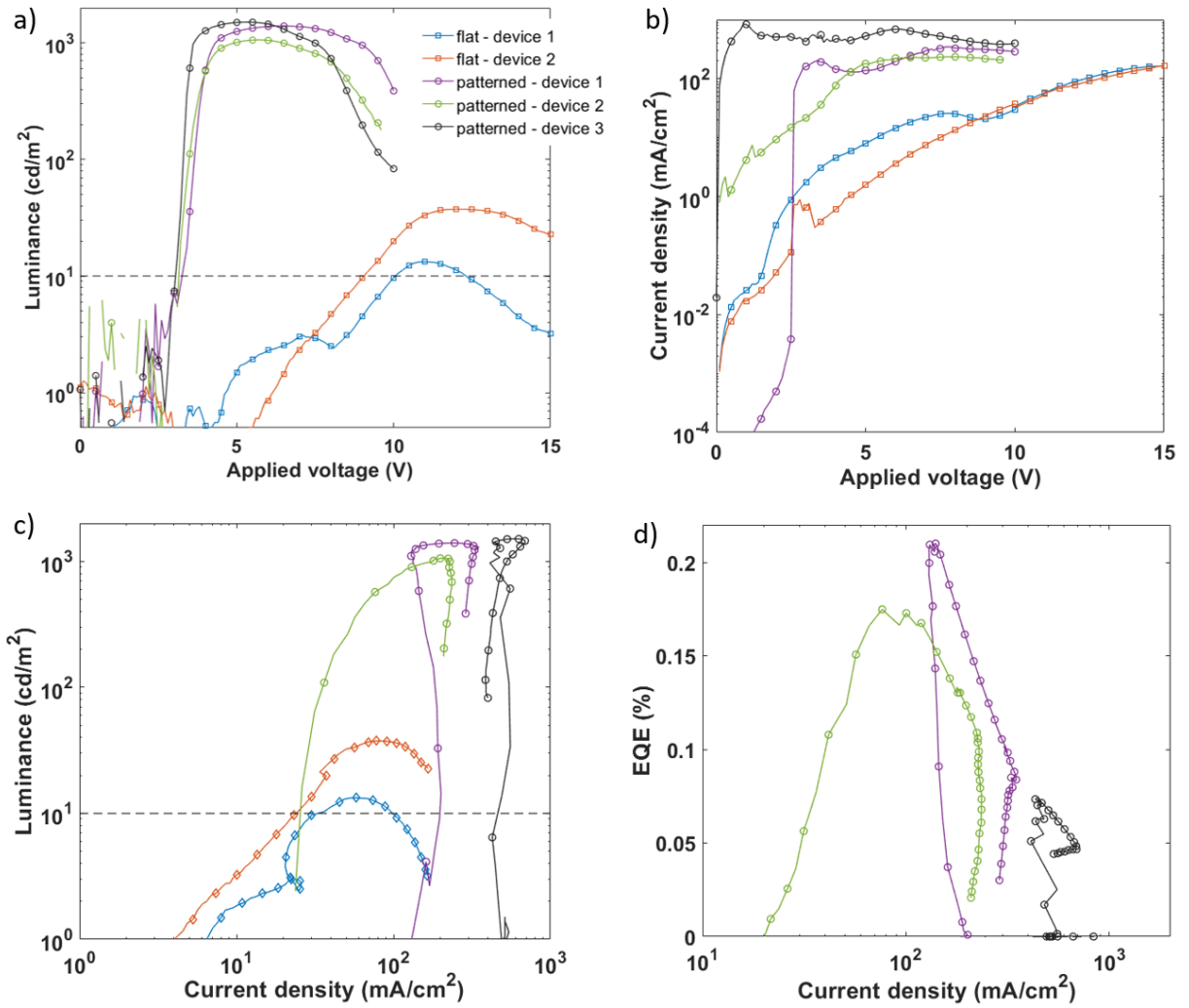
Figure IV.17. Device performance of the flat and metasurface-driven PeLEDs fabricated in the second batch: a) L-V curves, b) J-V curves, c) L-J curves, and d) EQE-J curves.

Focusing on the metasurface-driven PeLEDs, it is generally observed that their EL characteristics were noticeably improved compared to the previous batch or those manually patterned. Indeed, all three patterned samples exhibited a relatively robust luminance level of ~ 1,000 cd/m^2 and a low turn-on voltage of 3 V, as evidenced in the L-V curves. It is even more interesting when examining the electrical properties of the device. Specifically, we can see that in the low bias regime (applied voltage < 3V), the diodes' behavior is predominantly influenced by substantial leakage currents (as depicted in Figure IV.17.b). Such leakage originates from defects on the perovskite surface upon the nanostructuration. However, once the bias voltage surpasses a certain threshold (~ 3 V), enabling it to bypass the energy barrier posed by the electronic nature of the emissive semiconductor as well as the interfaces between the emissive and transporting layers, the injected charge carriers recombine and emit photons quite effectively, characterized by the low voltage at maximum luminance (~ 5 V) and the vertical L-J curves. With respect to the power conversion efficiency, these prototypes recorded a maximum EQE value of 0.2%, with typical roll-off effects. In addition, it is worth noting that, without having a reliable flat PeLED as a reference, it is difficult to evaluate the outcoupling efficiency or the effects of charge accumulation on the performance of the patterned PeLEDs in this case.

Next, we characterized the spectral properties of the EL from the metasurface-driven PeLEDs. As illustrated in Figure IV.18.a, the emission spectrum exhibits a peak at 531 nm and an FWHM of 24 nm. To compare, these metrics for neat quasi-2D PeLEDs are 520 nm and 26 nm, respectively, as previously presented in Chapter 2. These findings suggest no discernible spectral enhancement in the devices employing perovskite metasurfaces, as opposed to the observed PL enhancement exhibited by the metasurfaces themselves. Besides, the shifting of the EL emission peak when nanostructuring the emissive surface can be attributed to several factors, including: 1) the photonic effect arising from the coupling of emitted light and photonic structure, 2) the changes in the morphology of the perovskite materials subjected to the thermal imprint, and 3) the modification of charge injection landscape at the interfaces between the emissive and transport layers. Unfortunately, because of the time constraints within the scope of this thesis, we did not have enough time to continue our experimentation to precisely determine the contribution of each of these factors to this phenomenon. Therefore, an in-depth study will be necessary in the next stage of the project to comprehensively address these issues.
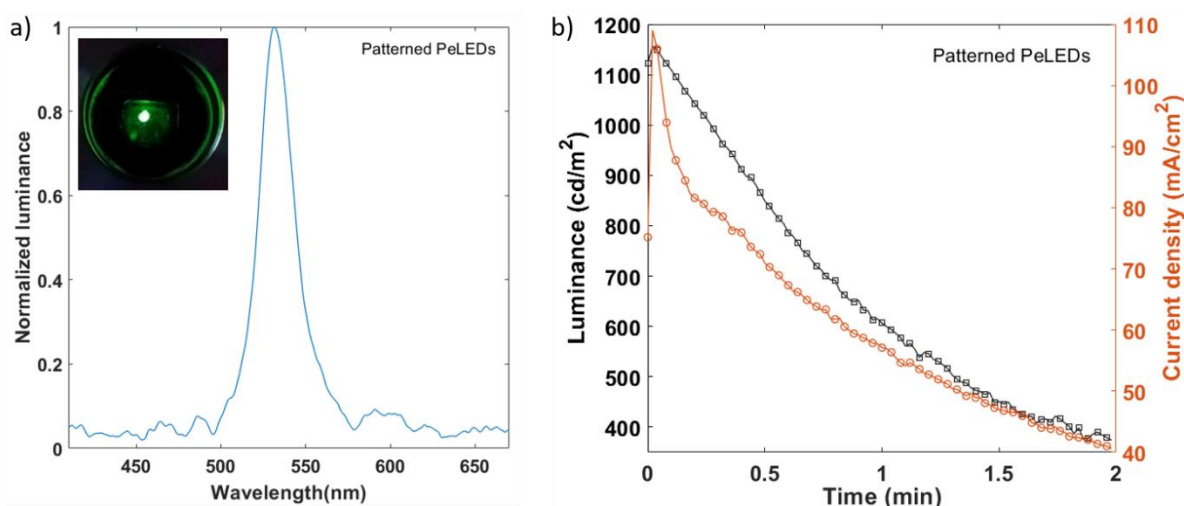
Figure IV.18. a) Electroluminescence spectrum (Inset: an optical image of a working prototype) and b) Operational stability of nanopatterned PeLEDs.

Lastly, Figure IV.18.b demonstrates the degradation in the emission intensity and current density of the patterned PeLEDs as a function of the operational duration. Quite interestingly, the device lifetime T_{50} exceeded 1 minute, which is a slight improvement compared to the non-imprinted PeLEDs (whose lifetime reaches only 30 seconds). This result is remarkable given the potential presence of defects from the nanoimprint process and the high current injection regime in which the device operates, and it suggests an enhancement in the structural stability of the low-dimensional perovskite material thanks to the compression treatment.

In summary, our study has achieved electroluminescence from perovskite metasurfaces, proving the capability to attain meaningful emission intensity and efficiency, with values reaching 1,000 cd/m^2 and 0.2%, respectively. Additionally, the obstacles constraining the realization of such imprinted metadevices, particularly those inherent to the imprinting process, have been thoroughly pointed out.

However, on the downside, it is necessary to admit that the hypothetical enhancement in light outcoupling has not been conclusively demonstrated in this work.

4.4 Summary and outlook

a. Summary

In this chapter, we have systematically studied the innovative strategy of improving the light extraction efficiency in PeLEDs via nanostructuring of the perovskite emissive layers.

Primarily, a design of 2D photonic structures based on low-dimensional perovskite thin films was proposed using the concept of broken vertical symmetry, together with a careful examination of the thermal nanoimprint lithography technique to effectively realize such metasurface structures in practice. Subsequently, we focused on the impacts of the thermal press processes on the properties of the perovskite thin films. Our results demonstrated that the flat-imprinted samples exhibited favorable optical characteristics compared to pristine counterparts, such as higher absorption coefficients or prolonged radiative decay, thanks to the improved compactness of the thin films. Concerning the nanostructure-imprinted perovskite films, the results were even more interesting as we observed a noticeable improvement in the photon extraction of these emissive layers, characterized by a two-fold enhancement in maximum PL intensity, a broadened emission spectrum, and resonant modes in the angle-resolved PL mapping.

We then attempted to integrate the imprinted perovskite layers into our PeLED structure but quickly realized the challenges constraining the fabrication of our hypothetical devices. In particular, one major challenge concerned the effective control of the imprint processes (e.g., imprint conditions, pressure application, mold-substrate alignment, demolding, substrate or mold contamination), in which the demolding issue and the degradation of the imprint mold's quality proved to be the most problematic to resolve. Another uncertainty we encountered was the transportation of samples between XLIM and INL, as it risked deteriorating the samples during transit. Despite these obstacles, we managed to fabricate several batches of PeLED prototypes employing nanostructured emissive layers. By comparing the EL performance of the samples among these batches, the importance of utilizing an automated nanoimprint system with comprehensive control over the patterning process becomes more evident. As a result, the first milestone of demonstrating operational PeLEDs (luminance of 1,000 cd/m^2, EQE of 0.2 %, T$_{50}$ of about 1 minute) with perovskite metasurface was achieved, despite that expected enhancement in light extraction has not been observed. Subsequently, this study paves the way for us to further progress the development of ultra-high-efficiency PeLEDs using emissive perovskite metasurface in the upcoming period.

b. Outlook

For future work, we plan to devise a more comprehensive strategy to incorporate the perovskite metasurface into the PeLEDs, aiming to address the existing limitations:

i) Enhancement of the imprint stamp's quality: This enhancement will encompass a multifaceted approach, which not only involves the optimization of the silanization process but also implies a revision of the master mold designs. Current limitations stem partly from the difference in the dimensions between the molds and the substrates, in which the smaller size of the imprint stamps may induce non-uniform compression and thereby risk breaking the substrates. A potential solution to this problem lies in the manufacturing of new molds that closely match the dimensions of the PeLEDs' glass substrate. Regrettably, we faced a significant time constraint during this thesis to proceed with this approach.

ii) Realization of flat and patterned devices on the same substrates: After facing many failures in fabricating and comparing patterned PeLEDs with separated flat devices, we determined that a reliable comparative analysis of the impacts of the nanostructuration on the emission behaviors of the PeLEDs could only be conducted when the patterned and control devices are from the same substrates (as illustrated in Figure IV.19). However, this task will demand a meticulous design of the mold patterning and will need to be synchronized with the previous task, thereby requiring close coordination between XLIM and INL.
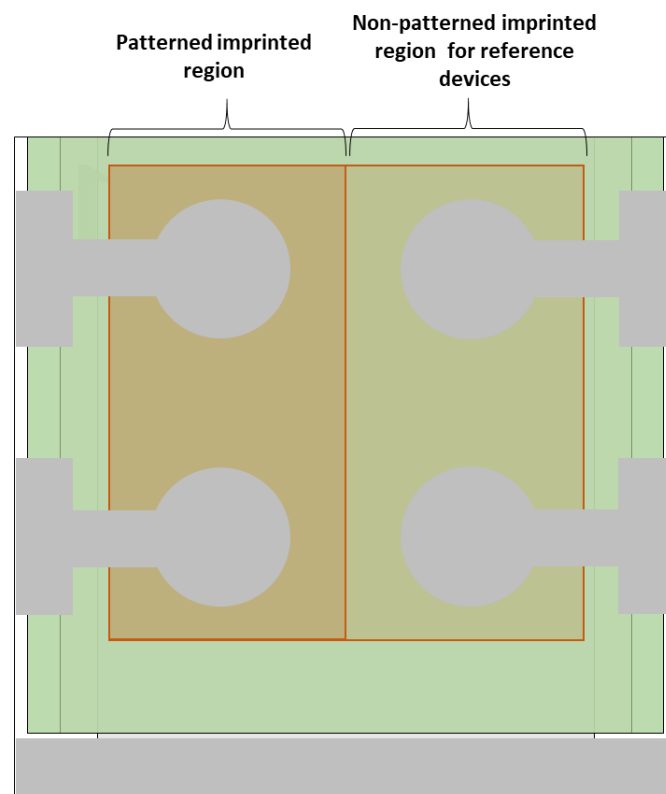
Figure IV.19. Substrate layout with patterned and flat imprinted regions.

iii) Characterization of the emission pattern with angle-resolved electroluminescence measurement: Central to our future investigations will be the characterization of emission patterns exhibited by metasurface-driven PeLEDs, as it will provide insights into the coupling dynamics of emitted light with the photonic crystals. An intricate understanding of this phenomenon is crucial for the evaluation of outcoupling efficiency and the optimization of photonic design. However, it is

noteworthy that this task encounters a challenge rooted in the incompatibility of measurement setups between XLIM (who is in charge of characterizing the EL behaviors) and INL (who is in charge of evaluating the emission pattern). To overcome this issue, standardization of PeLED characterization protocols between the two laboratories will be essential.

iv) Realization of flat and patterned devices on the same substrates in the glove box with a small hydraulic press to reduce problems lies to the transport in ambient air.

CONCLUSION

To conclude, this research systematically studied various strategies to develop bright and efficient green PeLEDs using halide perovskites.

In the beginning, we focused on examining the fabrication of PeLEDs based on polycrystalline perovskites, such as 3D methylammonium lead bromide (MAPB) or quasi-2D phenylethylammonium methylammonium lead bromide ($PEA_2MA_{n-1}Pb_nBr_{3n+1}$) thin films. In particular, the deposition of the polycrystalline emissive layers was carefully investigated, with a primary emphasis on the impacts of the perovskite's precursor ratio on the films' morphological and photoluminescent properties. We then entailed a PeLED architecture employing the perovskite thin films as an active layer, in which the quasi-2D perovskites outperformed the 3D counterparts in electroluminescent performance thanks to their favorable surface morphology and efficient energy cascade. Also, our device structure was incorporated with an ultra-thin LiF buffer layer to effectively mitigate interfacial degradation between the hole transfer (PEDOT:PSS). Furthermore, we extended the study to explore the impacts of extraneous variables in perovskite's inert deposition environment (e.g., gloveboxes) on the crystallization of the material and associated device-to-device reproducibility. Accordingly, several factors, including minor variations in residual oxygen and moisture concentration along with undetectable chemical contaminants, were identified, which are often neglected by researchers but can indeed lead to significant variations in the quality of the perovskite thin films. Subsequently, we introduced a set of best practices for perovskite deposition (e.g., regular inertization of the glovebox atmosphere, careful chemical storage and equipment arrangement) to minimize deviation in the performance of our quasi-2D PeLEDs, allowing us to achieve reliable benchmark devices with reasonable performance (luminance > 1,000 cd/m^2, EQE ~ 0.4%, T_{50} of 30 seconds, standard deviation in device-to-device performance of approximately 0.4).

Next, we sought to develop efficient PeLEDs using perovskite quantum dots (QDs) synthesized through a novel soft-chemistry method. In detail, a method for direct deposition of high-quality thin films from colloidal QD solutions was initially studied based on wet-coating techniques. Nonetheless, we discovered the technological challenges inherent to the insufficient wetting properties of the QD's dispersing solvent and the hole transfer layer of the PeLEDs. Consequently, we introduced an original strategy for incorporating perovskite material with highly processable inert polymers, such as polymethyl methacrylate (PMMA) or poly(ethylene oxide) (PEO), to facilitate the processability of the QD solution. By carefully adjusting the ratio between colloidal QD and polymer materials, we succeeded in producing thin composite layers with good surface coverage and homogeneous QD dispersion. As a result, the PeLEDs constructed from these composite materials were realized, showcasing remarkable performance metrics, including a maximum luminance of 5,000 cd/m^2 (in the case of QD/PEO devices) or a maximum external quantum efficiency of 1.4% (for QD/PMMA devices). These results marked the first successful application of soft-chemistry-synthesized perovskite QDs in optoelectronic devices. Although the

performance was promising, the composite PeLEDs exhibited a drawback in operational stability, with a very brief EL lifetime attributed to the electrically-induced instability of the perovskite QDs, charge injection imbalances, and Joule-heating effect. This limitation virtually opens up new opportunities in the future to explore other polymer alternatives with customized functionalities for developing devices with better stability and efficiency.

Lastly, we shifted our focus toward addressing the long-standing challenge of managing light out-coupling in PeLEDs through the nanostructuring of the perovskite emissive layers. Our approach revolved around harnessing the enhanced emissivity of perovskite photonic structures to fabricate PeLEDs with improved light extraction efficiency. Correspondingly, a 2D photonic structure design based on quasi-2D perovskite thin films was proposed utilizing the concept of broken vertical symmetry. We then employed the thermal nanoimprint technique to pattern the metasurface structures practically, observing promising results concerning the photoluminescence enhancement in these nanopatterned perovskite films in comparison to those unimprinted. However, when attempting to integrate these imprinted perovskite layers into PeLED structures, various challenges emerged, particularly in controlling the imprint process and consistently producing high-quality perovskite photonic structures. Besides, the transportation of samples between different locations introduced the risk of sample deterioration. Nevertheless, we managed to fabricate the first PeLED prototypes employing the nanostructured emissive layers. While the conclusive evidence of light-outcoupling enhancement has yet to be observed, the patterned PeLEDs proved to effectively emit light with a luminance of 1,000 cd/m², EQE of 0.2%, and a T_{50} of about 1 minute, laying the foundation for further exploration of this research topic in the future.

BIBLIOGRAPHY

[1]   A. S. Bhalla, R. Guo, and R. Roy, "The perovskite structure—a review of its role in ceramic science and technology," *Materials Research Innovations*, vol. 4, no. 1, pp. 3–26, Nov. 2000, doi: 10.1007/s100190000062.

[2]   "Organometal Halide Perovskites as Visible-Light Sensitizers for Photovoltaic Cells | Journal of the American Chemical Society." Accessed: Feb. 16, 2023. [Online]. Available: https://pubs.acs.org/doi/10.1021/ja809598r

[3]   "CaTiO3 (perovskite) - Solid State Chemistry @Aalto - Aalto University Wiki." Accessed: Feb. 16, 2023. [Online]. Available: https://wiki.aalto.fi/pages/viewpage.action?pageId=165133842

[4]   S. I. Seok and T.-F. Guo, "Halide perovskite materials and devices," *MRS Bulletin*, vol. 45, no. 6, pp. 427–430, Jun. 2020, doi: 10.1557/mrs.2020.140.

[5]   Z. Xiao, Z. Song, and Y. Yan, "From Lead Halide Perovskites to Lead-Free Metal Halide Perovskites and Perovskite Derivatives," *Adv. Mater.*, vol. 31, no. 47, p. 1803792, Nov. 2019, doi: 10.1002/adma.201803792.

[6]   G. Schileo and G. Grancini, "Lead or no lead? Availability, toxicity, sustainability and environmental impact of lead-free perovskite solar cells," *J. Mater. Chem. C*, vol. 9, no. 1, pp. 67–76, Jan. 2021, doi: 10.1039/D0TC04552G.

[7]   S. Krishnamurthy *et al.*, "Organic–inorganic hybrid and inorganic halide perovskites: structural and chemical engineering, interfaces and optoelectronic properties," *J. Phys. D: Appl. Phys.*, vol. 54, no. 13, p. 133002, Jan. 2021, doi: 10.1088/1361-6463/abd0ad.

[8]   R. L. Z. Hoye, J. Hidalgo, R. A. Jagt, J.-P. Correa-Baena, T. Fix, and J. L. MacManus-Driscoll, "The Role of Dimensionality on the Optoelectronic Properties of Oxide and Halide Perovskites, and their Halide Derivatives," *Advanced Energy Materials*, vol. 12, no. 4, p. 2100499, 2022, doi: 10.1002/aenm.202100499.

[9]   R. F. Kahwagi, S. T. Thornton, B. Smith, and G. I. Koleilat, "Dimensionality engineering of metal halide perovskites," *Front. Optoelectron.*, vol. 13, no. 3, pp. 196–224, Sep. 2020, doi: 10.1007/s12200-020-1039-6.

[10]   X. Chen, H. Zhou, and H. Wang, "2D/3D Halide Perovskites for Optoelectronic Devices," *Front. Chem.*, vol. 9, p. 715157, Aug. 2021, doi: 10.3389/fchem.2021.715157.

[11]   X.-K. Liu and F. Gao, "Organic–Inorganic Hybrid Ruddlesden–Popper Perovskites: An Emerging Paradigm for High-Performance Light-Emitting Diodes," *J. Phys. Chem. Lett.*, vol. 9, no. 9, pp. 2251–2258, May 2018, doi: 10.1021/acs.jpclett.8b00755.

[12]   H. Fu, "Dion–Jacobson halide perovskites for photovoltaic and photodetection applications," *J. Mater. Chem. C*, vol. 9, no. 20, pp. 6378–6394, May 2021, doi: 10.1039/D1TC01061A.

[13]   T. M. Koh *et al.*, "Nanostructuring Mixed-Dimensional Perovskites: A Route Toward Tunable, Efficient Photovoltaics," *Advanced Materials*, vol. 28, no. 19, pp. 3653–3661, 2016, doi: 10.1002/adma.201506141.

[14]   L. Zhang *et al.*, "High-performance quasi-2D perovskite light-emitting diodes: from materials to devices," *Light Sci Appl*, vol. 10, no. 1, p. 61, Dec. 2021, doi: 10.1038/s41377-021-00501-0.

[15]   T. Cheng, C. Qin, S. Watanabe, T. Matsushima, and C. Adachi, "Stoichiometry Control for the Tuning of Grain Passivation and Domain Distribution in Green Quasi-2D Metal Halide Perovskite Films and Light-Emitting Diodes," *Adv. Funct. Mater.*, vol. 30, no. 24, p. 2001816, Jun. 2020, doi: 10.1002/adfm.202001816.

[16]   Z. Yuan *et al.*, "Unveiling the synergistic effect of precursor stoichiometry and interfacial reactions for perovskite light-emitting diodes," *Nat Commun*, vol. 10, no. 1, p. 2818, Jun. 2019, doi: 10.1038/s41467-019-10612-3.

[17]   Y. Iso and T. Isobe, "Review—Synthesis, Luminescent Properties, and Stabilities of Cesium Lead Halide Perovskite Nanocrystals," *ECS J. Solid State Sci. Technol.*, vol. 7, no. 1, pp. R3040–R3045, 2018, doi: 10.1149/2.0101801jss.

[18]   A. Dey *et al.*, "State of the Art and Prospects for Halide Perovskite Nanocrystals," *ACS Nano*, vol. 15, no. 7, pp. 10775–10981, Jul. 2021, doi: 10.1021/acsnano.0c08903.

[19]   H. Bhatia, B. Ghosh, and E. Debroye, "Colloidal FAPbBr$_3$ perovskite nanocrystals for light emission: what's going on?," *J. Mater. Chem. C*, vol. 10, no. 37, pp. 13437–13461, 2022, doi: 10.1039/D2TC01373H.

[20] J. M. Richter *et al.*, "Direct Bandgap Behavior in Rashba-Type Metal Halide Perovskites," *Advanced Materials*, vol. 30, no. 52, p. 1803379, 2018, doi: 10.1002/adma.201803379.

[21] V. Sarritzu *et al.*, "Direct or Indirect Bandgap in Hybrid Lead Halide Perovskites?," *Advanced Optical Materials*, vol. 6, no. 10, p. 1701254, 2018, doi: 10.1002/adom.201701254.

[22] N.-G. Park, "Perovskite solar cells: an emerging photovoltaic technology," *Materials Today*, vol. 18, no. 2, pp. 65–72, Mar. 2015, doi: 10.1016/j.mattod.2014.07.007.

[23] J. S. Manser, J. A. Christians, and P. V. Kamat, "Intriguing Optoelectronic Properties of Metal Halide Perovskites," *Chem. Rev.*, vol. 116, no. 21, pp. 12956–13008, Nov. 2016, doi: 10.1021/acs.chemrev.6b00136.

[24] S. Sun *et al.*, "The origin of high efficiency in low-temperature solution-processable bilayer organometal halide hybrid solar cells," *Energy Environ. Sci.*, vol. 7, no. 1, pp. 399–407, Dec. 2013, doi: 10.1039/C3EE43161D.

[25] M. A. Green, A. Ho-Baillie, and H. J. Snaith, "The emergence of perovskite solar cells," *Nature Photon*, vol. 8, no. 7, Art. no. 7, Jul. 2014, doi: 10.1038/nphoton.2014.134.

[26] R. L. Milot *et al.*, "Charge-Carrier Dynamics in 2D Hybrid Metal–Halide Perovskites," *Nano Lett.*, vol. 16, no. 11, pp. 7001–7007, Nov. 2016, doi: 10.1021/acs.nanolett.6b03114.

[27] S. Zhou *et al.*, "Understanding Charge Transport in All-Inorganic Halide Perovskite Nanocrystal Thin-Film Field Effect Transistors," *ACS Energy Lett.*, vol. 5, no. 8, pp. 2614–2623, Aug. 2020, doi: 10.1021/acsenergylett.0c01295.

[28] H. Oga, A. Saeki, Y. Ogomi, S. Hayase, and S. Seki, "Improved Understanding of the Electronic and Energetic Landscapes of Perovskite Solar Cells: High Local Charge Carrier Mobility, Reduced Recombination, and Extremely Shallow Traps," *J. Am. Chem. Soc.*, vol. 136, no. 39, pp. 13818–13825, Oct. 2014, doi: 10.1021/ja506936f.

[29] S. P. Senanayak *et al.*, "Charge transport in mixed metal halide perovskite semiconductors," *Nat. Mater.*, vol. 22, no. 2, Art. no. 2, Feb. 2023, doi: 10.1038/s41563-022-01448-2.

[30] C. Motta, F. El-Mellouhi, and S. Sanvito, "Charge carrier mobility in hybrid halide perovskites," *Sci Rep*, vol. 5, no. 1, Art. no. 1, Aug. 2015, doi: 10.1038/srep12746.

[31] C. C. Stoumpos, C. D. Malliakas, and M. G. Kanatzidis, "Semiconducting Tin and Lead Iodide Perovskites with Organic Cations: Phase Transitions, High Mobilities, and Near-Infrared Photoluminescent Properties," *Inorg. Chem.*, vol. 52, no. 15, pp. 9019–9038, Aug. 2013, doi: 10.1021/ic401215x.

[32] S. Gholipour and M. Saliba, "Bandgap tuning and compositional exchange for lead halide perovskite materials," in *Characterization Techniques for Perovskite Solar Cell Materials*, M. Pazoki, A. Hagfeldt, and T. Edvinsson, Eds., in Micro and Nano Technologies. , Elsevier, 2020, pp. 1–22. doi: 10.1016/B978-0-12-814727-6.00001-3.

[33] E. L. Unger, L. Kegelmann, K. Suchan, D. Sörell, L. Korte, and S. Albrecht, "Roadmap and roadblocks for the band gap tunability of metal halide perovskites," *J. Mater. Chem. A*, vol. 5, no. 23, pp. 11401–11409, Jun. 2017, doi: 10.1039/C7TA00404D.

[34] D. B. Straus and R. J. Cava, "Tuning the Band Gap in the Halide Perovskite CsPbBr3 through Sr Substitution," *ACS Appl. Mater. Interfaces*, vol. 14, no. 30, pp. 34884–34890, Aug. 2022, doi: 10.1021/acsami.2c09275.

[35] Q. A. Akkerman *et al.*, "Tuning the Optical Properties of Cesium Lead Halide Perovskite Nanocrystals by Anion Exchange Reactions," *J. Am. Chem. Soc.*, vol. 137, no. 32, pp. 10276–10281, Aug. 2015, doi: 10.1021/jacs.5b05602.

[36] B. R. Sutherland and E. H. Sargent, "Perovskite photonic sources," *Nature Photon*, vol. 10, no. 5, Art. no. 5, May 2016, doi: 10.1038/nphoton.2016.62.

[37] S. A. Kulkarni, T. Baikie, P. P. Boix, N. Yantara, N. Mathews, and S. Mhaisalkar, "Band-gap tuning of lead halide perovskites using a sequential deposition process," *Journal of Materials Chemistry A*, vol. 2, no. 24, pp. 9221–9225, 2014, doi: 10.1039/C4TA00435C.

[38] "Tin Halide Perovskites: From Fundamental Properties to Solar Cells - Pitaro - 2022 - Advanced Materials - Wiley Online Library." Accessed: Mar. 24, 2023. [Online]. Available: https://onlinelibrary.wiley.com/doi/10.1002/adma.202105844

[39] R. Prasanna *et al.*, "Band Gap Tuning via Lattice Contraction and Octahedral Tilting in Perovskite Materials for Photovoltaics," *J. Am. Chem. Soc.*, vol. 139, no. 32, pp. 11117–11124, Aug. 2017, doi: 10.1021/jacs.7b04981.

[40] J. Xing *et al.*, "Color-stable highly luminescent sky-blue perovskite light-emitting diodes," *Nat Commun*, vol. 9, no. 1, Art. no. 1, Aug. 2018, doi: 10.1038/s41467-018-05909-8.

[41] M. Li *et al.*, "Low threshold and efficient multiple exciton generation in halide perovskite nanocrystals," *Nat Commun*, vol. 9, no. 1, Art. no. 1, Oct. 2018, doi: 10.1038/s41467-018-06596-1.

[42] B. Das, Z. Liu, I. Aguilera, U. Rau, and T. Kirchartz, "Defect tolerant device geometries for lead-halide perovskites," *Mater. Adv.*, vol. 2, no. 11, pp. 3655–3670, Jun. 2021, doi: 10.1039/D0MA00902D.

[43] F. Wang, S. Bai, W. Tress, A. Hagfeldt, and F. Gao, "Defects engineering for high-performance perovskite solar cells," *npj Flex Electron*, vol. 2, no. 1, Art. no. 1, Aug. 2018, doi: 10.1038/s41528-018-0035-z.

[44] S. Bera *et al.*, "Review of defect engineering in perovskites for photovoltaic application," *Materials Advances*, vol. 3, no. 13, pp. 5234–5247, 2022, doi: 10.1039/D2MA00194B.

[45] M. Pratheek, T. Abhinav, S. Bhattacharya, G. K. Chandra, and P. Predeep, "Recent progress on defect passivation in perovskites for solar cell application," *Materials Science for Energy Technologies*, vol. 4, pp. 282–289, Jan. 2021, doi: 10.1016/j.mset.2021.07.003.

[46] G. Kim and A. Petrozza, "Defect Tolerance and Intolerance in Metal-Halide Perovskites," *Adv. Energy Mater.*, vol. 10, no. 37, p. 2001959, Oct. 2020, doi: 10.1002/aenm.202001959.

[47] S. Singh, Laxmi, and D. Kabra, "Defects in halide perovskite semiconductors: impact on photo-physics and solar cell performance," *J. Phys. D: Appl. Phys.*, vol. 53, no. 50, p. 503003, Oct. 2020, doi: 10.1088/1361-6463/abb487.

[48] X. Zhang, M. E. Turiansky, J.-X. Shen, and C. G. Van de Walle, "Defect tolerance in halide perovskites: A first-principles perspective," *Journal of Applied Physics*, vol. 131, no. 9, p. 090901, Mar. 2022, doi: 10.1063/5.0083686.

[49] Y. Lei, Y. Xu, M. Wang, G. Zhu, and Z. Jin, "Origin, Influence, and Countermeasures of Defects in Perovskite Solar Cells," *Small*, vol. 17, no. 26, p. 2005495, 2021, doi: 10.1002/smll.202005495.

[50] W. Li, R. Long, J. Tang, and O. V. Prezhdo, "Influence of Defects on Excited-State Dynamics in Lead Halide Perovskites: Time-Domain ab Initio Studies," *J. Phys. Chem. Lett.*, vol. 10, no. 13, pp. 3788–3804, Jul. 2019, doi: 10.1021/acs.jpclett.9b00641.

[51] T. Hu *et al.*, "Defect Behaviors in Perovskite Light-Emitting Diodes," *ACS Materials Lett.*, vol. 3, no. 12, pp. 1702–1728, Dec. 2021, doi: 10.1021/acsmaterialslett.1c00474.

[52] Y.-H. Kim, H. Cho, and T.-W. Lee, "Metal halide perovskite light emitters," *Proc Natl Acad Sci U S A*, vol. 113, no. 42, pp. 11694–11702, Oct. 2016, doi: 10.1073/pnas.1607471113.

[53] T.-H. Han, K. Y. Jang, Y. Dong, R. H. Friend, E. H. Sargent, and T.-W. Lee, "A roadmap for the commercialization of perovskite light emitters," *Nat Rev Mater*, vol. 7, no. 10, pp. 757–777, Aug. 2022, doi: 10.1038/s41578-022-00459-4.

[54] I. Pelant and J. Valenta, "Channels of radiative recombination in semiconductors," in *Luminescence Spectroscopy of Semiconductors*, I. Pelant and J. Valenta, Eds., Oxford University Press, 2012, p. 0. doi: 10.1093/acprof:oso/9780199588336.003.0005.

[55] X.-K. Liu *et al.*, "Metal halide perovskites for light-emitting diodes," *Nat. Mater.*, vol. 20, no. 1, pp. 10–21, Jan. 2021, doi: 10.1038/s41563-020-0784-7.

[56] I. Pelant and J. Valenta, "Luminescence of excitons," in *Luminescence Spectroscopy of Semiconductors*, I. Pelant and J. Valenta, Eds., Oxford University Press, 2012, p. 0. doi: 10.1093/acprof:oso/9780199588336.003.0007.

[57] K. Tanaka, T. Takahashi, T. Ban, T. Kondo, K. Uchida, and N. Miura, "Comparative study on the excitons in lead-halide-based perovskite-type crystals CH3NH3PbBr3 CH3NH3PbI3," *Solid State Communications*, vol. 127, no. 9, pp. 619–623, Sep. 2003, doi: 10.1016/S0038-1098(03)00566-0.

[58] A. Miyata *et al.*, "Direct measurement of the exciton binding energy and effective masses for charge carriers in organic–inorganic tri-halide perovskites," *Nature Phys*, vol. 11, no. 7, Art. no. 7, Jul. 2015, doi: 10.1038/nphys3357.

[59] P. Kumar, Q. Shi, and K. J. Karki, "Enhanced Radiative Recombination of Excitons and Free Charges Due to Local Deformations in the Band Structure of MAPbBr3 Perovskite Crystals," *J. Phys. Chem. C*, vol. 123, no. 22, pp. 13444–13450, Jun. 2019, doi: 10.1021/acs.jpcc.9b01968.

[60] L. N. Quan, F. P. García de Arquer, R. P. Sabatini, and E. H. Sargent, "Perovskites for Light Emission," *Advanced Materials*, vol. 30, no. 45, p. 1801996, 2018, doi: 10.1002/adma.201801996.

[61] C. Katan, N. Mercier, and J. Even, "Quantum and Dielectric Confinement Effects in Lower-Dimensional Hybrid Perovskite Semiconductors," *Chem. Rev.*, vol. 119, no. 5, pp. 3140–3192, Mar. 2019, doi: 10.1021/acs.chemrev.8b00417.

[62] Y. Wei, "Synthesis and optical properties of self-assembled 2D layered organic-inorganic perovskites for optoelectronics," Ecole Normale Superieure de Cachan, 2012. [Online]. Available: https://theses.hal.science/tel-00905415

[63] Q.-H. Do, "Synthesis and optical properties of low-dimensional layered hybrid perovskites," Cachan, Sep. 2020.

[64] J.-C. Blancon *et al.*, "Scaling law for excitons in 2D perovskite quantum wells," *Nat Commun*, vol. 9, no. 1, Art. no. 1, Jun. 2018, doi: 10.1038/s41467-018-04659-x.

[65] Y.-H. Chang, J.-C. Lin, Y.-C. Chen, T.-R. Kuo, and D.-Y. Wang, "Facile synthesis of two-dimensional Ruddlesden–Popper perovskite quantum dots with fine-tunable optical properties," *Nanoscale Res Lett*, vol. 13, no. 1, p. 247, Aug. 2018, doi: 10.1186/s11671-018-2664-5.

[66] Y. Jiang, J. Wei, and M. Yuan, "Energy-Funneling Process in Quasi-2D Perovskite Light-Emitting Diodes," *J. Phys. Chem. Lett.*, vol. 12, no. 10, pp. 2593–2606, Mar. 2021, doi: 10.1021/acs.jpclett.1c00072.

[67] M. Yuan *et al.*, "Perovskite energy funnels for efficient light-emitting diodes," *Nature Nanotech*, vol. 11, no. 10, pp. 872–877, Oct. 2016, doi: 10.1038/nnano.2016.110.

[68] N. Yantara *et al.*, "Designing Efficient Energy Funneling Kinetics in Ruddlesden-Popper Perovskites for High-Performance Light-Emitting Diodes," *Adv. Mater.*, vol. 30, no. 33, p. 1800818, Aug. 2018, doi: 10.1002/adma.201800818.

[69] H.-S. Kim *et al.*, "Lead Iodide Perovskite Sensitized All-Solid-State Submicron Thin Film Mesoscopic Solar Cell with Efficiency Exceeding 9%," *Sci Rep*, vol. 2, no. 1, Art. no. 1, Aug. 2012, doi: 10.1038/srep00591.

[70] W. Rehman *et al.*, "Charge-Carrier Dynamics and Mobilities in Formamidinium Lead Mixed-Halide Perovskites," *Advanced Materials*, vol. 27, no. 48, pp. 7938–7944, 2015, doi: 10.1002/adma.201502969.

[71] L. Tao *et al.*, "Stability of mixed-halide wide bandgap perovskite solar cells: Strategies and progress," *Journal of Energy Chemistry*, vol. 61, pp. 395–415, Oct. 2021, doi: 10.1016/j.jechem.2021.03.038.

[72] H. Tan *et al.*, "Dipolar cations confer defect tolerance in wide-bandgap metal halide perovskites," *Nature Communications*, vol. 9, no. 1, 2018, doi: 10.1038/s41467-018-05531-8.

[73] T. He *et al.*, "Reduced-dimensional perovskite photovoltaics with homogeneous energy landscape," *Nat Commun*, vol. 11, no. 1, Art. no. 1, Apr. 2020, doi: 10.1038/s41467-020-15451-1.

[74] H. Tsai *et al.*, "High-efficiency two-dimensional Ruddlesden–Popper perovskite solar cells," *Nature*, vol. 536, no. 7616, Art. no. 7616, Aug. 2016, doi: 10.1038/nature18306.

[75] I. C. Smith, E. T. Hoke, D. Solis-Ibarra, M. D. McGehee, and H. I. Karunadasa, "A Layered Hybrid Perovskite Solar-Cell Absorber with Enhanced Moisture Stability," *Angewandte Chemie International Edition*, vol. 53, no. 42, pp. 11232–11235, 2014, doi: 10.1002/anie.201406466.

[76] S. Ghosh, S. Mishra, and T. Singh, "Antisolvents in Perovskite Solar Cells: Importance, Issues, and Alternatives," *Advanced Materials Interfaces*, vol. 7, no. 18, p. 2000950, 2020, doi: 10.1002/admi.202000950.

[77] S.-G. Kim *et al.*, "How antisolvent miscibility affects perovskite film wrinkling and photovoltaic properties," *Nat Commun*, vol. 12, no. 1, Art. no. 1, Mar. 2021, doi: 10.1038/s41467-021-21803-2.

[78] S. Paek *et al.*, "From Nano- to Micrometer Scale: The Role of Antisolvent Treatment on High Performance Perovskite Solar Cells," *Chem. Mater.*, vol. 29, no. 8, pp. 3490–3498, Apr. 2017, doi: 10.1021/acs.chemmater.6b05353.

[79] M. C. López-González *et al.*, "Evaluation of Active Layer Thickness Influence in Long-Term Stability and Degradation Mechanisms in CsFAPbIBr Perovskite Solar Cells," *Applied Sciences*, vol. 11, no. 24, Art. no. 24, Jan. 2021, doi: 10.3390/app112411668.

[80] M. Rai, L. H. Wong, and L. Etgar, "Effect of Perovskite Thickness on Electroluminescence and Solar Cell Conversion Efficiency," *J. Phys. Chem. Lett.*, vol. 11, no. 19, pp. 8189–8194, Oct. 2020, doi: 10.1021/acs.jpclett.0c02363.

[81] H. Li and W. Zhang, "Perovskite Tandem Solar Cells: From Fundamentals to Commercial Deployment," *Chem. Rev.*, vol. 120, no. 18, pp. 9835–9950, Sep. 2020, doi: 10.1021/acs.chemrev.9b00780.

[82] R. Lin *et al.*, "All-perovskite tandem solar cells with improved grain surface passivation," *Nature*, vol. 603, no. 7899, Art. no. 7899, Mar. 2022, doi: 10.1038/s41586-021-04372-8.

[83] X. Luo *et al.*, "Efficient Perovskite/Silicon Tandem Solar Cells on Industrially Compatible Textured Silicon," *Advanced Materials*, vol. 35, no. 9, p. 2207883, 2023, doi: 10.1002/adma.202207883.

[84] "NREL's Best Research-Cell Efficiency Chart," National Renewable Energy Labs (NREL). Accessed: Jul. 30, 2023. [Online]. Available: https://www.nrel.gov/pv/interactive-cell-efficiency.html

[85] H. Zhang, X. Ji, H. Yao, Q. Fan, B. Yu, and J. Li, "Review on efficiency improvement effort of perovskite solar cell," *Solar Energy*, vol. 233, pp. 421–434, Feb. 2022, doi: 10.1016/j.solener.2022.01.060.

[86] H. Wang *et al.*, "A Review of Perovskite-Based Photodetectors and Their Applications," *Nanomaterials*, vol. 12, no. 24, Art. no. 24, Jan. 2022, doi: 10.3390/nano12244390.

[87] X. Hu *et al.*, "High-Performance Flexible Broadband Photodetector Based on Organolead Halide Perovskite," *Advanced Functional Materials*, vol. 24, no. 46, pp. 7373–7380, 2014, doi: 10.1002/adfm.201402020.

[88] H. Gu, S. Chen, and Q. Zheng, "Emerging Perovskite Materials with Different Nanostructures for Photodetectors," *Adv. Optical Mater.*, vol. 9, no. 5, p. 2001637, Mar. 2021, doi: 10.1002/adom.202001637.

[89] L. Fan, Z. Pei, P. Wang, and Z. Zheng, "Research Progress on the Stability of Organic–Inorganic Halide Perovskite Photodetectors in a Humid Environment Through the Modification of Perovskite Layers," *J. Electron. Mater.*, vol. 51, no. 6, pp. 2801–2818, Jun. 2022, doi: 10.1007/s11664-022-09548-0.

[90] Y. Li, Z.-F. Shi, X.-J. Li, and C.-X. Shan, "Photodetectors based on inorganic halide perovskites: Materials and devices*," *Chinese Phys. B*, vol. 28, no. 1, p. 017803, Jan. 2019, doi: 10.1088/1674-1056/28/1/017803.

[91] B. R. Sutherland *et al.*, "Sensitive, Fast, and Stable Perovskite Photodetectors Exploiting Interface Engineering," *ACS Photonics*, vol. 2, no. 8, pp. 1117–1123, Aug. 2015, doi: 10.1021/acsphotonics.5b00164.

[92] T. A. Qasuria *et al.*, "Stable perovskite based photodetector in impedance and capacitance mode," *Results in Physics*, vol. 15, p. 102699, Dec. 2019, doi: 10.1016/j.rinp.2019.102699.

[93] L. He *et al.*, "Highly Sensitive Tin-Lead Perovskite Photodetectors with Over 450 Days Stability Enabled by Synergistic Engineering for Pulse Oximetry System," *Advanced Materials*, vol. 35, no. 10, p. 2210016, 2023, doi: 10.1002/adma.202210016.

[94] T. Sun *et al.*, "High performance p-i-n Perovskite Photodetectors and Image Sensors with Long-term Operational Stability Enabled by Corrosion-resistant TiN Back Electrode," *Nanoscale*, Mar. 2023, doi: 10.1039/D3NR00410D.

[95] L. Mei *et al.*, "Hybrid Halide Perovskite-Based Near-Infrared Photodetectors and Imaging Arrays," *Advanced Optical Materials*, vol. 10, no. 9, p. 2102656, May 2022, doi: 10.1002/adom.202102656.

[96] Z. He *et al.*, "Antisolvent-Treated MAPbI3 and PbS Quantum Dots for High-Performance Broadband Photodetectors," *ACS Appl. Nano Mater.*, vol. 6, no. 2, pp. 1119–1128, Jan. 2023, doi: 10.1021/acsanm.2c04619.

[97] T. Liu, W. Tang, S. Luong, and O. Fenwick, "High charge carrier mobility in solution processed one-dimensional lead halide perovskite single crystals and their application as photodetectors," *Nanoscale*, vol. 12, no. 17, pp. 9688–9695, May 2020, doi: 10.1039/D0NR01495H.

[98] G. Li *et al.*, "High detectivity photodetectors based on perovskite nanowires with suppressed surface defects," *Photon. Res., PRJ*, vol. 8, no. 12, pp. 1862–1874, Dec. 2020, doi: 10.1364/PRJ.403030.

[99] Y. C. Kim *et al.*, "Printable organometallic perovskite enables large-area, low-dose X-ray imaging," *Nature*, vol. 550, no. 7674, Art. no. 7674, Oct. 2017, doi: 10.1038/nature24032.

[100] S. W. Eaton *et al.*, "Lasing in robust cesium lead halide perovskite nanowires," *Proceedings of the National Academy of Sciences*, vol. 113, no. 8, pp. 1993–1998, Feb. 2016, doi: 10.1073/pnas.1600789113.

[101] Z.-K. Tan *et al.*, "Bright light-emitting diodes based on organometal halide perovskite," *Nature Nanotech*, vol. 9, no. 9, pp. 687–692, Sep. 2014, doi: 10.1038/nnano.2014.149.

[102] Y. Bae, J. Ryu, S. Yoon, and D.-W. Kang, "Recent progress in quasi-two-dimensional and quantum dot perovskite light-emitting diodes harnessing the diverse effects of ligands: A review," *Nano Res.*, vol. 15, no. 7, pp. 6449–6465, Jul. 2022, doi: 10.1007/s12274-022-4252-3.

[103] A. Fakharuddin *et al.*, "Perovskite light-emitting diodes," *Nat Electron*, vol. 5, no. 4, pp. 203–216, Apr. 2022, doi: 10.1038/s41928-022-00745-7.

[104] W. Bai *et al.*, "Perovskite Light-Emitting Diodes with an External Quantum Efficiency Exceeding 30%," *Advanced Materials*, vol. n/a, no. n/a, p. 2302283, doi: 10.1002/adma.202302283.

[105] F. Deschler *et al.*, "High Photoluminescence Efficiency and Optically Pumped Lasing in Solution-Processed Mixed Halide Perovskite Semiconductors," *J. Phys. Chem. Lett.*, vol. 5, no. 8, pp. 1421–1426, Apr. 2014, doi: 10.1021/jz5005285.

[106] M. Saliba *et al.*, "Structured Organic-Inorganic Perovskite toward a Distributed Feedback Laser," *Adv Mater*, vol. 28, no. 5, pp. 923–929, Feb. 2016, doi: 10.1002/adma.201502608.

[107] S. Chen, C. Zhang, J. Lee, J. Han, and A. Nurmikko, "High- Q , Low-Threshold Monolithic Perovskite Thin-Film Vertical-Cavity Lasers," *Advanced Materials*, vol. 29, p. 1604781, Feb. 2017, doi: 10.1002/adma.201604781.

[108] H. Zhang *et al.*, "2D Ruddlesden-Popper Perovskites Microring Laser Array," *Adv Mater*, vol. 30, no. 15, p. e1706186, Apr. 2018, doi: 10.1002/adma.201706186.

[109] C. Qin *et al.*, "Stable room-temperature continuous-wave lasing in quasi-2D perovskite films," *Nature*, vol. 585, no. 7823, pp. 53–57, Sep. 2020, doi: 10.1038/s41586-020-2621-1.

[110] S. Li *et al.*, "Water-resistant perovskite nanodots enable robust two-photon lasing in aqueous environment," *Nat Commun*, vol. 11, no. 1, Art. no. 1, Mar. 2020, doi: 10.1038/s41467-020-15016-2.

[111] S. Yakunin *et al.*, "Low-threshold amplified spontaneous emission and lasing from colloidal nanocrystals of caesium lead halide perovskites," *Nat Commun*, vol. 6, no. 1, Art. no. 1, Aug. 2015, doi: 10.1038/ncomms9056.

[112] Q. Zhang, R. Su, X. Liu, J. Xing, T. C. Sum, and Q. Xiong, "High-Quality Whispering-Gallery-Mode Lasing from Cesium Lead Halide Perovskite Nanoplatelets," *Advanced Functional Materials*, vol. 26, no. 34, pp. 6238–6245, 2016, doi: 10.1002/adfm.201601690.

[113] Z. Wu *et al.*, "All-Inorganic CsPbBr3 Nanowire Based Plasmonic Lasers," *Advanced Optical Materials*, vol. 6, no. 22, p. 1800674, 2018, doi: 10.1002/adom.201800674.

[114] T. Wang *et al.*, "Electrically Pumped Polarized Exciton-Polaritons in a Halide Perovskite Microcavity," *Nano Lett.*, vol. 22, no. 13, pp. 5175–5181, Jul. 2022, doi: 10.1021/acs.nanolett.2c00906.

[115] G. S. B. Ganandran, T. M. I. Mahlia, H. C. Ong, B. Rismanchi, and W. T. Chong, "Cost-Benefit Analysis and Emission Reduction of Energy Efficient Lighting at the Universiti Tenaga Nasional," *ScientificWorldJournal*, vol. 2014, p. 745894, 2014, doi: 10.1155/2014/745894.

[116] P. Kusuma, P. M. Pattison, and B. Bugbee, "From physics to fixtures to food: current and potential LED efficacy," *Hortic Res*, vol. 7, no. 1, Art. no. 1, Mar. 2020, doi: 10.1038/s41438-020-0283-7.

[117] P. Morgan Pattison, M. Hansen, and J. Y. Tsao, "LED lighting efficacy: Status and directions," *Comptes Rendus Physique*, vol. 19, no. 3, pp. 134–145, Mar. 2018, doi: 10.1016/j.crhy.2017.10.013.

[118] G. B. Nair and S. J. Dhoble, "Current trends and innovations," *The Fundamentals and Applications of Light-Emitting Diodes*, pp. 253–270, 2021, doi: 10.1016/B978-0-12-819605-2.00010-0.

[119] A. Ren *et al.*, "Emerging light-emitting diodes for next-generation data communications," *Nat Electron*, vol. 4, no. 8, Art. no. 8, Aug. 2021, doi: 10.1038/s41928-021-00624-7.

[120] G. Lozano, "The Role of Metal Halide Perovskites in Next-Generation Lighting Devices," *J. Phys. Chem. Lett.*, vol. 9, no. 14, pp. 3987–3997, Jul. 2018, doi: 10.1021/acs.jpclett.8b01417.

[121] A. Liu, C. Bi, R. Guo, M. Zhang, X. Qu, and J. Tian, "Electroluminescence Principle and Performance Improvement of Metal Halide Perovskite Light-Emitting Diodes," *Advanced Optical Materials*, vol. 9, no. 18, p. 2002167, Sep. 2021, doi: 10.1002/adom.202002167.

[122] M. Koden, "Fundamentals of OLEDs," in *OLED Displays and Lighting*, IEEE, 2017, pp. 12–16. doi: 10.1002/9781119040477.ch2.

[123] H. Cheng, Y. Feng, Y. Fu, Y. Zheng, Y. Shao, and Y. Bai, "Understanding and minimizing non-radiative recombination losses in perovskite light-emitting diodes," *J. Mater. Chem. C*, vol. 10, no. 37, pp. 13590–13610, Sep. 2022, doi: 10.1039/D2TC01869A.

[124] E. F. Schubert, Ed., "LED basics: Electrical properties," in *Light-Emitting Diodes*, 2nd ed., Cambridge: Cambridge University Press, 2006, pp. 59–85. doi: 10.1017/CBO9780511790546.005.

[125] "Performance of OLEDs," in *OLED Displays and Lighting*, John Wiley & Sons, Ltd, 2016, pp. 117–126. doi: 10.1002/9781119040477.ch7.

[126] Laxmi and D. Kabra, "Optimization of Composition with Reduced Phase Impurity in Quasi-2D Perovskite for Electroluminescence," *Adv Photo Res*, vol. 2, no. 6, p. 2000164, Jun. 2021, doi: 10.1002/adpr.202000164.

[127] M. Anaya *et al.*, "Best practices for measuring emerging light-emitting diode technologies," *Nat. Photonics*, vol. 13, no. 12, Art. no. 12, Dec. 2019, doi: 10.1038/s41566-019-0543-y.

[128] Q. Dong, L. Lei, J. Mendes, and F. So, "Operational stability of perovskite light emitting diodes," *J. Phys. Mater.*, vol. 3, no. 1, p. 012002, Jan. 2020, doi: 10.1088/2515-7639/ab60c4.

[129] K. Y. Islam, I. Ahmad, D. Habibi, M. I. A. Zahed, and J. Kamruzzaman, "Green Underwater Wireless Communications Using Hybrid Optical-Acoustic Technologies," *IEEE Access*, vol. 9, pp. 85109–85123, 2021, doi: 10.1109/ACCESS.2021.3088467.

[130] M. F. Ali, D. N. K. Jayakody, and Y. Li, "Recent Trends in Underwater Visible Light Communication (UVLC) Systems," *IEEE Access*, vol. 10, pp. 22169–22225, 2022, doi: 10.1109/ACCESS.2022.3150093.

[131] I. Dursun *et al.*, "Perovskite Nanocrystals as a Color Converter for Visible Light Communication," *ACS Photonics*, vol. 3, no. 7, pp. 1150–1156, Jul. 2016, doi: 10.1021/acsphotonics.6b00187.

[132] E. López-Fraguas *et al.*, "Visible Light Communication system using an organic emitter and a perovskite photodetector," *Organic Electronics*, vol. 73, pp. 292–298, Oct. 2019, doi: 10.1016/j.orgel.2019.06.028.

[133] C. H. Kang *et al.*, "High-speed colour-converting photodetector with all-inorganic CsPbBr3 perovskite nanocrystals for ultraviolet light communication," *Light Sci Appl*, vol. 8, no. 1, Art. no. 1, Oct. 2019, doi: 10.1038/s41377-019-0204-4.

[134] X. Liu *et al.*, "White-Light GaN-μLEDs Employing Green/Red Perovskite Quantum Dots as Color Converters for Visible Light Communication," *Nanomaterials*, vol. 12, no. 4, Art. no. 4, Jan. 2022, doi: 10.3390/nano12040627.

[135] N. A. Merdad *et al.*, "Visible-light communication using thermally evaporated CsPbBr3 perovskite thin films," *AIP Advances*, vol. 13, no. 5, p. 055114, May 2023, doi: 10.1063/5.0147303.

[136] C. M. MacLaughlin, "Opportunities and Challenges in Perovskite-Based Display Technologies: A Conversation with Andrey Rogach and Haibo Zeng," *ACS Energy Lett.*, vol. 4, no. 4, pp. 977–979, Apr. 2019, doi: 10.1021/acsenergylett.9b00647.

[137] H. J. An, M. S. Kim, and J.-M. Myoung, "Strategy for the fabrication of perovskite-based green micro LED for ultra high-resolution displays by micro-molding process and surface passivation," *Chemical Engineering Journal*, vol. 453, p. 139927, Feb. 2023, doi: 10.1016/j.cej.2022.139927.

[138] H. Cho *et al.*, "Overcoming the electroluminescence efficiency limitations of perovskite light-emitting diodes," *Science*, vol. 350, no. 6265, pp. 1222–1225, Dec. 2015, doi: 10.1126/science.aad1818.

[139] S. Lee *et al.*, "Growth of Nanosized Single Crystals for Efficient Perovskite Light-Emitting Diodes," *ACS Nano*, vol. 12, no. 4, pp. 3417–3423, Apr. 2018, doi: 10.1021/acsnano.7b09148.

[140] J. Oh and M.-Y. Ryu, "Effect of Antisolvent Application Volume on CH3NH3PbI3 Films," *Applied Science and Convergence Technology*, vol. 31, no. 1, pp. 28–30, Jan. 2022, doi: 10.5757/ASCT.2022.31.1.28.

[141] S. Sandrez, "Diodes électroluminescentes à base de pérovskites hybrides quasi-2D," These de doctorat, Bordeaux, 2021. Accessed: Jan. 21, 2022. [Online]. Available: http://www.theses.fr/2021BORD0150

[142] S. Lee *et al.*, "Amine-Based Passivating Materials for Enhanced Optical Properties and Performance of Organic–Inorganic Perovskites in Light-Emitting Diodes," *J. Phys. Chem. Lett.*, vol. 8, no. 8, pp. 1784–1792, Apr. 2017, doi: 10.1021/acs.jpclett.7b00372.

[143] H. Su, J. Chen, J. Qin, K. Zhu, and G. Li, "Enhancing the electroluminescence of perovskite light-emitting diodes by optimizing the morphology of perovskite film to suppress leakage current," *Appl. Opt.*, vol. 59, no. 26, p. 7975, Sep. 2020, doi: 10.1364/AO.400296.

[144] Y. Ling *et al.*, "Enhanced Optical and Electrical Properties of Polymer-Assisted All-Inorganic Perovskites for Light-Emitting Diodes," *Adv Mater*, vol. 28, no. 40, pp. 8983–8989, Oct. 2016, doi: 10.1002/adma.201602513.

[145] H. M. Kim, Y. C. Kim, H. J. An, and J.-M. Myoung, "Highly stretchable and contact-responsive light-emitting diodes based on MAPbBr3–PEO composite film," *Journal of Alloys and Compounds*, vol. 819, p. 153360, Apr. 2020, doi: 10.1016/j.jallcom.2019.153360.

[146] Y. C. Kim, Y. Porte, S.-D. Baek, S. R. Cho, and J.-M. Myoung, "High-Performance Green Light-Emitting Diodes Based on MAPbBr3-Polymer Composite Films Prepared by Gas-Assisted Crystallization," *ACS Appl Mater Interfaces*, vol. 9, no. 50, pp. 44106–44113, Dec. 2017, doi: 10.1021/acsami.7b14544.

[147] L. Song *et al.*, "Efficient Inorganic Perovskite Light-Emitting Diodes with Polyethylene Glycol Passivated Ultrathin CsPbBr3 Films," *J. Phys. Chem. Lett.*, vol. 8, no. 17, pp. 4148–4154, Sep. 2017, doi: 10.1021/acs.jpclett.7b01733.

[148] G. Li *et al.*, "Efficient light-emitting diodes based on nanocrystalline perovskite in a dielectric polymer matrix," *Nano Lett*, vol. 15, no. 4, pp. 2640–2644, Apr. 2015, doi: 10.1021/acs.nanolett.5b00235.

[149] J. Byun *et al.*, "Efficient Visible Quasi-2D Perovskite Light-Emitting Diodes," *Adv. Mater.*, vol. 28, no. 34, pp. 7515–7520, Sep. 2016, doi: 10.1002/adma.201601369.

[150] Z. Xiao *et al.*, "Efficient perovskite light-emitting diodes featuring nanometre-sized crystallites," *Nature Photon*, vol. 11, no. 2, pp. 108–115, Feb. 2017, doi: 10.1038/nphoton.2016.269.

[151] M. Luo, Y. Jiang, T. He, and M. Yuan, "Metal halide perovskites for blue light emitting materials," *APL Materials*, vol. 8, no. 4, p. 040907, Apr. 2020, doi: 10.1063/1.5144101.

[152] S. Akin, B. Dong, L. Pfeifer, Y. Liu, M. Graetzel, and A. Hagfeldt, "Organic Ammonium Halide Modulators as Effective Strategy for Enhanced Perovskite Photovoltaic Performance," *Adv Sci (Weinh)*, vol. 8, no. 10, p. 2004593, Mar. 2021, doi: 10.1002/advs.202004593.

[153] X. Yang *et al.*, "Efficient green light-emitting diodes based on quasi-two-dimensional composition and phase engineered perovskite with surface passivation," *Nat Commun*, vol. 9, no. 1, p. 570, Dec. 2018, doi: 10.1038/s41467-018-02978-7.

[154] X. Yang *et al.*, "Effects of Organic Cations on the Structure and Performance of Quasi-Two-Dimensional Perovskite-Based Light-Emitting Diodes," *J. Phys. Chem. Lett.*, vol. 10, no. 11, pp. 2892–2897, Jun. 2019, doi: 10.1021/acs.jpclett.9b00910.

[155] Y. Shang, G. Li, W. Liu, and Z. Ning, "Quasi-2D Inorganic CsPbBr3 Perovskite for Efficient and Stable Light-Emitting Diodes," *Advanced Functional Materials*, vol. 28, no. 22, p. 1801193, 2018, doi: 10.1002/adfm.201801193.

[156] K. Sim *et al.*, "Performance boosting strategy for perovskite light-emitting diodes," *Applied Physics Reviews*, vol. 6, no. 3, p. 031402, Sep. 2019, doi: 10.1063/1.5098871.

[157] Y. Shang *et al.*, "Highly stable hybrid perovskite light-emitting diodes based on Dion-Jacobson structure," *Science Advances*, vol. 5, no. 8, p. eaaw8072, Aug. 2019, doi: 10.1126/sciadv.aaw8072.

[158] Y. Jiang *et al.*, "Reducing the impact of Auger recombination in quasi-2D perovskite light-emitting diodes," *Nat Commun*, vol. 12, no. 1, Art. no. 1, Jan. 2021, doi: 10.1038/s41467-020-20555-9.

[159] M.-K. Wei, C.-W. Lin, C.-C. Yang, Y.-W. Kiang, J.-H. Lee, and H.-Y. Lin, "Emission Characteristics of Organic Light-Emitting Diodes and Organic Thin-Films with Planar and Corrugated Structures," *Int J Mol Sci*, vol. 11, no. 4, pp. 1527–1545, Apr. 2010, doi: 10.3390/ijms11041527.

[160] L. N. Quan *et al.*, "Tailoring the Energy Landscape in Quasi-2D Halide Perovskites Enables Efficient Green-Light Emission," *Nano Lett.*, vol. 17, no. 6, pp. 3701–3709, Jun. 2017, doi: 10.1021/acs.nanolett.7b00976.

[161] Z. Li, K. Cao, J. Li, X. Du, Y. Tang, and B. Yu, "Modification of interface between PEDOT:PSS and perovskite film inserting an ultrathin LiF layer for enhancing efficiency of perovskite light-emitting diodes," *Organic Electronics*, vol. 81, p. 105675, Jun. 2020, doi: 10.1016/j.orgel.2020.105675.

[162] P. Chen *et al.*, "Nearly 100% Efficiency Enhancement of $CH_3NH_3PbBr_3$ Perovskite Light-Emitting Diodes by Utilizing Plasmonic Au Nanoparticles," *J. Phys. Chem. Lett.*, vol. 8, no. 17, pp. 3961–3969, Sep. 2017, doi: 10.1021/acs.jpclett.7b01562.

[163] S. Sandrez *et al.*, "Halide Perovskite Precursors Dope PEDOT:PSS," *Adv. Electron. Mater.*, vol. 7, no. 9, p. 2100394, Sep. 2021, doi: 10.1002/aelm.202100394.

[164] S. Lee *et al.*, "Control of Interface Defects for Efficient and Stable Quasi-2D Perovskite Light-Emitting Diodes Using Nickel Oxide Hole Injection Layer," *Advanced Science*, vol. 5, no. 11, p. 1801350, 2018, doi: 10.1002/advs.201801350.

[165] Y. Zou *et al.*, "Boosting Perovskite Light-Emitting Diode Performance via Tailoring Interfacial Contact," *ACS Appl. Mater. Interfaces*, vol. 10, no. 28, pp. 24320–24326, Jul. 2018, doi: 10.1021/acsami.8b07438.

[166] M. Ban *et al.*, "Solution-processed perovskite light emitting diodes with efficiency exceeding 15% through additive-controlled nanostructure tailoring," *Nat Commun*, vol. 9, no. 1, Art. no. 1, Sep. 2018, doi: 10.1038/s41467-018-06425-5.

[167] F. Meng *et al.*, "Co-Interlayer Engineering toward Efficient Green Quasi-Two-Dimensional Perovskite Light-Emitting Diodes," *Advanced Functional Materials*, vol. 30, no. 19, p. 1910167, 2020, doi: 10.1002/adfm.201910167.

[168] C. Wu *et al.*, "Alternative Type Two-Dimensional–Three-Dimensional Lead Halide Perovskite with Inorganic Sodium Ions as a Spacer for High-Performance Light-Emitting Diodes," *ACS Nano*, vol. 13, no. 2, pp. 1645–1654, Feb. 2019, doi: 10.1021/acsnano.8b07632.

[169] C. Sun *et al.*, "High-performance large-area quasi-2D perovskite light-emitting diodes," *Nat Commun*, vol. 12, no. 1, p. 2207, Apr. 2021, doi: 10.1038/s41467-021-22529-x.

[170] J. Song, J. Li, X. Li, L. Xu, Y. Dong, and H. Zeng, "Quantum Dot Light-Emitting Diodes Based on Inorganic Perovskite Cesium Lead Halides ($CsPbX_3$)," *Adv. Mater.*, vol. 27, no. 44, pp. 7162–7167, Nov. 2015, doi: 10.1002/adma.201502567.

[171] J. Li *et al.*, "50-Fold EQE Improvement up to 6.27% of Solution-Processed All-Inorganic Perovskite $CsPbBr_3$ QLEDs via Surface Ligand Density Control," *Adv. Mater.*, vol. 29, no. 5, p. 1603885, Feb. 2017, doi: 10.1002/adma.201603885.

[172] H. Huang *et al.*, "Emulsion Synthesis of Size-Tunable $CH_3NH_3PbBr_3$ Quantum Dots: An Alternative Route toward Efficient Light-Emitting Diodes," *ACS Appl. Mater. Interfaces*, vol. 7, no. 51, pp. 28128–28133, Dec. 2015, doi: 10.1021/acsami.5b10373.

[173] J. Pan *et al.*, "Highly Efficient Perovskite-Quantum-Dot Light-Emitting Diodes by Surface Engineering," *Adv. Mater.*, vol. 28, no. 39, pp. 8718–8725, Oct. 2016, doi: 10.1002/adma.201600784.

[174] J. H. Park *et al.*, "Surface Ligand Engineering for Efficient Perovskite Nanocrystal-Based Light-Emitting Diodes," *ACS Appl. Mater. Interfaces*, vol. 11, no. 8, pp. 8428–8435, Feb. 2019, doi: 10.1021/acsami.8b20808.

[175] J. Song *et al.*, "Organic–Inorganic Hybrid Passivation Enables Perovskite QLEDs with an EQE of 16.48%," *Adv. Mater.*, vol. 30, no. 50, p. 1805409, Dec. 2018, doi: 10.1002/adma.201805409.

[176] S. Yuan, Z.-K. Wang, M.-P. Zhuo, Q.-S. Tian, Y. Jin, and L.-S. Liao, "Self-Assembled High Quality CsPbBr$_3$ Quantum Dot Films toward Highly Efficient Light-Emitting Diodes," *ACS Nano*, vol. 12, no. 9, pp. 9541–9548, Sep. 2018, doi: 10.1021/acsnano.8b05185.

[177] S. He *et al.*, "Tailoring the refractive index and surface defects of CsPbBr3 quantum dots via alkyl cation-engineering for efficient perovskite light-emitting diodes," *Chemical Engineering Journal*, vol. 425, p. 130678, Dec. 2021, doi: 10.1016/j.cej.2021.130678.

[178] H. Zhao *et al.*, "High-Brightness Perovskite Light-Emitting Diodes Based on FAPbBr$_3$ Nanocrystals with Rationally Designed Aromatic Ligands," *ACS Energy Lett.*, vol. 6, no. 7, pp. 2395–2403, Jul. 2021, doi: 10.1021/acsenergylett.1c00812.

[179] S.-J. Woo, J. S. Kim, and T.-W. Lee, "Characterization of stability and challenges to improve lifetime in perovskite LEDs," *Nat. Photon.*, vol. 15, no. 9, pp. 630–634, Sep. 2021, doi: 10.1038/s41566-021-00863-2.

[180] H. Wang *et al.*, "Trifluoroacetate induced small-grained CsPbBr3 perovskite films result in efficient and stable light-emitting devices," *Nat Commun*, vol. 10, no. 1, Art. no. 1, Feb. 2019, doi: 10.1038/s41467-019-08425-5.

[181] X. Yu *et al.*, "Tailoring the Surface Morphology and Phase Distribution for Efficient Perovskite Electroluminescence," *J. Phys. Chem. Lett.*, vol. 11, no. 15, pp. 5877–5882, Aug. 2020, doi: 10.1021/acs.jpclett.0c01252.

[182] C. Qin *et al.*, "Triplet management for efficient perovskite light-emitting diodes," *Nat. Photonics*, vol. 14, no. 2, Art. no. 2, Feb. 2020, doi: 10.1038/s41566-019-0545-9.

[183] S. Mazumdar, Y. Zhao, and X. Zhang, "Stability of Perovskite Solar Cells: Degradation Mechanisms and Remedies," *Frontiers in Electronics*, vol. 2, 2021, Accessed: Mar. 27, 2023. [Online]. Available: https://www.frontiersin.org/articles/10.3389/felec.2021.712785

[184] N. Moody *et al.*, "Assessing the Regulatory Requirements of Lead-Based Perovskite Photovoltaics," *Joule*, vol. 4, no. 5, pp. 970–974, May 2020, doi: 10.1016/j.joule.2020.03.018.

[185] B. Chen, C. Fei, S. Chen, H. Gu, X. Xiao, and J. Huang, "Recycling lead and transparent conductors from perovskite solar modules," *Nat Commun*, vol. 12, no. 1, Art. no. 1, Oct. 2021, doi: 10.1038/s41467-021-26121-1.

[186] C.-H. Chen, S.-N. Cheng, L. Cheng, Z.-K. Wang, and L.-S. Liao, "Toxicity, Leakage, and Recycling of Lead in Perovskite Photovoltaics," *Advanced Energy Materials*, vol. 13, no. 14, p. 2204144, 2023, doi: 10.1002/aenm.202204144.

[187] Z. Ma, L. Wang, X. Ji, X. Chen, and Z. Shi, "Lead-Free Metal Halide Perovskites and Perovskite Derivatives as an Environmentally Friendly Emitter for Light-Emitting Device Applications," *J. Phys. Chem. Lett.*, vol. 11, no. 14, pp. 5517–5530, Jul. 2020, doi: 10.1021/acs.jpclett.0c01378.

[188] T. Xuan and R.-J. Xie, "Recent processes on light-emitting lead-free metal halide perovskites," *Chemical Engineering Journal*, vol. 393, p. 124757, Aug. 2020, doi: 10.1016/j.cej.2020.124757.

[189] N. Pradhan, "Growth of Lead Halide Perovskite Nanocrystals: Still in Mystery," *ACS Phys. Chem Au*, vol. 2, no. 4, pp. 268–276, Jul. 2022, doi: 10.1021/acsphyschemau.2c00001.

[190] Y. Tidhar *et al.*, "Crystallization of Methyl Ammonium Lead Halide Perovskites: Implications for Photovoltaic Applications," *J. Am. Chem. Soc.*, vol. 136, no. 38, pp. 13249–13256, Sep. 2014, doi: 10.1021/ja505556s.

[191] H. Gao *et al.*, "Nucleation and Crystal Growth of Organic–Inorganic Lead Halide Perovskites under Different Relative Humidity," *ACS Appl. Mater. Interfaces*, vol. 7, no. 17, pp. 9110–9117, May 2015, doi: 10.1021/acsami.5b00895.

[192] O. Shargaieva, H. Näsström, J. Li, D. M. Többens, and E. L. Unger, "Temperature-Dependent Crystallization Mechanisms of Methylammonium Lead Iodide Perovskite From Different Solvents," *Frontiers in Energy Research*, vol. 9, 2021, Accessed: Jul. 23, 2023. [Online]. Available: https://www.frontiersin.org/articles/10.3389/fenrg.2021.749604

[193] H. Zhang *et al.*, "Effects of substrate temperature on the crystallization process and properties of mixed-ion perovskite layers," *Journal of Materials Chemistry A*, vol. 7, Jan. 2019, doi: 10.1039/C8TA10170A.

[194] T. Dewinggih, Shobih, L. Muliani, Herman, and R. Hidayat, "The Temperature Effect on the Working Characteristics of Solar Cells Based on Organometal Halide Perovskite Crystals," *J. Phys.: Conf. Ser.*, vol. 877, no. 1, p. 012043, Jul. 2017, doi: 10.1088/1742-6596/877/1/012043.

[195] J. Schlipf *et al.*, "In Situ Monitoring the Uptake of Moisture into Hybrid Perovskite Thin Films," *The Journal of Physical Chemistry Letters*, vol. 9, Apr. 2018, doi: 10.1021/acs.jpclett.8b00687.

[196] B. Wygant *et al.*, "Moisture-Driven Formation and Growth of Quasi-2D Organolead Halide Perovskite Crystallites," *ACS Applied Energy Materials*, vol. XXXX, Jun. 2020, doi: 10.1021/acsaem.0c00423.

[197] C. Zuo *et al.*, "Crystallisation control of drop-cast quasi-2D/3D perovskite layers for efficient solar cells," *Commun Mater*, vol. 1, no. 1, p. 33, Jun. 2020, doi: 10.1038/s43246-020-0036-z.

[198] R.-I. Biega *et al.*, "Dynamic Distortions of Quasi-2D Ruddlesden-Popper Perovskites at Elevated Temperatures: Influence on Thermal and Electronic Properties." arXiv, Apr. 20, 2023. Accessed: Jul. 23, 2023. [Online]. Available: http://arxiv.org/abs/2303.05852

[199] Y. Han *et al.*, "Significance of Ambient Temperature Control for Highly Reproducible Layered Perovskite Light-Emitting Diodes," *ACS Photonics*, vol. 7, no. 9, pp. 2489–2497, Sep. 2020, doi: 10.1021/acsphotonics.0c00779.

[200] Z. Molenda, S. Chambon, D. M. Bassani, and L. Hirsch, "Assessing the Impact of Ambient Fabrication Temperature on the Performance of Planar CH3NH3PbI3 Perovskite Solar Cells," *European Journal of Inorganic Chemistry*, vol. 2021, no. 25, pp. 2533–2538, 2021, doi: 10.1002/ejic.202100329.

[201] X.-B. Shi *et al.*, "Optical Energy Losses in Organic–Inorganic Hybrid Perovskite Light-Emitting Diodes," *Advanced Optical Materials*, vol. 6, no. 17, p. 1800667, 2018, doi: 10.1002/adom.201800667.

[202] S.-S. Meng, Y.-Q. Li, and J.-X. Tang, "Theoretical perspective to light outcoupling and management in perovskite light-emitting diodes," *Organic Electronics*, vol. 61, pp. 351–358, Oct. 2018, doi: 10.1016/j.orgel.2018.06.014.

[203] Q. Zhang *et al.*, "Three-Dimensional Perovskite Nanophotonic Wire Array-Based Light-Emitting Diodes with Significantly Improved Efficiency and Stability," *ACS Nano*, vol. 14, no. 2, pp. 1577–1585, Feb. 2020, doi: 10.1021/acsnano.9b06663.

[204] Q. Zhang *et al.*, "Efficient metal halide perovskite light-emitting diodes with significantly improved light extraction on nanophotonic substrates," *Nat Commun*, vol. 10, no. 1, Art. no. 1, Feb. 2019, doi: 10.1038/s41467-019-08561-y.

[205] R. M. Lyaudoz, "Sources photoniques à base de métasurfaces et de pérovskite hybride organique-inorganique pour des applications de télécommunications en espace libre," phdthesis, Ecole Centrale de Lyon, 2022. Accessed: Oct. 11, 2023. [Online]. Available: https://theses.hal.science/tel-04030942

[206] C. Cho *et al.*, "The role of photon recycling in perovskite light-emitting diodes," *Nat Commun*, vol. 11, no. 1, Art. no. 1, Jan. 2020, doi: 10.1038/s41467-020-14401-1.

[207] D. K. Flattery, C. R. Fincher, D. L. LeCloux, M. B. O'Regan, and J. S. Richard, "Clearing the Road to Mass Production of OLED Television," *Information Display*, vol. 27, no. 10, pp. 8–13, 2011, doi: 10.1002/j.2637-496X.2011.tb00432.x.

[208] F. Yan and H. V. Demir, "Vacuum-evaporated lead halide perovskite LEDs [Invited]," *Opt. Mater. Express, OME*, vol. 12, no. 1, pp. 256–271, Jan. 2022, doi: 10.1364/OME.442770.

[209] S. Bhaumik, M. R. Kar, B. N. Thorat, A. Bruno, and S. G. Mhaisalkar, "Vacuum-Processed Metal Halide Perovskite Light-Emitting Diodes: Prospects and Challenges," *ChemPlusChem*, vol. 86, no. 4, pp. 558–573, 2021, doi: 10.1002/cplu.202000795.

[210] F. Hermerschmidt *et al.*, "Finally, inkjet-printed metal halide perovskite LEDs – utilizing seed crystal templating of salty PEDOT:PSS," *Mater. Horiz.*, vol. 7, no. 7, pp. 1773–1781, Jul. 2020, doi: 10.1039/D0MH00512F.

[211] J. Zhao, L.-W. Lo, H. Wan, P. Mao, Z. Yu, and C. Wang, "High-Speed Fabrication of All-Inkjet-Printed Organometallic Halide Perovskite Light-Emitting Diodes on Elastic Substrates," *Advanced Materials*, vol. 33, no. 48, p. 2102095, 2021, doi: 10.1002/adma.202102095.

[212] S. Chu *et al.*, "Large-area and efficient perovskite light-emitting diodes via low-temperature blade-coating," *Nat Commun*, vol. 12, no. 1, Art. no. 1, Jan. 2021, doi: 10.1038/s41467-020-20433-4.

[213] H. Chen, R. Wang, W. Ma, H. Zhang, and L. Yang, "One-step spray coating strategy toward a highly uniform large-area CsPbBr$_3$@PMMA composite film for backlit display," *Opt. Express, OE*, vol. 30, no. 12, pp. 20241–20249, Jun. 2022, doi: 10.1364/OE.457990.

[214] Y.-S. Jung, K. Hwang, Y.-J. Heo, J.-E. Kim, D. Vak, and D.-Y. Kim, "Progress in Scalable Coating and Roll-to-Roll Compatible Printing Processes of Perovskite Solar Cells toward Realization of Commercialization," *Advanced Optical Materials*, vol. 6, no. 9, p. 1701182, 2018, doi: 10.1002/adom.201701182.

[215] C. Zou, C. Zhang, Y.-H. Kim, L. Y. Lin, and J. M. Luther, "The Path to Enlightenment: Progress and Opportunities in High Efficiency Halide Perovskite Light-Emitting Devices," *ACS Photonics*, vol. 8, no. 2, pp. 386–404, Feb. 2021, doi: 10.1021/acsphotonics.0c01394.

[216] K. Ji, M. Anaya, A. Abfalterer, and S. D. Stranks, "Halide Perovskite Light-Emitting Diode Technologies," *Advanced Optical Materials*, vol. 9, no. 18, p. 2002128, Sep. 2021, doi: 10.1002/adom.202002128.

[217] Sudip K. Saha, "Comparison between Direct and Indirect Architectures in Perovskite Light-Emitting Diodes,"

[218] C. Bi, Q. Wang, Y. Shao, Y. Yuan, Z. Xiao, and J. Huang, "Non-wetting surface-driven high-aspect-ratio crystalline grain growth for efficient hybrid perovskite solar cells," *Nat Commun*, vol. 6, no. 1, Art. no. 1, Jul. 2015, doi: 10.1038/ncomms8747.

[219] S. Cho *et al.*, "Phenylethylammonium-formamidinium-methylammonium quasi-2D/3D tin wide-bandgap perovskite solar cell with improved efficiency and stability," *Chemical Engineering Journal*, vol. 446, p. 137388, Oct. 2022, doi: 10.1016/j.cej.2022.137388.

[220] A. Liang *et al.*, "Ligand-Driven Grain Engineering of High Mobility Two-Dimensional Perovskite Thin-Film Transistors," *J. Am. Chem. Soc.*, vol. 143, no. 37, pp. 15215–15223, Sep. 2021, doi: 10.1021/jacs.1c06337.

[221] J. Liang *et al.*, "Efficient perovskite light-emitting diodes by film annealing temperature control," *RSC Adv.*, vol. 6, no. 75, pp. 71070–71075, 2016, doi: 10.1039/C6RA14393H.

[222] Y.-H. Kim, H. Cho, J. H. Heo, S. H. Im, and T.-W. Lee, "Effects of thermal treatment on organic-inorganic hybrid perovskite films and luminous efficiency of light-emitting diodes," *Current Applied Physics*, vol. 16, no. 9, pp. 1069–1074, Sep. 2016, doi: 10.1016/j.cap.2016.06.002.

[223] M. Ahmed, S. Islam, and F. Ahmed, "Comparative Study on the Crystallite Size and Bandgap of Perovskite by Diverse Methods," *Advances in Condensed Matter Physics*, vol. 2022, pp. 1–7, May 2022, doi: 10.1155/2022/9535932.

[224] E. V. Péan, S. Dimitrov, C. S. De Castro, and M. L. Davies, "Interpreting time-resolved photoluminescence of perovskite materials," *Phys. Chem. Chem. Phys.*, vol. 22, no. 48, pp. 28345–28358, 2020, doi: 10.1039/D0CP04950F.

[225] "Calcium - Element information, properties and uses | Periodic Table." Accessed: Jul. 04, 2023. [Online]. Available: https://www.rsc.org/periodic-table/element/20/calcium

[226] Q. Shan *et al.*, "High Performance Metal Halide Perovskite Light-Emitting Diode: From Material Design to Device Optimization," *Small*, vol. 13, no. 45, p. 1701770, 2017, doi: 10.1002/smll.201701770.

[227] W. Zou *et al.*, "Minimising efficiency roll-off in high-brightness perovskite light-emitting diodes," *Nat Commun*, vol. 9, no. 1, p. 608, Dec. 2018, doi: 10.1038/s41467-018-03049-7.

[228] C. Zou, Y. Liu, D. S. Ginger, and L. Y. Lin, "Suppressing Efficiency Roll-Off at High Current Densities for Ultra-Bright Green Perovskite Light-Emitting Diodes," *ACS Nano*, vol. 14, no. 5, pp. 6076–6086, May 2020, doi: 10.1021/acsnano.0c01817.

[229] D. G. Zheng and D. H. Kim, "Degradation mechanisms of perovskite light-emitting diodes under electrical bias," *Nanophotonics*, vol. 12, no. 3, pp. 451–476, Feb. 2023, doi: 10.1515/nanoph-2022-0569.

[230] H. Kim *et al.*, "Hybrid perovskite light emitting diodes under intense electrical excitation," *Nat Commun*, vol. 9, no. 1, p. 4893, Dec. 2018, doi: 10.1038/s41467-018-07383-8.

[231] F. Ye, Q. Shan, H. Zeng, and W. C. H. Choy, "Operational and Spectral Stability of Perovskite Light-Emitting Diodes," *ACS Energy Lett.*, vol. 6, no. 9, pp. 3114–3131, Sep. 2021, doi: 10.1021/acsenergylett.1c01545.

[232] T. Cheng, G. Tumen-Ulzii, D. Klotz, S. Watanabe, T. Matsushima, and C. Adachi, "Ion Migration-Induced Degradation and Efficiency Roll-off in Quasi-2D Perovskite Light-Emitting Diodes," *ACS Appl. Mater. Interfaces*, vol. 12, no. 29, pp. 33004–33013, Jul. 2020, doi: 10.1021/acsami.0c06737.

[233] E. Bandiello, J. Ávila, L. Gil-Escrig, E. Tekelenburg, M. Sessolo, and H. J. Bolink, "Influence of mobile ions on the electroluminescence characteristics of methylammonium lead iodide perovskite diodes," *J. Mater. Chem. A*, vol. 4, no. 47, pp. 18614–18620, 2016, doi: 10.1039/C6TA06854E.

[234] H. Wang *et al.*, "Dynamic Redistribution of Mobile Ions in Perovskite Light-Emitting Diodes," *Advanced Functional Materials*, vol. 31, no. 8, p. 2007596, 2021, doi: 10.1002/adfm.202007596.

[235] C. Féry, B. Racine, D. Vaufrey, H. Doyeux, and S. Cinà, "Physical mechanism responsible for the stretched exponential decay behavior of aging organic light-emitting diodes," *Applied Physics Letters*, vol. 87, no. 21, p. 213502, Nov. 2005, doi: 10.1063/1.2133922.

[236] J. Lee, "Lifetime modeling for organic light-emitting diodes: a review and analysis," *Journal of Information Display*, vol. 24, no. 1, pp. 57–70, 2022, doi: 10.1080/15980316.2022.2126018.

[237]   kyonghwan Oh, S.-K. Hong, and O.-K. Kwon, "Lifetime Extension Method for Active Matrix Organic Light-Emitting Diode Displays Using a Modified Stretched Exponential Decay Model," *IEEE Electron Device Letters*, vol. 36, no. 3, pp. 277–279, Mar. 2015, doi: 10.1109/LED.2015.2394451.

[238]   F. Lou *et al.*, "Distinguishing the migration time scale of ion species in perovskite solar cells," *Chemical Physics Letters*, vol. 796, p. 139570, Jun. 2022, doi: 10.1016/j.cplett.2022.139570.

[239]   J. H. Warby *et al.*, "Revealing Factors Influencing the Operational Stability of Perovskite Light-Emitting Diodes," *ACS Nano*, vol. 14, no. 7, pp. 8855–8865, Jul. 2020, doi: 10.1021/acsnano.0c03516.

[240]   H. Lee, D. Ko, and C. Lee, "Direct Evidence of Ion-Migration-Induced Degradation of Ultrabright Perovskite Light-Emitting Diodes," *ACS Appl. Mater. Interfaces*, vol. 11, no. 12, pp. 11667–11673, Mar. 2019, doi: 10.1021/acsami.8b22217.

[241]   A. Turak, "On the Role of LiF in Organic Optoelectronics," *Electronic Materials*, vol. 2, no. 2, Art. no. 2, Jun. 2021, doi: 10.3390/electronicmat2020016.

[242]   C. R. Mayer *et al.*, "Synthesis of highly calibrated CsPbBr3 nanocrystal perovskites by soft chemistry," *Chem. Commun.*, vol. 58, no. 40, pp. 5960–5963, May 2022, doi: 10.1039/D2CC01028C.

[243]   D. Han *et al.*, "Efficient Light-Emitting Diodes Based on in Situ Fabricated FAPbBr3 Nanocrystals: The Enhancing Role of the Ligand-Assisted Reprecipitation Process," *ACS Nano*, vol. 12, no. 8, pp. 8808–8816, Aug. 2018, doi: 10.1021/acsnano.8b05172.

[244]   J. Xing *et al.*, "High-Efficiency Light-Emitting Diodes of Organometal Halide Perovskite Amorphous Nanoparticles," *ACS Nano*, vol. 10, no. 7, pp. 6623–6630, Jul. 2016, doi: 10.1021/acsnano.6b01540.

[245]   W. Deng *et al.*, "Organometal Halide Perovskite Quantum Dot Light-Emitting Diodes," *Advanced Functional Materials*, vol. 26, no. 26, pp. 4797–4802, 2016, doi: 10.1002/adfm.201601054.

[246]   X. Li *et al.*, "CsPbX3 Quantum Dots for Lighting and Displays: Room-Temperature Synthesis, Photoluminescence Superiorities, Underlying Origins and White Light-Emitting Diodes," *Advanced Functional Materials*, vol. 26, no. 15, pp. 2435–2445, 2016, doi: 10.1002/adfm.201600109.

[247]   S. Sun *et al.*, "0D Perovskites: Unique Properties, Synthesis, and Their Applications," *Advanced Science*, vol. 8, no. 24, p. 2102689, Dec. 2021, doi: 10.1002/advs.202102689.

[248]   Y. Tang, N. Yan, Z. Wang, H. Yuan, Y. Xin, and H. Yin, "Precursor solution volume-dependent ligand-assisted synthesis of CH3NH3PbBr3 perovskite nanocrystals," *Journal of Alloys and Compounds*, vol. 773, pp. 227–233, Jan. 2019, doi: 10.1016/j.jallcom.2018.09.054.

[249]   C. Zheng *et al.*, "High-brightness perovskite quantum dot light-emitting devices using inkjet printing," *Organic Electronics*, vol. 93, p. 106168, Jun. 2021, doi: 10.1016/j.orgel.2021.106168.

[250]   C.-H. Kuan and S.-H. Yang, "Surface ligand engineering of perovskite nanocrystals with a conjugated sulfonate ligand for light-emitting applications," *Mater. Adv.*, vol. 3, no. 21, pp. 7824–7832, Oct. 2022, doi: 10.1039/D2MA00595F.

[251]   G. Li *et al.*, "Highly Efficient Perovskite Nanocrystal Light-Emitting Diodes Enabled by a Universal Crosslinking Method," *Advanced Materials*, vol. 28, no. 18, pp. 3528–3534, 2016, doi: 10.1002/adma.201600064.

[252]   X. Wang, W. Liu, J. He, Y. Li, and Y. Liu, "Synthesis of All-Inorganic Halide Perovskite Nanocrystals for Potential Photoelectric Catalysis Applications," *Catalysts*, vol. 13, no. 7, Art. no. 7, Jul. 2023, doi: 10.3390/catal13071041.

[253]   M. T. Hoang *et al.*, "Surface Treatment of Inorganic CsPbI3 Nanocrystals with Guanidinium Iodide for Efficient Perovskite Light-Emitting Diodes with High Brightness," *Nano-Micro Lett.*, vol. 14, no. 1, p. 69, Mar. 2022, doi: 10.1007/s40820-022-00813-9.

[254]   T. C. A. da Silva, C. Fernández-Saiz, R. S. Sánchez, A. F. Gualdrón-Reyes, I. Mora-Seró, and B. Julián-López, "A soft-chemistry route to prepare halide perovskite nanocrystals with tunable emission and high optical performance," *J Sol-Gel Sci Technol*, Jul. 2023, doi: 10.1007/s10971-023-06171-1.

[255]   F. Chen, Y. Liu, and M. Salerno, "Dispersing solvent effect on halide perovskite nanocrystals-based films and devices," *J Mater Sci*, vol. 57, no. 3, pp. 1902–1913, Jan. 2022, doi: 10.1007/s10853-021-06777-2.

[256]   Y. Sun *et al.*, "Research on the influence of polar solvents on CsPbBr 3 perovskite QDs," *RSC Advances*, vol. 11, no. 44, pp. 27333–27337, 2021, doi: 10.1039/D1RA04485K.

[257]   H. Wang *et al.*, "Formation and dispersion of organometal halide perovskite nanocrystals in various solvents," *Journal of Colloid and Interface Science*, vol. 529, pp. 575–581, Nov. 2018, doi: 10.1016/j.jcis.2018.06.053.

[258]   R. Wu, Y. Yang, M. Li, D. Qin, Y. Zhang, and L. Hou, "Solvent Engineering for High-Performance PbS Quantum Dots Solar Cells," *Nanomaterials*, vol. 7, p. 201, Jul. 2017, doi: 10.3390/nano7080201.

[259] I. Poli, X. Liang, R. Baker, S. Eslava, and P. J. Cameron, "Enhancing the hydrophobicity of perovskite solar cells using C18 capped CH3NH3PbI3 nanocrystals," *J. Mater. Chem. C*, vol. 6, no. 26, pp. 7149–7156, Jul. 2018, doi: 10.1039/C8TC01939H.

[260] B. Jewłoszewicz, K. A. Bogdanowicz, W. Przybył, A. Iwan, and I. Plebankiewicz, "PEDOT:PSS in Water and Toluene for Organic Devices—Technical Approach," *Polymers*, vol. 12, no. 3, Art. no. 3, Mar. 2020, doi: 10.3390/polym12030565.

[261] W. Chen, N. D. Pham, H. Wang, B. Jia, and X. Wen, "Spectroscopic Insight into Efficient and Stable Hole Transfer at the Perovskite/Spiro-OMeTAD Interface with Alternative Additives," *ACS Appl. Mater. Interfaces*, vol. 13, no. 4, pp. 5752–5761, Feb. 2021, doi: 10.1021/acsami.0c19111.

[262] N. Tomczak, D. Jańczewski, M. Han, and G. J. Vancso, "Designer polymer–quantum dot architectures," *Progress in Polymer Science*, vol. 34, no. 5, pp. 393–430, May 2009, doi: 10.1016/j.progpolymsci.2008.11.004.

[263] H. Moon, C. Lee, W. Lee, J. Kim, and H. Chae, "Stability of Quantum Dots, Quantum Dot Films, and Quantum Dot Light-Emitting Diodes for Display Applications," *Advanced Materials*, vol. 31, no. 34, p. 1804294, 2019, doi: 10.1002/adma.201804294.

[264] H. Woo *et al.*, "Robust, processable, and bright quantum dot/organosilicate hybrid films with uniform QD distribution based on thiol-containing organosilicate ligands," *J. Mater. Chem. C*, vol. 1, no. 10, pp. 1983–1989, Feb. 2013, doi: 10.1039/C3TC00719G.

[265] J. Phelipot, "New fluorescent organic-inorganic nanohybrid materials for optoelectronic applications," These de doctorat, Aix-Marseille, 2022. Accessed: Aug. 22, 2023. [Online]. Available: https://www.theses.fr/2022AIXM0067

[266] H. Sun *et al.*, "Chemically Addressable Perovskite Nanocrystals for Light-Emitting Applications.," *Adv Mater*, vol. 29, no. 34, Sep. 2017, doi: 10.1002/adma.201701153.

[267] C. Yoon, K. P. Yang, J. Kim, K. Shin, and K. Lee, "Fabrication of highly transparent and luminescent quantum dot/polymer nanocomposite for light emitting diode using amphiphilic polymer-modified quantum dots," *Chemical Engineering Journal*, vol. 382, p. 122792, Feb. 2020, doi: 10.1016/j.cej.2019.122792.

[268] Y. Wang *et al.*, "Ultrastable, Highly Luminescent Organic–Inorganic Perovskite–Polymer Composite Films," *Adv. Mater.*, vol. 28, no. 48, pp. 10710–10717, Dec. 2016, doi: 10.1002/adma.201603964.

[269] S.-Y. Park *et al.*, "Long-term stability of CdSe/CdZnS quantum dot encapsulated in a multi-lamellar microcapsule," *Nanotechnology*, vol. 26, no. 27, p. 275602, Jun. 2015, doi: 10.1088/0957-4484/26/27/275602.

[270] H. Yu *et al.*, "A MAPbBr 3 :poly(ethylene oxide) composite perovskite quantum dot emission layer: enhanced film stability, coverage and device performance," *Nanoscale*, vol. 11, no. 18, pp. 9103–9114, 2019, doi: 10.1039/C8NR10298H.

[271] J. C. Yu, A.-Y. Lee, D. B. Kim, E. D. Jung, D. W. Kim, and M. H. Song, "Enhancing the Performance and Stability of Perovskite Nanocrystal Light-Emitting Diodes with a Polymer Matrix," *Adv. Mater. Technol.*, vol. 2, no. 6, p. 1700003, Jun. 2017, doi: 10.1002/admt.201700003.

[272] Q. Zhou, Z. Bai, W. Lu, Y. Wang, B. Zou, and H. Zhong, "In Situ Fabrication of Halide Perovskite Nanocrystal-Embedded Polymer Composite Films with Enhanced Photoluminescence for Display Backlights," *Advanced Materials*, vol. 28, no. 41, pp. 9163–9168, 2016, doi: 10.1002/adma.201602651.

[273] Y. Wei *et al.*, "Enhancing the Stability of Perovskite Quantum Dots by Encapsulation in Crosslinked Polystyrene Beads via a Swelling–Shrinking Strategy toward Superior Water Resistance," *Advanced Functional Materials*, vol. 27, no. 39, p. 1703535, 2017, doi: 10.1002/adfm.201703535.

[274] J. Gerhardt, M. Miller, H. Yoo, and T. Akhavan, "Estimating OLED Display Device Lifetime from pixel and screen brightness and its application," *Color and Imaging Conference*, vol. 2019, pp. 331–338, Oct. 2019, doi: 10.2352/issn.2169-2629.2019.27.60.

[275] Z. Wen, F. Xie, and Wallace. C. H. Choy, "Stability of electroluminescent perovskite quantum dots light-emitting diode," *Nano Select*, vol. 3, no. 3, pp. 505–530, 2022, doi: 10.1002/nano.202100203.

[276] Z. Shi *et al.*, "High-Efficiency and Air-Stable Perovskite Quantum Dots Light-Emitting Diodes with an All-Inorganic Heterostructure," *Nano Lett.*, vol. 17, no. 1, pp. 313–321, Jan. 2017, doi: 10.1021/acs.nanolett.6b04116.

[277] C. Otero-Martínez, N. Fiuza-Maneiro, and L. Polavarapu, "Enhancing the Intrinsic and Extrinsic Stability of Halide Perovskite Nanocrystals for Efficient and Durable Optoelectronics," *ACS Appl. Mater. Interfaces*, vol. 14, no. 30, pp. 34291–34302, Aug. 2022, doi: 10.1021/acsami.2c01822.

[278] Y. Ye *et al.*, "Ultra-low EQE roll-off and marvelous efficiency perovskite quantum-dots light-emitting-diodes achieved by ligand passivation," *Nano Energy*, vol. 90, p. 106583, Dec. 2021, doi: 10.1016/j.nanoen.2021.106583.

[279] J.-S. Yao *et al.*, "Suppressing Auger Recombination in Cesium Lead Bromide Perovskite Nanocrystal Film for Bright Light-Emitting Diodes," *J. Phys. Chem. Lett.*, vol. 11, no. 21, pp. 9371–9378, Nov. 2020, doi: 10.1021/acs.jpclett.0c02777.

[280] A. Ali, A. Mitra, and B. Aïssa, "Metamaterials and Metasurfaces: A Review from the Perspectives of Materials, Mechanisms and Advanced Metadevices," *Nanomaterials (Basel)*, vol. 12, no. 6, p. 1027, Mar. 2022, doi: 10.3390/nano12061027.

[281] J. Hu, S. Bandyopadhyay, Y. Liu, and L. Shao, "A Review on Metasurface: From Principle to Smart Metadevices," *Frontiers in Physics*, vol. 8, 2021, Accessed: Oct. 10, 2023. [Online]. Available: https://www.frontiersin.org/articles/10.3389/fphy.2020.586087

[282] A. S. Solntsev, G. S. Agarwal, and Y. S. Kivshar, "Metasurfaces for quantum photonics," *Nat. Photonics*, vol. 15, no. 5, pp. 327–336, May 2021, doi: 10.1038/s41566-021-00793-z.

[283] K. Wang, M. Chekhova, and Y. Kivshar, "Metasurfaces for quantum technologies," *Physics Today*, vol. 75, pp. 38–44, Aug. 2022, doi: 10.1063/PT.3.5062.

[284] M. K. Chen and T. Tanaka, "Metalenses for revolutionary imaging," *pi*, vol. 2, no. 1, p. C01, 2023, doi: 10.3788/PI.2023.C01.

[285] W. Li, J. Qi, and A. Sihvola, "Meta-Imaging: from Non-Computational to Computational," *Advanced Optical Materials*, vol. 8, no. 23, p. 2001000, 2020, doi: 10.1002/adom.202001000.

[286] Y.-Y. Xie *et al.*, "Metasurface-integrated vertical cavity surface-emitting lasers for programmable directional lasing emissions," *Nat. Nanotechnol.*, vol. 15, no. 2, Art. no. 2, Feb. 2020, doi: 10.1038/s41565-019-0611-y.

[287] A. Krasnok, M. Tymchenko, and A. Alù, "Nonlinear metasurfaces: a paradigm shift in nonlinear optics," *Materials Today*, vol. 21, no. 1, pp. 8–21, Jan. 2018, doi: 10.1016/j.mattod.2017.06.007.

[288] Y. Nishijima, N. To, A. Balčytis, and S. Juodkazis, "Absorption and scattering in perfect thermal radiation absorber-emitter metasurfaces," *Opt. Express, OE*, vol. 30, no. 3, pp. 4058–4070, Jan. 2022, doi: 10.1364/OE.447885.

[289] R. Alaee, M. Albooyeh, and C. Rockstuhl, "Theory of metasurface based perfect absorbers," *J. Phys. D: Appl. Phys.*, vol. 50, no. 50, p. 503002, Nov. 2017, doi: 10.1088/1361-6463/aa94a8.

[290] M. Makarenko, A. Burguete-Lopez, F. Getman, and A. Fratalocchi, "Metasurface design platform for highly efficient wavefront engineering," in *2021 Conference on Lasers and Electro-Optics Europe & European Quantum Electronics Conference (CLEO/Europe-EQEC)*, Jun. 2021, pp. 1–1. doi: 10.1109/CLEO/Europe-EQEC52157.2021.9542717.

[291] K. Kang, S. Im, C. Lee, J. Kim, and D. Kim, "Nanoslot metasurface design and characterization for enhanced organic light-emitting diodes," *Sci Rep*, vol. 11, no. 1, Art. no. 1, Apr. 2021, doi: 10.1038/s41598-021-88641-6.

[292] C. M. Carter, "Device and metasurface designs for next-generation blue-emitting organic LEDs: cost, sustainability, efficiency, and stability," Rutgers University - School of Graduate Studies, 2018. doi: 10.7282/T33N26MW.

[293] L. Zhou *et al.*, "Tailoring Directive Gain for High-Contrast, Wide-Viewing-Angle Organic Light-Emitting Diodes Using Speckle Image Holograpy Metasurfaces," *ACS Appl. Mater. Interfaces*, vol. 8, no. 34, pp. 22402–22409, Aug. 2016, doi: 10.1021/acsami.6b06748.

[294] A. Vaskin *et al.*, "Manipulation of quantum dot emission with semiconductor metasurfaces exhibiting magnetic quadrupole resonances," *Opt. Express, OE*, vol. 29, no. 4, pp. 5567–5579, Feb. 2021, doi: 10.1364/OE.414011.

[295] Y. Park *et al.*, "Metasurface electrode light emitting diodes with planar light control," *Sci Rep*, vol. 7, no. 1, p. 14753, Nov. 2017, doi: 10.1038/s41598-017-15254-3.

[296] H. Huang, S. Zheng, and W. Sun, "Beam manipulation for quantum dot light-emitting diode with an Ag grating and a phase-gradient metasurface," *Opt. Express, OE*, vol. 30, no. 16, pp. 28345–28357, Aug. 2022, doi: 10.1364/OE.463772.

[297] Z. Liu, K. Ren, G. Dai, and J. Zhang, "A Review on Micro-LED Display Integrating Metasurface Structures," *Micromachines*, vol. 14, p. 1354, Jun. 2023, doi: 10.3390/mi14071354.

[298] W.-J. Joo *et al.*, "Metasurface-driven OLED displays beyond 10,000 pixels per inch," *Science*, vol. 370, no. 6515, pp. 459–463, Oct. 2020, doi: 10.1126/science.abc8530.

[299] C. Soci *et al.*, "(INVITED) Roadmap on perovskite nanophotonics," *Optical Materials: X*, vol. 17, p. 100214, Feb. 2023, doi: 10.1016/j.omx.2022.100214.

[300] B. Gholipour *et al.*, "Organometallic Perovskite Metasurfaces," *Advanced Materials*, vol. 29, no. 9, p. 1604268, Mar. 2017, doi: 10.1002/adma.201604268.

[301] G. Adamo *et al.*, "Metamaterial Enhancement of Metal-Halide Perovskite Luminescence," *Nano Lett.*, vol. 20, no. 11, pp. 7906–7911, Nov. 2020, doi: 10.1021/acs.nanolett.0c02571.

[302] J. Tian *et al.*, "Optical Rashba Effect in a Light-Emitting Perovskite Metasurface," *Advanced Materials*, vol. 34, no. 12, p. 2109157, 2022, doi: 10.1002/adma.202109157.

[303] G. Long *et al.*, "Perovskite metasurfaces with large superstructural chirality," *Nat Commun*, vol. 13, no. 1, Art. no. 1, Mar. 2022, doi: 10.1038/s41467-022-29253-0.

[304] Z. Li *et al.*, "Active Perovskite Hyperbolic Metasurface," *ACS Photonics*, vol. 7, no. 7, pp. 1754–1761, Jul. 2020, doi: 10.1021/acsphotonics.0c00391.

[305] C. Huang *et al.*, "Ultrafast control of vortex microlasers," *Science*, vol. 367, no. 6481, pp. 1018–1021, Feb. 2020, doi: 10.1126/science.aba4597.

[306] J. Tian *et al.*, "Phase-Change Perovskite Microlaser with Tunable Polarization Vortex," *Advanced Materials*, vol. 35, no. 1, p. 2207430, 2023, doi: 10.1002/adma.202207430.

[307] R. Mermet-Lyaudoz *et al.*, "Taming Friedrich–Wintgen Interference in a Resonant Metasurface: Vortex Laser Emitting at an On-Demand Tilted Angle," *Nano Lett.*, vol. 23, no. 10, pp. 4152–4159, May 2023, doi: 10.1021/acs.nanolett.2c04936.

[308] Y. Wang, J. Tian, M. Klein, G. Adamo, S. T. Ha, and C. Soci, "Directional Emission from Electrically Injected Exciton–Polaritons in Perovskite Metasurfaces," *Nano Lett.*, vol. 23, no. 10, pp. 4431–4438, May 2023, doi: 10.1021/acs.nanolett.3c00727.

[309] Y. Jia, R. A. Kerner, A. J. Grede, A. N. Brigeman, B. P. Rand, and N. C. Giebink, "Diode-Pumped Organo-Lead Halide Perovskite Lasing in a Metal-Clad Distributed Feedback Resonator," *Nano Lett.*, vol. 16, no. 7, pp. 4624–4629, Jul. 2016, doi: 10.1021/acs.nanolett.6b01946.

[310] H. Wang *et al.*, "Nanoimprinted perovskite metasurface for enhanced photoluminescence," *Opt. Express, OE*, vol. 25, no. 24, pp. A1162–A1171, Nov. 2017, doi: 10.1364/OE.25.0A1162.

[311] L. Gu *et al.*, "3D Arrays of 1024-Pixel Image Sensors based on Lead Halide Perovskite Nanowires," *Adv Mater*, vol. 28, no. 44, pp. 9713–9721, Nov. 2016, doi: 10.1002/adma.201601603.

[312] S. S. Chou *et al.*, "Laser Direct Write Synthesis of Lead Halide Perovskites," *J Phys Chem Lett*, vol. 7, no. 19, pp. 3736–3741, Oct. 2016, doi: 10.1021/acs.jpclett.6b01557.

[313] X. He, P. Liu, H. Zhang, Q. Liao, J. Yao, and H. Fu, "Patterning Multicolored Microdisk Laser Arrays of Cesium Lead Halide Perovskite," *Adv Mater*, vol. 29, no. 12, Mar. 2017, doi: 10.1002/adma.201604510.

[314] Z. Gu *et al.*, "Direct-Writing Multifunctional Perovskite Single Crystal Arrays by Inkjet Printing," *Small*, vol. 13, no. 8, p. 1603217, 2017, doi: 10.1002/smll.201603217.

[315] M. S. Alias *et al.*, "Enhanced Etching, Surface Damage Recovery, and Submicron Patterning of Hybrid Perovskites using a Chemically Gas-Assisted Focused-Ion Beam for Subwavelength Grating Photonic Applications," *J. Phys. Chem. Lett.*, vol. 7, no. 1, pp. 137–142, Jan. 2016, doi: 10.1021/acs.jpclett.5b02558.

[316] D. K. Oh, T. Lee, B. Ko, T. Badloe, J. G. Ok, and J. Rho, "Nanoimprint lithography for high-throughput fabrication of metasurfaces," *Front Optoelectron*, vol. 14, no. 2, pp. 229–251, Apr. 2021, doi: 10.1007/s12200-021-1121-8.

[317] N. H. M. Dang *et al.*, "Tailoring Dispersion of Room-Temperature Exciton-Polaritons with Perovskite-Based Subwavelength Metasurfaces," *Nano Lett.*, vol. 20, no. 3, pp. 2113–2119, Mar. 2020, doi: 10.1021/acs.nanolett.0c00125.

[318] N. H. M. Dang *et al.*, "Realization of Polaritonic Topological Charge at Room Temperature Using Polariton Bound States in the Continuum from Perovskite Metasurface," *Advanced Optical Materials*, vol. 10, no. 6, p. 2102386, 2022, doi: 10.1002/adom.202102386.

[319] R. Mermet-Lyaudoz *et al.*, "Multiscale Simulation for Visible Light Communication using Perovskite Metasurface," in *2021 17th International Symposium on Wireless Communication Systems (ISWCS)*, Sep. 2021, pp. 1–6. doi: 10.1109/ISWCS49558.2021.9562213.

[320] M. Klein *et al.*, "Polarization-Tunable Perovskite Light-Emitting Metatransistor," *Advanced Materials*, vol. 35, no. 1, p. 2207317, 2023, doi: 10.1002/adma.202207317.

[321] R. Mermet-Lyaudoz *et al.*, *Realization of Bound state In the Continuum induced by vertical symmetry breaking in photonic lattice*. 2019.

[322] F. Berry *et al.*, "Light Management in Perovskite Photovoltaic Solar Cells: A Perspective," *Advanced Energy Materials*, vol. 12, no. 20, p. 2200505, 2022, doi: 10.1002/aenm.202200505.

[323] C. He *et al.*, "Refractive Index Dispersion of Organic–Inorganic Hybrid Halide Perovskite CH3NH3PbX3 (X═Cl, Br, I) Single Crystals," *Crystal Research and Technology*, vol. 54, no. 5, p. 1900011, 2019, doi: 10.1002/crat.201900011.

[324] M. I. Khan *et al.*, "Improving the Structural, Optical and Photovoltaic Properties of Sb- and Bi- Co-Doped MAPbBr3 Perovskite Solar Cell," *Coatings*, vol. 12, no. 3, Art. no. 3, Mar. 2022, doi: 10.3390/coatings12030386.

[325] L. Velasco Davoise, R. Peña Capilla, and A. M. Díez-Pascual, "Isotropic and Anisotropic Complex Refractive Index of PEDOT:PSS," *Polymers*, vol. 15, no. 15, Art. no. 15, Jan. 2023, doi: 10.3390/polym15153298.

[326] "192198-85-9 | 2,2′,2″-(1,3,5-Benzenetriyl)tris[1-phenyl-1H-benzimidaz," Hoffman Fine Chemicals. Accessed: Oct. 14, 2023. [Online]. Available: https://hoffmanchemicals.com/ko/products/2-2-2-1-3-5-benzinetriyl-tris1-phenyl-1-h-benzimidazole

ANNEX

Annex 1: Experimental methods

1. Materials

a. Perovskite precursors

Perovskite materials: Phenylethyl Ammonium Bromide (PEABr) and Lead Bromide (PbBr$_2$) were purchased from Sigma-Aldrich (USA). Methyl Ammonium Bromide (MABr) was purchased from DYESOL (Australia). N,N-Dimethylformamide (DMF, > 99.8 %) solvent was purchased from Sigma-Aldrich.

Precursor preparation:

- 3D perovskites: A 0.5 M MAPB precursor solution is prepared by dissolving excess MABr and PbBr$_2$ in Dimethylformamide (DMF) solvent with a molar ratio of 2:1 or 3:1. The precursor solution is mixed at 50 °C for 24 hours and filtered using 0.2-µm hydrophobic PTFE 10 minutes before the deposition.
- Quasi-2D perovskites: A 0.5 M quasi-2D perovskite precursor solution is prepared by dissolving PEABr, MABr, and PbBr2 in DMF solvent at different stoichiometric ratios. The precursor solutions are then mixed for at least 24 hours at 50 °C and filtered before deposition. The detailed precursor recipes are summarized in Table A1.

Table A2. Precursor recipes to prepare polycrystalline perovskite thin films

		m_{PEABr} (mg)	m_{MABr} (mg)	m_{PBBr2} (mg)	V_{DMF} (µL)
3D perovskites	**MAPB 2:1**	0	112	184	1000
	MAPB 3:1	0	168	184	1000
Quasi-2D perovskites	**PEA:MA = 4:1**	13	34	103	500
	PEA:MA = 2:1	26	34	115	500

(with molecular weights: M_{PEABr} = 202.09 g, M_{MABr} = 111.97 g, and M_{PBBr2} = 367.01 g)

- Perovskite QDs: CsPbBr$_3$ nanocrystals solutions were prepared by Dr. Cédric Mayer and his colleagues at Laboratory LUMIN (Saclay, France)

b. Perovskite QD/Polymers composites

Polymer materials: Poly(methyl methacrylate) (PMMA, Mw ~ 15,000) and anhydrous Toluene (99.8%) were sourced from Sigma-Aldrich. Poly(ethylene oxide) (PEO, Mw ~ 600,000) was purchased from Acros Organics.

Polymer precursor preparation:

- PMMA precursor: the PMMA powder is dissolved in Toluene with a mass concentration of 10 mg/mL at room temperature. The solution is mixed using a magnetic stirrer at 500 rpm overnight before use.

- PEO precursor: the PEO powder is dissolved in Toluene with a mass concentration of 5 mg/mL. The solution is mixed using a magnetic stirrer at 500 rpm at 70 °C for 15 minutes until the polymer is completely dissolved ant then mixed constantly at 50 °C. 15 minutes before use, the stirring temperature is gradually decreased to room temperature.

Composite precursor preparation: The composite solutions are then prepared by mixing the perovskite and polymer precursors at targeting ratios. For QD/PMMA composites, the $CsPbBr_3$/PMMA mass ratios vary between 1:1, 10:1 to 20:1. These values in the case of QD/PEO composites are 1:1. 5:1, and 10:1. The solutions are shaken (not stirred) gently before use.

c. PeLED materials

12 mm × 12 mm Indium Tin Oxide (ITO)-coated substrates were purchased from VisionTek Systems Ltd (UK). Poly(3,4-ethylenedioxythiophene) polystyrene sulfonate (PEDOT:PSS - Al 4083) and 2,2',2"-(1,3,5-Benzinetriyl)-tris(1-phenyl-1-H-benzimidazole) (TPBi, > 99.5 %) were purchased from Ossila (UK). Lithium Fluoride (LiF) (powder, > 99.995 %) was purchased from Sigma-Aldrich. Calcium (Ca, 99.9 %) was purchased from Neyco (France). Silver wires (Ag, 99.9 %) were purchased from GoodFellow Cambridge (UK).

2. Thin-film depositions

a. Perovskite depositions

Inert-gas workstation set-ups:

- At the beginning of the study, the preparation and deposition of the perovskite precursors were performed in an MBRAUN UNIlab glovebox workstation filled with nitrogen gas. The residual oxygen and moisture content inside the workstation is probed using integrated analyzers and maintained at < 10 ppm. The gas purifier of the glovebox is regenerated when there is a significant increase in the H_2O/O_2 concentration (> 100 ppm) or, in normal operating conditions, once every six months.

- Then, in the second stage of the research, the precursor solutions are prepared in a separate glovebox (MBRAUN MB200B) before being transferred to the first glovebox for spin-coating. The second glovebox is also nitrogen-filled, with a humidity level between 5% and 10% and an O_2 concentration of < 1 ppm. Concerning the perovskite deposition, the glovebox is purged with the inert gas one day before the experiment to remove solvent vapor and ensure low H_2O/O_2 concentrations (< 0.01 ppm) during the spin-coating. The temperature of the gloveboxes corresponds to that of the ambient environment.

Substrate preparation:

- Glass substrates: First, the substrates are cleaned with Isopropanol in an ultrasonic bath for 15 minutes, followed by a drying procedure using Nitrogen flow to eliminate residual solvent or dust. The glass substrates are then exposed to UV-Ozone for 15 minutes to improve the surface wettability.

- PEDOT:PSS-coated substrates: The substrates are subjected to UV-Ozone treatment for 15 minutes

- In the case of perovskite QDs, the substrates are spin-coated with a layer of Toluene solvent and left for 5 minutes at ambient environment until dry.

Spin-coating deposition:

- 3D perovskites: 60 µL of the filtered MAPB precursor solution is dropped on the treated substrates and spin-coated at 3000 rpm for 40 seconds. After spin-coating, the samples are quickly transferred to a preset hot plate for thermal annealing at 90 °C for 120 minutes. The substrates are then rested for at least 15 minutes before characterization. The final thickness of the perovskite layers is approximately 150 nm.

- Quasi-2D perovskites: The precursor solutions are spin-coated at a high speed of 7,000 rpm for 40 seconds, followed by thermal annealing at 90 °C for 15 minutes. The thickness of the thin films is 150 nm – 160 nm.

- Perovskite QDs: 60 µl of the NC solution is dropped on toluene-treated glass substrates and spin-coated at 3000 rpm for 40 seconds. The samples are also left to dry naturally for 15 minutes and cleaned before further characterization (All processes are conducted in ambient conditions).

- Perovskite QD/polymer composites: 60 µl of the composite solutions is deposited on the substrates using spin-coating at 3000 rpm for 40 seconds. After the deposition, the samples dry naturally for 15 minutes (All processes are conducted in ambient conditions).

b. PeLED fabrication

The fabrication process of PeLEDs follows the below procedures:

i) *ITO cathodes:* Preliminarily, the ITO-coated substrates are chemically etched to avoid a short-circuit occurring during the electrical characterization of PeLEDs. Accordingly, two edges of the substrates (around 1 mm on each side) are covered with scotch tapes, while the rest of the surface will be coated with one or two layers of nitrocellulose (rich in fingernail polish). This polymer coating is allowed to dry for 2-3 hours. Next, the substrates are dipped into hydrochloric acid 35% solution for 2-3 minutes at 50 °C, preferably in an ultrasonic bath, to accelerate the reaction. The etched ITO samples are then cleaned consecutively in deionized water (for removal of residual acid), acetone (for removal of the nail polish), ethanol, and Isopropanol. The ITO substrates are dried with nitrogen flow and treated with UV-Ozone for 15 minutes before transferring to the next step.

ii) ***PEDOT:PSS HTLs:*** PEDOT:PSS is deposited by spin-coating at ambient conditions. In particular, 30 minutes before the deposition, 1 mL of PEDOT:PSS solution is re-dissolved using an ultrasonic bath (15 minutes) and a magnetic stirrer hot plate (15 minutes at 50 °C). The solution is then filtered using a 0.45-µm hydrophobic PTFE filter. Next, 60 µL of the solution is dropped onto the substrate and spin-coated at 3000 rpm for 50 seconds, followed by thermal treatment at 100 °C for 40 minutes.

iii) ***LiF blocking layers:*** A LiF layer of ~ 1 nm is deposited via low-vacuum thermal evaporation. The evaporation is performed manually at low deposition rate of 2-3 Angstroms per second, under a high vacuum of 10^{-7} mbar.

iv) ***TPBi ETLs, Ca EILs, Ag electrodes:*** The depositions of these layers are performed using vacuum thermal evaporation technique. They are automatically conducted using preset programs at a deposition rate of 1 nm per second and under a high vacuum of 10^{-7} mbar. To shape the electrodes, we use a shadow mask defining four active areas of 4.53 mm² per substrate. The design of the mask is shown in Figure A1.
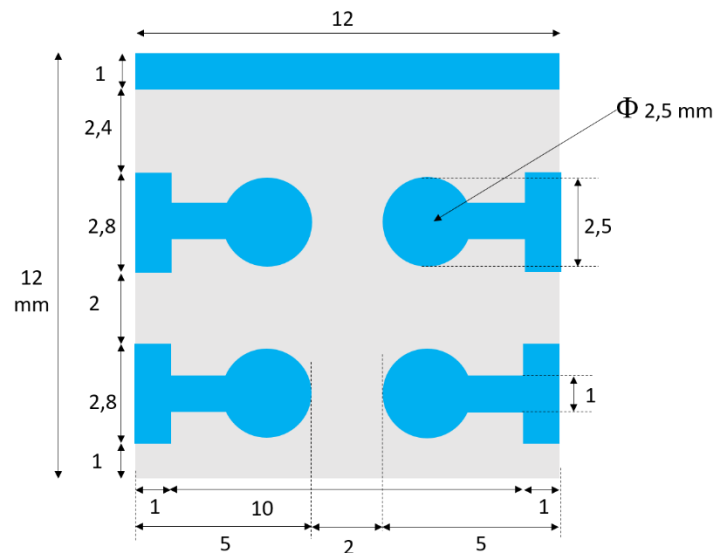

Figure A1. Schematic illustration of a shadow mask for cathode deposition

v) ***Al electrodes:*** Al electrodes are deposited via electron beam evaporation. The rate of deposition is < 1nm per second.

3. Thin-film characterization

a. Crystallinity and Morphology

- X-Ray Diffraction: we used a Bruker XRD platform - model D8 "Advance," CuKα X-ray source, λ = 0.154 nm, equipped with a focusing Kα1 mono filter, and detector LynxEye, model "A17-B60".

- Optical microscope: The microscopy images of the samples were taken using a Leica inspection microscope type DM12000M, connected with a Leica Digital Color Camera, type DFC295.

- Profilometry: thin films' thickness was measured using a Bruker profiler type DektakXT.

- SEM and FIB-SEM: we employed a focused ion beam - scanning electron microscope from Zeiss, model ZEISS Crossbeam 550

- TEM: High resolution TEM (HRTEM) images were taken with a Microscope Titan3 G2 80-300 (FEI ThermoFishers) operating at 200 kV.

- AFM: The measurements were conducted using a Nano-Observer AFM microscope from CSInstruments (Germany). The treatment of collected AFM images is done using the Gwyddion software (http://gwyddion.net/, Czech Republic). In particular, the root-mean-square roughness of the surface is estimated using the embedded roughness tools. The surface coverage is obtained by marking the upward crystal grains using the segmentation method before dividing the grain area by the total surface area.

b. Optical characterization

- UV-Vis absorption: The measurements were carried out by a Cary 300 Spectrometer from Agilent Technologies (US).

- Photoluminescence: The steady-state and time-resolved photoluminescence (PL) was measured using an FLS980 Spectrometer purchased from Edinburgh Instrument (UK). The analysis of the PL decay kinetics is proceeded using the built-in Fluorescence Analysis Software Technology (FAST) software.

- Micro-photoluminescence: The angle-resolved PL measurement was conducted using homemade micro-PL system at INL. Its set-up is shown in Figure A2.
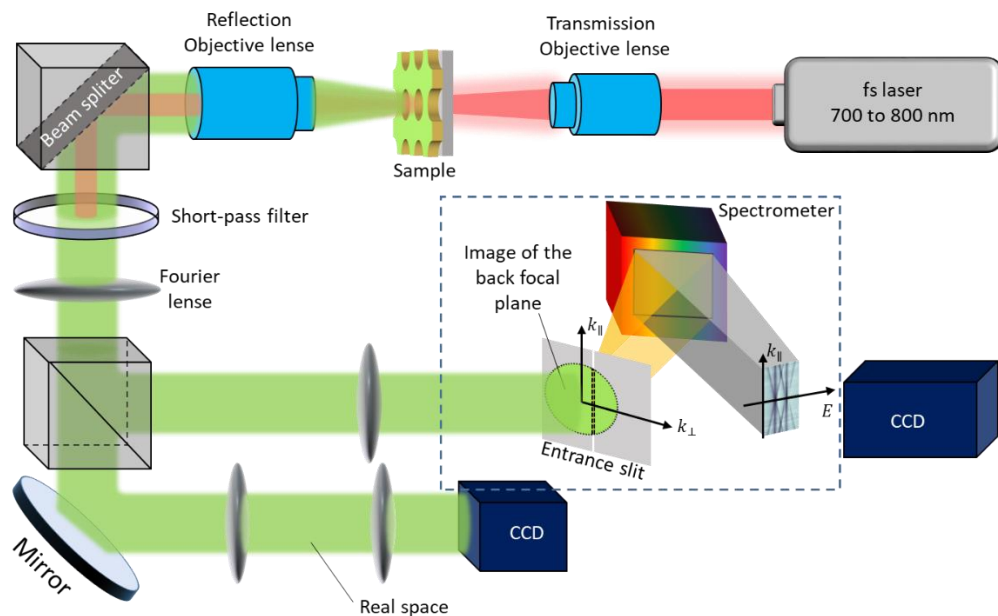

Figure A2. Micro-PL set-up for angle-resolved emission measurement at INL.

c. Temperature measurement

To record the temperature inside the spin-coating chamber, a digital thermometer RS40, with a resolution of 0.1 °C and a measurement rate of 1 Hz, from RS PRO (UK) was used.

4. PeLED characterization

a. Electroluminescence spectrum

The set-up to measure EL spectra (depicted in Figure A3) comprises: 1) a concave grating spectrometer BLACK-Comet from StellarNet, 2) an optical fiber to transmit the emitted light to the spectrometer, 3) a sourcemeter Keithley series-2400 fabricated by Keithley Instrument (USA) to supply the LEDs, and 4) a computer interface to read the data from the spectrometer.
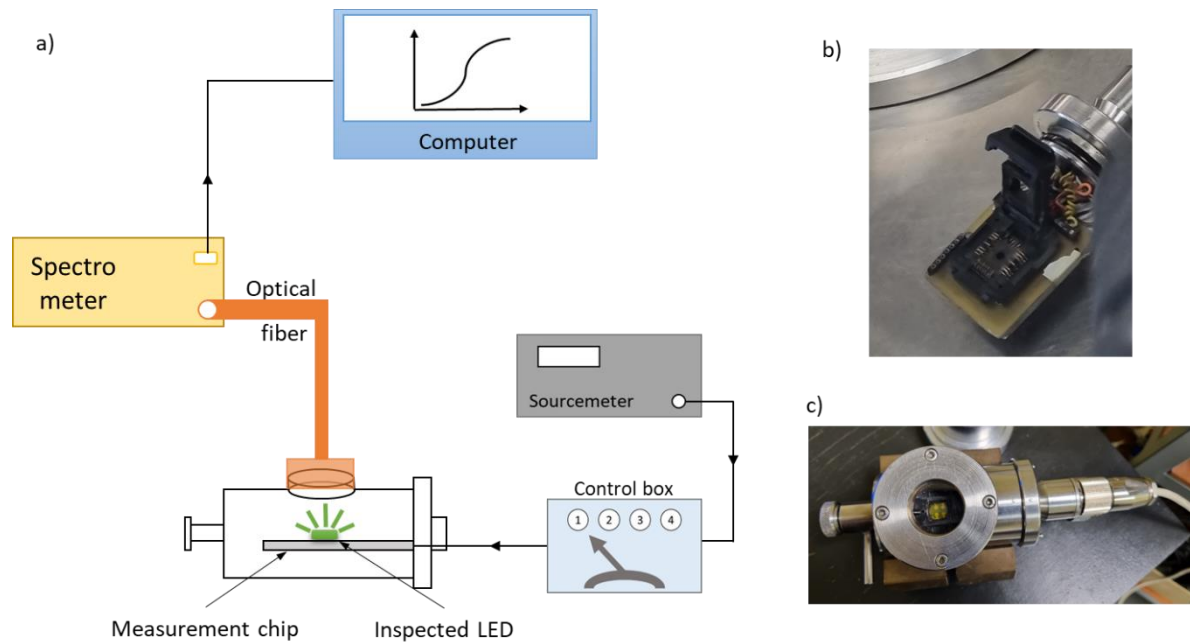

Figure A3. a) Set-up for the measurement of electroluminescence spectrum; Photos of b) the measurement chip and c) the substrate holder.

To prevent the impacts from ambient environment on the performance of PeLEDs, the test specimens are encapsulated inside a homemade enclosed holder filled with inert gas during the measurement. The electrical contact to the sourcemeter is realized using an integrated chip mounted inside the holder, which is connected to a control unit for choosing the specific pixels to examine. The photos of the measurement chip and holder are shown in Figures A3.b and c.

b. Measurement of J-L-V characteristics

The J-L-V measurement set-up comprises 1) a calibrated reference Centronic (UK) photodiode (type QD 100-5T with a 100 mm² active area), 2) a sourcemeter Keithley series-2400 fabricated by Keithley Instrument (USA) to supply the LEDs, 3) a Keithley series-2700 multimeter to measure the diode current, 4) a dedicated active amplifier to amplify the intensity I_{ph} at the output of the photodiode and 5) a computer interfaced through Labview to control the voltage source and read the voltage V_{ph} and the intensity I at the output of the multimeter and the source-meter unit.
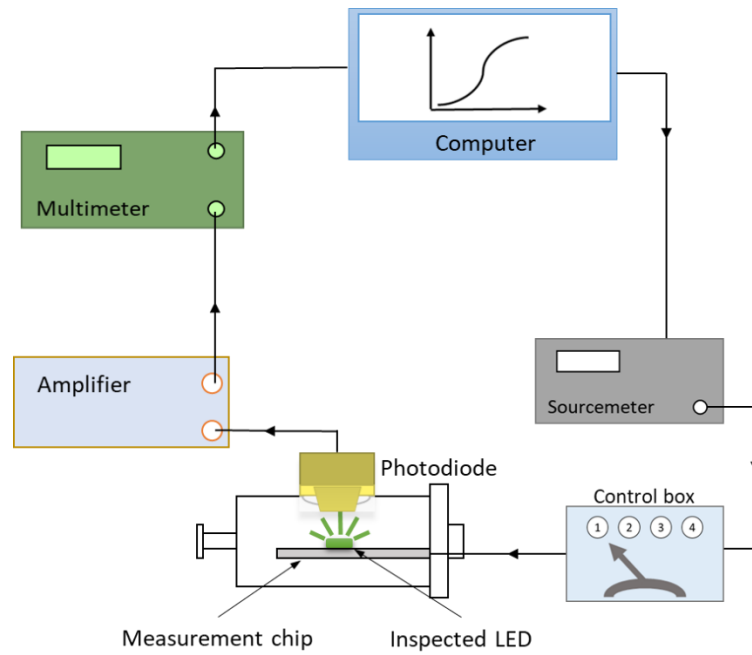
Figure A4. Set-up for measurement of PeLED's characteristic curves

c. Calculation of device metrics

In this study, the derivation of the PeLED's metrics, such as luminance, EQE, or luminous efficiency, follows the calculation presented by Anaya et. al. for a similar measurement set-up [127].

First, we need to deduce the effective solid angle Ω from which the point-source LED can see the active area of the photodiode, given the geometry of the measurement set-up (as depicted in Figure A5).
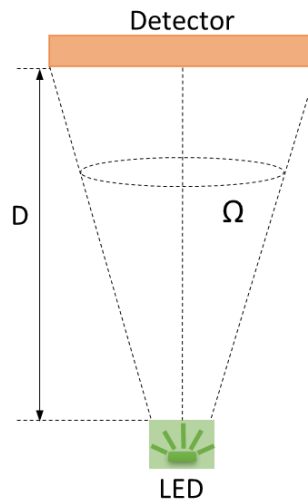

Figure A5. Geometrical dimensions between the LED and the photodetector in a LED measurement set-up.

Accordingly, the effective solid angle can be calculated as:

$$\Omega = 2\pi \left(1 - cos \frac{\sqrt{A_{det}/\pi}}{D} \right) \qquad \text{(Equation A1)}$$

in which A_{det} is the active area of the photodiode and D is the distance between the measured pixel and the photodiode. In our case, $A_{det} = 100 \text{ mm}^2$ and $D = 55 \text{ mm}$, then $\Omega = 0.033 \text{ sr}$.

Then, the EQE can be obtained based on its definition:

$$EQE = \frac{number\ of\ emitted\ photons\ escaping\ to\ free\ space}{number\ of\ electrons\ injected\ into\ the\ LED} = \frac{\phi}{I_{LED}/q} \qquad \textit{(Equation A2)}$$

with q is the elementary charge ($1.60217663 \times 10^{-19}$ Coulombs), ϕ is the photon flux from the LED passing to the forward viewing hemisphere, and I_{LED} is the read-out current of the measured device. In addition, the photon flux can be calculated from the effective solid angle and the characteristics of the photodiode itself, such as:

$$\phi = \pi \cdot \frac{H}{C} \cdot \frac{V_{det}}{\Omega} \qquad \textit{(Equation A3)}$$

with H is the sensitivity of the photodetector, C is the photodetector's quantum efficiency weighted by the EL spectrum of the emitting device, and V_{det} is the output voltage of the photodetector.

The PeLED's luminance is computed as:

$$L = \frac{H}{C} \cdot \frac{K}{\Omega . A_{LED}} \cdot V_{det} \qquad \textit{(Equation A4)}$$

with K is a conversion constant representing the perception of light by the human's eyes ($K = 8.36 \ x10^{-17}$ lm·s·photon^{-1}) and A_{LED} is the active area of the examined PeLED (in our case, $A_{LED} = 4.53$ mm^2).

And, therefore, the luminous efficiency can be deduced as:

$$LE = \frac{\pi.H.K}{C.\Omega} \cdot \frac{V_{det}}{V_{LED}.I_{LED}} \qquad \textit{(Equation A5)}$$

d. Estimation of measurement errors

• The Keithley error ($\Delta V_{ph}/V_{ph}$) associated with V_{ph} measurement is 5.5%;

• The error for the charge resistance ($\Delta R/R$) is estimated at 0.5%;

• The error of the photodiode sensitivity at 530 nm ($\Delta\sigma/\sigma$) is approximately 1%;

• The LED diameter error ($\Delta D/D$) for the LED surface value is close to 4%;

• The error on the distance between LED and photodiode ($\Delta d/d$) is 1.2%.

So, cumulatively, the measurement error is estimated as:

$$(\Delta L/L) = (\Delta V_{ph}/V_{ph}) + (\Delta R/R) + (\Delta\sigma/\sigma) + 2(\Delta D/D) + 2(\Delta d/d) = 17.4\ \% \qquad \textit{(Equation A6)}$$

Annex 2: Fitting of photoluminescence decay in perovskite thin films

The exponential component analysis of PL decay regarding perovskite thin films in general and MAPB in particular follows the below function:

$$R(t) = \sum_{i=1}^{n} A_i . exp\left(-\frac{t}{\tau_i}\right) \qquad \textit{(Equation A7)}$$

in which, *R(t)* is the number of counted photons at a time t, A_i is the amplitude of the ith exponential component, and τ_i is the time constant of the ith component.

Figure A6 shows the fitting of an experimental measurement of MAPB's PL lifetime using bi-exponential (i.e., n = 2) and tri-exponential (i.e., n = 3) decay models, implying that the emission decay kinetics can only be sufficiently explained using the tri-exponential analysis. The fitting parameters are detailed in Tables A2 and A3.
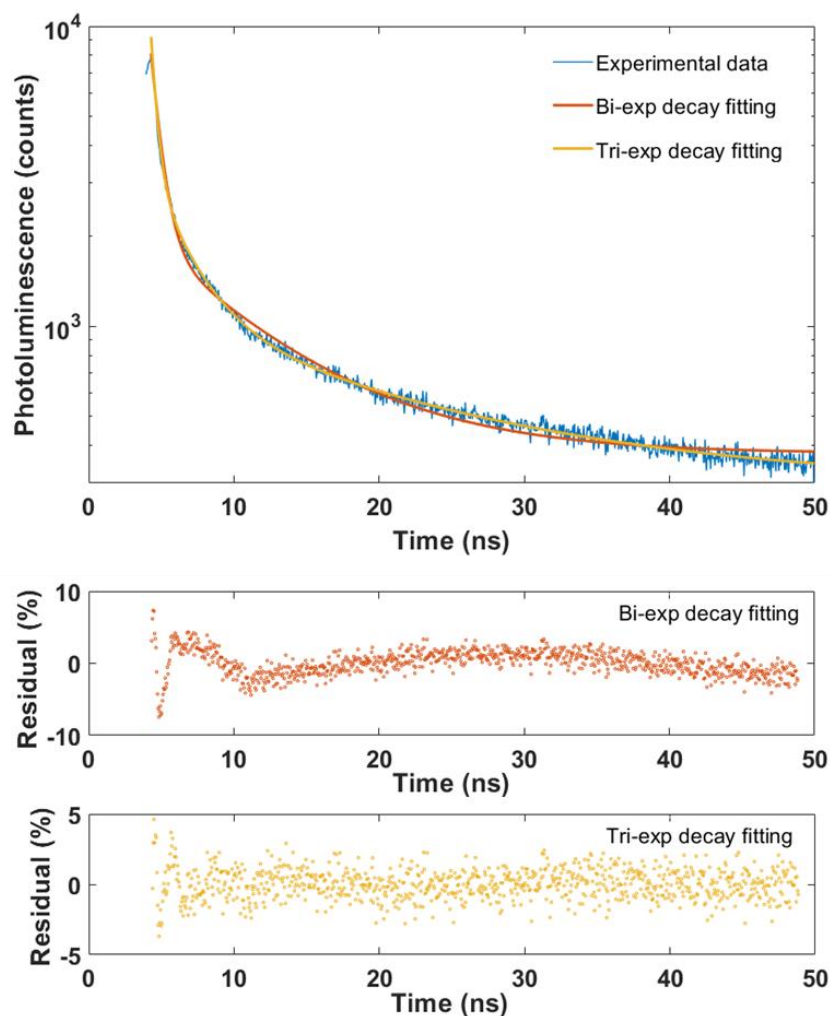

Figure A6. Fitting of MAPB's photoluminescence decay using bi and tri-exponential decay models.

Table A3: Exponential component analysis of MAPB's decay using Bi-exponential decay model

	A_i (counts)	τ_i (ns)	p_i (%)	
1	6229.0420	0.680	25.576	$\chi^2 = 3.009$
2	1517.8165	8.116	74.424	

Table A4: Exponential component analysis of MAPB's decay using Tri-exponential decay model

	A_i (counts)	τ_i (ns)	p_i (%)	
1	5988.1587	0.403	11.576	$\chi^2 = 1.198$
2	2138.9036	2.576	26.429	
3	790.5627	16.351	61.351	

Annex 3: Device performance of PeLEDs

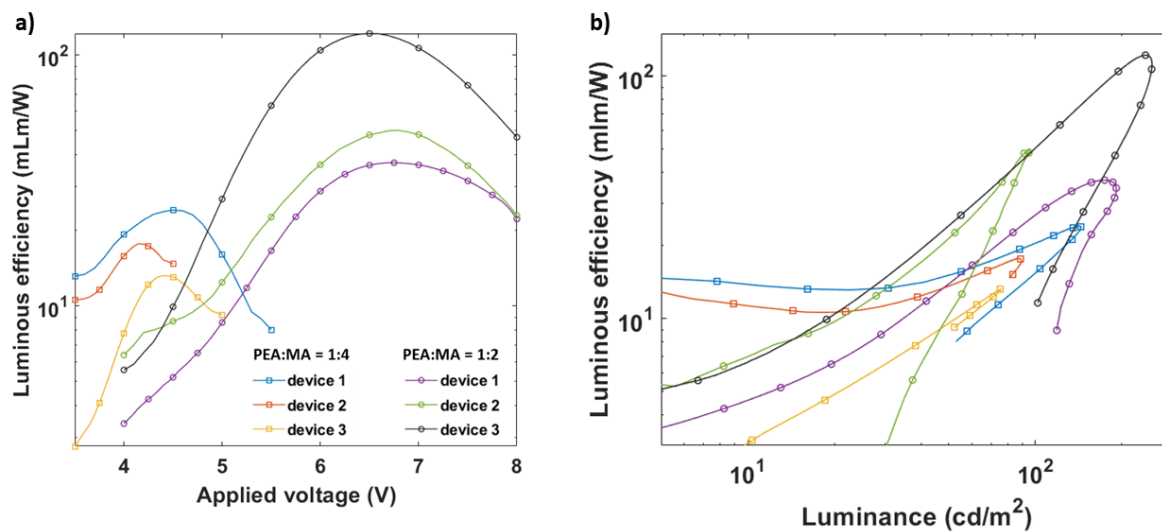### 1. Quasi-2D PeLEDs without LiF interlayer

Figure A7. Evolution of luminous efficiency with a) bias voltage and b) luminance in non-passivated quasi-2D PeLEDs.

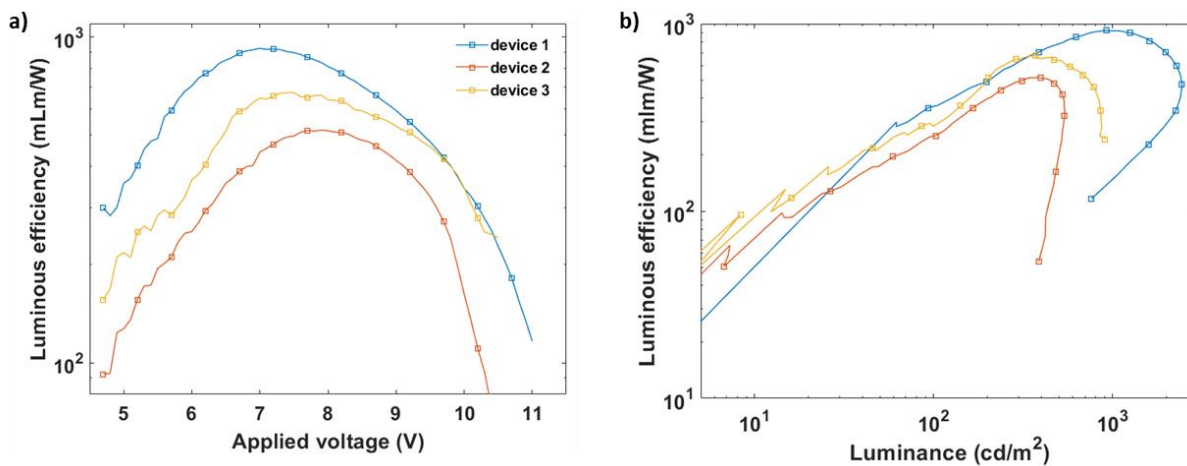### 2. Quasi-2D PeLEDs with LiF interlayer

Figure A8. Evolution of luminous efficiency with a) bias voltage and b) luminance in LiF-integrated quasi-2D PeLEDs.

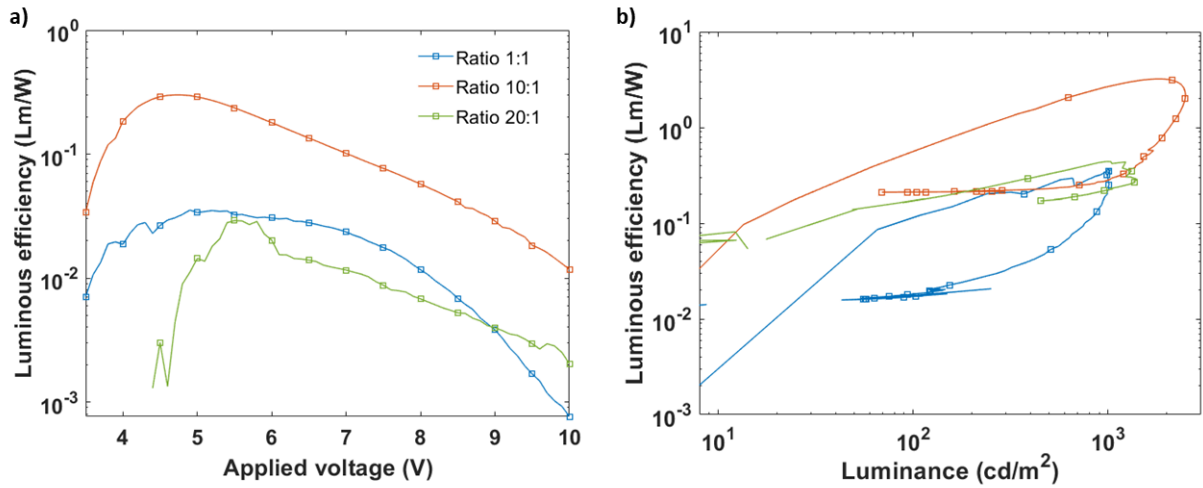### 3. Quantum dot PeLEDs based on QD/PMMA composites

Figure A9. Evolution of luminous efficiency with a) bias voltage and b) luminance in PeLEDs based on perovskite QD/PMMA composites

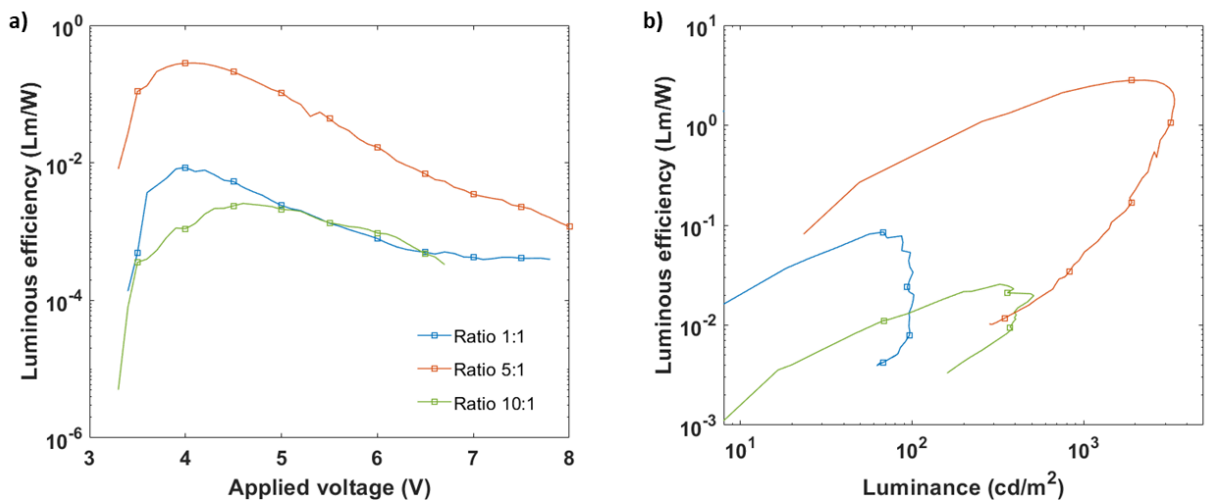### 4. Quantum dot PeLEDs based on QD/PEO composites

Figure A10. Evolution of luminous efficiency with a) bias voltage and b) luminance in PeLEDs based on perovskite QD/PEO composites